Magnetic Resonance Angiography

27th Annual International Conference – www.mraclub.com

Cincinnati 2015 Abstracts

President: Jeffrey Maki

Organizers: Charles Dumoulin
Robert Fleck

September 15-18, 2015
Cincinnati, Ohio

Table of Contents

Oral Presentations

14. Greater non-compacted myocardial mass index in patients with clinically significant LVNC
Jeremy Collins

15. 4D flow MRI for intracranial hemodynamic assessment in Alzheimer's disease
Leonardo Rivera

16. PC-MRI based simulation of contrast-injection in cerebral aneurysms
Loic Boussel

17. Absolute Local Normalized Helicity in Patients with Bicuspid Valve and Aortic Dilatation
Julio Garcia

18. Left Atrial 4D Flow MRI: Stasis and Velocity Mapping in Patients with Atrial Fibrillation
Michael Markl

19. Differences between 4D flow, 2D One-directional and 2D Three-directional Velocity-encoded MRI Sequences for the Estimation of Aortic Flow and Velocity
Emilie Bollache

20. Turbulence tensor quantification using ICOSA6 flow encoding
Henrik Haraldsson

21. High Resolution 4D Flow and CE-MRA utilizing Ultrashort Echo Times: Feasibility of linking Vessel Wall Enhancement, Morphology, and Hemodynamics **Kevin Johnson**

22. Identifying Motion Corruption in DCE Radial Stack of Stars Data
Jason Mendes

23. Very Short Blood T2* with Gd-based Contrast Reagents: Investigating BMS Shift
Gregory Wilson

24. DESIRE: Efficient MRI reconstruction with Split Bregman initialization and sparse regularization based on pre-learned dictionary **Artem Migukin**

25. Vessel- and Dose-specific Differences in Contrast-enhanced Time-resolved 4D-MRA: An Intra-individual Quantitative and Qualitative Comparison of Gadopentetate Dimeglumine and Gadobutrol in Minipig **Vera Keil**

26. Accelerated Time Resolved Contrast Enhanced MRA of Dural Arteriovenous Fistulas using Highly Constrained Reconstruction of Sparse Cerebrovascular Datasets
Zachary Clark

27. Steady-state ferumoxytol enhanced magnetic resonance angiography of the lower extremities provides optimal characterization of vascular lesions for peripheral arterial disease patients with renal failure **Evan Lehrman**

28. Ferumoxytol enhanced Magnetic Resonance Angiography in stage 4 and 5 Chronic Kidney Disease **Alex Vesey**

29. Ferumoxytol in TAVR Workup **Paul Finn**

30. Ferumoxytol MRA as an Alternative to CTA for Common Chest Indications: TAVR and Pulmonary Embolism **Michael Hope**

31. DARC-MR Lymphangiography Using a Combination of Gadolinium and USPIO Contrast: an Update **Jeffrey H. Maki**

32. Ferumoxytol in Pediatric Congenital Heart Disease: Early Results with 4D Multiphase Steady State Imaging with Contrast (MUSIC) Enhancement **Kim-Lien Nguyen**

33. Adverse reactions to intravenous administration of ferumoxytol intended for use as magnetic resonance imaging contrast **Alex Vesey**

34. Ferumoxytol MRA: Minimizing Table Time in Claustrophobic Patients **Paul Finn**

35. Ferumoxytol-Enhanced Motion-Corrected Accelerated 4D Flow MRI as a Single Sequence Congenital Heart Disease Exam: Validation of Functional and Segmental Analysis **Joseph Cheng**

36. Accelerated Four-dimensional, Multi-phase, Steady-state Imaging with Contrast Enhancement using Parallel Imaging and Compressed Sensing **Ziwu Zhou**

37. Cardiac and Respiratory Self-Gated 4D Multi-phase Steady-state Imaging with Ferumoxytol Contrast (MUSIC) **Fei Han**

38. Quantitative myocardial perfusion with dynamic ferumoxytol enhanced MRI **Aleksandra Radjenovic**

39. Flip-Angle optimization in Ferumoxytol-MRA: Preliminary results using different dose schemes and comparison with Gadobenate-MRA **Tilman B. Schubert**

40. Time of Arrival Parametric Mapping derived from Fast High Resolution Whole Brain Contrast Enhanced 4D MRA improves the anatomic display of contrast kinetics in patients with brain vascular malformations. **Tilman B. Schubert**

41. Intracranial Dual-Venc 4D flow MRI at 7T **Susanne Schnell**

42. Comprehensive Cerebrospinal Venous Assessment in Patients and Healthy Controls – Results from CCSVI Study **Eric M Schrauben**

43. Evaluation of the renal arterial wall with High Resolution MR imaging after endovascular renal denervation **Salim Si-mohamed**

44. Flow induced artifacts in two-point Dixon fat-water separation: Incidence and potential diagnostic pitfalls **Tilman B. Schubert**

45. Compact 3T Scanner: Initial Experience with 80 mT/m, 700 T/m/s Gradients **Matt A. Bernstein**

46. Contrast-Enhanced Perianal Fistula Imaging with Dixon-Based Fat Suppression **Eric Stinson**

47. Revisit of Non-Contrast Aortic Arch FBI at 3T **Mitsue Miyazaki**

48. 7-Minutes Fresh Blood Imaging using Variable TR and Variable Refocusing Flip Angle for Non-Contrast Peripheral MR Angiography at 3T **Xiangzhi Zhou**

49. Breath-hold Inner-Volume Radial Quiescent-Interval Slice-Selective (QISS) of the Heart, Aorta and Renal Arteries **Robert R. Edelman**

50. Quiescent-Interval Slice-Selective Fast Low-Angle Shot Magnetic Resonance Angiography of the Extracranial Carotid Arteries **Ioannis Koktzoglou**

51. Non-Contrast Myocardium Perfusion: Technical Differences between 4D Time-SLIP with Tagging Aortic Root and FAIR **Mitsue Miyazaki**

52. Characteristic Streak Frequency Filtering with Modulo-Prime Spokes (MoPS) Cine-CMR **Keigo Kawaji**

53. A qualitative assessment of first-pass perfusion bolus timings in the assessment of myocardial ischemia: A magnetic resonance study **Jonathan Weir McCall**

54. Longitudinal assessment of renal perfusion and oxygenation in transplant donor-recipient pairs using ASL and BOLD MRI **Sean Fain**

55. High resolution MRI for characterization of inflammation within abdominal aortic aneurysm **Chengcheng Zhu**

56. Motion insensitive Carotid Artery Wall Imaging Using Stack of Stars technique and Inversion Recovery preparation (3D IR-Prep-SOS) **Seong-Eun Kim**

57. 3D Black Blood VISTA Magnetic Resonance Vessel Wall Imaging of the Thoracic Aorta in Young, Healthy Adults: Reproducibility and Implications for Efficacy Trial Sample Sizes Tim Leiner

58. Intracranial Vessel Wall MR Registry **Qi Yang**

59. Intracranial Vessel Wall Imaging at 3T and 7T **David Saloner**

60. Evaluation of Dissecting Aneurysm Wall of Vertebral Artery Using 3T MRI **Keiji Igase**

61. Carotid plaque permeability measured by high and low molecular weight contrast **Jason Mendes**

62. A Paradigm Shift in Cardiac MRI? Motion Reconstruction Rather Than Motion Correction **Matthias Stuber**

63. **Bayer Gold Sponsor Talk:** Two International, Multicenter Phase 3 Studies Evaluating both the Assessability and Quantitative Accuracy of Gadobutrol Enhanced MRACompared to Time-of-Flight (ToF) MRA in the Supra-Aortic and Renal Arteries **Jacob Agris**

Poster Presentations

P1. Classification of human peripheral arterial atherosclerotic plaques with T2 and Ultra-short echo time MRI **Trisha Roy**

P2. Global measures of myocardial strain predict infiltrative cardiomyopathy at heart deformation analysis: A feasibility study at 1.5T **Marcos Ferreira Botelho**

P3. Dynamic MR Imaging of Carotid Webs **Mari E. Boesen**

P4. In vivo Cardiac Blood Oxygen Saturation Mapping using Quantitative Susceptibility Mapping **Yan Wen**

P5. High Resolution Whole Heart Coronary Plaque Characterization with Integrated Anatomical Reference **Yibin Xie**

P6. Patient-specific 3D printed models of the aorta for pre-procedural planning in transcatheter aortic valve replacement: A proof of concept study **Beth Ripley**

P7. MR Evaluation of the Cerebrovasculature in the Neonatal ICU **Jean Tkach**

P8. Ferumoxytol across the Age Spectrum: a Single Center Experience of Safety **Kim-Lien Nguyen**

P9. Black-Blood Late Gadolinium-Enhancement MR Imaging of Myocardium **Gregory Wilson**

P10. Assessment of tortuosity and flow in abdominal aortic aneurysms with ferumoxytol-enhanced magnetic resonance imaging **Farshid Faraji**

P11. Signal intensity measurement of the liver vessels in patients suffering from liver lesions with Gd-Eob-DTPA and Gd-BOPTA enhanced MRI/ MRA **Manuela Aschauer**

P12. Diffuse myocardial fibrosis in diabetes mellitus type-II (DM-II) assessed by Cardiac Magnetic Resonance T1 mapping technique: preliminary results. **Federica Ciolina**

P13. Application of Full Turbulent Tensor in Estimation of MR-Based Relative Pressure **Sarah Kefayati**

P14. Feasibility of time-of-flight MR angiography in human pregnancy for imaging the fetal and placental vasculature **Uday Krishnamurthy**

P15. A 9 Channel Carotid Coil Designed for Integration with Clinical Head coils **Michael J. Beck**

P16. Fusion of Ferumoxytol MRA and Non-Contrast CT in TAVR Planning
Takegawa Yoshida

P17. Estimating brain distensibility with quantitative magnetic resonance cerebrospinal fluid flow measurements **Annamarie T. Helpling**

P18. Arm position alters the geometry of Brachial artery and Basilic vein
Conor Macdonald

P19. Free-Breathing Non-Contrast Pulmonary MRA in the Neonatal ICU
Jean Takch

P20. Quantification of myocardial motion patterns in patients with hypertrophic- and dilated-cardiomyopathy using heart deformation analysis **Kai Lin**

P21. Linear sign in cystic brain lesions ≥ 5mm on T2-weighted images and time-of-flight MR angiography: A suggestive feature of enlarged perivascular space on 3.0-T MR imaging
Bum-Soo Kim

P22. Single Breath-Hold Real-Time Cardiac Cine MR for Evaluation of Left Ventricular Function
Tomoyuki Kido

P23. Carotidynia MRI imaging findings **George Bolotin**

Optimizing Bolus Injection of Gd-Based Contrast Agents for MR Angiography

Gregory J. Wilson and Jeffrey H. Maki
University of Washington, Department of Radiology, Seattle, WA, USA

Introduction: Contrast-enhanced MRA (CE-MRA) is performed during the 1st pass of a gadolinium contrast agent. Typically, the full dose of contrast is injected by a power injector at a rate of 1.5 – 2 ml/s, followed by saline flush at the same rate. Centric image acquisition begins at peak enhancement using "fluoro" triggering or a test bolus. The temporal variation in enhancement can cause blurring and ringing artifacts in the images. The purpose of this study is to improve the enhancement profile, and ultimately improve CE-MRA image quality.

Methods: This study was approved by the local IRB. 20 subjects were randomized to receive either a standard or "tailored" injection (antecubital vein via power injector) of single-dose (0.1 mmol/kg) gadoteridol, and resulting signal intensity profiles were measured for 100 sec to capture pre-Gd baseline, 1st pass, and recirculation. Prior to each full injection, a test bolus was administered. Standard injections were non-diluted, single-dose volumes (less the test bolus volume) injected at our institutional standard 1.6 ml/s. The test bolus for this group consisted of 1 ml at 1.6 ml/s. Tailored injections utilized a novel optimization algorithm to determine the best multi-phase ($\leq$ 3 phases) injection of single-dose, diluted (with saline to 40 ml total volume) gadoteridol (Bracco, Princeton, NJ). The optimization utilized linear prediction of contrast concentration profiles (based on the response from the test bolus) for arbitrary injection schemes, and targeted a signal intensity (SI) plateau of 15-20 sec duration. The test bolus for this group consisted of 2 ml diluted contrast, injected at 2 ml/s. Signal intensity profiles for all injections were measured at 3T (Ingenia, Philips, Best, the Netherlands) using a multi-dynamic, 3D, T1-FFE acquisition (temporal resolution < 2 s) covering the entire aorta to reduce inflow effects. Time-intensity curves were gathered from a single ROI placed in the descending aorta inferior to the diaphragm. After normalization to baseline SI, maximum SI and full width at 80% max (FWM_{80}) SI were measured.

Results: The single-phase injections were markedly "peaked", demonstrating a quite narrow maximum SI duration (Fig. 1 left), with FWM_{80} = 8.8 $\pm$ 3.8 s. The bolus-tailoring prediction algorithm worked well to achieve the desired result of a uniform SI plateau (Fig. 1 right) with significantly increased duration, FWM_{80} = 23.7 $\pm$ 2.5 s (Fig. 2 top - $p < 0.01$). At the same time, only a small degree of SI was sacrificed to achieve this longer duration tailored bolus (-19.5%, Fig. 2 bottom - $p = 0.05$).

Discussion: Using a predictive algorithm with a small test bolus of contrast allows for patient-specific "shaping" of an enhancement profile to achieve a much longer and more uniform plateau than does a single-phase injection. As suggested based on the multi-factorial sub-linearity of SI with increasing contrast concentration (1,2), this prolonged plateau comes at the expense of only mild SI decrease (ie, almost three times the peak duration while maintaining ~80% of the peak signal). A longer bolus duration more matching image acquisition will likely decrease artifacts caused by vascular signal decay during peripheral k-space acquisition, and should improve CE-MRA image resolution and quality. This suggests the conventional method of injecting Gd contrast at a fixed and relatively fast rate is flawed. Future work will evaluate the impact of tailored boluses on CE-MRA image quality.

References: (1) Wilson GJ, Woods M, Springer CS Jr, Bastawrous S, Bhargava P, Maki JH. *Magn Reson Med* 2014;72:1746–54. (2) Wilson GJ, Springer CS Jr, Woods M, Bastawrous S, Bhargava P, Maki JH. *PISMRM*, Salt Lake City, UT, 2013, p4459.

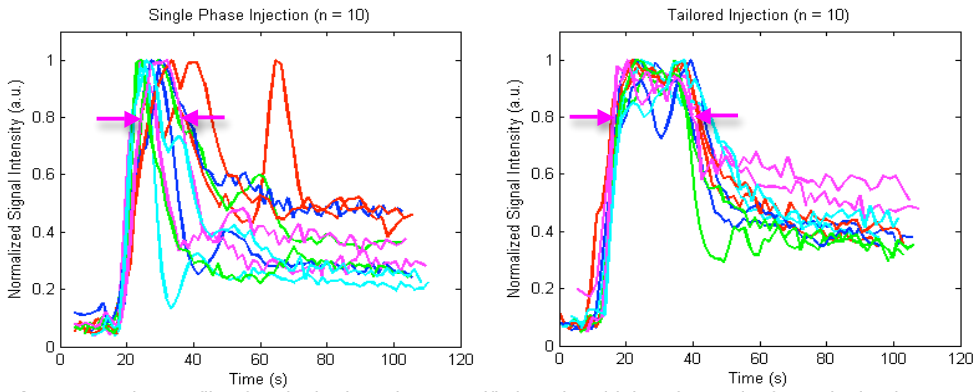

Figure 1. Bolus profiles for single-dose (0.1 mmol/kg) gadoteridol. Left: results from single-phase, 1.6 ml/s injections. Right: results from tailored injections. Profiles were time-shifted to align bolus arrival times and normalized to maximum peak height. Arrows demonstrate full width at 80% max duration for magenta curve. Note sharp and variable duration profiles from the standard injection (one outlier [red curve] had exceptionally large secondary peak), while tailored injections produced consistent approximately 20 s duration signal intensity profiles.

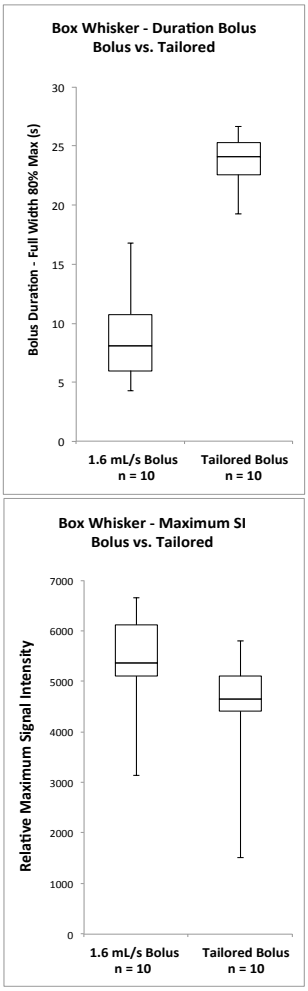

Figure 2. Box Whisker plots demonstrating bolus duration (Full-Width 80% Maximum SI) (top) and Maximum SI (bottom) for single-phase vs. tailored injections. Note plateau SI duration was dramatically greater for tailored injection ($p < 0.01$), with only slight SI loss ($p = 0.05$).

The Safety and Efficacy of Pediatric Contrast Enhanced Magnetic Resonance Angiography using Multihance (Gadobenate Dimeglumine)

Sarah N Khan,MD; Elena Karavaeva MD, Leila Mostafavi MD, Simon Gabriel MD, Ines Boechat MD; J. Paul Finn, MD

Purpose:
The safety and efficacy of gadolinium based contrast agents (GBCA) in neonates and infants with immature renal function has not clearly been established. Nephrogenic systemic fibrosis has been associated with exposure to GBCAs in patients with kidney disease and is used with caution in neonates and infants. The purpose of this study is to investigate the safety and efficacy of gadobenate dimeglumine 'Multihance' (Bracco Diagnostics Inc., Princeton, USA) for vascular evaluation in pediatric patients, as reflected in the incidence of adverse events and the technical and diagnostic quality of MR angiograms at 1.5T and 3.0T.

Methods:
188 pediatric patients referred for non-neurological assessment at 3.0T (107) or 1.5T (81), were retrospectively reviewed. Indications were cardiac (84), vascular (47), liver (32), gastrointestinal (18), genitourinary (n = 4) and pulmonary (3) disease. Age and Multihance dosage (mmol/kg): 0-1 month (n=12, 0.19 ± 0.03); 1-6 months (n=8, 0.16 ± 0.03); 6 months – 1 yr (n=12, 0.15 ± 0.03); 1 yr – 2 yrs (n=14, 0.14 ± 0.05); 2 yrs-5 yrs (n=24, 0.14 ± 0.04); 5 yr-12 yrs (n=44, 0.13 ± 0.03); 12 yrs -18 yrs (n=74, 0.11 ± 0.33). 95 patients underwent controlled ventilation, 93 underwent breath holding without sedation. Technical and diagnostic quality was assessed by SNR and CNR calculations and scoring of vessels for image quality, artifacts, vessel definition. Serious adverse events, vital signs and serum laboratory values were noted.

Results:
All studies were good or excellent diagnostic quality. Image quality and artifact scores were higher at 3.0T than 1.5T (3.77 ± 0.42 and 3.55 ± 0.53) and (1.48 ± 0.46 and 1.00 ± 0.71). SNR and CNR were higher ($p<0.05$) for arteries at 3.0T than 1.5T. The heart rate, blood pressure and serum levels (sodium, urea, calcium, creatinine, chloride, albumin, bilirubin, liver enzymes) were unchanged in 100% of patients after the MR study.

Conclusion:
Our results show that high resolution MR imaging of the thorax, abdomen and pelvis can be performed safely and reliably in children of all ages over a broad spectrum of disease, using gadobenate dimeglumine at a dose of ~ 0.2 mmol /kg. The efficacy end points of this study were reflected in the technical success and high diagnostic quality of the angiographic images. No serious adverse events or changes in vital signs or laboratory data were found.

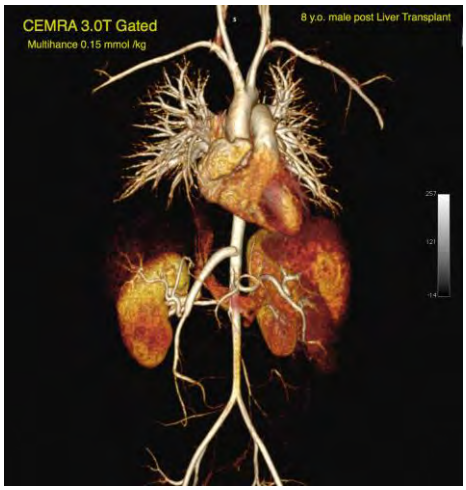

Figure 1: Volume rendered CEMRA with Multihance 0.15 mmol /kg in an 8 year old male patient status post successful liver and small bowel transplantation. Note the widely patent donor hepatic and mesenteric arteries

Combined low-dose time-resolved and single-phase high resolution spinal CE MRA: evaluation of spinal vascular malformation

Bum-soo Kim[1], Jieun Baek[1], Jinhee Jang[1], Hyun Seok Choi[1], So-Lyung Jung[1], Kook-Jin Ahn[1], Tae-Sub Chung[2]

[1]The Catholic University of Korea, [2]Yonsei University Medical College, Seoul, Korea

Introduction and Purpose: Spinal cord MRA is useful in preangiographic evaluation of spinal vascular diseases, but limited FOV makes their detection in a single MRA session difficult1-3. We report combined low-dose time-resolved and single-phase high-resolution (HR) contrast-enhanced MRA (CE-MRA) at 3.0T that has the potential to be performed in a single session.

Methods: We retrospectively reviewed the CE-MRA of 10 consecutive patients with a spinal vascular disease confirmed by DSA. All patients underwent combined low-dose time-resolved CE-MRA and 3D single-phase HR CE-MRA at 3T. Lesions were analyzed for the type of spinal vascular disease, the side, level, and number of arterial feeders.

Results: CE-MRA correctly diagnosed spinal AVM (n=5) and spinal dural arteriovenous fistula (DAVF) (n=5). Low-dose time-resolved CE-MRA demonstrated early venous visualization and aided proper placement of following HR CE-MRA in all patients including 2 patients with high or low level of shunt and feeding artery. HR CE-MRA exactly localized the arterial feeder in 8 patients, and within one vertebral level in remaining one patient.

Discussion: With injection of 0.03 mmol/kg of gadolinium-based contrast agent, low-dose time-resolved CE-MRA in our protocol facilitated evaluation of the arteriovenous shunt and flow pattern of venous drainage. In addition, low-dose time-resolved CE-MRA in our series was used as a test bolus sequence to ensure timely bolus arrival during acquisition of the following single-phase HR CE-MRA with injection of 0.1 mmol/kg of contrast agent, which allows less repeated examination and smaller total dose (0.13 mmol/kg) of injected contrast media compared to previous reports [1-3].

Conclusion: Combined acquisition of low-dose time-resolved CE-MRA and single-phase HR CE-MRA at 3T is useful for preangiographic evaluation of spinal vascular diseases in a single session.

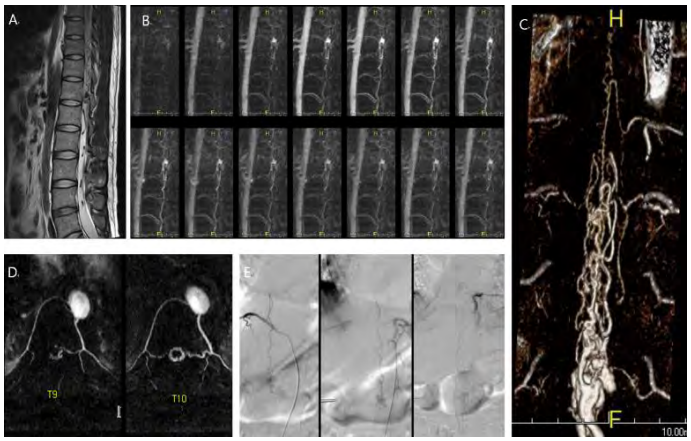

Figure 1. A 31-yr-old man with spinal perimedullary AVF. Sagittal T2WI (A) showed vascular signal voids. Serial MIP images of low-dose time-resolved CE-MRA (B) showed early visualization of dilated venous sac. VR reconstruction image (C) and segmental MIP images (D) of HR CE-MRA suggested feeders of the shunt including anterior spinal artery from left T9 level and posterior spinal arteries from both T10 levels. Spinal DSA (E) confirmed spinal perimedullary AVF with matched level of feeding arteries from posterior spinal arteries,, and collateral supply to the fistula from anterior spinal artery from left T9 level through the basket.

The impact of intensive training in inexperienced observers on analysis of stenosis and global atheroma burden in whole-body magnetic resonance angiography

Lynne McCormick[1], Sylvie Aikman Green[2], Jonathan Weir-McCall[1], Richard White[3], Emmanuel Trucco[4], J Graeme Houston[1]

1. The Institute of Cardiovascular Research, University of Dundee, UK. 2. School of Medicine, University of Dundee, UK. 3 Clinical Radiology, University Hospital of Wales, UK. 4 School of Computing, University of Dundee, UK.

Purpose:
Whole-body magnetic resonance angiography (WB-MRA) allows the stratification and quantification of systemic atheroma burden. Currently interpretation and scoring of the image datasets requires extensive analysis and radiological expertise. This study aims to investigate if a short intensive teaching period can result in accurate analysis of these datasets by observers without prior experience in magnetic resonance imaging.

Methods:
WB-MRA was performed on a 3T MRI scanner with gadoterate meglumine using a dual bolus injection technique. The WB-MRA datasets of 20 patients were analysed by two radiologists (R1 and R2) and two students (S1 and S2) who had undergone a short intensive training period. The whole body angiogram was divided into 37 separate arteries, with longer vessels divided into up to 5 segments, giving a total of 159 segments to score per dataset. Each segment was scored according to the most severe stenosis in that segment using a categorical grading scale: 0= no stenotic disease; 1= 1-30% stenosis; 2= 31-50% stenosis; 3= 51-70% stenosis, 4= 71-99% stenosis; 5= complete occlusion of the vessel. From this the whole body atheroma score was calculated by summating the results and normalising to the number of assessable segments. Analysis was performed twice by all observers to derive inter and intra-observer reproducibility. Cohens kappa was used to calculate intra- and inter-observer reproducibility for the ordinal stenosis scoring, while a spearman rank correlation co-efficient was used to calculate correlation of the whole body atheroma score between readers. All statistical analysis was performed using SPSS v21 (Chigaco, IL, USA).

Results:
For categorical stenosis grading of the 159 arterial segments: intra-observer reproducibility was fair for both radiologists (kappa R1=0.49±0.02, R2=0.54±0.02) and for the students (kappa S1=0.5±0.02 and S2=0.41±0.02); Inter-observer reproducibility was fair between the radiologists (kappa R1xR2=0.53±0.01), and fair between the radiologist and both students (kappa R2xS1=0.5±0.01 and R1xR2=0.4±0.02). For whole body atheroma scoring there was high intra-observer correlation for both groups (R1: R=0.87, R2: R= 0.93, S1: R= 0.92, S2: R= 0.89), with similar high inter-observer correlations between radiologists (R1xR2: R= 0.97) and between the radiologists and students (R2xS1: R= 0.95, R2xS2: R= 0.95, S1xS2: R= 0.93).

Conclusions:
After a short training period students demonstrated fair levels of reproducibility for stenosis categorization and high correlation for whole body atheroma quantification. Both reproducibility and correlation for the students were only slightly lower than that for the experienced radiologists. Thus it is possible to train inexperienced observers for whole body MRA analysis in a relatively short period of time.

Robust and Efficient Estimation of Optimum Perfusion Parameters in Dynamic Contrast-Enhanced MRI of the Prostate

Soudabeh Kargar[1], Eric G. Stinson[2], Eric A. Borisch[2], Adam T. Froemming[2], Akira Kawashima[2], Lance A. Mynderse[2], Joshua D. Trzasko[2], Stephen J. Riederer[2]

[1]Biomedical Engineering and Physiology, Mayo Graduate School, [2]Mayo Clinic, Rochester, MN, United States

Introduction: Dynamic Contrast-Enhanced MRI (DCE-MRI) is a vital component of multi parametric MRI for diagnosis and staging of prostate cancer. It is particularly useful for assessment of tumor angiogenesis and monitoring the effectiveness of therapy and recurrence. It is known that the pharmacokinetic parameters $K_{trans}[min^{-1}]$ (volume transfer constant between blood plasma and extravascular extracellular space or transfer constant) [1] and $K_{ep}[min^{-1}]$ (rate constant) vary between benign and malignant tissue. Thus, it is critical to obtain accurate estimates of these parameters. The purpose of this work is to develop a robust and efficient numerical optimization strategy to find the (nonlinear) least squares estimates of K_{trans} and K_{ep} from a time series of 3D images showing contrast transit.

$$I = I(K_{trans}, K_{ep}, t) = K_{trans} e^{-K_{ep} t} = H(K_{ep}) K_{trans} \quad (1)$$

$$P(t) = AIF \otimes I = AI = AH(K_{ep}) K_{trans} \quad (2)$$

$$J(K_{trans}, K_{ep}) = \left\| AIF \otimes I(K_{trans}, K_{ep}, t) - C(t) \right\|_2^2 = \left\| AH(K_{ep}) K_{trans} - C(t) \right\|_2^2 \quad (3)$$

$$\nabla_{K_{trans}}(J) = 0 \Rightarrow K_{trans} = \left(AH(K_{ep}) \right)^{\dagger} C(t) = B^{\dagger} C(t) \quad where, B^{\dagger} = (B^* B)^{-1} B^* \quad (4)$$

$$J(K_{ep}) = \left\| BB^{\dagger} C(t) - C(t) \right\|_2^2 \equiv -C^* BB^{\dagger} C \quad (5)$$

Methods: The goal of pharmacokinetic parameter estimation is to fit the acquired perfusion, $C(t)$, to a perfusion model for each voxel in the region of interest. Here, we used the Tofts[1] model shown in $Eq.1$ and $Eq.2$, where $P(t)$ is the modeled tissue perfusion, AIF is the Arterial Input Function chosen from an artery near to the prostate, $I(K_{trans}, K_{ep}, t)$ is the tissue input response function, and $\otimes$ is the convolution operator. Because only a finite amount of data is collected, this model is re-expressed in linear algebraic form, where A is a convolution matrix and $H(K_{ep})$ is the exponential part of I. The optimum K_{trans} and K_{ep}, will minimize the difference between the acquired and estimated perfusion curves, $C(t)$ and $P(t)$, respectively, as expressed using the cost function J in $Eq.3$. J is a function of both K_{trans} and K_{ep} and is minimized using a 2D optimization. However, because K_{trans} is quadratic in J, a closed-form expression for its optimizing value (dependent on K_{ep}) can be derived: $Eq.4$. The dimensionality of J is reduced from 2D to 1D ($Eq.5$) by embedding $Eq.4$ into $Eq.3$ (i.e., variable projection (VARPRO)) [2], and the optimum K_{ep} is efficiently determined via line search[3].

Using an accelerated 3D time-resolved CE-MRA/DCE-MRI sequence[4] (256×384×38, 0.86×1.15×3.0 mm^3), a total of 55 time frames were acquired of the prostate with a 6.6 sec frame time. Perfusion parameters were estimated from the image series with the proposed method and a commercially available clinical software package (DynaCAD) for comparison.

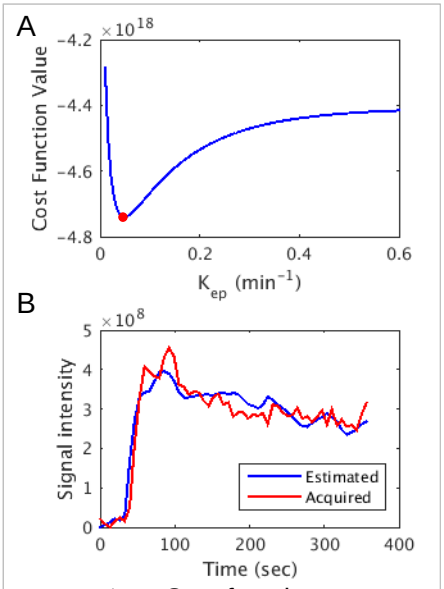

Fig. **1:** ***A***: Cost function vs K_{ep} ***B***: Estimated vs acquired perfusion for one voxel

Results: $Fig.1A$ shows a plot of J as a function of K_{ep} ($Eq.5$), for a representative voxel, and the optimum was readily found. $Fig.1B$ shows the resultant perfusion estimate $P(t)$ and the acquired data, $C(t)$. $Fig.2$ shows the optimum perfusion parameter maps (K_{trans}, K_{ep}) for prostate using the VARPRO method, exhibit similar morphology to the results from DynaCAD. For a 2D region-of-interest (ROI) of ~4200 pixels, our optimization only takes about 5 sec (Matlab) to generate pharmacokinetic maps of K_{trans} and K_{ep}.

Conclusion: Optimum pharmacokinetic mapping of K_{trans} and K_{ep} can be performed quickly using the VARPRO technique described here from 3D DCE-MRI images of the prostate.

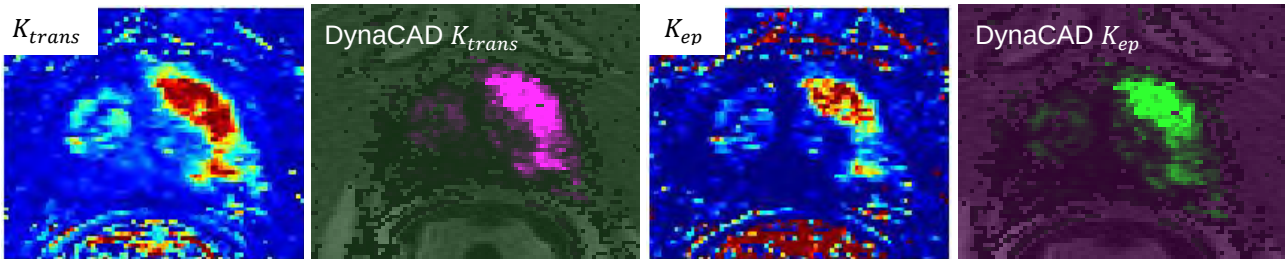

Fig. **2**: Qualitative comparison of K_{trans} and K_{ep} maps with DynaCAD shows a close match

References: **[1]** Tofts P.S. et al, *JMRI*.10:223-232(1999) **[2]** Golub, G.H., and Victor Pereyra, *SIAM J. Numer. Anal.* 10.2: 413-432 (1973) **[3]** Trzasko J.D. et al, *MRM* 69.6: 1787-1794 (2013) **[4]** Froemming A.T. et al, *ISMRM* #1169 (2015)

3D black-blood thrombus imaging (BTI) for the diagnosis of deep vein thrombosis

Guoxi Xie[1,2], Hanwei Chen[3], Qi Yang[2,4], Jianke Liang[3], Xueping He[3], Shi Su[1], Xin Liu[1], Debiao Li[2], Zhaoyang Fan[2]
1, Lauterbur Research Center for Biomedical Imaging, Shenzhen Institutes of Advanced Technology, CAS, China
2, Biomedical Imaging Research Institute, Cedars-Sinai Medical Center, Los Angeles, CA, USA
3, Department of Radiology，Guangzhou Panyu Central Hospital, China
4. Xuanwu Hospital, Beijing, China

Purpose: Deep vein thrombosis (DVT) is a common but elusive illness that can lead to fatal pulmonary embolism and sudden death. Effective treatment of DVT requires accurate evaluation of thrombus distribution and stage. Ultrasonography (US) is typically used for the diagnosis of DVT, but its sensitivity is operator dependent and thrombus staging is impossible with US. MRI is an alternative diagnostic imaging modality, and two conventional methods are MPRAGE [1] and contrast-enhanced MR venography (CE-MRV) [2]. Recently, 3D T1-weigted variable-flip-angle turbo spin-echo (SPACE), was proposed for the detection of DVT [3]. However, signal suppression of tremendously slow venous blood flow remains a challenge for SPACE. The unsuppressed blood signal could be a confounder in thrombus identification [3]. To address this issue, we developed a 3D black-blood thrombus imaging (BTI) technique [4] that combines SPACE with DANTE black-blood preparation [5] (DANTE-SPACE) for the cerebral venous sinus system. In this work, we further accommodated the technique to the deep vein system and conducted preliminary clinical validation.

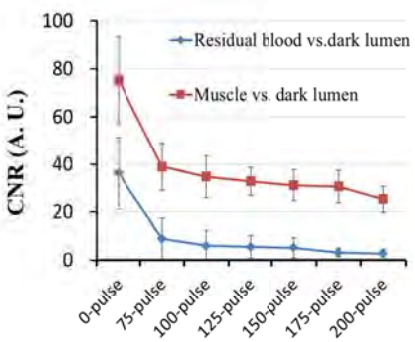

Fig.1 DANTE with 125-175 pulses is of good dark-blood effect without much signal loss in static tissue.

Methods: The DANTE-SPACE sequence was first optimized on 6 healthy subjects (3F 3M) on a 3T system (Tim Trio, Siemens, Germany) with two standard 12-channel coils positioned anteriorly and an integrated spine coil located posteriorly. Seven scans with different DANTE pulse train lengths (0, 75, 100, 125, 150, 175, 200) were conducted with all other parameters held fixed (flip angle 15°, RF gap 1 ms, gradient strength 20 mT/m). Imaging parameters for SPACE readout included: 3D coronal scan with a 352-mm craniocaudal coverage , isotropic resolution of 1.1×1.1×1.1 mm^3 (interpolated to 0.55×0.55×0.55 mm^3), TR/TE 650/9.8 ms, echo train length 40, GRAPPA factor 2, partial Fourier 6/8, scan time 4min47sec. The optimized sequence was then tested on 8 patients (4F 4M) with subacute to chronic DVT. The scan was targeted to the thrombus region that was pre-determined by US within 3 days. Conventional SPACE, MPRAGE, and CE-MRV were conducted for comparison.

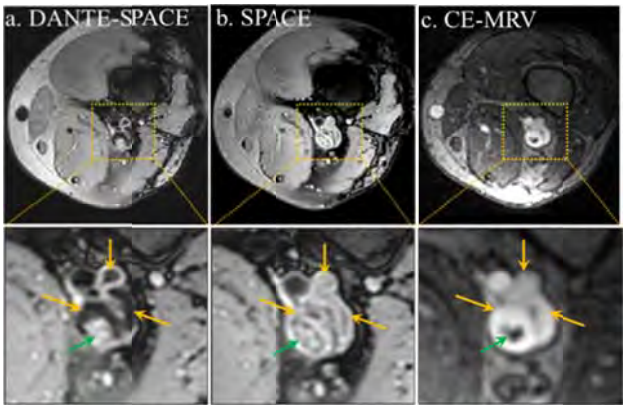

Fig.2. Representative images from a patient subject. The thrombus-mimicking venous blood signal with the SPACE sequence (yellow arrows on b) can be effectively eliminated by DANTE-SPACE. The thrombus identified by DANTE-SPACE matched nicely with that by CE-MRV (green arrows on a&b)

Results: According to contrast-to-noise ratio (CNR) analysis, DANTE with 125-175 pulses appeared to be a suitable preparation to yield sufficient blood flow suppression without considerable signal loss in static tissues (Fig. 1). Compared to conventional SPACE, DANTE-SPACE effectively nulled the residual blood that would otherwise be mistaken as part of thrombus (Fig. 2). In contrast to MPRAGE that only detected the acute or sub-acute thrombus (Fig.3b), DANTE-SPACE was able to depict the DVT regardless the thrombus stage as the venous blood flow around the thrombus was suppressed (Fig.3a). The thrombus detected by DANTE-SPACE matched nicely with that by CE-MRV (Fig. 3a&c).

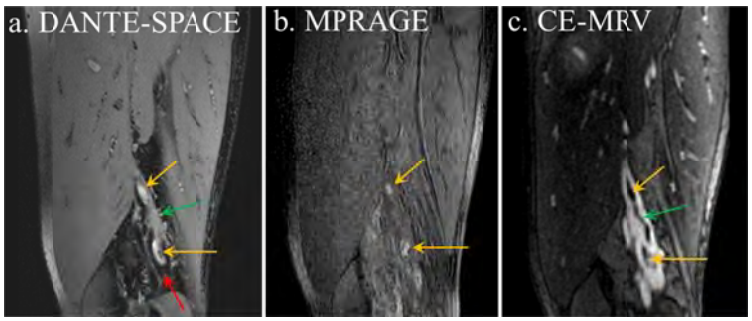

Fig. 3. Representative images from a patient subject. MPRAGE only detected the DVT in the acute or sub-acute stage because of short T1 relaxation time (yellow arrows on b), while DANTE-SPACE depicted the DVT well regardless of the thrombus stage (yellow and green arrows on a) as the venous blood flow (red arrow on a) around the thrombus was effectively suppressed. The thrombus distribution matched well between DANTE-SPACE (a) and CE-MRV (c).

Conclusion: DANTE-SPACE is a BTI technique providing excellent venous blood signal suppression and definitive thrombus detection. The preliminary patient study has demonstrated that the technique may outperform conventional SPACE, MPRAGE, and CEMRV in the diagnosis of DVT.

References: [1] Moody, et al. Radiol. 1998, 209:349-355. [2] Arnoldussen C, et al. Phlebology. 2014, 29:119–124. [3] Treitl, et al. Invest Radiol. 2015, 50:401-408. [4] Fan, et al. ISMRM. 2015. p0295. [5] Li L, et al. MRM, 2012, 68: 1423-1438

3D Black-blood Thrombus Imaging (BTI) for the Diagnosis of Cerebral Venous Thrombosis

Zhaoyang Fan[1], Qi Yang[1,2], Jiangang Duan[1,3], Xiaofeng Qu[1,4], Yibin Xie[1], Guoxi Xie[1,5], Xiaoming Bi[6], Debiao Li[1]
1. Biomedical Imaging Research Institute, Cedars-Sinai Medical Center, Los Angeles, CA, USA; 2. Department of Radiology, Xuanwu Hospital, Beijing, China; 3. Department of Neurology, Xuanwu Hospital, Beijing, China; 4. Department of Radiology, the 2nd Hospital of Dalian Medical University, Dalian, China; 5. Lauterbur Research Center for Biomedical Imaging, Shenzhen Institutes of Advanced Technology, Chinese Academy of Sciences, Guangdong, China; 6. MR R&D, Siemens Healthcare, Los Angeles, CA, USA.

Purpose: Cerebral venous thrombosis (CVT) is a disorder potentially leading to devastating disability and even death if not timely diagnosed and treated [1]. While time-of-flight (TOF) MR venography (MRV) is most commonly used for diagnosing CVT, the accuracy can be compromised by the flow voids caused by slow or complex flow patterns and in-plane flow saturation. Several other MRI techniques, relying on characteristic image contrast of CVT, may also involve confusion in image interpretation due to venous flow and other anatomic structures. In addition, given the variation in venous anatomy, it is sometimes impossible to exclude CVT with current non-invasive imaging modalities. Recently, we developed a **3D black-blood thrombus imaging (BTI)** technique, namely DANTE-prepared SPACE (DANTE-SPACE), which is able to suppress venous flow signals while depicting CVT [2]. In this work, a preliminary validation on CVT patients was performed.

Methods: *Sequence* Suppressing slower venous blood flow remains a challenge for SPACE. To better detect CVT, particularly in the chronic stage, we combined T1-weighted SPACE with the DANTE black-blood preparation to achieve BTI [3]. *Imaging Experiment* Using a 3T system (Siemens Verio) and 32-ch coil, 13 patients with chronic (13) or subacute CVT (3) were scanned. All subjects had prior conventional imaging data available. BTI using DANTE-SPACE was conducted pre- and post-contrast injection. Imaging parameters included: sagittal whole-brain coverage, isotropic 0.75mm resolution, TR/TE 600/12ms, echo train length 36, GRAPPA factor 2, 150 DANTE pulses, scan time 5-6 min (depending on how many slices). TOF MRV was also acquired. BTI images were blindly reviewed by two independent radiologists. Diagnosis of thrombus on a per-segment basis was performed in 14 segments. The combination of conventional imaging data (computed tomography venography, x-ray angiography) served as the reference for sensitivity and specificity calculation.

Results: In 13 patients, all 182 segments are diagnostic on DANTE-SPACE-based BTI images. According to reference methods, a total of 39 thrombosed segments were detected. Of them, 36 segments were identified by BTI, resulting in a sensitivity of 92.3%. With BTI, 138 of 143 segments were correctly ruled out, resulting in a specificity of 96.5%). On T1-weighted BTI images, subacute CVT was depicted as hyper-intense with respect to surrounding brain tissues, thus making diagnosis straightforward (**Fig. 1**). In contrast, chronic CVT appeared iso-intense. However, due to adequate signal suppression of venous flow, chronic CVT was well visualized (**Fig. 2**). The findings on BTI were all in agreement with the identified filling defects on TOF MRV. On post-contrast BTI images, chronic CVT was enhanced and exhibited hyperintense appearance (**Fig. 3**). BTI was shown to be able to depict partially recanalized chronic thrombosis (**Fig. 4**). Small irregular recanalized channels were better visualized with minimum-intensity-projection BTI (arrows).

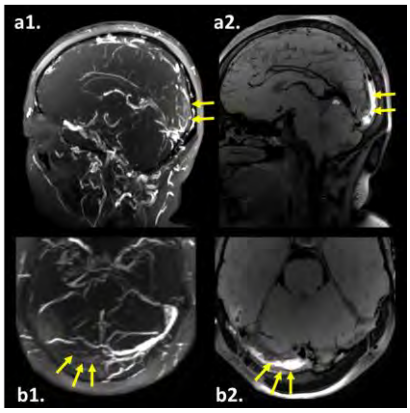

Fig. 1 Subacute thrombus (arrows) is shown as filling defect on MRV (a1, b1)and hyperintense on BTI (a2, b2).

Conclusion: This preliminary study demonstrated that BTI is a promising methodology for the diagnosis of CVT, regardless of the age of thrombus. Subacute thrombus can be easily detected due to its hyper-intense appearance with any T1-weighted MR sequences including DANTE-SPACE. However, challenges remain for chronic thrombus that could be indistinguishable from surrounding tissues due to its iso-intense appearance. Adequate venous flow suppression by using DANTE black-blood preparation is the key here to dramatically facilitate visualization of thrombi. This methodology could be applicable to other venous vascular beds such as the deep veins of the lower-limb.

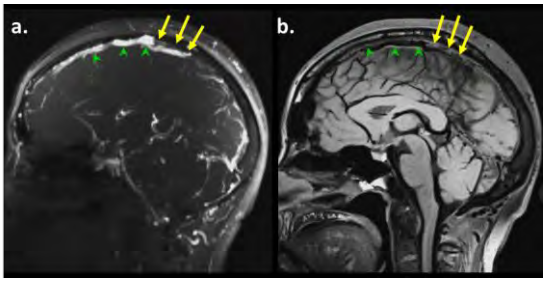

Fig. 2 Chronic thrombus (arrows) is better visualized on BTI as flow signals (arrowheads) are suppressed.

References: [1] Leach JL et al. Radiographics 2006;26:S19-S43; [2] Fan et al. ISMRM proceedings 2015; [3] Li L et al MRM 2012;68:1423-1438.

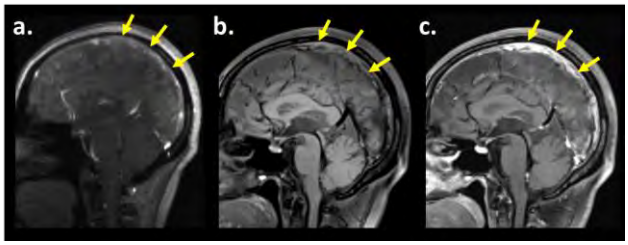

Fig. 3 Chronic thrombus (arrows) is both detected on MRV (a.) and BTI (b.) and appears hyper-intense with contrast media (c.).

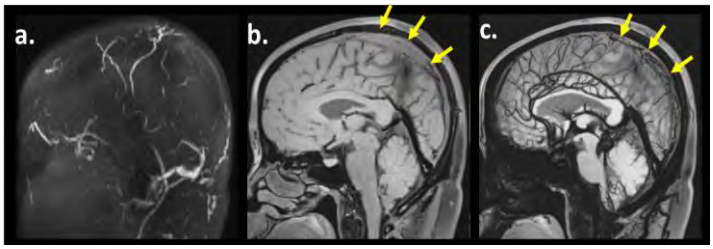

Fig. 4 Compared with MRV (a.), BTI can not only detect chronic thrombus (b.) but also depict small recanalization using MinIP (c.).

Characterization of Atherosclerotic Disease in the Thoracic Aorta:A 3D Multicontrast Vessel Wall Imaging Study

Changwu Zhou[1,2],Xihai Zhao[1], Huiyu Qiao[1], Le He[1], Huijun Chen[1], Qiang zhang[1], Cheng Li[2], Chun Yuan[1,3]

[1]*Center for Biomedical Imaging Research, Department of Biomedical Engineering, Tsinghua University School of Medicine, Beijing, China;* [2]*Department of Radiology, Yangzhou First People's Hospital, Yangzhou, China;* [3]*Department of Radiology, University of Washington, Seattle, Washington, USA*

Purpose: Atherosclerotic vulnerable plaque in the aortic arch is a major embolic source ofischemic stroke. Previous studies have shown that the advanced atherosclerotic plaques in the thoracic aorta areprevalent in patients with ischemic cerebrovascular events[1], particularly for those with cryptogenic stroke[2]. Therefore, characterization of atherosclerotic plaques that occur in the thoracic aorta prior to the onset of events, especially in the aortic arch, is important for stroke prevention. This study sought to investigate the characteristics of atherosclerotic plaque distribution, components and burden in the thoracic aorta using 3D multicontrast MRimaging techniques.

Methods: Sixty-six asymptomatic subjects (age ≥ 60 yrs.) were enrolled in the community study of Cardiovascular Risk of Older Population (CROP) after IRB approval and informed consent was obtained. Thoracic aorta was imaged with a 3.0T Philips Achieva TX scanner with a custom-designed 36-channel neurovascular coil. 3D PD-VISTA[3] and 3DSNAP[4] sequences were acquired with the following imaging parameters: 3D PD-VISTA: TSE, TR/TE 262/135ms, FOV 25 x 16 x 6.4cm^3, resolution 1.25 x 1.25 x 1.25mm^3,scan time 3minutes; 3DSNAP: TFE, TR/TE 7.5/3.7ms, FOV 22 x 28 x 3.7cm^3, resolution 1.5 x 1.5 x 1.5mm^3,scan time 5 minutes. Images were resliced to axial format along the centreline of the thoracic aorta and analysed by experienced radiologists using custom-designed software "3D CASCADE". Plaque burden, measured by NWI (normalized wall index=wall area x [lumen area + wall area] x 100%),presence or absence of atherosclerotic plaque and intraplaque hemorrhage (IPH)/mural thrombus (MT)defined as hyperintense regions on SNAP images, were determined for each subject. The thoracic aorta was divided into 3 segments: ascending aorta (AAO), aortic arch (AOA), and descending aorta (DOA). Prevalence of atherosclerotic plaques in different segments of the thoracic aorta was also calculated.

Results: Of 66 recruited subjects (mean age 72.3±6.2 yrs, 30 males), 55 (83.3%) had atherosclerotic plaques in the thoracic aorta. The prevalence of atherosclerotic plaques by segment of AAO, AOA, and DAO was 4.5%, 72.7%, and 71.2% (**Fig 1**), respectively. We found that 62.1% of subjects developed atherosclerotic plaques in both the AOA and DAO segments. In addition, we found that 21.2% of subjects had IPH/MT in the thoracic aorta on SNAP images (**Fig 2, Fig 3**). Prevalence of IPH/MT in segments of AAO, AOA and DAO was 0%, 13.6%, 12.1%, respectively (**Fig 1**). The aortic wall showed the highest NWI in DAO (34.1%±4.8%), followed by AOA (31.2%±5%), and AAO (26.8%±3.3%). In this study, a 3D multicontrast vessel wall imaging protocol including PD-VISTA and SNAP imaging sequences was applied. PD-VISTA enables delineation of arterial wall boundaries due to its superior signal to noise ratio and excellent contrast between arterial wall and lumen and surrounding tissues[3]. Whereas, SNAP imaging is capable of depicting components with short T1, such as IPH/MT[4]. Benefiting from the large coverage and capability todetect high risk plaque features, this 3D multicontrast protocol can capture vulnerable atherosclerotic lesions in any segment of thoracic aorta. Atherosclerotic plaques and vulnerable lesions were found to be prevalent in this study, particularly in the aortic arch, indicating the high likelihood of cerebrovascular events in the elderly.

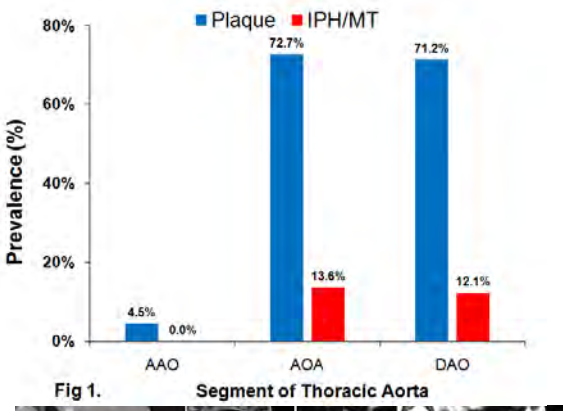

Fig 1.

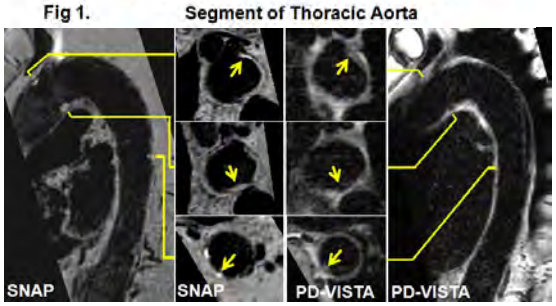

Fig 2. Multiple high risk lesions in aorta (arrows).

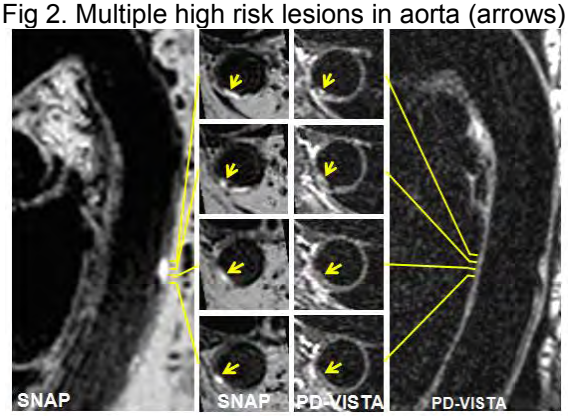

Fig 3. High risk lesion in descending aorta (arrows).

Conclusion: 3D multicontrast vessel wall imaging is capable of characterizing atherosclerotic plaques in the thoracic aorta due to its large coverage and high sensitivity in detecting vulnerable lesions. The findings of a substantial number of elderly subjects with high risk atherosclerotic lesions in the aortic arch suggest that clinical protocols for early screening of aortic vulnerable lesions in the elderly may help prevent cardiovascular events.

References: [1] Mendel T, et al. Neurol res. 2002;24:491-4. [2] Amarenco P, et al. N Engl J Med 1992;326:221-5. [3] Qiao Y, et al. JMRI. 2011;34:22-30. [4] Wang J, et al. MRM. 2013;69:337-45.

Title: **Use of T1 map in acute myocardial infarction: can it distinguish between infarct area and area-at-risk?**

Authors: N. Galea, P. Palumbo, A. Fiorelli, V. Noce, M. Francone, C. Catalano, **I. Carbone**.
Institution: Department of Radiological Sciences, Oncology and Pathology Sapienza University of Rome, Italy

Purpose:

Combined assessment of edema and necrosis using T2-weighted sequences and late gadolinium enhanced (LGE) imaging has been established as the reference standard for in-vivo assessment of myocardial damage in acute myocardial infarction (AMI). However the standard CMR protocol is time-consuming, not always tolerated by patients and needs of gadolinium administration. Our purpose was to investigate the capability of native T1 mapping to differentiate infarcted area, healthy myocardium and area-at-risk.

Methods & Materials:

Twenty-sevenf consecutive patients performed CMR within the first 7 days following ST-elevated myocardial infarction. CMR protocol included conventional modified Look-Locker inversion recovery (MOLLI) sequence with the following scheme 3(3)3(3)5, STIR T2w and cineMR sequences.
LGE images were acquired after 0.2 mmol/kg of body weight gadoterate meglumine (Gd-DOTA) administration. MOLLI images were analyzed with a dedicated software (Cvi42, Circle) by placing four ROIs within necrotic areas (LGE area, excluding MVO), area-at-risk (hyperintense area on STIR images without LGE) and remote myocardium (nor LGE neither hyperintensity on STIR images). Acquisition time of each sequence was measured. Results are expressed on mean±SD and compared with Student's t test.

Results:

Mean T1 native value of patients (age 58±10yrs) was 1354±75ms in necrotic area (LGE+/MVO-),1132±49ms in area-at-risk (LGE-/STIR+) and 951±85ms in remote myocardium (LGE-/STIR-). Significant differences were found in the comparison of T1 values between all regions ($p<0.01$ for all). Infarct size was 26±21% of left ventricular mass. Acquisition time of cineMR+mapping protocol was 22.2±8.9min, whereas standard CMR protocol was 48.6±9.8min ($p<0.01$).

Conclusion:

Native T1 mapping may reliably distinguish between necrotic area and area-at-risk in reperfused AMI and might offer a complete assessment of myocardial injury in shorter time and without contrast injection compared to conventional CMR approach.

References:

1. Abdel-Aty H, Friedrich MG, Schulz-Menger J: **Myocardial infarction after coronary revascularization: role of cardiovascular magnetic resonance oedema imaging**. *European heart journal* 2004, **25**(23):2172; author reply 2173.
2. Dall'Armellina E, Piechnik SK, Ferreira VM, Si QL, Robson MD, Francis JM, Cuculi F, Kharbanda RK, Banning AP, Choudhury RP *et al*: **Cardiovascular magnetic resonance by non contrast T1-mapping allows assessment of severity of injury in acute myocardial infarction**. *Journal of cardiovascular magnetic resonance : official journal of the Society for Cardiovascular Magnetic Resonance* 2012, **14**:15.

T1 estimation from 3D late gadolinium enhancement: Application to left atrial LGE

Dana C. Peters, Ita Caroline, Steffen Huber, Yale School of Medicine, New Haven, CT USA

Purpose: High resolution LGE images of the left atrium are currently being used as evidence of atrial fibrosis (1), and their correlation to electroanatomic voltage mapping has been analyzed at multiple signal thresholds (2,3). However, the true correlate to the clinical and physiological metrics of atrial remodeling, such as voltage, is the collagen extent, or the extra-cellular volume fraction (ECV). We investigated the possibility of "scaling" LGE images to provide an estimate of T1 and thus ECV, using Bloch equations to model spin history.

Methods: The longitudinal magnetization M0 in 3D LGE image can be described by Bloch equations, for particular scan parameters and T1 value. Figure 1 plots Mz vs. time for 6 RRs for typical 3D LGE parameters, (T1=350ms). The resulting Mz+ (magnetization after multiple RR's, just before acquisition of k=0 data) depends on T1. In order to scale Mz+ into MR signal (S), the mean signal of a known reference T1 (i.e. blood T1 which is easily measured) is obtained, as normalization factor. This results in a lookup table (S vs. T1) for the LGE slice. The Bloch equation description was validated with T1 standards in a uniform head coil using the LGE sequence. In-vivo, signal also depends spatially on coil sensitivity and proton density (PD). The variation of PD in blood and myocardium was measured in 5 healthy subjects using a 3D GRE sequence with a 4◦ flip angle. Finally, 3D atrial LGE images were scaled into T1 maps, and into ECV maps. T1 maps were converted to ECV maps using average values $T1^{b}_{0}$=1500ms, and $T1^{m}_{0}$=900ms, and HCT=0.45.

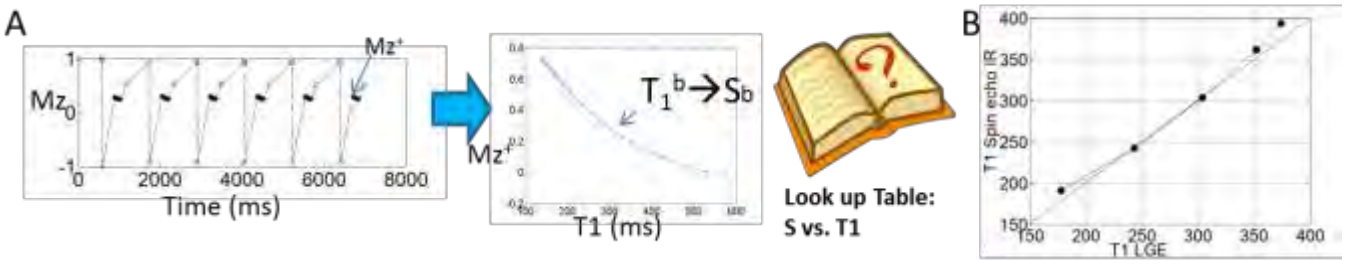

Figure 1: A) Flow chart showing estimation of T1 from LGE. Bloch equation parameters: TR/θ/vps/RR/TI/T1=5.7ms/20°/25, RR/TI=/1000ms/305ms. B) True T1 vs. T1 LGE estimate in T1 standards shows an average difference of 8ms in a relevant range (200-400ms).

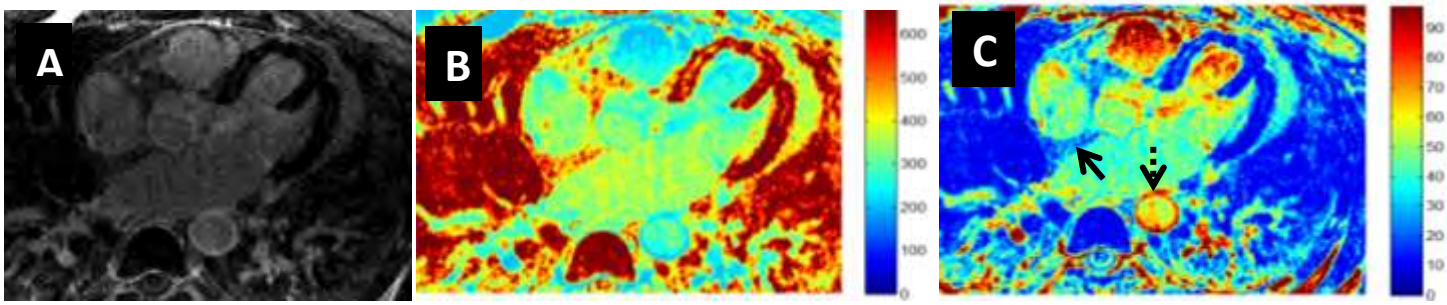

Figure 2: A) Left atrial LGE image of AF subject. B) T1 estimate (ms). C) ECV image (%) estimate shows reasonable values. Arrows in C show a region of normal atrial wall (solid arrow, ECV~25%), and fibrotic wall (dashed arrow, ECV~85%). Errors due to coil sensitivity remain.

Results: The signal difference between small adjacent ROIs in septal myocardium and blood showed a PD signal difference of 6%. Figure 1B plots T1 measured on multiple TI spin echo IR vs. T1 estimated through LGE, showing a mean difference of 8ms, in the important range of 200-400ms. Figure 2 shows an LGE image, and its corresponding T1 map, and ECV map Scan parameters were obtained from the DICOM header, and T1 of blood (350ms) was estimated from the TI scout.

Discussion: Several recent studies (4-8) have shown the adding a priori knowledge of spin history can improve quantification. Without the PD scan employed by others, we demonstrate the possibility of estimating T1 from LGE data in phantoms using a reference T1 and Bloch equations. Further, we present preliminary results quantifying left atrial ECV in-vivo.

1) Marrouche NF, JAMA 2014. 2) Malcolme-Lawes, Heart Rhythm 2013. 3) Khurram, Heart Rhythm, 2014. 4) Block, KT IEEE TMI, 2009. 5) Warntjes, MJ. BMC Med Imaging 2010. 6) Cernicanu A, Acad Radiol. 2006. 7) CJ Xanthis et al, ISMRM 2015, #182. 8). Jiaxin Shao, SCMR 2015.

Relationship between Ventricular Diastolic Dysfunction and Atrial Fibrosis: a study of phasic left ventricular and atrial volumes, and atrial late gadolinium enhancement

Karl Grunseich[1], Lauren Baldassarre[1,2], Albert Sinsuas[1,2], Mark Marieb[2], Hamid Mojibian[1], Daniel Cornfeld[1], Dana Peters[1] Yale School of Medicine: [1]Department of Radiology, [2]Department of Cardiology

Purpose: Late gadolinium enhancement (LGE) of the left atrium (LA) has become a useful tool for evaluating the extent of atrial fibrosis in patients with atrial fibrillation (AF)[1]. Some LA fibrosis is hypothesized to precede the development of AF, but less is known about patterns of left atrial LGE in patients without AF. Because conditions associated with risk of AF, such as congestive heart failure and hypertrophic cardiomyopathy, are associated with diastolic dysfunction, we hypothesized that diastolic dysfunction may be associated with left atrial LGE in patients without AF.

Methods: This study was a retrospective review of 42 subjects imaged with a late enhancement cardiac MRI sequence at our institution from 2012 to 2013. Imaging was performed on Siemens 1.5T MR scanners with a respiratory and ECG gated, 3D gradient echo sequence during mid ventricular diastole. LGE in the LA was scored by its presence or absence in 18 segments of the LA. LA volume throughout the entire cardiac cycle was measured using the biplane method on 2 chamber and 4 chamber cine SSFP sequences. Atrial emptying was divided into passive and active phases based on changes in slope of the time volume curve. Similarly, ventricular volumes were also quantified across the cardiac cycle from a short axis cine stack and used to calculate diastolic functional measures of peak filling rate (PFR), time to PFR, and time to 80% diastolic volume recovery[2]. All post processing was done using Circle Cardiovascular Imaging software v4.2. Correlations and multivariate analysis were performed using JMP v8 (SAS Institute Cary, NC)

Results: There was no direct relationship between atrial fibrosis and markers of diastolic dysfunction (including PFR, time to PFR, or time to 80% diastolic volume recovery; r_s= 0.072 p=0.653, r_s=-0.015 p=0.925, r_s=-0.016 p=0.922 respectively). There were strong correlations between both ventricular PFR and time to PFR with passive atrial ejection fraction (EF) (r = 0.723 p<0.001; r =-0.502 p<0.001 respectively), which indicates that passive atrial EF is strongly influenced by diastolic function, and has been well-corroborated in many studies. After adjustment for the relationship of PFR and time to PFR with passive atrial EF, those subjects in the highest LA LGE quartile had lower passive atrial ejection fraction when compared to those in the lower two LA LGE quartiles (p=0.020; Figure 1). In multivariate analysis, PFR (p<0.001) but not time to PFR (p=0.063) was independently associated with passive LA EF. There was also a lower active atrial ejection fraction in subjects in the highest compared to the lowest LA LGE quartile (p=0.047 Figure 1).

Conclusions: Although ventricular diastolic measurements are not directly correlated with left atrial fibrosis by LGE in this study, we did find a relationship between atrial functions and atrial LGE in subjects without AF. Assessment of degree of diastolic dysfunction requires multiple measures in echocardiography. It is possible that a more complete assessment of diastolic function/dysfunction by MRI may be needed to elucidate direct relationships of ventricular dysfunction with atrial fibrosis.

References:

1. Peters DC, Wylie JV, Hauser TH, et al. Detection of pulmonary vein and left atrial scar after catheter ablation with 3D navigator-gated DE MR imaging. Radiology 2007;243:690-5.
2. Kawaji K, Codella NC, Prince MR, et al. Automated segmentation of routine clinical cardiac magnetic resonance imaging for assessment of LV diastolic dysfunction. Circ CV imaging 2009;2:476-84.

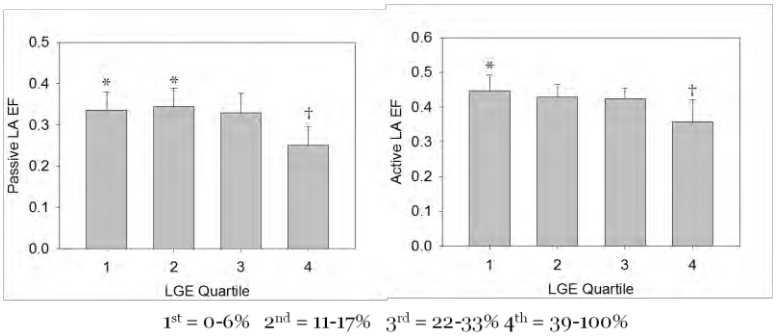

Figure 1: Subjects with the greatest LA LGE score percentages had lower passive and active LA ejection fractions.

Free-Breathing 3D Whole-Heart Coronary MRA Using Respiratory Motion-Resolved Sparse Reconstruction

Davide Piccini[1,2,3], Li Feng[4], Gabriele Bonanno[2,3], Simone Coppo[2,3], Jérôme Yerly[2,3], Ruth P. Lim[5], Juerg Schwitter[6], Daniel K. Sodickson[4], Ricardo Otazo[4], and Matthias Stuber[2,3]

[1]Advanced Clinical Imaging Technology, Siemens Healthcare, Lausanne Switzerland; [2]Department of Radiology, University Hospital (CHUV) and University of Lausanne (UNIL); [3]Center for Biomedical Imaging (CIBM), Lausanne, Switzerland; [4]Center for Advanced Imaging Innovation and Research, Department of Radiology, New York University School of Medicine, New York (NY), USA; [5]Department of Radiology, Austin Health, Melbourne, Victoria, Australia; [6]Division of Cardiology and cardiac MR Center, University Hospital of Lausanne (CHUV), Lausanne, Switzerland.

Purpose: Free-breathing whole-heart coronary MRA commonly uses navigators to counteract the effects of respiratory motion [1], but suffers from lengthy and unpredictable acquisition times. Conversely, self-navigation (SN) [2,3] promises 100% scan efficiency, but requires motion correction over a broad range of respiratory displacements, which may introduce image artifacts. We propose a respiratory motion-resolved approach based on 3D radial phyllotaxis sampling, respiratory motion sorting and sparse reconstruction to reconstruct an additional respiratory-state dimension.

Methods: Examinations in N=11 healthy volunteers (9 male, mean age: 29±4years, range: 26-34years) were performed on a 1.5T clinical MRI scanner (MAGNETOM Aera, Siemens Healthcare GmbH, Erlangen, Germany). A T_2-prepared, fat-saturated prototype 3D radial phyllotaxis bSSFP imaging sequence [4] was acquired segmented and ECG triggered. Parameters: TR/TE 3.1/1.56 ms, FOV $(220mm)^3$, matrix 192^3, voxel size $(1.15mm)^3$, RF excitation angle 115°, and receiver bandwidth 898 Hz/Px. A total of about 12,000 radial readouts were acquired in 385 heartbeats during free breathing with 100% scan efficiency. Using a respiratory signal directly extracted from the imaging data (via modulations of the k-space centre amplitude) [5], individual signal-readouts were binned according to the respiratory state at which they were acquired (Fig. 1). The resulting series of undersampled 3D respiratory states were reconstructed using an eXtra-Dimensional Golden-angle RAdial Sparse Parallel imaging (XD-GRASP) [6] algorithm, which exploits sparsity along the newly created respiratory-state dimension. Datasets for 4 and 6 respiratory states (phases) were reconstructed. Image quality was compared to 1D respiratory self-navigation in terms of vessel sharpness [7], visible length and diagnostic quality on a scale from 0 (non-visible) to 2 (diagnostic).

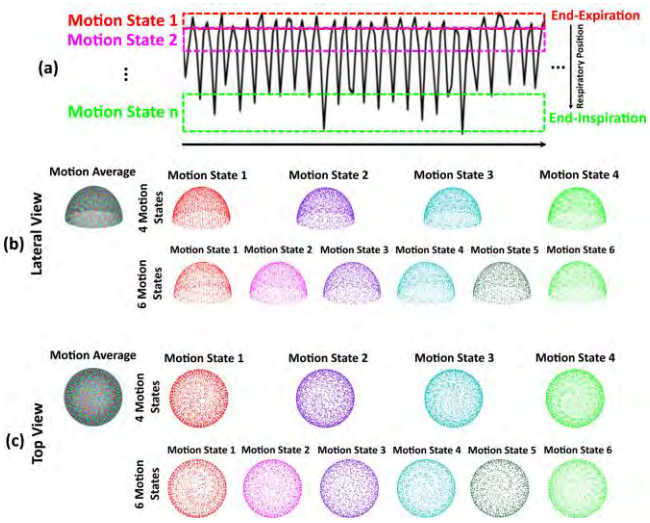

Figure 1: All acquired data are sorted into different respiratory motion states. Such states represent the temporal dimension used for XD-GRASP reconstruction.

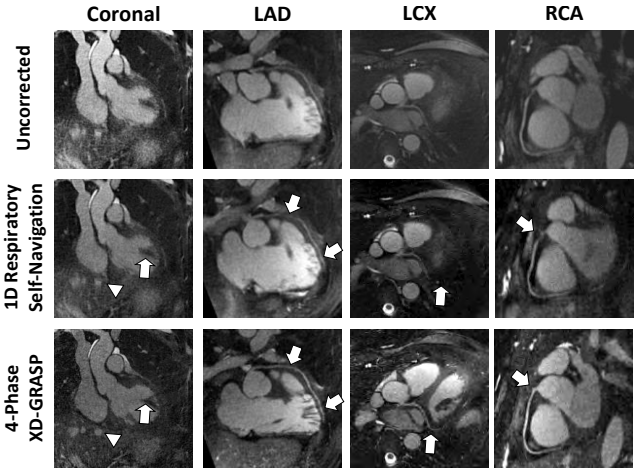

Figure 2: Example of results showing the improvements (arrows) between uncorrected motion, 1D SN and XD-GRASP reconstruction.

Results: Respiratory-resolved XD-GRASP reconstruction (both 4- and 6-phases) effectively suppresses respiratory motion artifacts in free-breathing whole-heart coronary MRA (Fig.2). Average coronary vessel sharpness and length were always superior for the respiratory-resolved datasets reaching statistical significance ($p<0.05$) for the left main coronary artery (LM), for the proximal and mid left anterior descending artery (LAD) (e.g. sharpness of mid LAD 40.8±9.1% vs 34.9±10.2%) and for the mid right coronary artery (RCA). Visualized length of the LM+LAD was also significantly increased with respect to 1D SN. The ratio of coronary segments labelled as diagnostic increased from 41/88 for 1D SN to 61/88 and 56/88 for the 4- and 6-phase XD-GRASP reconstructions, respectively. The 4-phase XD-GRASP reconstruction reached 100% diagnostic quality for LM, proximal-LAD, and proximal-RCA. The XD-GRASP framework can be exploited to reconstruct respiratory motion-resolved 3D images of the heart without the need for breath-holding, navigators, or complex 3D respiratory motion correction schemes.

Coronary	Segment	1D Respiratory Self-Navigation	4-Phase XD-GRASP	6-Phase XD-GRASP
LM:	-----	1.8±0.4	2.0±0.0*	2.0±0.0*
LAD:	Prox.	1.6±0.5	2.0±0.0*	1.7±0.5
	Mid	1.3±0.6	1.4±0.5	1.5±0.5
	Dist.	0.9±0.5	1.3±0.5	1.3±0.5
LCX:	Prox.	1.4±0.7	1.4±0.7	1.4±0.7
RCA:	Prox.	1.8±0.4	2.0±0.0	2.0±0.0
	Mid	1.3±0.5	1.7±0.5	1.5±0.5
	Dist.	1.4±0.7	1.7±0.5	1.6±0.5
Total Diagnostic Segments		41/88 (47%)	61/88 (70%)	56/88 (63%)

All values are expressed as mean ± one standard deviation
* Indicates statistical significance compared to 1D Respiratory Self-Navigation.
Diagnostic Grading: 0 = non-visible, 1 = visible but non diagnostic and 2 = visible and diagnostic

Table 1: Diagnostic grading for all coronary segments.

Conclusion: Instead of discarding data or enforcing motion models for motion correction, XD-GRASP makes constructive use of all respiratory phases to improve image quality, and achieves superior quality compared to 1D respiratory SN. The phyllotaxis trajectory and XD-GRASP reconstruction provide a synergistic combination that may lead coronary MRA closer to clinical practice.

References: 1. Ehman RL, Radiology 1989; 173:255-263 **2.** Stehning C, MRM 2005; 54:476-480 **3.** Piccini D, Radiology 2014;270:378-386 **4** Piccini D, MRM 2011; 66:1049-1056 **5** Bonanno G, ISMRM 2014; 936 **6.** Feng L, MRM 2015, in press **7.** Etienne A, MRM 2002; 48:658-666

Coronary Vein Imaging by MRI vs Intra-Procedural X-Ray Venography for Targeted Left Ventricular Lead Placement in Cardiac Resynchronization Therapy

Adrian Lam, BS[1], Ankit Parikh, MD[2], Gregory R. Hartlage, MD[2], Patrick T. Strickland BS[2], Erica Okene, MPH[2], Faisal M. Merchant, MD[2], Michael S. Lloyd, MD[2], John N. Oshinski Ph.D[1,2]

1. Emory University School of Medicine, Atlanta, GA; 2. Georgia Institute of Technology/Emory University, Atlanta, GA

Purpose

Cardiac Resynchronization Therapy (CRT) uses a biventricular pacemaker to restore synchronous myocardial contraction in heart failure patients with evidence of ventricular dyssynchrony. The left ventricular (LV) pacing lead is ideally placed in the latest contracting area that is not predominantly scar to ensure optimal patient improvement from therapy [1,2]. In CRT, the LV lead is delivered transvenously through the coronary veins, limiting the potential sites for implantation. In practice, the coronary venous anatomy is only imaged by x-ray venography during the CRT procedure. Therefore, it is unknown whether the LV lead can be implanted at an ideal location before CRT procedure.

MRI can assess mechanical dyssynchrony by processing short-axis SSFP cine images and can image the coronary veins by 3D, navigator- and ECG-gated contrast-enhanced, inversion recovery FLASH. Therefore MRI could be used to locate an optimal target location for the LV lead. The purpose of this study was to: 1) develop and apply an MRI protocol to image coronary veins and 2) determine how often a coronary vein was available for targeting LV lead placement to the latest contracting segment as compared to x-ray venography.

Methods

Fourteen (14) patients referred for CRT that had undergone a 1.5T MRI study (Avanto, Siemens Healthcare, Erlangen, Germany) prior to biventricular pacemaker implantation were evaluated. To assess dyssynchrony, SSFP short-axis cine images were acquired over the left ventricle. The coronary venous anatomy was acquired using a 3D whole-heart, navigator and ECG-gated, inversion recovery FLASH sequence during slow infusion of a gadolinium-based contrast agent. Other sequence parameters were: TR/TE/FA = 3.3 ms/1.44 ms /15°, acceleration factor of 2. 96 acquired partitions were interpolated to 192 slices with a final voxel size of 0.76 x 0.76 x 0.75 mm^3.

The latest contracting left ventricular segment was identified for each patient from the short-axis cines and mapped to the American Heart Association (AHA) 17-segment bullseye [3]. The coronary venous anatomy was segmented into a point cloud and projected onto the AHA bullseye, Figure 1. AHA bullseye segments where the coronary vein branches passed over the latest contracting segment were treated as potential implantation sites. Intra-procedural coronary x-ray venograms were acquired during the CRT procedure and also registered to the AHA bullseye. The X-ray images were considered the gold standard to identify coronary veins suitable for LV lead placement in the latest contracting segments.

Results

MRI was able to visualize the coronary veins in all subjects and the vein images were successfully projected to the AHA bullseye showing contraction timing. Coronary vein images acquired by MRI suggested that 9/14 patients had a coronary vein suitable for LV lead placement in the latest contracting or an adjacent segment. The x-ray images suggested that venous anatomy was able to reach the latest contracting or an adjacent subject in 13/14 subjects. The majority of the latest contracting segments for the patients that MRI could not find suitable LV lead pacing sites were located at an apical segment, suggesting that MRI has difficulty identifying the most distal portions of the coronary venous anatomy. Generally, the LV pacing lead is not placed in the apical segments so the difficulty in visualizing these segments may not be an important practical issue. Also, it may be possible to assess coronary vein access to a given segment by estimating the trajectory of the branches to still allow adequate pre-procedural LV lead planning.

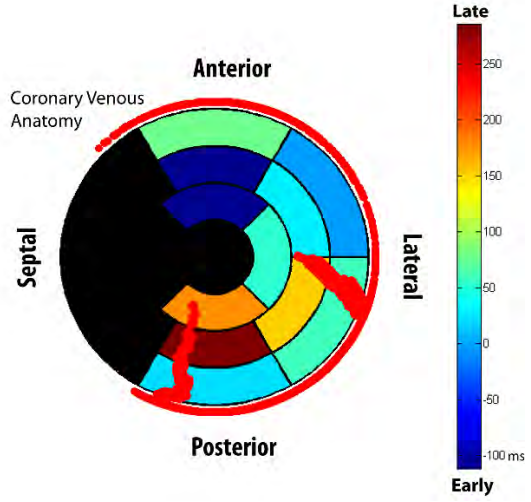

Figure 1: AHA 17-segment bullseye showing early/late contraction patterns with coronary venous overlay. The posterior branch which passes over the latest contracting segment (dark red) is suitable for LV lead placement

Conclusions

A coronary vein suitable for LV lead placement was present either directly at or within one segment of the latest contracting segment in the left ventricle in 93% of patients as imaged by x-ray venography and 64% of patients as imaged by MRI. Identification of the latest contracting segment by CMR may help provide guidance for targeted LV lead placement in the future, but MR coronary venography needs improvement imaging the distal anterior veins.

References

[1] Becker et al (2007) Heart, 93(10), 1197-1203. [2] Bleeker et al (2006) J. Cardiovasc. Electrophysiol. 17(8), 899-901. [3] Suever et al (2011) JMRI. 34(4), 811-815.

Greater non-compacted myocardial mass index in patients with clinically significant LVNC

Jeremy D Collins, MD[1]; Brian L Dubin, MD[2]; Iram T Azam, MD[2]; James C Carr, MD[1]
[1]Department of Radiology, Northwestern University, Chicago, IL; [2]Department of Radiology, UCLA, Los Angeles, CA

Purpose: Left ventricular non-compaction (LVNC) is a diagnosis made at imaging with uncertain prognostic value. The Jenni echo and Petersen cardiac MR (CMR) criteria utilize a single long axis view to quantify the maximal ratio of non-compacted to compacted myocardial thickness, but these have not been shown to correlate with clinical status or disease progression (1,2). Quantitation of the trabecular mass is now simple to perform using advanced post-processing tools. Prior studies demonstrated that elevated LV trabecular mass helps differentiate patients with LVNC from healthy controls and patients with other non-ischemic cardiomyopathies, but distinguishing patients with morphologic LVNC (M-LVNC) from those with clinically significant LVNC (CS-LVNC) is problematic (3). The purpose of this study was to evaluate the performance of trabecular mass quantification at CMR to differentiate patients with CS-LVNC and M-LVNC.

Methods: We conducted a retrospective analysis of 36 consecutive patients imaged at our institution with a Cardiac MR meeting Petersen's criteria and an available echocardiogram. Two independent observers quantified noncompacted and compacted myocardial mass at end-diastole using QMass 7.6 (Medis, Leiden, Netherlands) on bright blood short-axis cine images. The non-compacted myocardial mass index (NCMMI) was calculated by dividing trabecular volume by body surface area and then multiplying by 1.05 g/mL, the density of myocardium. CS-LVNC was defined by a clinical history of heart failure, ventricular arrhythmia, or a cardioembolic event. Two-sided t-tests were applied to compare NCMMI between groups. Subgroup analysis was performed excluding subjects with negative echocardiograms and an ejection fraction (EF) > 55%. Receiver operating characteristic (ROC) analysis was used to estimate cutoff values, sensitivities, and specificities. Interobserver agreement was assessed using the intraclass correlation coefficient (ICC).

Results: 22 patients met criteria for CS-LVNC (50% men, 45±16 yrs) versus 14 patients with M-LVNC (57% men, 44±17 yrs). Those with CS-LVNC exhibited a significantly greater NCMMI compared to those with M-LVNC (60.8 vs 47.2 g, p= 0.029). There was also a greater average difference between NCMMI and compacted myocardial mass index (29.6 vs. 19.4 g, p=0.038). ROC analysis demonstrated fair discrimination between CS-LVNC and M-LVNC (AUC 0.74, p=0.018), which significantly improved after excluding 11 patients with EF > 55% (AUC 0.87, p=0.002) and even further after excluding an additional 10 patients with echocardiograms characteristic of LVNC (AUC 0.96, p=0.003) yielding ideal cutoff values and test characteristics defined in Table 1. Interobserver agreement was excellent for NCMMI measurements (ICC=0.85, p<0.001). Blood pool volume, compacted myocardial mass, and ratios of non-compacted to compacted mass were not significantly different between patients with CS-LVNC and M-LVNC (P>0.05).

Conclusion: Trabecular mass quantification at CMR is a promising technique to identify patients with clinically significant LV non-compaction. Screening patients first with echocardiography and then applying the NCMMI cutoff of 54.8 g/m^2 in the context of a CMR determined LVEF < 55% yielded the best performance to identify CS-LVNC. Additional studies are warranted to validate our results in other cohorts.

References:
(1) Jenni *et al*. Heart 2001; 86: 666-71
(2) Kawel *et al*.,Circ Cardiovasc Imaging 2012; 5:357-66
(3) Grothoff *et al.* Eur Radiol; 22: 2699-709

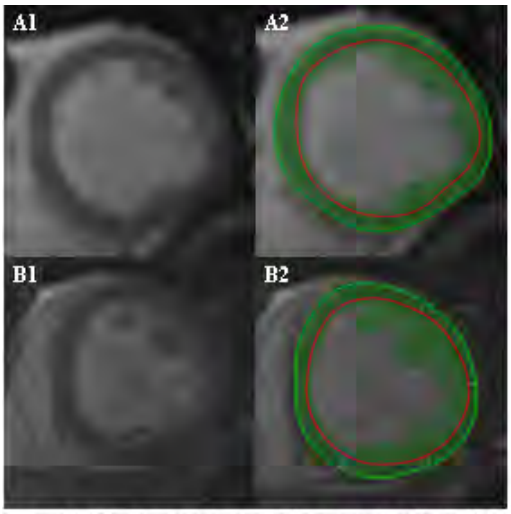

Figure 1. Mid-chamber segments of two patients with LVNC by Petersen criteria. Patient A has M-LVNC and NCMMI of 29.9 g/m² vs. patient B with CS-LVNC and NCMMI of 102.6 g/m². Images A2 and B2 depict epicardial contours (green circle), endocardial contours (red circle), and myocardial/trabeculated mass (green coloring).

Table 1: ROC analysis of morphologic vs clinically significant LVNC

	All Patients (n=36)	EF<55% (n=25)	EF<55% and negative echo (n=15)
AUC	0.74	0.87	0.96
P-value	0.018	0.002	0.003
Ideal Cutoff Value (g/m2)	54.0	53.5	54.8
Sensitivity (%)	72.7	100	100
Specificity (%)	71.4	70.0	83.3
PPV (%)	80.0	83.3	90.0
NPV (%)	62.5	100	100

4D flow MRI for intracranial hemodynamic assessment in Alzheimer's disease

Leonardo A. Rivera[1], Patrick Turski[1, 3], Kevin M Johnson[1], Carson Hoffman[1], Sterling C. Johnson[2], and Oliver Wieben[1, 3]
[1]Medical Physics, [2]Medicine, [3]Radiology, University of Wisconsin-Madison, Madison, WI, United States

Purpose: There is increasing evidence that cerebral arteries are often morphologically altered and dysfunctional in Alzheimer's disease (AD) [1]. Therefore, there is growing interest in the non-invasive assessment of cranial hemodynamics as potential systemic indicators of AD [2]. Recent advances in MR hardware, data acquisition, and reconstruction have facilitated 4D flow MRI in clinically feasible scan times, thereby providing dynamic velocity vector maps with volumetric coverage. With adequate spatial and temporal resolution, such 4D flow MRI approaches seem ideally suited for comprehensive hemodynamic assessment. In this study, we investigated intra-cranial flow features; particularly mean flow, pulsatility index (PI), resistive index (RI) and lumen area in patients with AD, mild cognitive impairment (MCI) and in healthy controls.

Methods: *Subjects*: The study population consisted of 314 subjects: 37 AD patients (age 57-91y, mean=73y, 13 F), 44 MCI patients (age 52-87y, mean=73y, 17 F), 59 normal old (age 63-89y, mean=73y, 34 F) and 174 normal middle age (age 43-62y, mean=57y, 114 F). With IRB approval and HIPAA compliance, informed consent was obtained for all study subjects. *MRI:* Volumetric, time-resolved PC MRI data with 3-directional velocity encoding were acquired on a 3T clinical MRI system (MR750, GE Healthcare,) with a 3D radially undersampled sequence, PC VIPR [3] with the following imaging parameters: V_{enc} = 80 cm/s, imaging volume = 22x22x11 cm^3, $(0.7\ mm)^3$ acquired isotropic spatial resolution, TR/TE=7.4/2.7ms, scan time ~ 7 min, retrospective cardiac gating into 20 cardiac phases with temporal interpolation[4]. *Flow analysis:* Vessel segmentation was performed in Matlab (The Mathworks, Natick, MA) from PC angiograms generated from the 4D flow MRI data while flow visualization and quantification was performed in EnSight (CEI, Apex, NC). Flow analysis planes were interactively placed orthogonal to the vessel orientation in 11 locations as shown in Fig. 1: internal carotid arteries, the basilar artery, the middle cerebral arteries and posterior cerebral arteries. 2D planes through each vessel segment were generated from the 4D flow MRI data and analyzed in a customized Matlab analysis tool [5]. Mean flow, PI, RI and lumen area were calculated for all vessel segments and groups were compared with ANOVA followed by post hoc tests. Anatomical variants of the Circle of Willis were cataloged into four groups according to [6]: textbook, P1 hypoplasia, A1 hypoplasia and other.

Results: Results for the analysis are summarized for all 11 vessel locations (left & right) in Figures 2 & 3. There is statistically significant difference in mean flow and PI between all groups for each segment except those marked with a bracket (26 out of 36 statistically significant pairs for mean flow and 24 out of 36 pairs for PI). Statistically significant differences were also found on RI (23 out of 36 statistically significant pairs) and for the lumen area. These results are similar to those reported in a study based on intracranial ultrasound and are thought to be a consequence of increased arterial rigidity and decreased arterial compliance combined with age-associated cardiovascular output declines [2]. The final count of anatomical variants was: 230 textbook, 50 P1 hypoplasia, 15 A1 hypoplasia and 19 other.

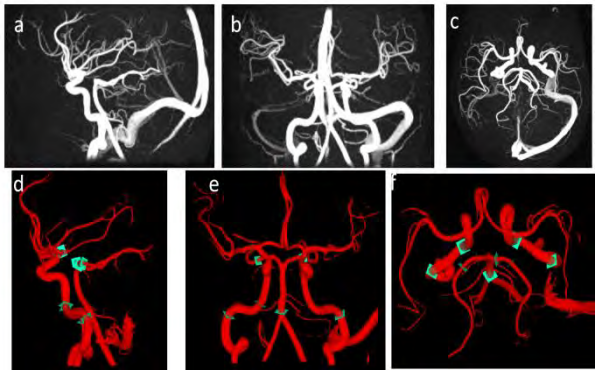

Figure 1: PC VIPR data shown as(a) sagittal, (b) coronal, and (c) axial MIP image of the PC angiogram and corresponding view of the segmented arteries with eleven flow analysis planes placed perpendicular to the vessel path (d,e,f).

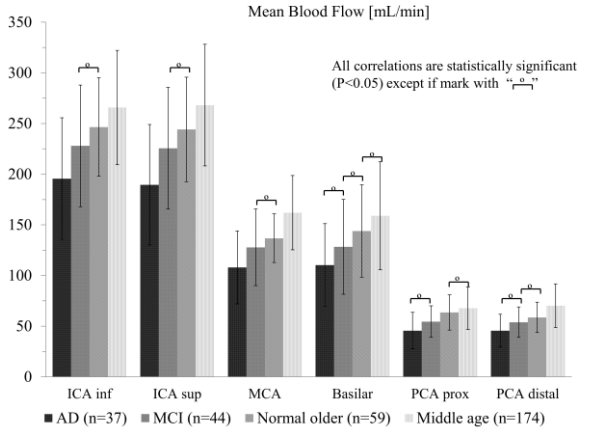

Fig 2: Mean flow (mL/min) for patients with Alzheimer's disease (AD), Mild Cognitive Impairment (MCI) and the normal control group. Left and right branches are reported together. For each vessel segment, the mean flow is statistically different among all cohorts, with exception of the 10 pairs indicated with brackets.

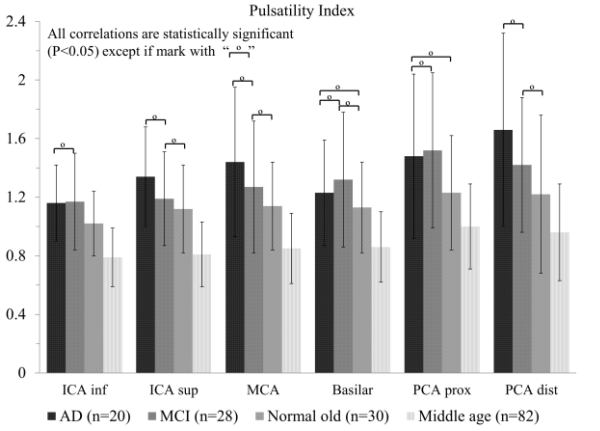

Fig 3: Pulsatility index.

Conclusions: This study demonstrates the feasibility of hemodynamic analysis over a large vascular territory in the context of Alzheimer's disease with 4D flow MRI within a 7 minute acquisition. Significant differences were demonstrated in the PI, RI, mean flow and lumen area between AD and MCI patients and a normal control group in most vessel segments. With the large volume coverage and high temporal and spatial resolution demonstrated here, 4D flow MRI can provide additional biomarkers of vascular health that can possibly contribute to identifying patients who could benefit from interventions to improve circulatory system functions.

References: [1] KA Jellinger et al., J Neural Transm 109:813-36 (2002). [2] A Roher et al., Alzheimer's & Dementia 7:445-455 (2011). [3] TL Gu et al. AJNR 26(4):743-9 (2005). [4] J Liu et al., IEEE TMI 25(2):148-57 (2006).[5] A. Stalder et al., MRM 60(5):1218-31 (2008). [6] H. Tanaka et al., AJNR 27:1770–1775 (2006).

PC-MRI based simulation of contrast-injection in cerebral aneurysms

Loic Boussel[1], Monica Sigovan[1], Joseph R. Leach[2], Nicolas Boisson[3], David Saloner[2] and Vitaliy L. Rayz[4]

[1]Creatis-Hospices Civils de Lyon, France; [2]Radiology and Biomedical Imaging, University of California San Francisco; [3]OptiFluides, Villeurbanne, France; [4]Neurosurgery, Medical College of Wisconsin.

Introduction: Catheter angiography shows filling and washout flow patterns in cerebral aneurysms, thus helping to determine regions with increased flow residence time, a hemodynamic parameter related to intra-aneurysmal thrombus deposition [1]. An alternative approach is to model the contrast agent injection with numerical simulations, using patient-specific velocity fields. These velocities can be obtained from Computational Fluid Dynamics (CFD) models based on MRA/MRI data, however that involves various modeling assumptions as well as the numerical solution of computationally-expensive flow equations. Phase-contrast MRI measurements (4D PC-MRI) can provide time-resolved 3D flow fields for the contrast transport simulations, thus providing a non-invasive assessment of the residence time while side-stepping solution of the Navier-Stokes equations. In this study we present preliminary results of contrast transport based on MRI-measured velocities and compare these to results based on CFD-simulated velocities.

Methods: In order to prove the concept of MRI-based contrast transport, a virtual injection was simulated in 3 patients with cerebral aneurysms. The patients were previously studied with 4D PC-MRI and these data were used for the contrast flow simulations. The measured flow field was projected onto divergence-free radial basis functions using an iterative least squares approach [2] to ensure mass conservation of the contrast. An open-source software, OpenFOAM, was used for the numerical solution of the advection-diffusion equation, thus obtaining the time dependent concentration of the virtual contrast in each computational voxel. To obtain velocities for CFD-based contrast simulation, patient-specific vascular geometries and inflow conditions were obtained from contrast-enhanced MR angiography and 2D through-plane PC-MRI measurements, and the flow equations were solved with the finite-volume software Fluent (ANSYS). The calculated velocities were used to solve the advection-diffusion equation and the results were compared to those obtained with MRI-based simulations of the contrast transport.

Results: A comparison of the MRI-based and CFD-based contrast transport is shown in Figures 1 and 2. Voxels filled with virtual contrast are shown in red. The images on both panels correspond to the same time following the start of contrast injection. Fig. 1 shows contrast filling of an ICA aneurysm. The contrast enters the lesion along the distal wall and recirculates in the aneurysmal sac. At the time when the contrast fills the vessel distal to the aneurysm, there is still a contrast-free region in the lower part of the aneurysm.

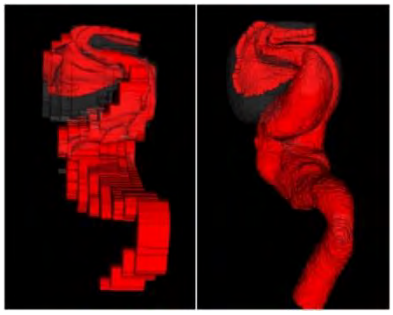

Figure 1. The MRI-based (left) and the CFD-based (right) simulation of the virtual contrast filling an ICA aneurysm

Contrast filling of a giant basilar artery aneurysm is shown in Fig. 2. A jet of the virtual contrast extends along the parent artery with most of the flow going towards the basilar apex, while some of the contrast enters the aneurysm at its distal end and flows along the opposite wall in a retrograde fashion. This results in strong recirculation of the contrast and a pronounced region with a delayed filling in the proximal, lower part of the aneurysm.

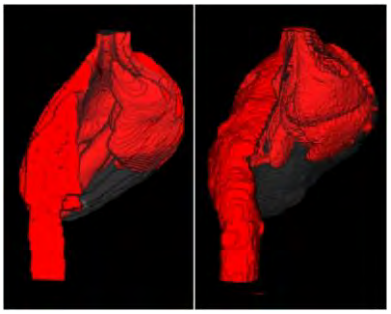

Figure 2. The MRI-based (left) and the CFD-based (right) simulation of virtual contrast filling a basilar artery aneurysm.

Discussion: The transport of virtual contrast in cerebral aneurysms was simulated using 4D PC-MRI velocities acquired in vivo. While there are some discrepancies between the MRI-based and CFD-based simulation of the virtual contrast, the important features of the flow are in good agreement. The virtual contrast simulation is based on in vivo flow measured with 4D PC-MRI, while with catheter angiography the flow may be altered by the radiopaque tracer injection. The virtual contrast simulation can be affected by segmentation errors of 4D PC-MRI data as well as spurious velocity measurements, thus requiring pre-processing filtering and robust numerical algorithms.

Conclusion: The results indicate that PC-MRI-based simulation of virtual contrast injection may provide important information on intra-aneurysmal flow patterns and can help in non-invasive diagnostics and treatment planning.

References: [1] Rayz et al., Ann Biomed Eng, 2010. [2] Busch et al., MRM, 2013.

Support of NIH grant HL115267 (VLR) is acknowledged.

Absolute Local Normalized Helicity in Patients with Bicuspid Valve and Aortic Dilatation

Julio Garcia[1], Alex J Barker[1], Jeremy Collins[1], James Carr[1], Michael Markl[1]
[1]Northwestern University

Purpose: Helical flow is often observed in patients with aortic dilation, aortic valve stenosis, or bicuspid aortic valve (BAV). In particular, local normalized helicity (LNH) can be used to characterize helical flow using both 2D measurements and multi-planar reformatting of 4D flow MRI[1-3]. To improve on the limited coverage of these approaches, this study aims to use the full volume of the 4D flow MRI velocity fields to demonstrate that: 1) LNH volumetric quantification may differentiate helical flow alterations in the aorta between healthy controls and BAV subjects; 2) LNH volume may correlate with BAV aortic dilation and peak velocity.

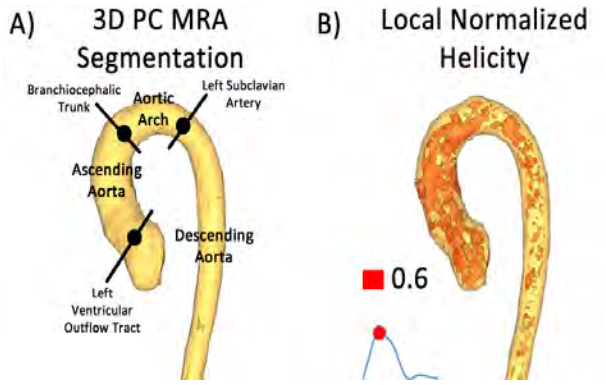

Fig 1. Workflow for the assessment of volumetric local normalized helicity.

Methods: 115 subjects (65 healthy controls and 50 subjects with BAV and aortic dilatation were identified via IRB-approved retrospective chart review. Imaging was performed on 1.5T (n=74) and 3T (n=41) MRI (Siemens, Erlangen, Germany). The MRI protocol employed ECG-gated 4D flow during free breathing with adaptive navigator respiratory gating[4]. Data were acquired in the sagittal oblique orientation, covering the entire aorta. Imaging parameters were: Venc=1.5–4 cm/s, TE/TR=2.3–2.84/4.6–5.4 ms, FOV=212–540 mm×132–326 mm, spatial resolution =1.66–2.81×1.66–2.81×2.2–3.7 mm³, temporal resolution =36.8–43.2 ms, FA =15°. A phase contrast MR angiogram[4] (MRA) was calculated from 4D flow MRI data (Fig. 1A) and used to performed 3D segmentation of the entire aorta. LNH[1-3] in was calculated by $LNH = \frac{V.\omega}{|V||\omega|}$, where V is the velocity field from 4D flow MRI and ω is the vorticity derived from V as given by ω=curl (V). A sensitivity analysis was perform to set the optimal absolute LNH threshold identifying elevated helicity within the flow domain. For LNH quantification, the aorta 3D segmentation was additionally subdivided in 3 segments: ascending aorta, aortic arch and descending aorta. The mean velocity in the entire aorta was used to identify peak systole, systole deceleration and mid-diastole phases.

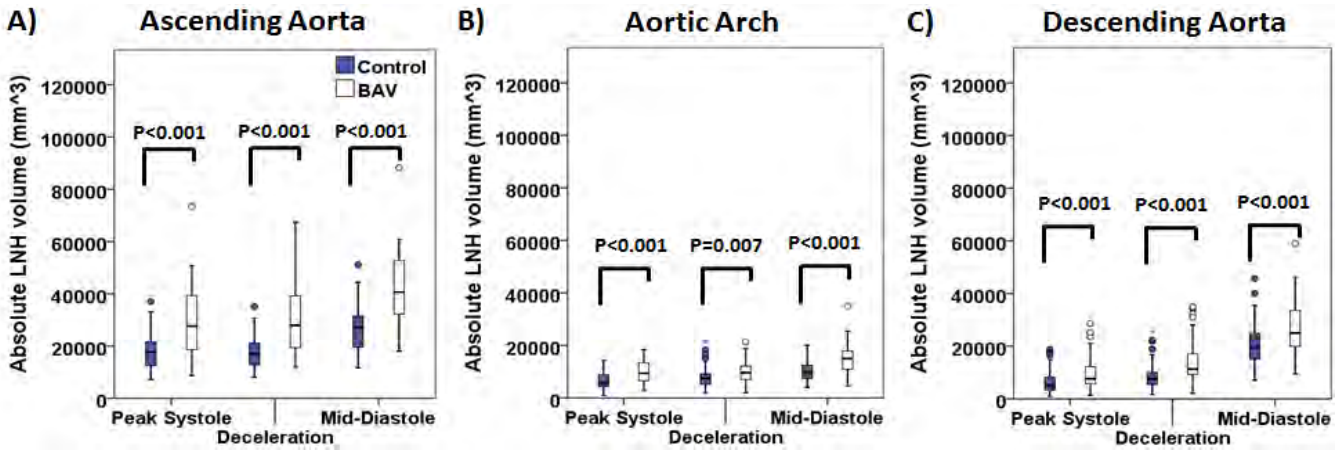

Fig 2. Local normalized helicity comparison between controls and patients with bicuspid valve and aortic dilatation.

Results and Discussion: Absolute LNH volume sensitivity analysis lead to an optimal analysis threshold of 0.6. Absolute LNH volume was significantly higher (P<0.001) in BAV patients in comparison with controls for all evaluated segments and phases (Fig. 2). Absolute LNH volume in the ascending aorta correlated with MAA diameter (r=0.83, P<0.001, at peak systole; r=0.84, P<0.001, at systole deceleration; r=0.88, P<0.001, at mid-diastole). Previous studies have associated BAV with eccentric flow and elevated flow helicity in the MAA section, and it has been suggested that these flow alterations may contribute to the dilation of the aorta. This study showed that: 1) helical flow alterations can be identified by LNH and can be quantified by volume; 2) elevated LNH can differentiate helical flow alterations in healthy and BAV subjects; 3) elevated LNH was associated with BAV aortic dilation.

Conclusion: In conclusion, this study demonstrates the potential usefulness of helical flow quantification to differentiate between controls and subjects with BAV and aortic dilation.

References: 1. Morbiducci et al. J Biomech 2013;46:102-109; 2. Lorenz et al. MRM 2014; 71:1542-53; 3. Garcia et al. J Biomech Eng 2013; 135(2):124501. 4. Markl et al. JMRI 2007; 25:824-831.

Left Atrial 4D Flow MRI: Stasis and Velocity Mapping in Patients with Atrial Fibrillation

[1,5]Michael Markl, PhD, [1,2,3]Daniel C. Lee, MD; [2,3]Jason Ng, PhD; [1]James Carr, MD; [2,3,4]Jeffrey J Goldberger, MD

Radiology[1], Division of Cardiology[2], Feinberg Cardiovascular Research Institute[3]; Center for Cardiovascular Innovation[4], Department of Biomedical Engineering[5] Northwestern University, Chicago, IL, USA

Introduction: Atrial fibrillation (AF) affects over 33 million patients worldwide. The most serious complication from AF is stroke, which is attributed to embolism of thrombus from the left atrium (LA)[1]. Studies utilizing transesophageal echocardiography (TEE) have shown that impaired flow and elevated stasis in the LA are independent risk factors for thrombus formation and stroke in AF[2,3]. However, TEE requires esophageal intubation and cannot fully assess the complex 3D LA flow patterns. 4D flow MRI can overcome these limitations by measuring 3D blood flow dynamics in-vivo[4,5]. It was the aim of this study to test the potential of novel 4D flow derived tools (anatomic maps of LA stasis, peak velocity, and time-to-peak (TTP) velocity) for the characterization of LA flow dynamics in patients with AF. We hypothesized that metrics of LA flow dynamics can detect differences between groups of AF patients and controls and identify relationships between global and regional LA flow, LA volume, and patient characteristics.

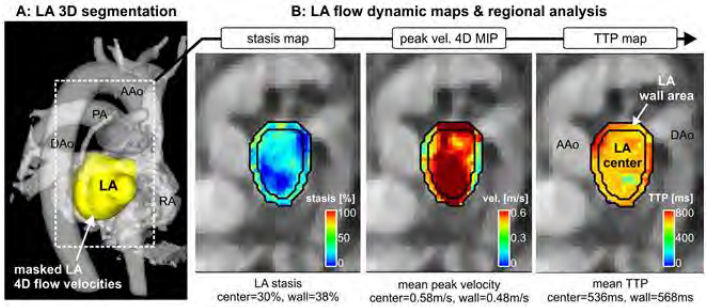

Fig. 1: 4D flow MRI data analysis in a 62 year old male patient with a history of AF (AF-sinus). **A:** 3D segmentation of the LA based on 4D flow derived 3D-PC-MRA data (gray shaded) and masking of velocities inside the segmented LA. **B:** Calculation of LA stasis maps for a velocity threshold of 0.1m/s (left), peak velocity maximum intensity projections (MIPs, mid), and time-to-peak velocity (TTP) maps. Regions for the analysis regional velocities and stasis in the LA center and adjacent to the LA wall are delineated by black lines. The mean for all three metrics of regional LA flow dynamics are listed below each map. AAo/DAo = asc../desc. aorta, PA = pulmonary artery.

Methods: 4D flow MRI for the in-vivo assessment of time-resolved 3D LA blood flow velocities was performed in 111 subjects: 42 patients with a history of AF and in sinus rhythm (AF-sinus, age=62±11yrs), 39 patients with persistent AF (AF-afib, age=66±11yrs), 10 young healthy volunteers (HV, age=24±2yrs), and 20 age appropriate controls (CTRL, age=59±7yrs). Data analysis included the 3D segmentation of the LA and the calculation of LA stasis, peak velocity and TTP maps. As the pathophysiology of thromboembolism in AF is based upon formation of mural thrombi, regional analysis focused on the region adjacent to the left atrial wall. Regional LA flow dynamics were quantified by calculating mean stasis, peak velocity and TPP in the LA center region and the region adjacent to the LA wall as shown in Fig. 1.

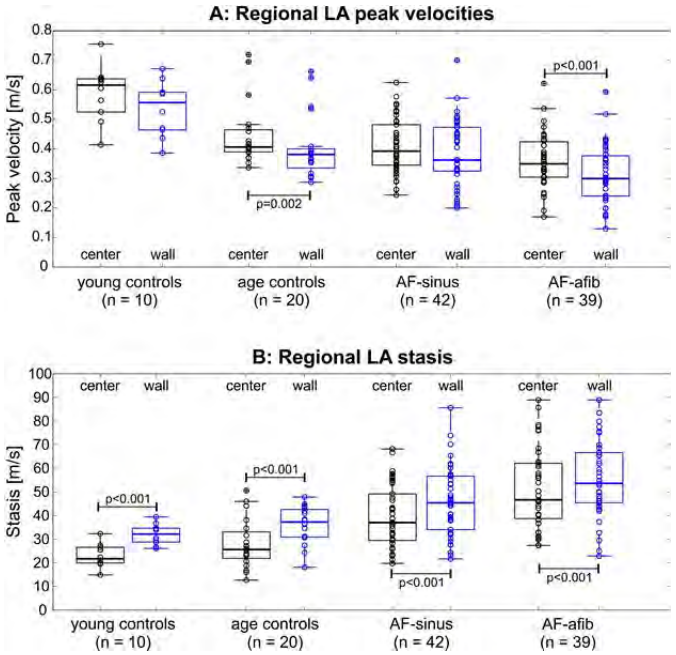

Fig. 2: Group wise comparisons of regional LA peak velocities (**A**) and LA stasis (**B**). Flow stasis adjacent to the LA wall was significantly elevated compared to the LA center for all subject groups. The box plots illustrate the median and the 25th and 75th percentiles (edges), the whiskers extend to the most extreme data points not considered outliers.

Results: A sensitivity analysis identified optimal thresholds for global LA stasis (<0.1m/s) and peak velocity (top 5% LA velocities) which detected significant differences between AF patients and controls for global LA stasis (HV=25±5%, CTRL=29±10%, AF-sinus=41±13%, AF-afib=52±17%) and peak velocity (HV=0.43±0.02m/s, CTRL=0.37±0.04m/s, AF-sinus=0.33±0.05m/s, AF-afib=0.30±0.05m/s). As shown in Fig. 2, regional analysis revealed significantly elevated stasis at both LA center and wall for AF patients compared to age appropriate controls (29%-84% difference, p<0.006) and for AF-afib vs. AF-sinus patients (22%-30% difference, p<0.004). In addition, stasis adjacent to the LA wall was significantly elevated (p<0.001) compared to the LA center for all subject groups. Multiple regressions revealed significant (R^2_{Adj}=0.45-0.50, p<0.001) relationships between impaired global LA flow (reduced velocity, increased stasis) with age (|β|=0.27-0.50, p<0.002) and LA volume (|β|=0.26-0.50, p<0.003).

Discussion: The findings of this study indicate that atrial 4D flow MRI and derived in-vivo peak velocity and stasis maps are robust tools for the detection changes in global and regional flow dynamics in the left atrium associated with atrial fibrillation, patient age and left atrial volume. Additional longitudinal studies are warranted to test the diagnostic value of LA flow metrics as potential risk factors for thromboembolic events.

References: 1. Fuster V, et al. Circulation. 2011;123:e269-367. **2.** Goldman ME, et al. J Am Soc Echocardiogr. 1999;12:1080-1087. **3.** Handke M, et al.. J Am Soc Echocardiogr. 2005;18:1366-1372. **4.** Markl M, et al. J Cardiovasc Magn Reson. 2011;13:7. **5.** Fluckiger JU, et al. J Magn Reson Imaging. 2013;38:580-587.

Funding Sources: American Heart Association (12GRNT12080032), National Institutes of Health (1R21HL113895).

Differences between 4D flow, 2D One-directional and 2D Three-directional Velocity-encoded MRI Sequences for the Estimation of Aortic Flow and Velocity

Emilie Bollache[1], Pim van Ooij[1], Alex Powell[1], James Carr[1], Michael Markl[1], Alex J Barker[1]

[1]Northwestern University, Chicago, USA

Purpose: Accurate quantification of cardiovascular hemodynamics is imperative for the diagnosis and management of patients with various diseases. Two dimensional through-plane velocity-encoded ('2D-1dir') CINE phase contrast (PC) MRI is routine in the clinic for blood flow quantification. However, positioning of the 2D acquisition plane perpendicular to the vessel flow may be challenging and lead to underestimation of velocity. This inherent limitation may be overcome by taking into account the three directions of velocity ('2D-3dir' velocity encoding). More recently, 4D flow MRI has proven useful for both three-directional flow visualization and quantification in a 3D volume, including in complex flow patterns [1]. Our aim was to systematically compare regional flow and velocity quantification in the ascending (AA) and descending (DA) aorta based on 4D flow MRI, 2D-1dir and 2D-3dir PC MRI, all acquired within the same scan session.

Methods: We studied 15 healthy volunteers (11 men; 51±19yrs) who underwent MRI (1.5T MAGNETOM Aera, Siemens). The exam comprised acquisition of the following data (Venc=150cm/s, table A): 1) 4D flow MRI covering the thoracic aorta in a sagittal oblique 3D volume; 2) 2D-1dir and 3) 2D-3dir PC MRI, both in a plane perpendicular to mid-AA and DA at the level of right pulmonary artery center. Data were acquired using prospective ECG gating, and respiration navigator gating for 4D flow and 2D-3dir MRI. All were automatically corrected for noise, velocity aliasing and eddy currents [2]. A 3D PC-MR angiogram was derived from 4D flow data and used to perform a 3D aortic segmentation (Mimics, Materialize). As shown in Fig A, 2D-1dir and 2D-3dir PC MRI plane locations were coregistered with 4D flow MRI data (Ensight, CEI, USA). Next, AA and DA lumen contours were semi-automatically delineated using Segment for 2D data and custom software for analyzing 4D flow MRI data. Net flow (stroke volume), peak flow, and through-plane velocity were calculated. Additionally, peak velocity magnitude taking into account the 3 components was computed for 4D and 2D-3dir techniques. Comparisons between 4D and 2D-3dir as well as between 2D-1dir and 2D-3dir indices were assessed using a paired Student t-test. The impact of eddy current correction on the computed indices was also assessed.

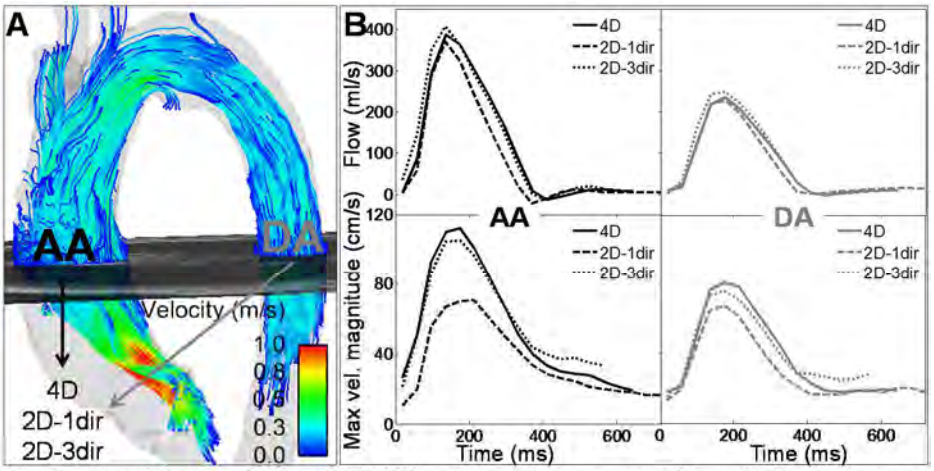

Fig: A. Coregistration of 4D and 2D MRI data. B. Group-averaged flow (up) and maximal velocity magnitude (bottom) time variations in the ascending (left) and descending (right) aorta calculated using 4D flow (solid lines), 2D-1dir (dashed lines) and 2D-3dir (dotted lines).

Results: Group-averaged 4D flow, 2D 1-, 3-dir PC MRI AA and DA flow and maximal velocity magnitude waveforms are illustrated in Fig B. Table B summarizes indices obtained using each sequence, indicating a significant underestimation of 2D-1dir when compared to 2D-3dir at both locations. Differences obtained for peak velocity calculated when considering only the through-plane component were lower than for magnitude. However, velocity obtained from 2D-1dir was still significantly lower than 2D-3dir through-plane peak velocity, suggesting the influence of physiological conditions (breath-holding *vs.* free breathing). Finally, eddy current correction resulted in <6% difference in indices (table B).

	A FB/ BH	SR (mm^3)	TR (ms)	B	AA: stroke volume DA: net flow (ml)	Peak flow (ml/s)	Peak magnitude velocity (m/s)	Peak through-plane velocity (m/s)
4D	FB	3.1x2.3x2.5	39.2	**AA**	77±21 *(6±3%)*	396±99 *(2.0±1.2%)*	121±34 *(0.7±0.3%)*	96±24 *(0.9±0.5%)*
				DA	49±12* *(6±4%)*	245±52* *(1.9±1.3%)*	85±26* *(1.1±0.9%)*	84±26* *(1.2±0.9%)*
2D-1dir	BH	1.8x2.5x6	38.4	**AA**	62±15† *(4±9%)*	376±72† *(0.8±1.6%)*	80±16† *(0.4±0.6%)*	80±16† *(0.4±0.6%)*
				DA	47±11† *(3±4%)*	235±44† *(0.8±1.3%)*	70±21† *(0.6±1.0%)*	70±21† *(0.6±1.0%)*
2D-3dir	FB	1.8x2.5x6	38.4	**AA**	83±13 *(4±3%)*	420±76 *(1.1±0.8%)*	115±22 *(1.3±1.7%)*	97±17 *(0.5±0.3%)*
				DA	56±10 *(6±3%)*	261±45 *(1.9±1.0%)*	80±25 *(1.6±1.1%)*	79±24 *(1.4±0.7%)*

Table: A. Acquisition during free-breathing (FB) or breath-holding (BH), spatial (SR) and temporal (TR) resolutions for each MRI sequence. B. Net and peak flow as well as magnitude and through-plane velocity peaks as measured using the 3 sequences in the ascending (in black) and descending (in grey) aorta. Absolute differences between indices estimated while correcting for eddy current effects or not in percentage of the mean values are provided in parentheses. *: p<0.05 between 4D and 2D-3dir; †: p<0.05 between 2D-1dir and 2D-3dir.

Conclusion: Differences observed between the 3 MRI sequences are likely due to the 3-directional nature of aortic blood flow, differing resolutions, partial volume artifacts, eddy currents, and 2D plane positioning. The hemodynamic status changes between acquisitions indicate that care should be taken when reporting aortic hemodynamics indices, especially net flow (i.e. stroke volume), and suggest the need for robust protocols designed to minimize measurement variability.

References: [1] Stankovic et al., Cardiovasc Diagn Ther 2014;4(2):173–192. [2] Bock et al., ISMRM 2007;p. 3138.

Turbulence Tensor Quantification using ICOSA6 Flow Encoding

Henrik Haraldsson[1], Sarah Kefayati[1], Petter Dyverfeldt[2], Belén Casas Garcia[2], Jonas Lantz[2], Tino Ebbers[2], and David Saloner[1]
[1] University of California, San Francisco, United States, [2] Linköping University, Sweden

Purpose: Turbulence is an important factor in hemodynamics and has been associated with thrombogenesis and energy dissipation. The three normal turbulence tensor components have previously been quantified with Phase Contrast MRI (PC-MRI) and a general theory has been presented relating the signal loss in the PC-MRI signal with the normal components [1]. Quantification of the full turbulence tensor, including both normal and shear turbulence components, enables further applications such as calculation of pressure losses. The shear components have previously been measured using PC-MRI by combining turbulence in two normal and bisecting directions [2], but this method was found to suffer from low SNR due to the additive nature of noise. Contrary to previous methods where each component was solved as a linear combination, we propose to use an ICOSA6 flow encoding regime [3] and calculate all tensor components as a least squares problem. The purpose of this work is to evaluate if ICOSA6 flow encoding could be used to decrease the error of the estimated shear turbulence components using numerical simulations, and perform a proof-of-concept study on the MRI system.

Methods: Constant flow through a rigid pipe with a cosine-shaped stenosis was simulated in ANSYS CFX 14.5 using Large Eddy Simulation (LES) to resolve turbulent flow. The simulated flow was used to emulate a PC-MRI acquisition by re-gridding the flow data into 1.5mm isotropic voxels, and by filling k-space lines with a 20ms interval from the flow simulation. Two different PC-MRI flow encodings schemes were used: Normal and Bisecting (NB), and ICOSA6 (see table 1).

The turbulence components were solved independently for the NB analogues to equation (1) for normal components and equation (2) for shear components, whereas equation (3) was solved as a single least squares system for both normal and shear components simultaneously.

Normal noise was added to the simulated PC-MRI data to evaluate noise sensitivity for the normal and shear components. The root mean square error (RMSE) was normalized (NRMSE) by dividing by the range of the components.

The ICOSA6 flow encoding was implemented on a PC-MRI sequence and data was acquired in a phantom study with similar geometry and flow condition as the simulated data. The acquisition had a FOV = 384×120×40 mm with 1mm isotropic resolution. TR/TE = 7.1/4.3ms. Data was acquired with flow encoding of both 0.75 and 1.00 m/s. The ICOSA6 PC-MRI data was phase-unwrapped [3] and turbulence was quantified using in-house developed software.

Result: ICOSA6 and NB show similar NRMSE for the normal tensor components; whereas the NRMSE is smaller for the shear components using ICOSA6 solved with a least squares minimization (see Figure 1). Despite small differences in geometry and flow conditions, the turbulence component derived with MRI using ICOSA 6 showed similar features to the flow simulation.

Conclusion: The simulation result shows that using an ICOSA6 flow encoding and determining the turbulence stress tensor by solving the least squares problem allows us to estimate turbulent shear components with lower noise sensitivity without compromising the result of the normal turbulence components. The phantom measurement provides a proof-of-concept demonstration of the feasibility of the technique.

References: [1] Dyverfeldt et al, Magn Reson Med (2006) 56(4):850-8. [2] Elkins et al, Exp Fluids (2009) 46:285–296. [3] Zwart and Pipe, Magn Reson Med (2013) 69(6):1553-64

Table 1: Flow encodings

Encoding	NB encoding	ICOSA6 encoding
0	0	0
1	ΔM1*x	ΔM1* (0.8507*x + 0.5257*y)
2	ΔM1*y	ΔM1*(0.8507*x - 0.5257*y)
3	ΔM1*z	ΔM1*(0.8507*y + 0.5257*z)
4	ΔM1*x + ΔM1*y	ΔM1*(0.8507*y - 0.5257*z)
5	ΔM1*x + ΔM1*z	ΔM1*(0.5257*x + 0.8507*z)
6	ΔM1*y + ΔM1*z	ΔM1*(0.5257*x - 0.8507*z)

$$\sigma_x^2 = \sigma_{v_1}^2 = -\frac{2}{|k_{v_1}|^2} ln\left(\frac{|S(k_{v_1})|}{|S(k_0)|}\right) \quad (1)$$

$$\sigma_{xy}^2 = \sigma_{v_4}^2 - \sigma_{v_1}^2/2 - \sigma_{v_2}^2/2 \quad (2)$$

$$k_{enc,i}\sigma_{ij}^2 k_{enc,j} = -2ln\left(\frac{|S(k_{v_{enc}})|}{|S(k_0)|}\right) \quad (3)$$

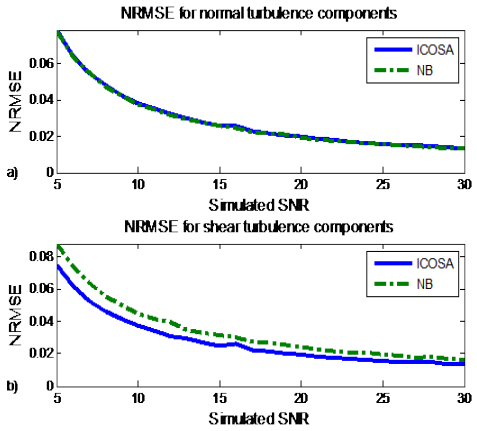

Figure 1: Normalized root-mean-square error for normal and shear turbulence components

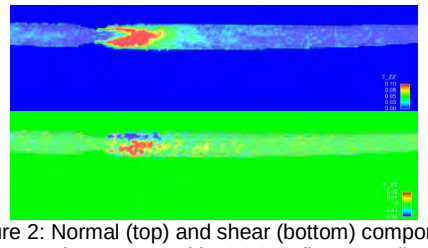

Figure 2: Normal (top) and shear (bottom) component assess by PC-MRI with ICOSA6 flow encoding.

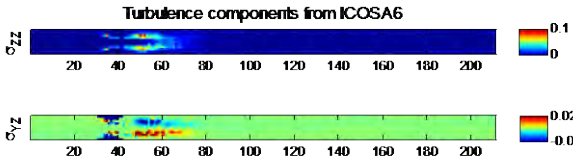

Figure 3: Normal (top) and shear (bottom) components of the flow simulated with CFD.

High Resolution 4D Flow and CE-MRA utilizing Ultrashort Echo Times : Feasibility of linking Vessel Wall Enhancement, Morphology, and Hemodynamics

Kevin M. Johnson[1], Yijing Wu[1], Oliver Wieben[1-2], Patrick A. Turski[2]
Departments of Medical Physics[1] and Radiology[2], University of Wisconsin – Madison

PURPOSE: It's well established that hostile hemodynamic conditions may predispose patients to the development and progression of intracranial vascular lesions such as atherosclerotic plaques and aneurysms. MRI presents an opportunity to explore dynamic flow-lesion interactions utilizing the combination of vessel wall imaging, 4D-flow, and morphology. Unfortunately, achieving the high spatial resolution required to quantitatively depict the intracranial vasculature is challenging due to competing factors including SNR, scan time, and artifacts. This is especially true for 4D-flow and CE-MRA which are limited in scan time due to the need for multiple flow encodes and contrast passage, respectively. Importantly, as the resolution increases the need for flow compensation increases[1] and in the case of contrast enhanced imaging, required scan times often lead to artifacts related to passage of contrast during the acquisition[2]. In this work, we investigate high spatial resolution angiography and 4D-flow utilizing accelerated ultra-short echo (UTE) imaging, which has the potential to dramatically increase acquisition efficiency while offering improved flow compensation and robustness to artifacts.

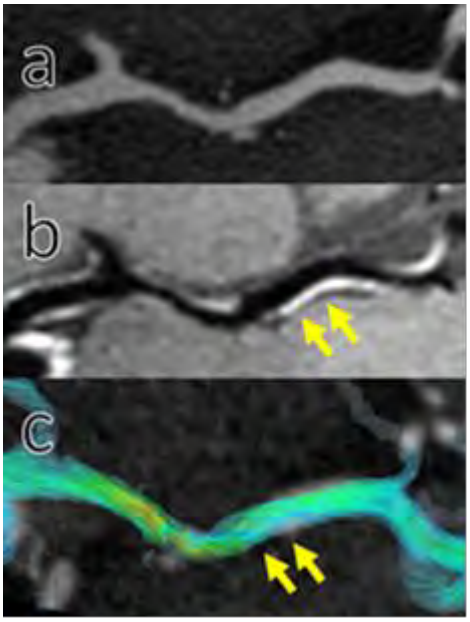

Figure 1. *Example images collected in a patient with significant and diffuse atherosclerosis. A moderate stenosis is seen on UTE-CE MRA(a). However, substantial wall enhancement is seen on post contrast BB (b) corresponding to a region of helical flow distal to the stenosis*

METHODS: The target imaging protocol consists of pre-contrast 3D black blood (BB) images, UTE CE-MRA, UTE 4D-flow, and finally, a post-contrast 3D BB images. BB imaging was achieved with 3D variable flip angle fast spin echo imaging with 2D parallel imaging. CE-MRA and 4D-flow data are collected with center out sampling utilizing either 3D center out radial or 3D radial-cones (rCUTE[2]) trajectories. Both these trajectories provide ultra-short echo times on the order of 80μs and near 100 duty cycle; however, radial-cones offers substantially higher k-space collection efficiency(~4x). As part of an ongoing, HIPPA compliant IRB approved study, subjects with known or suspected vascular disease (N=8) were recruited from the clinical imaging service. Subjects were scanned on a 3T clinical scanner (MR740, GE Healthcare, Waukesha, WI) with a 32 ch coil (Nova Medical, Wilmington, MA, USA): 1) UTE CE-MRA (0.57mm isotropic spatial resolution, flip=10°, scan time=2:45, TE/TR=0.1/4.1ms), 2) UTE 4D-flow (0.57mm isotropic spatial resolution, flip=10°,scan time=2:45, TE/TR=1.6/6.4ms, 5pt flow encoding, V_{enc} =100cm/s, scan time=7:28). 3) Pre/post contrast T1 3D FSE (Spatial Resolution=0.75x0.8x0.8mm^3, TE/TR=24/550ms, 2x2 auto-calibrated parallel imaging, scan time=4:22). In addition, a standard 3D TOF exam was acquired for comparison. During UTE CE-MRA, a single dose of Gadobenate Dimeglumine (0.1mm/kg, 500mM) was administered at an injection rate 0.5ml/s followed by at least 30ml saline flush. UTE data were reconstructed offline. Resulting images were registered were registered and incorporated into a commercial flow visualization package (Ensight, CEI, Apex, NC, USA) allowing joint visualization of morphology, flow, and vessel wall enhancement.

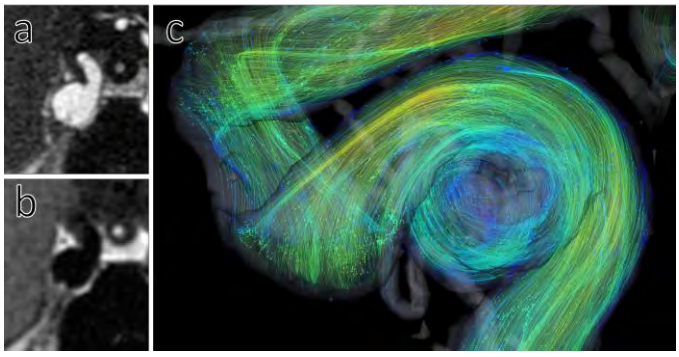

Figure 2. *Example UTE CE-MRA (a), BB (b), and 4D-flow (c) images collected in a patient with an aneurysm off of the internal carotid artery. No wall enhancement is seen with the large vortex core seen in 4D-flow.*

RESULTS: Images of diagnostic quality were obtained in all cases. In one case, inter scan motion led to some blurring. Figure 1 shows example co-visualized images from a patient with atherosclerotic disease showing vessel wall enhancement distal to a moderate stenosis. Figure 2 shows images collected in subject with a cavernous carotid aneurysm. In this case, no wall enhancement is visualized, the high resolution CE-MRA clearly defines the aneurysm lumen and 4D Flow confirms the presence of a stable vortex flow pattern.

DISCUSSION AND CONCLUSION: High resolution UTE angiography and 4D-flow appear to a promising image scheme. Utilizing accelerated UTE imaging, a complete depiction of large vessel disease is possible in less than 20minutes. This suggests potential application to prospective patient studies for further investigation

ACKNOWLEDGMENTS: We gratefully acknowledge GE Healthcare for their assistance and support.

REFERENCES: **1.** Parker et al. 03' JMRI 18(1). **2.** Fain et al. 99' MRM 42:1106. **3.** Johnson ISMRM 12' #285

Identifying Motion Corruption In DCE Radial Stack of Stars Data

Jason K. Mendes[1], Scott McNally[2], Seong-Eun Kim[1], Bradley D. Bolster[3], John Roberts[1], Gerald S. Treiman[1,2,4] and Dennis L. Parker[1]

[1]Utah Center for Advanced Imaging Research, [2]University of Utah Department of Surgery, [3]Siemens Healthcare, [4]Department of Veterans Affairs (VASLCHCS)

Purpose: Inflammation is integral to the development of carotid atherosclerosis (1) and is an indicator of plaque instability (2,3). Inflammation (defined by the presence of macrophages and increased vascular density) can be detected from kinetic analysis of dynamic contrast enhanced (DCE) images. Radial DCE sequences (4) have an intrinsic ability to reduce artifacts from patient swallowing and other patient motion due to the oversampled center of Kspace. However, when data becomes highly undersampled (5) the amount of redundancy at the center of kspace is reduced and motion artifacts become more apparent. We propose an easy way to identify motion corrupted lines which can be retrospectively removed to improve image quality.

Methods: All imaging was performed on a Siemens Trio scanner with a 3D radial stack of stars sequence. Acquisition matrix was 192x304x12, resolution 0.8mmx0.8mmx1.5mm, TE/TR=2ms/10ms, 14 total measurements over 434s (31s per measurement). Data was reconstructed using the KWIC algorithm into 16 temporal frames per measurement (2s effective temporal resolution). Each measurement was sorted as a Sinogram and each line in the Sinogram was compared to the adjacent lines on either side to evaluate motion corruption. The two adjacent lines were first averaged to predict the central line which was then compared to the line of interest. The difference is averaged across partitions and coil channels to get an error measurement for each acquired line. Corrupt data lines can be identified with a threshold cutoff and replaced with an estimate calculated using neighboring temporal frames.

Results: When the full measurement data set is used (Fig. 1a), a single swallow event is not as noticeable due to the heavy oversampling at the center of Kspace. However, when the data is divided into smaller temporal frames (such as with the KWIC reconstruction) the temporal frame that occurred when the patient swallowed has significant motion artifact (Fig. 1b). The corrupt data lines are visible when the Sinogram corresponding to the corrupt temporal frame is considered (Fig 1d). The error estimate for each line in two consecutive measurements is shown in Fig 1f. In this case a threshold value of 0.2 was used to identify corrupt lines. The corrupt lines appear periodically spaced since the radial data is acquired in a pseudo golden angle fashion. Corrupt data was replaced in the Sinogram using linear interpolation in time of neighboring measurements (Fig 1e). The resulting image (Fig 1c) shows considerable improvement in motion artifact (especially near the cavity of the pharynx).

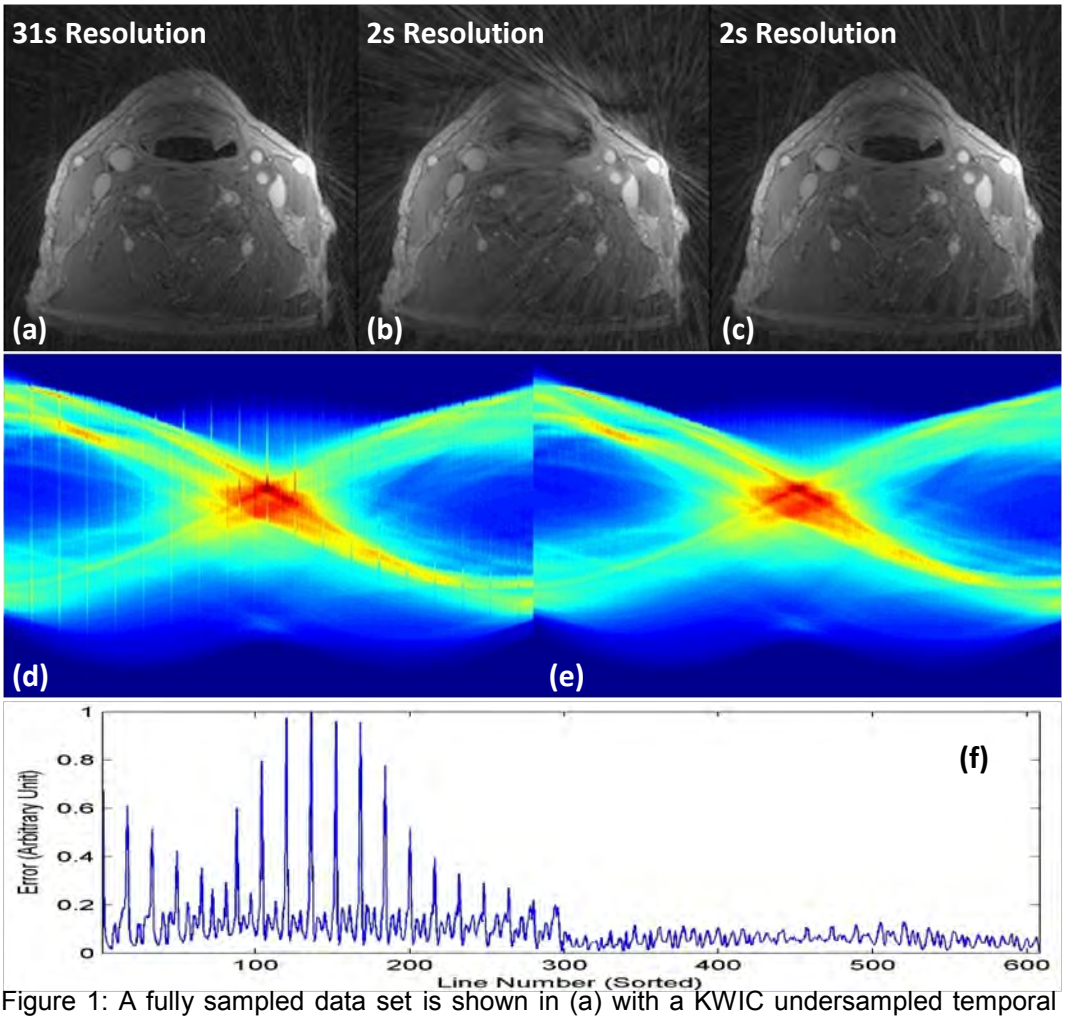

Figure 1: A fully sampled data set is shown in (a) with a KWIC undersampled temporal frame shown in (b) and the motion corrected image shown in (c). The Sinograms corresponding to (b) and (c) are shown in (d) and (e) respectively. Each line in the Sinogram from (d) is compared to adjacent lines to form a motion error measurement (f).

Conclusion: We have shown a quick and easy way to identify motion corrupted lines. Image quality is improved when the identified lines are replaced.

References: 1. Moulton et al. Proc Natl Acad Sci U S A 2003;100(8):4736-4741., 2. Fleiner et al. Circulation 2004;110(18):2843-2850., 3. Libby et al. Circulation 2002;105(9):1135-1143., 4. Wu et al. Am J Roentgenol 2014:in press., 5. Song et al. Magn Reson Med. 2000 Dec;44(6):825-32.

Very Short Blood T_2* with Gd-based Contrast Reagents: Investigating BMS Shift

Gregory J. Wilson[1], Charles S. Springer, Jr.[2], Mark Woods[2,3], Sarah Bastawrous[1,4], Jeffrey H. Maki[1]

[1]University of Washington, Department of Radiology, Seattle, WA, USA,
[2]Oregon Health and Science University, Advanced Imaging Research Center, Portland, OR, USA,
[3]Portland State University, Department of Chemistry, Portland, OR, USA,
[4]Puget Sound VA HCS, Radiology, Seattle, WA, USA.

Purpose: To investigate the mechanism of rapid blood transverse relaxation in the presence of gadolinium-based contrast reagents (GBCR). In vitro measurements have shown markedly increased transverse relaxation (R_2*) in oxygenated blood compared to plasma.[1] This has important implications for the effective use of contrast reagents in MR angiography. This study explores the mechanism of rapid transverse relaxation using a molecular dynamic simulation of water diffusion and transmembrane water exchange.

Methods: Monte Carlo computer simulations (Matlab) were performed to predict the transverse ^1H_2O relaxation in oxygenated whole blood with various GBCR concentrations ([CR]) (Figure 1). Water molecules randomly walked in 3 dimensions inside and outside red blood cells, with simulated membrane permeability adjusted to provide average intracellular residence time of 10 ms. In the extracellular space, water protons experienced a frequency shift due to the dipolar magnetic field inhomogeneities from each cell given by:

$$I_e = \frac{\chi_i - \chi_e}{3}(3\cos^2\alpha - 1)\frac{R^3}{r^3}$$

where χ_i and χ_e are intracellular and extracellular susceptibilities, α is the angle between the water position vector and the external field, R is the cell radius, and r is the distance from the cell center. χ_e - χ_i was approximated as 0.31x[CR] (ppm), with [CR] in mM. In the intracellular space, water protons experience a bulk magnetic susceptibility (BMS) frequency shift which can be approximated by the BMS shift for an infinite disk:

$$\delta_{ie} = \frac{\chi_e - \chi_i}{3}(3\cos^2\phi - 1)$$

where ϕ is the angle the disk normal makes with the external field. Signal vectors from 13,000 water protons diffusing through an ensemble of 2744 spherical cells [radius 3.2 μm, diffusion coefficient 1.5 μm²/ms, hematocrit of 38%] were summed at each 1 μs time step to estimate signal dephasing over the 60 ms walk duration. Though the simulated cells were spherical, RBC's are more closely approximated as oblate ellipsoids, thus each was assigned a random "disk" orientation to calculate the BMS shift. Simulated R_2* was estimated by fitting the 1.8 ms interval-sampled signal decay to a mono-exponential curve. Simulated R_2 was estimated by inverting each proton's phase every 6.7 ms (3T) or 4.8 ms (1.5T), then fitting the spin echo signals to a mono-exponential curve. R_2' is the difference between R_2* and R_2.

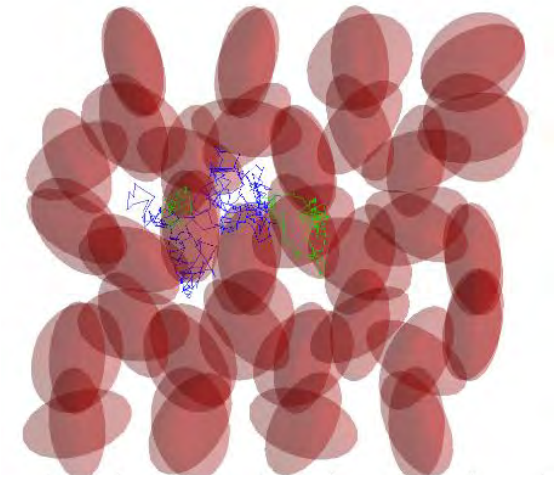

Figure 1. Illustration of random walk through oblate ellipsoid cells. Random walk steps outside cells are blue, steps inside cells are green. The simulation is displayed as a 2D projection of semi-transparent cells. Phase was accumulated at each step of the random walk due to extracellular field inhomogeneities or intracellular BMS shift.

Results: Simulated blood R_2' (filled circles) are shown in Figure 2 for ten CR concentrations at 1.5T and 3T. There was remarkable agreement with in vitro measurements (hollow circles). Additionally, the simulations were performed (filled diamonds) with no dephasing contribution from the intracellular space (ie, BMS shift was turned off). R_2' without BMS shift (Sim $R_{2e'eff}$) is near zero.

Conclusion: BMS shift inside RBC's and trans-cell-membrane water exchange likely contribute to the high R_2' observed in blood samples.

References: Wilson GJ et al., PISMRM 2014, p3862.

Figure 2. Results of Monte Carlo simulations (filled circles) showing remarkable agreement with in vitro measurements (hollow circles). Note Sim R_2' increases super-linearly with [CR] and approximately doubles from 1.5T to 3T. Turning off the BMS frequency shift in the simulations results in Sim $R_{2e'eff}$ (filled diamonds). Without the BMS contribution, simulated R_2' is near zero. Thus, intracellular BMS shift is likely an important contributor to transverse relaxation.

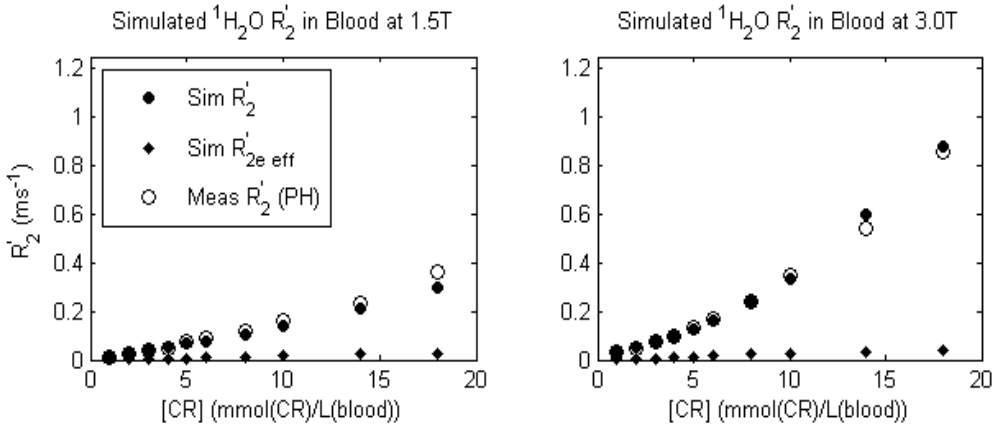

DESIRE: Efficient MRI reconstruction with Split Bregman initialization and sparse regularization based on pre-learned dictionary

Artem Migukin[1], Dmitry Korobchenko[1], Mikhail Sirotenko[1], Kirill Gavrilyuk[1], Sangcheon Choi[2], Praveen Gulaka[2], Michael Rychagov[1]

[1] *Samsung R&D Institute Russia LLC, SEC, 12 Dvintsev str., 127018, Moscow, Russia*
[2] *Medical System Lab, DMC R&D Center, SEC, Yeongtong-gu, 442742, Suwon, Korea*

1. INTRODUCTION

Magnetic resonance imaging (MRI) is one of the most widely used and irreplaceable tools in contemporary clinics. Conventionally, time-consuming MRI data acquisition is accelerated by partial sampling (undersampling). Actively developing compressed sensing (CS) techniques demonstrate good reconstruction quality for a moderate undersampling factor. Ever-growing demands of industry require, however, rapid recovering of tiny high-frequency details. In this work we propose a novel CS approach for accurate MRI reconstruction from highly-undersampled data. According to sparsity hypothesis, each small portion (patch) $\mathbf{x}_i$ of the object $\mathbf{x}$ can be represented as a linear combination of atom functions from a dictionary $\mathbf{D}$ with very few non-zero weights $\mathbf{z}_i$. Following [1, 2], our synthesis-based approach is formulated as the following constrained optimization

$$\min_{\mathbf{x}_i,\mathbf{z}_i} \| \mathbf{x}_i - \mathbf{D}\mathbf{z}_i \|_2^2 + \lambda \| \mathbf{z}_i \|_0 \; \forall i \quad s.t. \; F_u(\mathbf{x}) = \mathbf{u},$$

where λ is a regularization parameter and F_u denotes the partial discrete Fourier transform. The consistency with the available undersampled k-space $\mathbf{u}$ is resolved by iterative projection algorithm with alternating sparse object approximation and restoring measured values. In contrast to [2], the dictionary $\mathbf{D}$ is *pre-learned* in advanced on a set of high-quality fully-sampled MR images. Since elements of $\mathbf{D}$ are free from aliasing artifacts and targeted on MRI specific features to be reconstructed, the usage of pre-learned dictionary is found to result in both a higher efficiency (no time-consuming relearning) and better reconstruction accuracy. Authors of MRI algorithms typically omit the problem of *initialization*. Nevertheless, one should take care of filling non-sampled k-space positions with adequate initial values. Split Bregman [3] is found to demonstrate a significant increase of convergence rate and enhancement of the image reconstruction.

We name the proposed CS MRI algorithm with an efficient Split Bregman based initialization and sparse regularization using a pre-learned dictionary **D**ictionary pr**E**-learned **S**parse **I**mage **R**econstruction and **E**nhancement or *DESIRE*. Our implementation on GPU demonstrates its excellent performance for T1-, T2-weighted images and 3D TOF angiography on experimental highly-undersampled clinic data.

2. EXPERIMENTAL RESULTS

In Fig. 1 and Fig. 2 we compare the reconstruction of 3D TOF angiography by DESIRE and state-of-the-art algorithms applicable for single coil-image, namely: the wavelet-based LDP [1] and online dictionary learning MRI (DLMRI, [2]). We also illustrate the influence of the Split Bregman initialization on the convergence rate and reconstruction accuracy. These results are shown for undersampling factor 4 with Poisson-disk sampling, and the best quality is in favor of the proposed method.

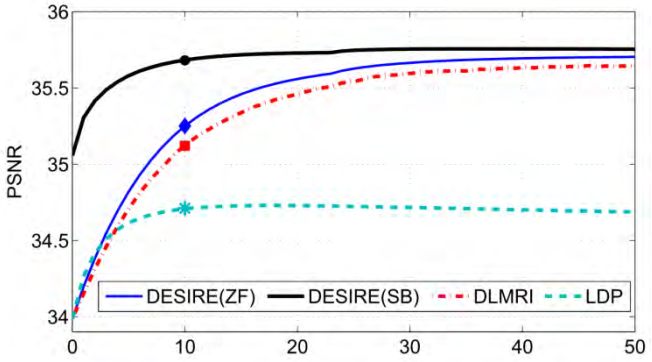

Fig.1. Convergence of CS MRI algorithms applied to 3D TOF angiography. Peak Signal-to-Noise Ratio (PSNR) for slice-wise LDP [1] (dashed curve), DLMRI [2] with online dictionary learning [2] (dashed-dotted curve), DESIRE with zero-filling (ZF) initialization (thin solid curve), and DESIRE with Split Bregman (SB) based initialization (thick solid curve).

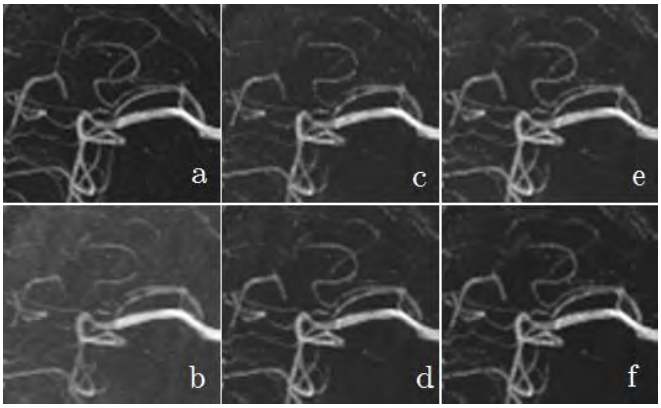

Fig.2. Fragments of the maximum intensity projections (MIP) of the (a) reference object and (b) the naive reconstruction by the inverse Fourier transform from the zero-filled undersampled k-space. The CS MRI reconstructions are obtained after 10 iteration by (c) slice-wise LDP [1], (d) DLMRI [2], (e) DESIRE with zero-filling (ZF) initialization and (f) DESIRE with Split Bregman (SB) based initialization.

REFERENCES

[1] M. Lustig et al, *Magn. Reson. Med*. **58** (2007).
[2] S. Ravishankar and Y. Bresler, *IEEE Trans. Med. Imaging* **30** (2011).
[3] T. Goldstein and S. Osher, *SIAM J. Imaging Sci.* **2** (2009).

Vessel- and Dose-specific Differences in Contrast-enhanced Time-resolved 4D-MRA: An Intra-individual Quantitative and Qualitative Comparison of Gadopentetate Dimeglumine and Gadobutrol in Minipigs

DR Hadizadeh[1], VC Keil[1], G Jost[2], H Pietsch[2], B Agha[1], C Marx[1], M.Weibrecht[3], M Perkuhn[3], HH Schild[1], WA Willinek[1,4]
[1] Department of Radiology, University Hospital Bonn; [2] MR and CT Contrast Media Research, Bayer Healthcare, Berlin, Germany; [3]Philips Technologie GmbH Innovative Technologies, Research Laboratories, Aachen, Germany, [4] Department of Radiology, Neuroradiology, Sonography and Nuclear Medicine, Brüderkrankenhaus, Trier, Germany

Purpose: Chemical properties and concentrations of contrast agents affect quantitative and qualitative aspects in 4-dimensional magnetic resonance angiography (4D-MRA) [1]. We investigated how bolus kinetics and diagnostic image quality are influenced by the choice of contrast agent and its concentration in time-resolved thoraco-abdominal 4D-MRA compared to quantitative gadolinium (Gd) measurements by computer tomographic angiography (CTA).

Methods: 7 anaesthetised Goettingen minipigs received dynamic thoraco-abdominal CT (Definition, Siemens Healthcare, Erlangen/Germany; transverse slices, 80 kV, 20s, 0.3s/dynamic frame) and 4D-MRA (4D-TRAK; TR/TE/α = 7.7/1.2/25°; 1. transverse slices, 30s, 0.49s/frame; 2. coronal slices, 70s, 1.3s/frame) on a 3.0T whole-body scanner (Intera, Philips Healthcare, Best/the Netherlands). CT attenuations were converted into Gd concentrations on the basis of previous phantom experiments [2]. Quantitative bolus characterization included measurement of first and second pass (recirculation) peaks of density (CT; i.e. Gd-concentration) and signal levels (MRI) as well as full width at half maximum (FWHM) bolus curve shape analyses. **First**, CTA was intra-individually compared to transverse 4D-MRA by measurements in the descending aorta at 0.1 (standard-dose) and 0.05 mmol/kg BW (half-dose) gadobutrol (Gadovist, Bayer, Leverkusen/Germany, flow: 1ml/s). **In a second step**, thoraco-abdominal MRA was performed for an intra-individual comparison of standard- and half-dose gadobutrol (each 1ml/s) and 0.1 mmol/kg BW gadopentetate dimeglumine (Magnevist, Bayer, Leverkusen/Germany, flow: 2ml/s). Quantitative analysis (2a) included bolus analyses in the descending aorta, celiac trunc, portal vein and inferior caval vein measuring the same parameters as in (1). Qualitative analysis (2b) was performed by three blinded readers rating vessel visibilities (15 arterial and 5 venous targets; rating: 0-2; non-visible to diagnostic). Inter-observer agreement was tested with Cronbach's alpha test and significance of rating differences by Wilcoxon tests.

Results: (1) Compared to standard dose gadobutrol-enhanced dynamic CTA, 50% dose reduction (half-dose) resulted in a peak signal loss of 39.0%, bolus length reduction of 32.4% and shorter FWHM (20.6%). The same dose-reduction in 4D-MRA resulted in a peak signal loss of 14.5%, bolus length reduction of 20.6% and shorting of FWHM by 33.8%. In 4D-MRA the bolus curves were significantly broader than the Gd based bolus shapes determined by dynamic CTA, with FWHM of 8.2s vs. 4.7s (half-dose) and 12.2s vs. 5.9s (standard-dose) for 4D-MRA and CTA respectively. In 4D-MRA the standard dose bolus curves were affected by saturation effects with truncated bolus peaks (n=5/7). As a result, in standard-dose 4D-MRA, the 2nd pass peak signal was almost as high as the 1st pass peak enhancement. **(2a)** In volumetric 4D-MRA no saturation effects were observed at standard-dose gadopentetate dimeglumine or after half-dose administration of gadobutrol, whereas they were observed at standard-dose gadobutrol. As a consequence, arterial bolus peak signals (1st pass) were in the same range for all 3 contrast protocols. 2nd pass peak signals were highest in the standard-dose gadobutrol protocol. No saturation effects were observed in 2nd pass. **(2b)** Inter-rater agreement of qualitative vessel readings was excellent for all three contrast protocols (0.92–0.93). Qualitative analysis of a total of 369 readings showed no significant difference in image quality between standard- and half-dose gadobutrol (p=0.61), visibility of vessel segments was rated significantly higher with both concentrations of gadobutrol compared to gadopentetate dimeglumine (p<0.001). Taking only venous segments into account (n=144), a strong tendency for better image quality after standard-dose gadobutrol compared to half-dose gadobutrol was observed (p=0.07).

Discussion/Conclusion: Gadobutrol offers significantly higher image quality than gadopentetate dimeglumine in 4D-MRA. During the arterial phase peak signals of all tested contrast regimens are in the same range (due to saturation effects after standard-dose gadobutrol administration compared to dynamic CT). In the venous phase of imaging, however, peak signals are markedly higher after application of standard-dose gadobutrol, which is desirable in dynamic 4D-MRA, where all phases of imaging are of interest. The results of this animal study using the 4D-TRAK sequence at 3.0T may help to optimize contrast protocols in clinical 4D-MRA.

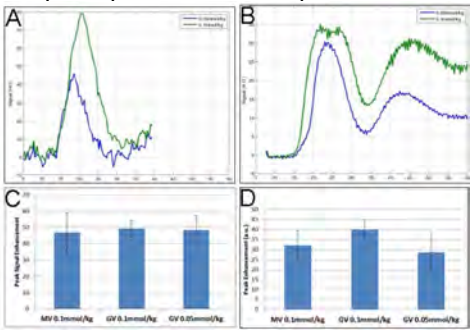

References:
[1] Voth M et al.; Eur Radiol 2011 Feb; 21(2):337-44;
[2] Hadizadeh DR et al.; Invest Radiol 2014 Jul; 49(7):457-64

Image:
Upper row: Standard dose and half-dose gadobutrol peak signals in dynamic CTA **(A)** and transverse 4D-MRA **(B)**
Lower Row: Peak signal levels with standard dose gadobutrol, half-dose gadobutrol and gadopentetate dimeglumine in 4D-MRA during the first pass **(C)** and second pass of bolus kinetics **(D).**

Accelerated Time Resolved Contrast Enhanced MRA of Dural Arteriovenous Fistulas using Highly Constrained Reconstruction of Sparse Cerebrovascular Datasets.

Zachary Clark MD*, Kevin M. Johnson PhD**, Yijing Wu PhD**, Myriam Edjlali MD***, Charles Mistretta PhD**, Oliver Wieben PhD**, Patrick Turski MD*

Affiliations: University of Wisconsin-Madison Departments of Radiology *, Medical Physics** and the Department of Morphologic and Functional Imaging, Université Paris Descartes, INSERM UMR 894, Hôpital Sainte Anne, Paris***

Purpose: Time resolved contrast enhanced magnetic resonance angiography (TR CEMRA) is commonly used to non-invasively characterize vascular malformations. However, the spatial and temporal resolution of current methods often compromises the clinical value of the exams. Constrained reconstruction is a temporal spatial correlation strategy that exploits the relative sparsity of vessels in space to dramatically reduce the amount of data required to generate fast high resolution TR CEMRA studies. In this study we describe our initial experience using a novel temporal spatial acceleration method termed HYPRFLow to diagnose and classify dural arteriovenous fistulas (DAVFs). Our hypothesis is that HYPRFLow images are of adequate diagnostic image quality to delineate the arterial and venous components of DAVFs and allow correct classification using the Cognard system.

Methods: 8 patients with known DAVFs underwent HYPRFlow imaging with isotropic resolution of 0.68 mm and temporal resolution of 0.75 s, 3D Time of Flight MRA (3DTOF) and DSA. 3DTOF images and HYPRFLow images were evaluated by 2 readers and scored for arterial anatomic image quality. Each DAVF was classified according to the Cognard system using HYPRFlow and DSA exams. DSA was considered the reference exam or gold standard.

Results: HYPRFlow imaging classification was concordant with DSA in all but one case. There was no difference in the arterial image quality scores between HYPRFlow and 3D TOF MRA (95% CI). Arterial to venous separation was rated excellent (n=3), good (n=4) or poor (n=1) and arteriovenous shunting was easily appreciated. Undersampling artifacts were reduced by using a low pass filter and did not interfere with the diagnostic quality of the exams.

Conclusion: HYPRFlow is a novel acquisition and reconstruction technique that exploits the relative sparsity of intracranial vessels in space to increase temporal and spatial resolution and provides accurate delineation of DAVF vasculature.

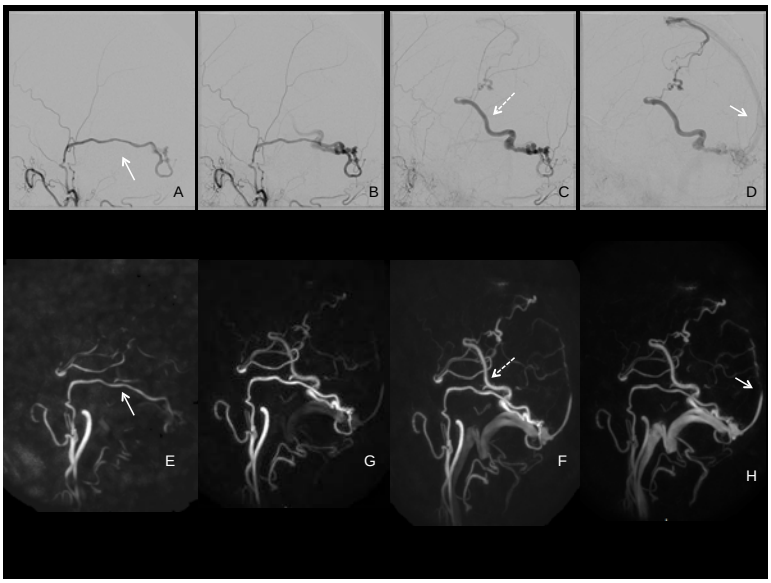

Cognard Type IV dural AVF. Top Row: Selective left external carotid DSA shows filling of a posterior branch of the middle meningeal artery (arrow) during the arterial phase (A), which connects via a dural fistula directly into a dilated (>5 mm diameter) cortical vein (dashed arrow) (B,C). The fistula ultimately drains into the superior sagittal sinus (arrow) (D). Bottom Row: Corresponding HYPRFLow images at similar time points in the angiographic series (E-H).

Steady-state ferumoxytol enhanced magnetic resonance angiography of the lower extremities provides optimal characterization of vascular lesions for peripheral arterial disease patients with renal failure

Evan Lehrman, Stefanie Weinstein, Judy Yee, Warren Gasper, Thomas Hope
University of California, San Francisco

PURPOSE: To evaluate ferumoxytol enhanced magnetic resonance angiography of the lower extremities for safety in renal failure patients and to compare steady state imaging versus first pass imaging in overall image quality and detection and characterization of vascular lesions.

METHODS: Forty patients with known or suspected peripheral arterial disease and renal impairment underwent ferumoxytol enhanced magnetic resonance angiography with both first pass and steady state image acquisition as part of a clinical workup. Any development of an adverse allergic reaction was noted. Each exam was evaluated and graded by two board certified radiologists with comparison of first pass acquisition to steady state acquisition for overall image quality and delineation of each vascular lesion including arterial stenosis, occlusion, dissection and aneurysm. Image quality and lesion delineation were graded from 0 to 3, with 3 being excellent and 0 being non-diagnostic.

RESULTS: Steady state imaging was superior in overall image quality in 18/40 cases (45%), first pass imaging was superior in 6/40 cases (15%), and both techniques were equivalent in 16/40 cases (40%). For overall image quality, mean grade for steady state was 2.65/3 and the mean for first pass was 2.32/3. A total of ninety lesions were identified in thirty-three of the patients. Steady state imaging was superior in lesion delineation in 69/90 lesions (77%). In 5/90 lesions (6%), first pass technique was superior. In 16/90 lesions (18%), the techniques were equivalent. For individual lesions, the mean grade for steady state was 2.68/3 and the mean for first pass was 1.76/3. No adverse allergic reactions developed and no subsequent nephrogenic systemic fibrosis was identified.
In the vast majority of cases, steady state imaging reveals superior detail of lower extremity arterial lesions compared to traditional first pass technique, particularly in the pelvis and thighs (see figure 1). Improved characterization of complex arterial lesions leads to improved pre-treatment planning by Vascular Surgeons and Interventional Radiologists. Conventional first pass technique remains important for delineation of tibial pathology, where venous contamination can be problematic in steady state imaging.

CONCLUSIONS: Ferumoxytol enhanced magnetic resonance angiography of the lower extremities is safe for peripheral arterial disease patients with renal failure. Steady state imaging provides optimal characterization of vascular lesions.

Figure 1: Distal superficial femoral artery plaque as depicted by steady state acquisition (a) and first pass acquisition (b) in a ferumoxytol enhanced MRA in a single patient.

a. Steady State Acquisition	b. First Pass Acquisition
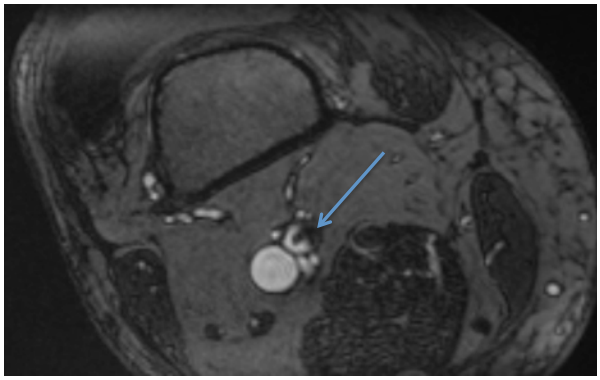	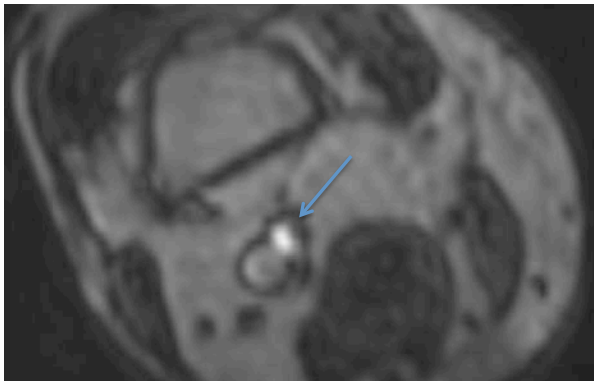

Ferumoxytol enhanced Magnetic Resonance Angiography in stage 4 and 5 Chronic Kidney Disease

Alex Vesey[1,3], Aleksandra Radjenovic[2], Martin Hennessy[3], Rosemary Woodward[3], Tracey Steedman[3], David Kingsmore[2,3], Patrick Mark[2,3], Paul Finn[4], Giles Roditi[2,3]

[1] British Heart Foundation Centre for Cardiovascular Science, College of Medicine, University of Edinburgh, UK;
[2] British Heart Foundation Glasgow Cardiovascular Research Centre, Institute of Cardiovascular and Medical Sciences, University of Glasgow, UK;
[3] NHS Greater Glasgow & Clyde, Glasgow, UK;
[4] Department of Radiology, University College Los Angeles, CA, USA

Purpose: Use of iodine and gadolinium based contrast is problematic in stage 4 or worse chronic kidney disease yet there is a heavy burden of vascular disease in affected patients and contrast-free angiography is often sub-optimal. An effective agent safe for use in renal failure is desirable. Ultrasmall superparamagnetic particles of iron oxide (ferumoxytol) are safe in chronic kidney disease and have been used for delayed enhancement MR imaging in a variety of pathologies due to their high relaxivity. They have a long half-life in the blood pool so hold promise for angiography. We sought to test the feasibility of ferumoxytol enhanced magnetic resonance angiography in patients with renal failure.

Methods: In this protocol development study we scanned 10 patients presenting with diverse pathology (all GFR < 30 $mLmin^{-1}1.73m^{-2}$, not on chronic renal replacement therapy) in whom non-invasive angiography was indicated. Imaging was performed on a 3T Verio (Siemens) clinical MRI system. A total dose of 4ml/kg of ferumoxytol was used. A fraction of the dose was administered initially as an infusion for first pass imaging with a dynamic contrast enhanced (DCE) technique. After the full dose was administered, steady state high-resolution imaging was undertaken using an ultrafast spoiled gradient echo sequences. Scan and infusion parameters were optimized and images assessed qualitatively and when available compared to subsequent invasive imaging.

Results: In all 10 patients, ferumoxytol was successfully administered and well tolerated with no adverse reactions. Ferumoxytol was able to strongly enhance the vasculature and provide subjectively high-quality diagnostic DCE and steady-state angiographic images (see example below). Management changes were made based on the imaging in all patients

Conclusion: Ferumoxytol is a promising agent for dynamic, first-pass and steady state cardiovascular imaging in patients with severe chronic renal impairment in whom traditional MR and CT contrast media are contraindicated. Minimal alteration to existing sequences is required. More work is required to define optimal dosing and infusion strategies

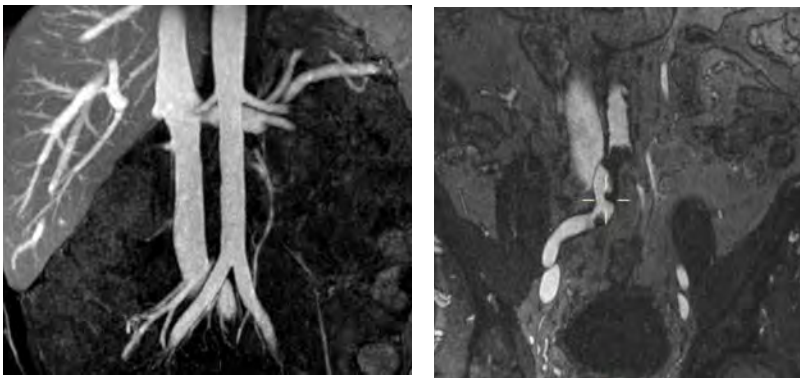

Two examples of ferumoxytol enhanced MRA of the abdominal aorta in patients with severe chronic kidney disease. **A** – MPR coronal reformat of a normal aorta. Panel **B** – Oblique reformat of sub-total occlusion of the distal aorta and proximal right common iliac causing claudication and transplant dysfunction

Ferumoxytol MRA for Pre-TAVR Assessment

[1]Paul Finn, [1]John Moriarty, [1]Adam Plotnik, [1]Takegawa Yoshida, [2]Olcay Aksoy, [2]Will Suh, [3]Richard Shemin.

UCLA [1]Radiological Sciences, [2]Division of Cardiology, [3]Division of Cardiothoracic Surgery.

Purpose: CT angiography (CTA) is the standard choice for assessment of arterial access anatomy in patients being considered for TAVR procedures (1,2). However, TAVR candidates are generally elderly with a higher prevalence of renal impairment than the general population (3) and because iodinated contrast media will be used during the TAVR procedure, it is desirable to minimize or eliminate their use prior to catheterization (4,5). Further, in patients with severe renal impairment, gadolinium based contrast agents may be problematic because of the perceived risk of NSF. We hypothesized that ferumoxytol may be a suitable alternative to CTA and Gd CEMRA in these patients.

Methods: Following informed consent and with approval from our IRB, we performed ferumoxytol enhanced MRA (FEMRA) for assessment of arterial access anatomy prior to TAVR in 20 patients (M/F = 15/5, mean age 84.5 yrs (+/- 8) with aortic stenosis and renal impairment (eGFR < 30 mls /m2.mn). FEMRA was performed at 3.0T in 15 patients and at 1.5T in 5, using a total dose of 4 mg /kg. Two patients had cardiac pacemakers. First pass and steady state FEMRA was performed in 16 patients and steady state imaging only in 4. The field of view extended from the neck to the proximal thighs in two overlapping stations. Images were post-processed with MIP and Volume Rendering.

Results: In all cases, FEMRA produced diagnostic studies, which formed the basis for confident TAVR planning. All patients remained stable throughout the FEMRA studies and there were no symptoms or significant changes in heart rate, blood pressure or blood oxygenation. Both first pass and steady state images were considered highly diagnostic but steady state images required more time for image processing. 12 patients had successful TAVR placement via a femoral approach with angiographic confirmation of FEMRA findings. 6 patients were not considered candidates for a femoral approach on the basis of FEMRA and had successful trans-apical placement. 2 patients are pending treatment.

Conclusion: In the current study, FEMRA was diagnostic, practical and safe at both 3.0T and 1.5T and provided sufficient information for confident planning of the access route for TAVR.

1. Achenbach, S., et al., *SCCT expert consensus document on computed tomography imaging before transcatheter aortic valve implantation (TAVI)/transcatheter aortic valve replacement (TAVR).* J Cardiovasc Comput Tomogr, 2012. **6**(6): p. 366-80.
2. Holmes, D.R., Jr., et al., *2012 ACCF/AATS/SCAI/STS expert consensus document on transcatheter aortic valve replacement.* J Am Coll Cardiol, 2012. **59**(13): p. 1200-54.
3. Sinning, J.M., et al., *Renal function as predictor of mortality in patients after percutaneous transcatheter aortic valve implantation.* JACC Cardiovasc Interv, 2010. **3**(11): p. 1141-9.
4. Bagur, R., et al., *Acute kidney injury following transcatheter aortic valve implantation: predictive factors, prognostic value, and comparison with surgical aortic valve replacement.* Eur Heart J, 2010. **31**(7): p. 865-74.
5. Yamamoto, M., et al., *Renal function-based contrast dosing predicts acute kidney injury following transcatheter aortic valve implantation.* JACC Cardiovasc Interv, 2013. **6**(5): p. 479-86.

Ferumoxytol MRA as an Alternative to CTA for Common Chest Indications: TAVR and Pulmonary Embolism

Michael D. Hope, Thomas A. Hope, Henrik Haraldsson, Farshid Faraji, Chengcheng Zhu, David Saloner
Department of Radiology and Biomedical Imaging, University of California, San Francisco

Introduction: CTA is routinely used in clinical practice for pre-procedure planning for transcatheter aortic valve (TAVR) placement and for the evaluation of pulmonary embolism (PE). One of its principal limitations is that iodinated contrast is contraindicated in patients with renal failure. For these patients, alternative approaches including MRI have been investigated, although using gadolinium as a contrast agent is also contraindicated. Ferumoxytol is an appealing substitute. As a treatment for the iron-deficiency anemia seen with chronic renal disease, it is appropriate for use in patients with renal failure. Here we explore the use of ferumoxytol MRA as an alternative to CTA for chest imaging.

Methods: Patients referred for TAVR planning (3) and evaluation of PE (8) were studied with ferumoxytol-enhanced MRA on a 3T system. Seven of the PE patients also had a CTA for comparison; the remaining patients did not because of impaired renal function. High-resolution 3D MRA examinations with 1.3-mm isotropic spatial resolution was performed on all patients with standard imaging parameters. Respiratory navigation and cardiac-gating was used for all TAVR studies at the equilibrium state of contrast enhancement, and respiratory-navigated sequences were employed for all PE studies.

Results: Ferumoxytol MRA for TAVR planning afforded crisp imaging of the aortic root with clear delineation of the aortic annulus, which is crucial for valve sizing (**Figure 1**).[1] The stair-step artifact that plagues CTA was not present with the volumetric acquisition of data. Additionally, the calcium blooming artifact that limits CTA evaluation of peripheral access vessels was not an issue. For PE studies, central and segmental emboli were identified with ferumoxytol MRA, but not smaller, subsegmental emboli. Respiratory gating improved imaging quality, and allowed for free-breathing though the acquisition (**Figure 2**).[1]

Discussion: Ferumoxtyol MRA offers some advantages for common chest CTA indications. Studies can be performed without radiation and in patients with renal failure. The stair-step and calcium blooming artifacts that are routinely seen with CTA for TAVR evaluation are not present. Free-breathing is possible for PE studies, which is particularly attractive for these patients who have trouble holding their breath.

Conclusion: Ferumoxytol MRA is a viable alternative to CTA in patients with renal failure for pre-procedure TAVR planning and evaluation of pulmonary embolism.

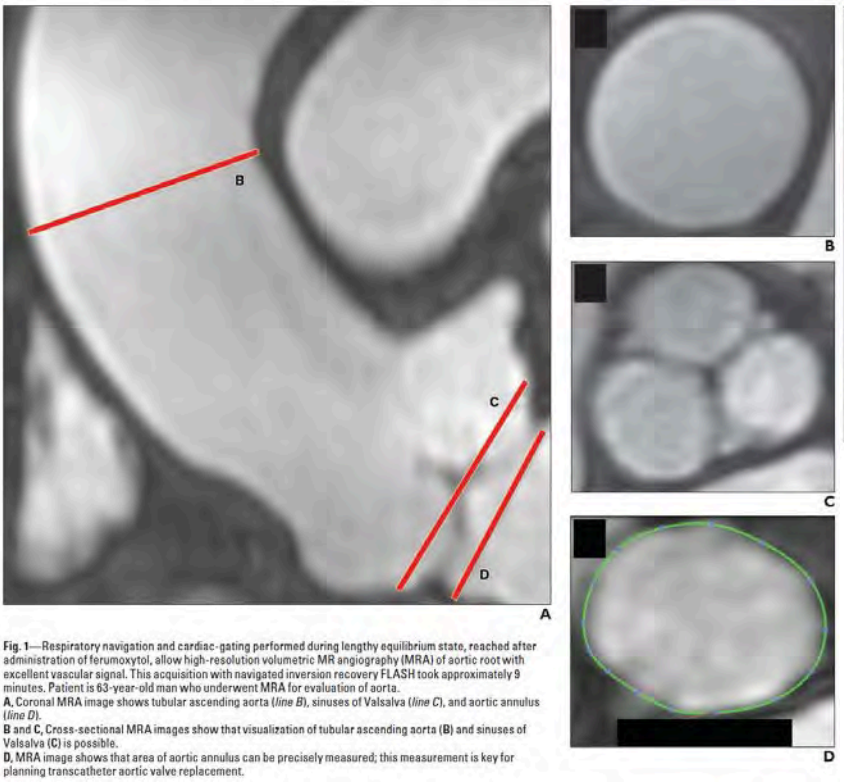

Fig. 1—Respiratory navigation and cardiac-gating performed during lengthy equilibrium state, reached after administration of ferumoxytol, allow high-resolution volumetric MR angiography (MRA) of aortic root with excellent vascular signal. This acquisition with navigated inversion recovery FLASH took approximately 9 minutes. Patient is 63-year-old man who underwent MRA for evaluation of aorta.
A, Coronal MRA image shows tubular ascending aorta (*line B*), sinuses of Valsalva (*line C*), and aortic annulus (*line D*).
B and **C**, Cross-sectional MRA images show that visualization of tubular ascending aorta (**B**) and sinuses of Valsalva (**C**) is possible.
D, MRA image shows that area of aortic annulus can be precisely measured; this measurement is key for planning transcatheter aortic valve replacement.

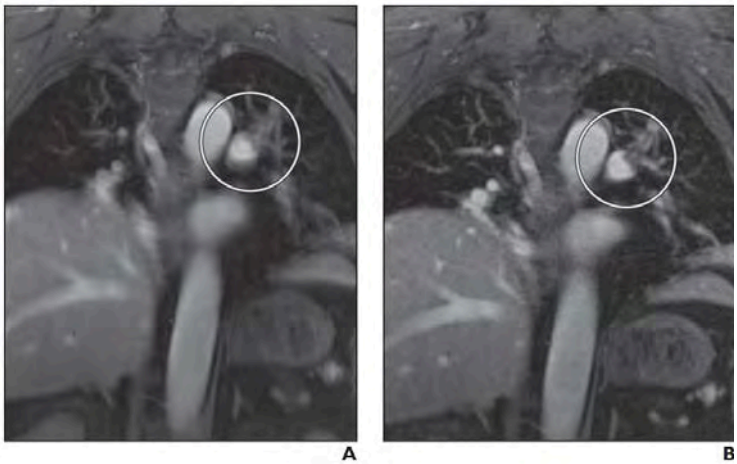

Figure 2: Steady-state MRA of a pulmonary embolism in the left upper lobe pulmonary artery without (**A**) and with (**B**) respiratory navigation.

Reference: 1) Hope MD et al. AJR:205, September 2015.

DARC-MR Lymphangiography Using a Combination of Gadolinium and USPIO Contrast: an Update

Jeffrey H. Maki, Peter C. Neligan, Gregory J. Wilson
University of Washington, Seattle, WA, USA

Introduction: Lymphedema is a chronic debilitating disease that is difficult to treat. Lymphaticovenous anastomosis (LVA) is an increasingly used microsurgical treatment for lymphedema that requires the pre-operative mapping of individual lymphatic channels. Traditional MR Lymphangiography (MRL), an MRA-like technique in which a Gd-based contrast agent (GBCA) is injected into webspaces of hands or feet has proven useful for such mapping, however the simultaneous enhancement of venous structures often makes it difficult to distinguish between lymphatics and veins. In response to this, DARC-MRL (Dual Agent Relaxation Contrast) was developed to exploit the blood-pool and T2* properties of the ultra-small superparamagnetic iron oxide (USPIO) ferumoxytol (AMAG Pharmaceuticals, MA, USA) to null any GBCA-enhancing veins.

Methods: As our new clinical MRL standard, intravenous ferumoxytol (5 mg/kg) was administered prior to intracutaneous gadolinium (gadobenate, Bracco Diagnostics, Princeton, NJ) for DARC-MRL in 50 consecutive patients (44 F, 6 M; 51 $\pm$ 15 years; 31 upper extremity, 14/5 uni-/bilateral lower extremity), all imaged at 3T (Ingenia, Philips, the Netherlands). Expected equilibrium blood ferumoxytol concentrations were in the range 0.06-0.08 ml/mg (1.0-1.4 mM), theoretically achieving a blood T2* < 2.0 ms at both 1.5T and 3T. Using 2-point Dixon imaging (mDixon, Philips), increasing TE times were tested (one TE near in-phase, the other near out-of-phase, starting at TE_1 = 3.5 ms, with TE_2 = TE_1 + 1.1 ms) and the shortest TE combination at which complete blood suppression could be achieved was determined. Following this, 1 ml intracutaneous GBCA (gadobenate) was administered into each webspace and DARC-MRL images (resolution 1.3 x 1.3 x 1.6 mm^3 upper station, 1.5 x 1.5 x 2.0 mm^3 lower station) were acquired for 30-90 min to follow the transit of GBCA up the lymphatics. At the study conclusion, short TE (1.4/2.5 ms) mDixon was performed to create a dual MRL/MRV and ensure no inadvertent lymphatic suppression. As part of a QC project, studies were evaluated for TE times required for venous suppression, any "break-through" venous enhancement, cases where lymphatics were significantly suppressed, and artifacts such as water-fat swaps or other types of image degradation.

Results: There were no adverse events related to ferumoxytol administration. Good image quality was seen in all patients (Fig. 1 demonstrates representative upper (a) and lower (b) extremity DARC-MRL). The majority (54%) of cases achieved good venous suppression at TE_1 = 5.8 ms, with an additional 30% suppressing at TE_1 = 4.6 ms. 4%, 3%, and 1% of the cases suppressed at TE_1 = 3.5, 6.9, and 8.0 ms respectively. Five (10%) cases demonstrated mild deep venous enhancement, typically proximally (above knee or elbow) in a single deep vein, none of which interfered with lymphatic evaluation. Water fat swaps were seen peripherally in 30% of cases (Fig. 1b), particularly with larger patients, but did not interfere with lymphatic evaluation. No instances of lymphatics being significantly suppressed were noted.

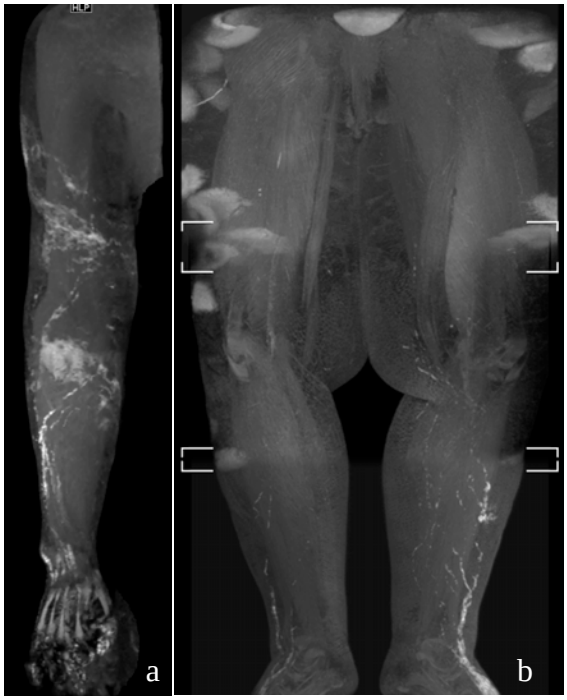

Figure 1. DARC MRL. (a) Upper extremity, 56F with RUE lymphedema s/p breast cancer therapy, 27 min post Gd, TE_1 = 7 ms. (b) Lower extremities, 52F with chronic lower extremity lymphedema, 50 min post Gd, TE_1 = 7 ms. Note no veins seen. Peripheral water-fat swaps noted superiorly lower extremity case only (bright "scalloping" along edges superiorly).

Discussion: DARC-MRL performed extremely well in 50 consecutive clinical patients, eliminating distracting venous enhancement too often seen in standard MRL. Despite a uniform ferumoxytol dose of 5 mg/kg, the TE's required for venous suppression varied moderately; with TE_1 for all $\leq$ 8.0 ms. Occasional non-problematic deep veins were seen, likely secondary to slow venous flow not achieving equilibrium ferumoxytol concentration. Despite the somewhat longer TE's used for DARC-MRL, mDixon image quality appears uncompromised without significant lymphatic suppression. Water fat swaps in the image periphery are more unsightly than problematic, and relate to inhomogeneities when imaging large FOV's or off-center extremities.

Ferumoxytol in Pediatric Congenital Heart Disease: Early Results with 4D Multiphase Steady State Imaging with Contrast (MUSIC) Enhancement

Kim-Lien Nguyen, MD, Fei Han, PhD, Daniel Z Brunengraber, MD, Stanislas Rapacchi, PhD, Ihab Ayad, MD, Gary Satou, MD, Peng Hu, PhD, J. Paul Finn, MD

Radiological Sciences (K.L.N, F.H., D.Z.B., S.R., I.A., G.S., P.H., J.P.F.), Division of Cardiology (K.L.N.), Division of Pediatric Cardiology (G.S.), Department of Anesthesiology (I.A.), David Geffen School of Medicine at UCLA, Los Angeles, CA; Division of Cardiology (K.L.N), VA Greater Los Angeles Healthcare System, Los Angeles, CA

Purpose: We recently described 4D MUSIC using ferumoxytol that generates isotropic high resolution 3D images over multiple, independent cardiac phases without breath holding. We evaluated the technique in a cohort of 42 pediatric patients with complex CHD and compared it to breath held CE-MRA.

Methods: Children with suspected or known complex CHD underwent ferumoxytol-enhanced MRA on a 3.0T MRI system between 2013 and 2015. Diagnostic image quality of named intra-cardiac structures and multiple vascular segments including the coronary arteries were graded on a four-point scale by two readers with advanced cardiovascular MRI training. Imaging findings were confirmed by surgery, correlative imaging or autopsy.

Results: Ages ranged from 3 days to 19 years, and weight from 1.2 kg to 62 kg. There were no adverse reactions to ferumoxytol. Intra-cardiac and vascular anatomy were significantly better visualized ($p<0.001$) with MUSIC imaging than with breath held CE-MRA. Coronary artery anatomy was routinely visualized with high confidence on MUSIC images. There was acceptable inter-observer correlation and concordance with correlative imaging, surgical findings and /or autopsy results was excellent.

Conclusions: Ferumoxytol-enhanced 4D MUSIC is superior to breath-held CEMRA in children with CHD. The implications for safe and rapid streamlining of data acquisition in pediatric CHD, and for diagnostic evaluation of patients previously too unstable for assessment with MRI, are significant.

References

Han F, Rapacchi S, Khan S, et al. Four-dimensional, multiphase, steady-state imaging with contrast enhancement (MUSIC) in the heart: A feasibility study in children. *Magn Reson Med* 2014 Oct 9 [Epub ahead of print]. PMID: 25302932

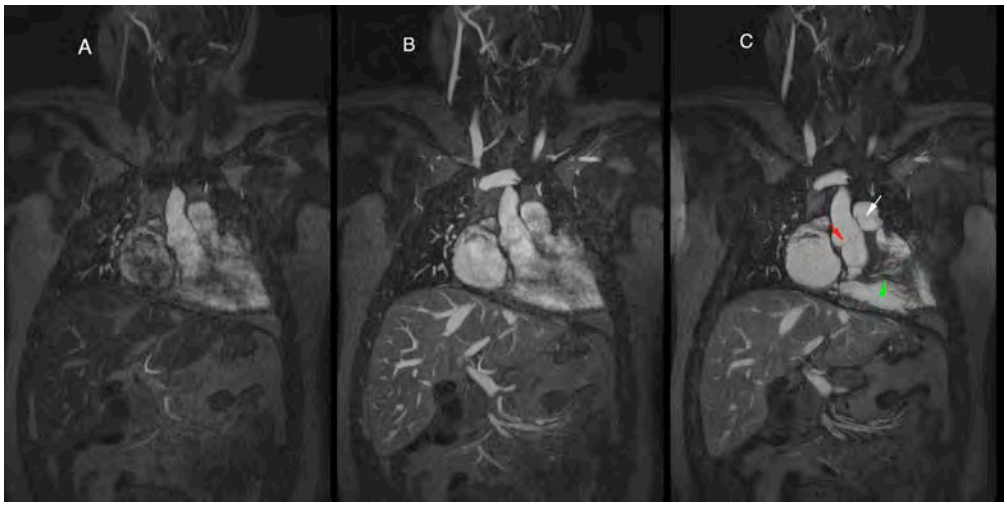

Figure 1(a,b,c). Breath held first pass (A), breath held steady state (B) and MUSIC (C) images in an 18 y.o. female with repaired tetralogy of Fallot. The arrows point to well defined aortic (red) and pulmonary (white) valve leaflets as well as thickened right ventricular trabeculae (green).

Adverse reactions to intravenous administration of ferumoxytol intended for use as MR imaging contrast

Alex Vesey[1,3], Olivia McBride[1], Rachael Forsythe[1], Nikhil Joshi[1], Scott Semple[1], Colin Stirrat[1], Giles Roditi[2,3], Jennifer Robson[1]
David Newby[1]

[1] British Heart Foundation Centre for Cardiovascular Science, College of Medicine, University of Edinburgh, UK;
[2] British Heart Foundation Glasgow Cardiovascular Research Centre, Institute of Cardiovascular and Medical Sciences, University of Glasgow, UK;
[3] NHS Greater Glasgow & Clyde, Glasgow, UK;
[4] Department of Radiology, University College Los Angeles, CA, USA

Purpose: Interest in the use of ultra-small superparamagnetic particles of iron oxide (ferumoxytol) for vessel or delayed enhancement magnetic resonance imaging is increasing but there have been reports of serious adverse hypersensitivity reactions. Our centers have been involved in several studies exploring the use of ferumoxytol. We present our experience of this agent in terms of tolerability and safety in the context of the latest global data and other commonly used intravenous contrast media and IV iron preparations.

Methods: A search using Google and the standard medical publication databases was undertaken. Manufacturer, national regulatory and pharmacovigilance agency (e.g. FDA) publications were also scrutinised. Data from these sources was extracted. Prospectively collected data from 7 clinical imaging studies in our institutions was pooled and analysed. The total number of patients, administered doses, adverse reaction (AR) rates and serious adverse reactions (SAR) rates were calculated.

Results: Our group has observed no SAR and a very low rate of AR relating to the use of ferumoxytol (per patient ARR 1/491 (0.2%); per infusion ARR, 1/691 (0.1%)). The quoted ARRs for ferumoxytol in the literature are highly variable but moderate to severe hypersensitivity reactions are reported in 0.2-2.6% of patients. These reaction rates are comparable with other iron containing infusions, but higher than those reported for gadolinium (0.01%) and iodinated contrast media (0.04-0.22%). Of note, the pharmacovigilance and study safety data pertain to large doses of ferumoxytol (>1g) given for anemia as a bolus injection; the imaging dose is typically < 300mg and is given as an infusion.

Conclusions: Our rate of severe hypersensitivity reactions is very low although our cohort is not large enough to detect rare reactions. The safety profile of ferumoxytol is slightly less favorable than gadolinium-based and iodinated contrast media, but these have disadvantages (use in renal failure and exposure to ionizing radiation) that may be complemented by ferumoxytol.

Ferumoxytol MRA: Minimizing Table Time in Claustrophobic Patients

[1]Paul Finn, [1]Takegawa Yoshida.

UCLA [1]Radiological Sciences.

Introduction: Modern CEMRA protocols are generally fast and efficient. Nonetheless, the requirement to time the first pass of a contrast bolus and to acquire multiple temporal phases adds complexity and imposes limits on how quickly a study can be set up and completed. Some patients with claustrophobia may be unable to tolerate any but the shortest periods within the scanner bore. We hypothesized that in patients with claustrophobia, ferumoxytol enhanced MRA (FEMRA) of the chest, abdomen and pelvis can be performed within 5 minutes from tuning to completion of FEMRA.

Methods: Following informed consent and with approval from our IRB, we performed FEMRA for assessment of venous anatomy of the chest, abdomen and pelvis in 10 patients (M/F = 7/4, mean age 42 yrs (range 16-73)) with severe renal impairment (eGFR < 30 mls /m2.mn) and varying levels of claustrophobia. FEMRA was performed at 3.0T in 9 patients and at 1.5T in 1, using a total dose of 4 mg /kg. Ferumoxytol was infused outside the scanner bore with continuous monitoring of heart rate, blood pressure and pulse oximetry. Patients were then advanced into the magnet bore and scout sequences were loaded and run without breath holding and without shimming. Based on the scout images, parameters and geometry factors were updated for a breath held acquisition of chest and upper abdomen. The table was then advanced 200-300 mm for a second breath held acquisition to complete a two station FEMRA study. The time from acquisition of the first scout images to completion of the first and of the second MRA station was noted.

Results: All patients tolerated the study well and were able to cooperate fully for the limited time within the scanner. The average time from first scout images to completion of the first MRA station was 2mn 10 secs and of the second station 4 mn 50 seconds. In all cases, FEMRA provided detailed images of all major venous and arterial structures from the neck to the thighs.

Conclusion: The stable steady state intravascular distribution of ferumoxytol supports protocols for FEMRA with ultra-short table times. The implications are significant for imaging of claustrophobic patients and more generally for scanning efficiency and throughput.

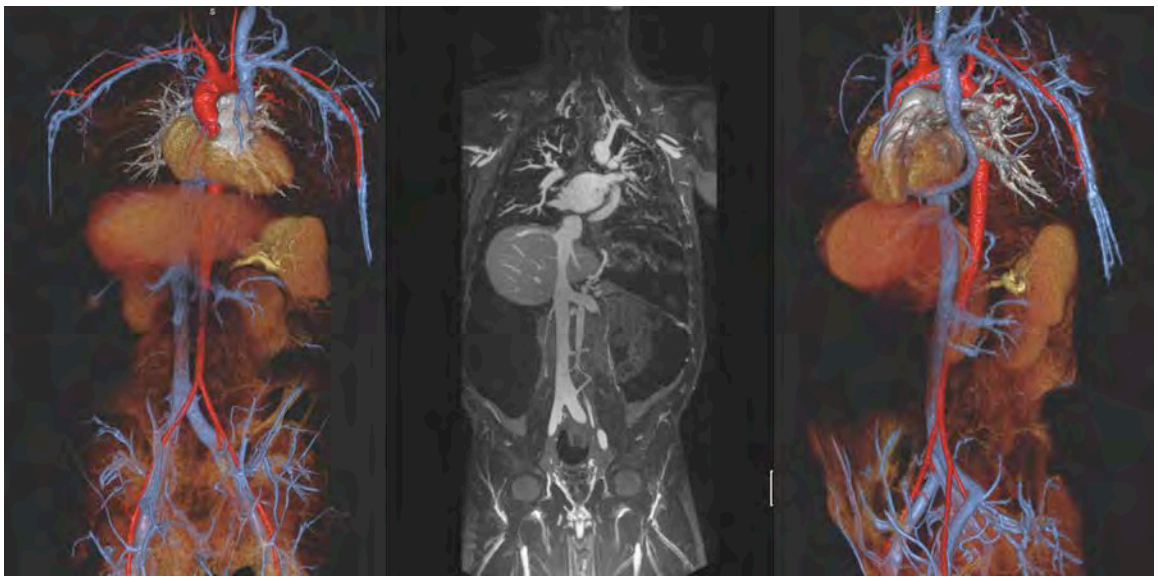

Figure 1. Volume rendered (left and right frames) and thin MIP (center frame) reconstructions in a 27 year old male with renal failure, cirrhosis, congenital heart disease and thoracic venous occlusion. The entire FEMRA study was acquired within 4 minutes of the initial scout sequence.

Ferumoxytol-Enhanced Motion-Corrected Accelerated 4D Flow MRI as a Single Sequence Congenital Heart Disease Exam: Validation of Functional and Segmental Analysis

Joseph Y. Cheng[1], Kate Hanneman[1,2], Tao Zhang[1], Marcus T. Alley[1], Peng Lai[3], Jonathan I. Tamir[4], Martin Uecker[4], John M. Pauly[5], Michael Lustig[4], Shreyas S. Vasanawala[1]

[1]Radiology, Stanford University, Stanford, California, USA, [2]University Health Network, University of Toronto, Ontario, CA, [3]Global Applied Science Laboratory, GE Healthcare, Menlo Park, California, USA, [4]Electrical Engineering and Computer Sciences, University of California, Berkeley, California, USA, [5]Electrical Engineering, Stanford University, Stanford, California, USA,

PURPOSE: To evaluate a motion-compensated compressed-sensing technique in 4D flow MRI for functional and anatomical segmental analysis for a comprehensive ferumoxytol-enhanced congenital heart disease (CHD) exam.

METHODS: A Cartesian 4D flow scan that is clinically used to quantify flow for CHD is assessed in the evaluation of function and anatomy. *Data Acquisition:* The 4D flow sequence was developed to enable (1) intrinsic navigation and (2) k-t sampling scheme. Acquiring data during the velocity-encoding gradients provided the setup to acquire Butterfly navigators[1] for motion monitoring at a high-temporal rate with no time penalty. The sampling scheme, VDRad, consisted of collecting groups of (k_y,k_z)-phase-encodes in a radial-like spoke with a golden-angle ordering that created a variable-density sampling pattern[2]. This scheme produced unique variable-density sampling patterns for each cardiac phase; this setup that has been shown to be beneficial for compressed-sensing reconstructions[3]. *Image Reconstruction*: Images were reconstructed using a compressed-sensing-enhanced parallel-imaging reconstruction combined with soft-gating for motion compensation[1]. Parallel imaging was achieved through a modified SENSE technique with eigenvalue-based sensitivity maps derived using ESPIRiT[4]. For compressed sensing, spatial wavelets and temporal finite differences were respectively used for spatial regularization and temporal regularization[5]. Images were reconstructed using alternating direction method of multipliers coded in C[6].

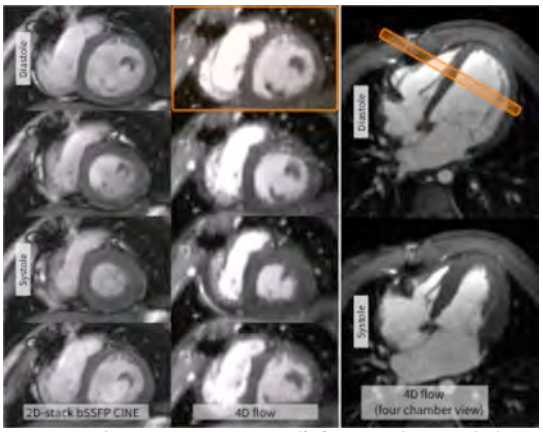

FIG 1: 2D bSSFP CINE scan (*left*, 3.1 min, resolution of 0.55×0.55 mm^2 with 7-mm-thick slices) and a 4D flow scan (*middle*: short-axis reformat, *right*: four-chamber reformat, R = 18.5, 9.4 min, resolution of 0.75×0.65×1.4 mm^3) of a 4.0-year-old female with a hypoplastic right ventricle. Four of 20 cardiac phases are displayed including end diastole and end systole. Even though 4D flow had lower spatial resolution and lower SNR, 4D flow provided similar assessment for myocardial borders and cardiac motion.

Experimental Setup: With IRB approval, informed consent, and HIPAA compliance, 16 patients (6 females, 7.6±5.7 yrs, heart rate of 88.2±24.0 BPM) referred for CHD MRI at 3T were prospectively recruited. Scans were performed after injection of 0.1 mL/kg ferumoxytol for blood pool enhancement. An RF-spoiled GRE 4D flow scan and a reference 2D short-axis stack bSSFP CINE scan were obtained for each patient using a 32-ch cardiac coil array. Parameters for 4D flow included matrix size of 320×220×120, flip angle of 15°, readout bandwidth of 83.33 kHz, velocity encoding range of 250 cm/sec for all axes, echo time (TE) of 1.8 ms, repetition time (TR) of 4.1 ms with a 5 ms fat-saturation pulse, and reduction factor (R) of 19.0±4.4 for a 8.6±1.8 min scan. For 2D bSSFP, parameters included TR of 3.4 ms, TE of 1.5 ms, flip angle of 60°, views-per-segment of 14, and 3 signal averages. Both sequences had similar temporal resolutions with a mean of 36.5 ms for 4D flow and 47.6 ms for 2D bSSFP.

Image Evaluation: Two cardiovascular radiologists evaluated the diagnostic performance of the 4D flow scan in standard segmental and anatomical analysis for CHD anatomy: superior/inferior vena cava connection, atrial situs, atrioventricular concordance, ventriculoarterial concordance, branch pulmonary artery stenosis, pulmonary vein connections and stenosis, arch vessel origins and stenosis, and coronary origins. The readers independently diagnosed each feature as being abnormal or normal. The interpretations were compared with the full patient medical record (MRI report, echocardiography, and operative notes). For functional assessment, side-by-side comparisons between the 4D flow (short-axis reformats) and 2D bSSFP scan were performed. Each reader scored the paired assessment for myocardial borders and cardiac motion on an ordinal scale of -2 (greater depiction in 2D bSSFP) to 2 (greater depiction in 4D flow). Wilcoxon test and weighted kappa (κ) were used to evaluate comparisons and inter-observer agreement, respectively.

RESULTS: Both readers had high sensitivity (≥ 0.85) as compared with the patient record. Due to the low frequency of some anatomical feature abnormalities, the 95% confidence interval for specificity was wider. Nevertheless, both readers had high specificity (1.00) for 9 out of the 10 anatomical features, and the readers had, at the minimum, substantial inter-observer agreement ($\kappa \geq 0.78$) for majority of the features. Compared with 2D bSSFP, 4D flow was significantly preferred by both readers for the depiction of the myocardial borders (score 0.9±1.0, $P < 0.05$, $\kappa = 0.94$). For the assessment of cardiac motion, readers ($\kappa = 0.77$) had no significant preference for either method (0.1±0.6). Fig. 1 shows an example.

CONCLUSION: Functional and segmental anatomical assessment in CHD is feasible with ferumoxytol-enhanced motion-corrected accelerated 4D flow. We have demonstrated that comprehensive assessment of CHD can be accomplished in ~10 min from a single sequence.

REFERENCES: [1] JY Cheng et al. ISMRM 2015, p451. [2] JY Cheng et al. JMRI 2015. [3] M Lustig et al. MRM 2007;58:1182–1195. [4] M Uecker et al. MRM 2014;71:990–1001. [5] L Feng et al. MRM 2013;70:64–74. [6] M Uecker ISMRM 2015, p2486.

Accelerated Four-dimensional, Multi-phase, Steady-state Imaging with Contrast Enhancement using Parallel Imaging and Compressed Sensing

Ziwu Zhou[1], Fei Han[1], Stanislas Rapacchi[1], Kim-Lien Nguyen[1], Daniel Z Brunengraber[1], J. Paul Finn[1], and Peng Hu[1]

[1]*Radiology, University of California, Los Angeles, Los Angeles, CA, United States*

Purpose: Breath-held first-pass contrast-enhanced magnetic resonance angiography (CE-MRA) is widely used for anatomical assessment of the cardiovascular system. It provides excellent visualization of the majority of extra-cardiac vessels. However, the need to capture first passage of Gadolinium-based contrast agent (GBCA) requires a non-cardiac-gated acquisition, leading to poor delineation of intra-cardiac structures such that supplemental 2D cine images is always required. In this work, we present an accelerated 4D non-breath-hold multiphase, steady-state ferumoxytol-enhanced imaging technique (MUSIC)[1] that supports simultaneous anatomical and functional assessment of the heart and related blood vessels using a single fast scan without breath holding in children with congenital heart disease (CHD).

Methods: The accelerated MUSIC sequence was a high bandwidth, spoiled gradient recalled echo (GRE) sequence. Cardiac motion and respiratory motion were compensated through ECG-triggered and respiratory-gated acquisition[1]. K-space was acquired in such a way that center ky-kz region is fully sampled while the outer k-space is under-sampled using a variable-density Poisson-Disk distribution (Fig.1d). The net acceleration rate is 7x compared with fully sampled k-space. Images were reconstructed separately for each cardiac phase by minimizing the following cost function:

$$\arg min_x \, ||DFSx - y||_2 + \mu||Wx||_1,$$

where S is the coil sensitivity map estimated using ESPIRiT[2], F and D are Fourier transform and under-sampling operations. x and y represent the reconstructed image and k-space measurement. Randomized shifting wavelets W were used as the regularization term. The algorithm was implemented in C/C++ based on the Berkeley Advanced Reconstruction Toolbox[3] (BART). Total reconstruction time for one 4D dataset (500x300x150x8) was less than 5 minutes on a conventional PC with GPU.

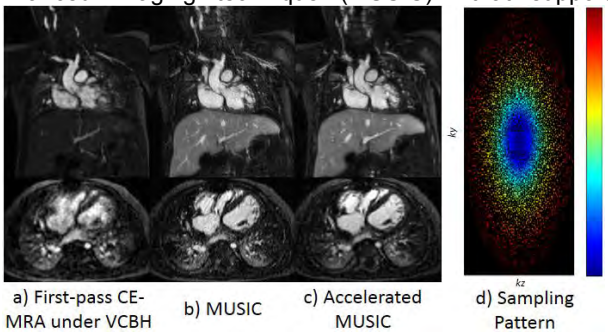

Figure 1 Selected slices of first-pass a) CE-MRA; b) MUSIC and c) accelerated MUSIC on a 9 m.o.boy. The intra-cardiac structures (e.g. cardiac chambers, aortic root and valves) are much better defined using MUSIC and accelerated MUSIC. d) Variable density Poisson-Disk k-space sampling pattern used in accelerated MUSIC. The fully sampled center k-space and under-sampled outer k-space result in net acceleration factor of 7x. The trajectory is depicted with samples colored based on the temporal sampling order

Thirteen pediatric CHD patients were scanned under general anesthesia and controlled ventilation. The breath-held CE-MRA was first performed under ventilator-controlled breath-holding (VCBH) during the first-pass of a ferumoxytol bolus injection (4 mg-Fe/kg). Subsequently, MUSIC[1] accelerated with GRAPPA 3X and the proposed accelerated MUSIC sequences were performed during the steady-state distribution phase of ferumoxytol without VCBH using the regular airway pressure signal for respiratory gating. Sequence parameters included: TR/TE: 2.9/0.9ms, FA: 25°, matrix size: 500x300x150, isotropic resolution: 0.8-1.0mm without interpolation, 6-9 cardiac phases, scan time: 8±2 min for MUSIC, 4±1 min for the accelerated MUSIC. In this validation study, spatial and temporal resolution were same for MUSIC and accelerated MUSIC. Subjective image quality scores (1=poor, 2=fair, 3=good, 4=excellent) in five different anatomical regions were visually assessed on both original MUSIC and accelerated MUSIC images by two board certified radiologists. In one patient, a supplemental accelerated MUSIC acquisition was performed incorporating 17 cardiac phases with 41ms temporal resolution.

	Coronary Origins	Aortic Root	Myocardium	Pulmonary Trunk	Descending Aorta
MUSIC	3.6±0.9	3.9±0.3	3.3±0.5	3.8±0.4	3.9±0.3
Accelerated MUSIC	3.6±0.9	4.0±0.0	3.4±0.5	4.0±0.0	4.0±0.0

Table 1 Subjective image quality score

Results and Discussion: Fig.1a-c compares first pass VCBH CE-MRA, MUSIC and accelerated MUSIC on a 9 m.o boy. Both MUSIC and accelerated MUSIC provide vastly better definition of intra-cardiac structures than first pass CE-MRA by eliminating cardiac motion. Subjective image scoring (Table 1) of accelerated MUSIC is similar to the original MUSIC, although acquisition time was halved. Fig. 2 shows reformatted cardiac four-chamber view and short axis view of MUSIC, accelerated MUSIC and 2D cine images. Comparing with cine images, the cardiac chambers were also well delineated for both systole and diastole phases of the cardiac cycle on original MUSIC and accelerated MUSIC images, which is important for accurate chamber segmentation and ventricular volumes measurement.

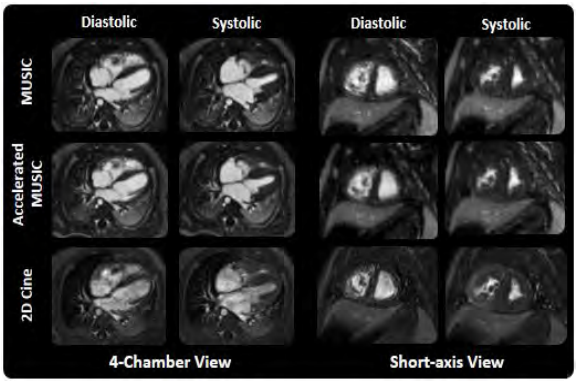

Figure 2 Diastolic and systolic phase of reformatted cardiac four-chamber (left two columns) and short-axis (right two columns) views based on original 4D MUSIC (first row), CS-PI 4D MUSIC (second row) and contrast-enhanced 2D FLASH cine (third row) on a 6-month-old, boy

Conclusion: This work demonstrates the feasibility of acquiring high spatial and temporal resolution, cardiac phase resolved, respiratory motion compensated, 4D images on anesthetized pediatric patients using Parallel Imaging and Compresses Sensing. The complete 4D dataset can be reconstructed in less than 5 minutes, suggesting the feasibility of inline image reconstruction on the MR host computer. As always, the acceleration can be either used to shorten the scan time or more importantly, increase the temporal/spatial resolution. Our study has limitations as the cohort size was relatively small and a more systematic comparison with traditional 2D cine images is needed.

References: [1] F Han et al, MRM 2014. [2] M Uecker et al, MRM 2014. [3] BART: v0.2.04.

Cardiac and Respiratory Self-Gated 4D Multi-phase Steady-state Imaging with Ferumoxytol Contrast (MUSIC)

Fei Han, Ziwu Zhou, Yu Gao, Paul Finn, Peng Hu

Department of Radiology, University of California, Los Angeles

Purpose: Conventional contrast-enhanced MRA is generally performed without cardiac gating due to the time constraint imposed by breath-hold and the first passage of the gadolinium based contrast agent and therefore provides limited delineation on blood vessels that are subject to cardiac motion. To address this issue, we recently proposed the MUSIC[1] approach where cardiac-phase-resolved 4D images are acquired without breath-holds during the steady-state distribution of ferumoxytol, an intravascular contrast agent. Using ECG and airway pressure signal for motion gating, the original MUSIC has been successfully used in pediatric patients and provides exquisitely detailed information on both intra- and extra-cardiac vascular anatomy. However, the airway pressure signal is only available when general anesthesia is performed and the ECG signal could be problematic especially in high field strength due to magneto-hemodynamic effects and interferences from the RF pulses and gradients. To overcome these limitations, we propose a self-gated MUSIC (sgMUSIC) approach where a retrospective motion self-gating technique is used to eliminate the need for external physiological signal and make the MUSIC approach potentially available on patients with spontaneous breathing. In this study, we test the sgMUSIC on pediatric patients under general anesthesia so that the derived motion signal can be validated against the recorded physiological signal and the images can be compared with the ones from original MUSIC.

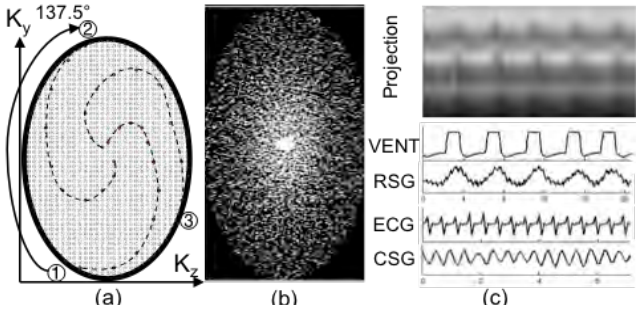

Fig.1 (a,b) the ROCK sampling pattern; (c) from top to bottom: projection image from k-space center-line, recorded ventilator airway pressure signal (VENT), respiratory motion self-gated signal (RSG), recorded ECG signal, cardiac motion self-gated signal (CSG).

Methods: ***(a) Data acquisition:*** A 3D gradient-echo sequence was modified with ROtating Cartesian K-space (ROCK) sampling pattern (Fig.1a-b) where $k_y k_z$ view of 3D Cartesian sampling grid was reordered in a quasi-spiral pattern with each arm starting from the center. The entire k-space was oversampled with relative higher density in the center region to allow retrospective sorting into multiple cardiac phases. ***(b) Data sorting:*** Cardiac and respiratory motion self-gating signal was derived from the repeatedly sampled k-space centerline using cross-correlation[2] and further separated by band-pass filter. The acquired data is then retrospectively soft-gated[3] based on the derived respiratory signal and sorted into different cardiac phase based on the derived cardiac signal. ***(c) Image Reconstruction:*** Images were reconstructed independently for each cardiac phase using ESPIRiT, a compressed sensing and parallel imaging combined approach[4]. The data sorting and image reconstruction algorithms were implemented in our GPU-accelerated image reconstruction framework[5] so that reconstructed 4D images are available at the scanner console 5-8 minutes after the scan. ***(d) Scan Protocol:*** 6 clinically indicated pediatric patients (aged 1 month to 8 years old) with congenital heart disease were included in this study. General anesthesia was performed with controlled mechanical ventilation. 4mg-Fe/kg ferumoxytol was administrated in each patient. The sgMUSIC was performed after our standard clinical protocol, which includes the original MUSIC with matching field-of-view and spatial resolution. Sequence parameters included: TE/TR=0.9/2.9ms, FA=25°, 500x300x150, 0.8-1.0mm isotropic resolution without interpolation, scan time=5±1min. The self-gated images were reconstructed without using ECG or ventilator pressure signal, but these signals were recorded for validation purpose. The datasets were retrospectively binned using two different temporal resolutions: 6 phases@100ms and 15 phases@40ms.

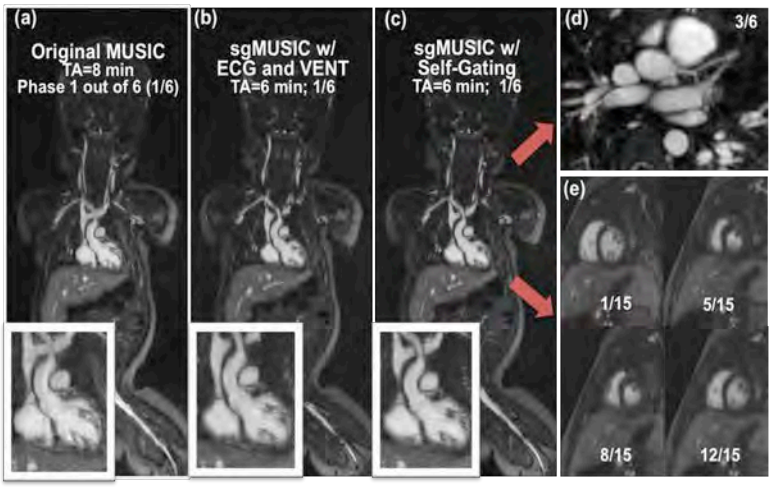

Fig.2 Image of the original MUSIC (a), sgMUSIC data reconstructed using physiological signal for gating (b) and sgMUSIC using self-gating (c). The sgMUSIC could be retrospectively reconstructed with different number of cardiac phases where the left coronary is visualized in a 6-phase-reconstruction (d) and a cardiac functional assessment could be performed based on a 15-phase reconstruction (e). Images were acquired from a 3-month-old female with congenital heart disease.

Results: All 6 scans were successfully completed. Fig.1c shows a time series of the center k-space projections (top) and the derived cardiac and respiratory self-gating signals. For comparison, the actual ECG and ventilator air pressure signal is also shown. Fig.2a-c shows the images from a 3-month-old female. These sgMUSIC images using self-gating signal have similar quality with the ones using physiological signal. When compared with the original MUSIC acquired in 8min with 4X GRAPPA, the sgMUSIC acquisition took 6min due to the use of variable density sampling pattern and non-linear image reconstruction algorithm. The number of cardiac phases in sgMUSIC can be retrospectively defined to fit different clinical need due to our golden angle reordering. The 2D image in Fig.2d was reconstructed into 6 phases where the left coronary artery is visualized on the third phase due to the high SNR from a relatively dense k-space sampling. The selected reformatted 2D cardiac short axis images in Fig.2e were reconstructed into 15 cardiac phases based on the same dataset, where the higher temporal resolution is desirable for cardiac functional evaluation.

Conclusion: The proposed cardiac and respiratory self-gated MUSIC eliminates the need of external physiological signal for motion gating, has slightly increased scan efficiency, and allows retrospective choice of temporal resolution, while maintaining or exceeding the image quality of the original MUSIC.

Ref: 1) Han et al, MRM2014; 2) Hu et al, MRM2012; 3) Cheng et al, JMRI2014; 4) Uecker et al, MRM2014; 5) Han et al, ISMRM2015;

Quantitative myocardial perfusion with dynamic ferumoxytol enhanced MRI

Aleksandra Radjenovic[1], Giles Roditi[1,2], Jianing Pang[3], Samuli Raulahammi[1], Patrick Mark[1,2], Alex Vesey[4], Martin Hennessy[2], Rosemary Woodward[1,2], Tracey Steedman[1,2], Peter Gatehouse[5], Paul Finn[6], Debiao Li[3], Colin Berry[1,2]

[1]British Heart Foundation Glasgow Cardiovascular Research Centre, Institute of Cardiovascular and Medical Sciences, University of Glasgow, UK; [2]NHS Greater Glasgow & Clyde, UK; [3]Biomedical Imaging Research Institute, Cedars-Sinai Medical Center, Los Angeles, CA; [4]BHF Centre for Cardiovascular Science, University of Edinburgh, UK; [5]NIHR Cardiac Biomedical Research Unit, Royal Brompton Hospital, London, UK; [6]Radiological Sciences, David Geffen School of Medicine at UCLA, CA

Purpose: Ferumoxytol is a pure intravascular ultrasmall superparamagnetic iron oxide (USPIO) contrast agent that has shown huge potential for clinical imaging of vascular anatomy. We hypothesise that dynamic, first-pass T1-weighted imaging, with ultra low dose ferumoxytol will enable simultaneous acquisition of arterial input function (AIF) and myocardial time-intensity curves required for quantitative assessment of myocardial blood flow (MBF).

Materials and methods: In-vitro experiments were conducted using ferumoxytol diluted from 0 to 76mM. Imaging was performed on a 3T Verio (Siemens) clinical MRI system using saturation recovery prepared fast gradient echo acquisition (TS = 90ms, TR/TE/FA =154/0.96/10, BW = 845Hz/px). Signal enhancement (dSI/dC>0) was observed up to 1:256 dilution (1.2mM). However, linear relationship started to break down for C>0.3mM.

In a healthy male volunteer (age 53, weight 80kg), DCE-MRI was acquired before and after intravenous administration of 4ml of diluted ferumoxytol (0.8ml pure ferumoxytol + 3.2ml saline), at the injection rate of 3ml/s, followed by 20ml saline. Total administered dose was therefore 0.8ml (0.01ml/kg, 0.17mg/kg or 0.003 mmol/kg).

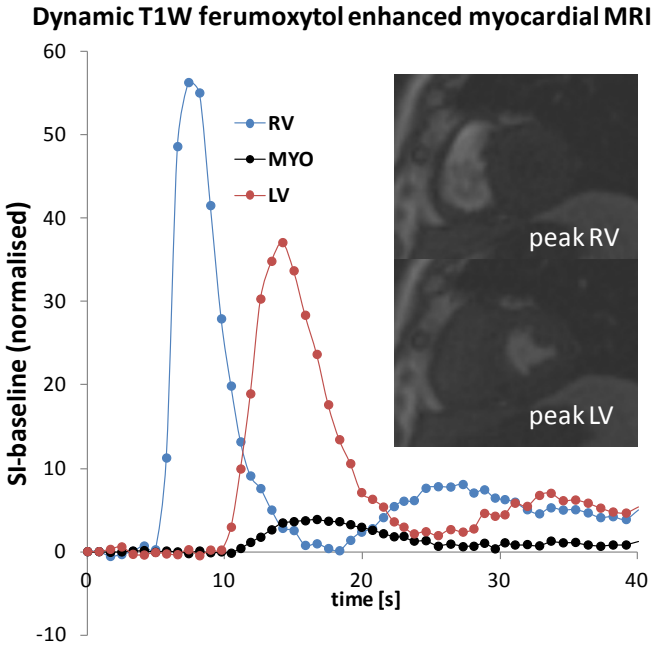

Figure 1. SI/time curves derived from RV, LV and mid-ventricular myocardium (MYO)

Results: Normalised signal intensity curves for RV and LV cavities are displayed in Figure 1, alongside myocardial SI/time curve (MYO). The onset of enhancement in the LV occurred 5.3 seconds after RV, with peak enhancement points separated by 6.3 seconds. Broadening of the LV curve compared to RV was observed (with time to peak, TTP of 2.6 vs 1.5s), alongside the reduction in peak enhancement (66 vs 44 a.u.). Area under the RV first-pass curve (244 a.u.) was marginally reduced by the time ferumoxytol bolus reached the LV (AUC = 240 a.u.). Model based deconvolution was used to estimate MBF values from six myocardial segments (2 in each coronary territory: LAD, LCX and RCA). Mean estimated MBF was 1.09 (0.22)ml/g/min, with LAD (1.34)>LCX (1.08) >RCA (0.86), in broad agreement with literature values.

Conclusion: We have demonstrated feasibility of ultra low dose ferumoxytol enhanced dynamic MRI as a tool for quantitative measurement of microvascular blood flow in the myocardium.

Further work is required to determine optimal dose ranges and imaging parameters for clinical perfusion imaging while maintaining reliable AIF. Parallel developments in designing methods for ferumoxytol enhanced cine and flow imaging, regional myocardial blood volume assessment, coronary anatomy and delayed contrast accumulation in sites of inflammation and scarring will provide a platform for comprehensive diagnostic assessment of a wide range of cardiac pathologies.

We acknowledge the support of the British Heart Foundation and Siemens Medical (WIP 713).

Flip-Angle optimization in Ferumoxytol-MRA: Preliminary results using different dose schemes and comparison with Gadobenate-MRA.

[1] T. Schubert, [1] U. Motosugi, [2] S. Sharma, [1] S. Kinner, [2] D. Hernando, [1,2] S. Reeder

Departments of [1]Radiology and [2]Medical Physics, University of Wisconsin – Madison, USA

Purpose

Ferumoxytol (FX) has gained interest as a positive MR-contrast agent (CA) in patients with renal failure [1]. Furthermore, due to the slow uptake in tissue, FX acts as a blood pool contrast agent, allowing MRA-acquisitions in delayed phases [1,2]. The purpose of this study is to a) compare FX-MRA with Gadobenate (GD)-MRA, b) evaluate the signal intensities (SI) with changing flip angle, and c) compare two different dose schemes with respect to SI and image quality.

Methods

FX-MRA was performed in five healthy volunteers one month after GD-MRA was acquired as reference standard. Volunteers were assigned to either full (FD; 0.07 mmol/kg) or half dose (HD; 0.035 mmol/kg) of FX. First pass MRA was performed with a flip angle (FA) of 50 degrees, and consecutive MR images were acquired with decreasing FAs down to 10°, in increments of 10°. MR data were evaluated qualitatively and quantitatively with respect to image quality (1=good, 2=suboptimal, 3=not usable) and SNR by two radiologists with 7 and 10 years of experience, respectively.

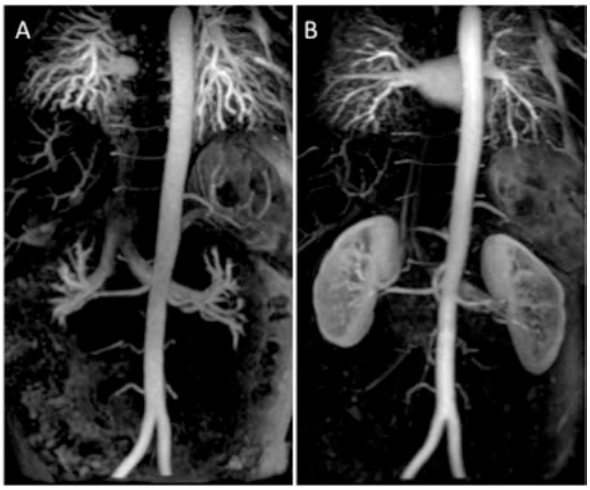

Fig. 1.: Ferumoxytol MRA (left, A) and Gadobenate MRA (right, B) of the same volunteer

Results

Relative aortal SI (Aorta/Muscle) in the arterial phase were higher with GD (27.1) compared to Ferumoxytol full dose (11.2) and half dose (6.6). In the portovenous phase, relative aortal SI were higher with full dose FX (7.2) than GD (6.4) and half dose FX (4.3). Relative aortal SI did not decrease with FX in the late phase 5 min p.i. (7.8 full dose, 5.2 half dose), whereas SI gradually declined with GD (2.8), Fig.2. For FX, aortal SI relative to muscle showed to be highest with a FA=40°, whereas arterial SI relative to liver tissue were highest with a FA=10°. Qualitative evaluation revealed a comparable performance of FX and GD with regard to large and small vessel depiction in the arterial phase (Fig. 1). As FX uptake takes places in macrophages of the reticuloendothelial system in a delayed fashion, less overlay of contrast enhancing tissues is seen in the late phase (Fig 2).

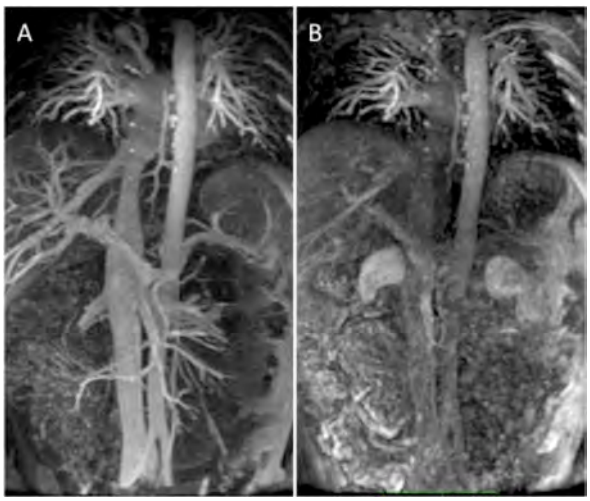

Fig. 2.: Late phase (5 min) after Ferumoxytol (left, A) and Gadobenate (right, B).

Conclusion

Ferumoxytol applied as MR-CA shows comparable performance compared to Gadobenate (Fig. 1) in the arterial phase and may be utilized even with reduced dose if warranted. Furthermore, FX is advantageous for imaging at later phases due to its blood pooling characteristic and reduced overlay of contrast enhancing tissue.

[1] Hope, AJR 2015
[2] Li, JMRI 2005

Time of Arrival Parametric Mapping derived from Fast High Resolution Whole Brain Contrast Enhanced 4D MRA improves the anatomic display of contrast kinetics in patients with brain vascular malformations.

[1] Schubert T, [2] Wu Y, [2] Johnson K, [1] Maksimovic J, [1,2] Wieben O, [1] Turski P.

Departments of [1]Radiology and [2]Medical Physics, University of Wisconsin – Madison, USA

PURPOSE

Time-of-arrival (TOA) maps can be derived from high temporal resolution 4D CEMRA datasets to provide a qualitative description of contrast material arrival time in each voxel. [1] The purpose of this project is to determine whether TOA enhanced 4D MRA and/or Virtual Bolus Imaging improve the display of contrast kinetics in patients with vascular malformations.

METHODS

High spatial resolution whole brain contrast enhanced 4D MRA with 0.75s temporal resolution were acquired by using radial acquisition and highly constrained projection reconstruction (4D CE HYPRFlow [3]). The TOA maps are based on signal intensity changes over time for each voxel. The TOA for each voxel was defined as the time point when the signal intensity reached 20% of its maximum. In the first method, TOA maps were generated, colored encoded and then multiplied with the time-resolved contrast enhanced MRA images at each time frame to form new 4D MRA images (TOA enhanced 4D CEMRA) which not only represents the contrast enhancement of vessels at different time frames, but also contain the contrast arrival times with defined color encoding. In the second method, each time frame was weighted by a Gaussian distribution in the time domain to form a virtual 4D bolus map. This 4D bolus map was then color coded and multiplied with the 4D MRA images to form a DSA-like virtual bolus visualization, where at each time frame, only vessels with certain TOA values within the defined bolus length appear. 4D CEMRA, TOA maps and virtual bolus images from seven AVM patients were scored by two observers for diagnostic confidence for detecting AVM arterial feeders, nidus and draining veins using DSA as the reference standard.

RESULTS

For both observers, 6/7 of the TOA maps improved identification of the arterial feeders and improved diagnostic confidence for the delineation of the nidus and venous drainage in all seven cases. The virtual bolus images increased diagnostic confidence of the venous drainage in 5/7 patients. Figure 1 demonstrates axial projection 4D CEMRA, TOA enhanced 4D MRA and virtual bolus (bottom row).

CONCLUSIONS

TOA enhanced 4D MRA provides serial images and time of arrival maps in one simple display. Our preliminary results suggest that TOA mapping improves delineation of the arterial supply, nidus and venous drainage in AVM patients. The virtual bolus method further improves diagnostic confidence of venous drainage by reducing vessel overlap.

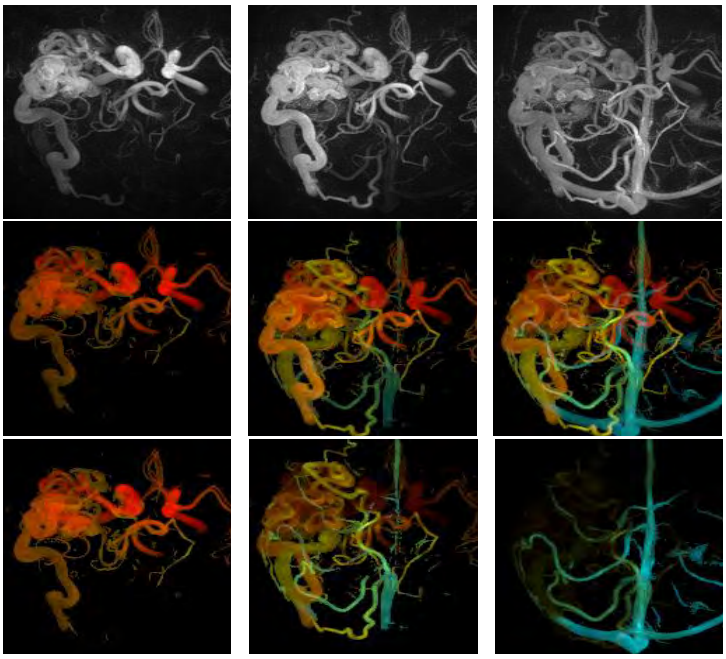

Figure 1: CE-MRA (top row), TOA Maps (second row), Virtual bolus maps (bottom row)

[1] Illies et al AJNR Aug 2013
[2] Riederer et al Radiology 2009
[3] Velkina et al., J Magn Reson Imaging. 2010 Feb;31(2):447-56
Support NIH RO1S066982 and GE Healthcare

Intracranial Dual-*Venc* 4D flow MRI at 7T

Susanne Schnell[1], Michael Markl[1], Can Wu[1], Pierre-Francois Van de Moortele[2], Sebastian Schmitter[2]
[1]Northwestern University, [2]University of Minnesota

Purpose: A number of studies have demonstrated the potential of 4D flow MRI for the assessment of changes in intracranial hemodynamics in patients with cerebrovascular diseases such as AVMs or aneurysms. However, previous applications of 4D flow MRI[1] were limited by insufficient spatial resolution for the assessment of hemodynamics, e.g. in small intracranial aneurysms (<7 mm)[2,3]. Furthermore, current 4D flow MRI methods have insufficient velocity range to fully resolve complex intra-aneurysmal flow patterns including high velocity inflow jets and slow vortex and helix type flow. In this work we addressed these technical limitations by developing *k-t* GRAPPA[4] accelerated dual-*venc* 4D flow MRI at 7Tesla. The aim was to utilize the high SNR at 7T in combination with reduced velocity noise of the dual-venc acquisition to achieve isotropic sub-millimeter high resolution 4D flow MRI in acceptable total scan times by k-t acceleration.

Methods: We have developed interleaved low- and high-*venc* PC-MRI using a fully integrated dual-*venc* 4D flow MRI sequence with a shared reference scan at 7T (12.5% reduction of total scan time compared to two separate high- and low-*venc* scans). The sequence was previously tested and evaluated on 3T MRI[5]. The high-*venc* data was used for complete velocity anti-aliasing of the low-venc data while maintaining the favorable velocity to noise ratio of the low-venc data. A validation study using a pneumatically controlled rotation phantom showed that the velocity aliasing could be successfully corrected for all voxels and that an expected reduction in velocity noise of 206% could be achieved. Pilot data on three healthy volunteers were acquired using a 7T system (Siemens MAGNETOM) with the following scan parameters: $venc_{low}$=45cm/s, $venc_{high}$=145cm/s, temporal/spatial resolution=150ms/0.8mm[3], *k-t* GRAPPA acceleration with R=5, scan time = 17±2min. In order to adjust for the optimal flip angle we acquired transmit B1 maps previous to the dual-*venc* acquisition.

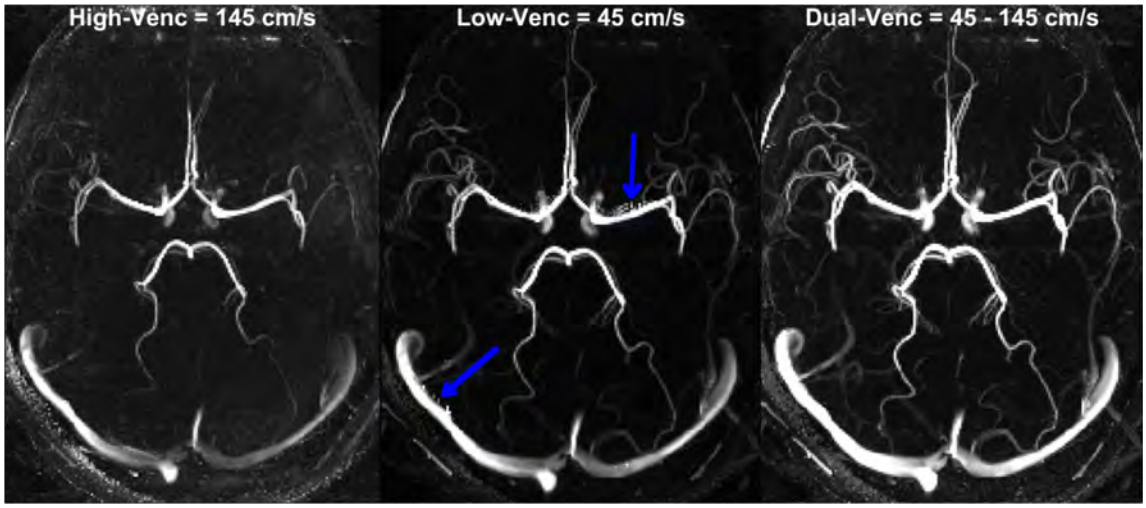

Figure 1: 3D PC-MR angiograms derived from dual-*venc* 4D flow MRI at 7T. for high-*venc* (145cm/s, left), low-*venc* (45 cm, middle) and dual-*venc* (right). Higher noise levels (less vessel details) for high-*venc* and velocity aliasing artifacts (arrows) in the low-*venc* 3D PC-MRA data can clearly be appreciated. Improved depiction of small vessels and successful correction of velocity aliasing apparent for the dual-*venc* 3D PC MRA.

Results and Discussion: Figure 1 illustrates the benefits the dual-*venc* acquisition compared to single high- and low-*venc* at 7T (more detailed depiction of smaller vessels with low flow and the successful elimination of aliasing artefacts).

Conclusion: The findings of this feasibility study show that *k-t* accelerated dual-*venc* 4D flow MRI at 7T can provide improved visualization of venous and arterial hemodynamics across a wide range of the velocity spectrum without velocity aliasing. In the future, optimized dual-*venc* 4D flow MRI can be applied for improved in-vivo measurement of intracranial arterial malformation or aneurysm hemodynamics.

References

1. Markl, M., A. Harloff, T.A. Bley, et al., Time-resolved 3D MR velocity mapping at 3T: improved navigator-gated assessment of vascular anatomy and blood flow. *J Magn Reson Imaging*, 2007. **25**(4): p. 824-31.
2. Meckel, S., A.F. Stalder, F. Santini, et al., In vivo visualization and analysis of 3-D hemodynamics in cerebral aneurysms with flow-sensitized 4-D MR imaging at 3 T. *Neuroradiology*, 2008. **50**(6): p. 473-84.
3. Schnell, S., S.A. Ansari, P. Vakil, et al., Three-dimensional hemodynamics in intracranial aneurysms: influence of size and morphology. *J Magn Reson Imaging*, 2014. **39**(1): p. 120-31.
4. Jung, B., P. Ullmann, M. Honal, et al., Parallel MRI with extended and averaged GRAPPA kernels (PEAK-GRAPPA): optimized spatiotemporal dynamic imaging. *J Magn Reson Imaging*, 2008. **28**(5): p. 1226-32.
5. Schnell, S., J. Garcia, C. Wu, et al. Dual-Velocity Encoding Phase-Contrast MRI: extending the dynamic range and lowering the velocity to noise ratio. in *ISMRM, 23rd Annual Meeting*. 2015. Toronto, Canada.

Comprehensive Cerebrospinal Venous Assessment in Patients and Healthy Controls – Results from CCSVI Study

Eric M. Schrauben[1], Jacob MacDonald[1], Aaron Field[2], Oliver Wieben[1,2]
Depts. of Medical Physics[1] and Radiology[2], University of Wisconsin – Madison, USA

PURPOSE: The chronic cerebrospinal venous insufficiency (CCSVI) hypothesis[1] theorizes venous reflux to the level of the deep cerebral veins as a potential means or exacerbation of multiple sclerosis (MS). Compared to Doppler ultrasound originally used to diagnose CCSVI, cerebrospinal venous flow measures of PC MR has been shown to be consistent[2], less user-dependent, and allows for a truly blinded study design. 4D flow MRI[3] provides volumetric coverage so that a number of venous structures may be interrogated with a single scan. The purpose of this study was to compare flow assessed using 4D flow MRI and contrast-enhanced MR-Venography (CE-MRV). This data was gathered and assessed in a blinded fashion in patients with MS, patients with other neurological disorders (OND) and healthy controls (HC).

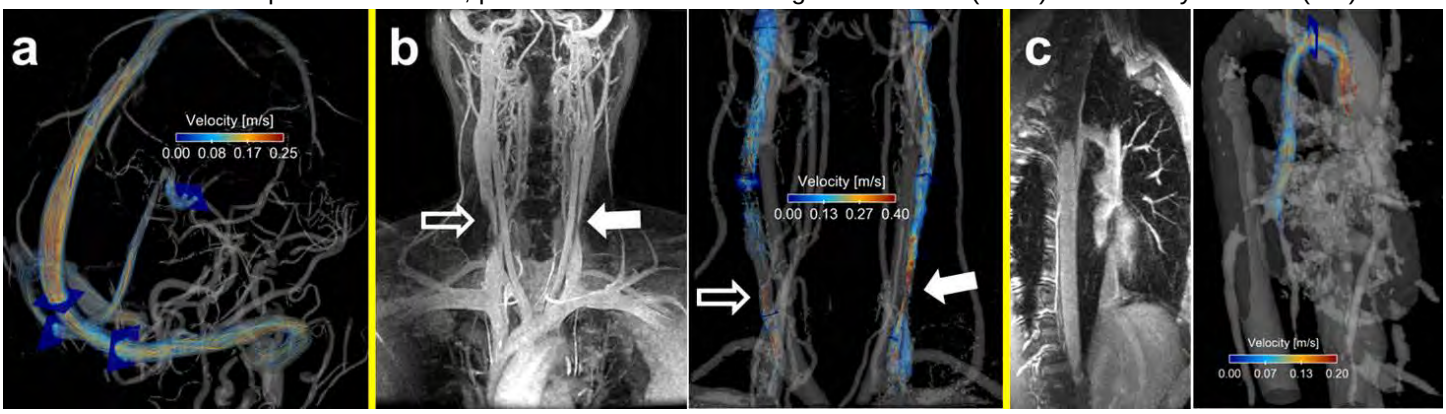

Figure 1. Vessels of interest - flow measurement planes are shown in blue. a: Velocity streamlines in the head from PC-VIPR angiogram. b: Limited MIP of CE-MRV of neck veins (left) and PC-VIPR streamlines (right). Areas of stenosis viewed on the CE-MRV MIP are complemented by PC-VIPR information: slow flow (open arrow) and velocity jet (closed arrow). c: limited MIP (left) and corresponding PC-VIPR data (right) in the azygous vein.

METHODS: *Demographics:* The study population consisted of 76 MS patients (Age: 46.1 ± 11.1 yrs, 27M/49F), 50 HCs (Age: 45.2 ± 10.6 yrs, 20M/30F), and 40 ONDs (Age: 49.4 ± 13.0 yrs, 14M/26F). *MR Acquisition:* A clinical 3T scanner (Discovery MR750, *GE Healthcare*, WI) was used to collect 4D flow MRI at 3 stations using a radially undersampled trajectory (PC-VIPR[4]): **1) Head** (TE/TR/α = 3.5ms/9.0ms/15°, resolution = (0.69 mm)^3 isotropic, Venc = 20 cm/s); **2) Neck** (TE/TR/α = 3.0ms/7.9ms/15°, resolution = (0.86 mm)^3 isotropic, Venc = 40-70 cm/s); **3) Chest** (TE/TR/α = 2.7ms/6.9ms/15°, resolution = (1.25 mm)^3 isotropic, Venc = 40 cm/s). CE-MRV of the neck and chest (same locations as PC-VIPR) was also performed and consisted of a single injection of gadofosveset trisodium (Ablavar, *Lantheus Medical Imaging*, MA) at a dose of 0.03-0.05 mmol/kg. *Processing:* All flow processing was completed by one person uninvolved with image acquisition and fully blinded to group membership. Fig. 1 displays anatomical location of the analysis planes in a single volunteer, as well as corresponding CE-MRV limited MIPs: **1) Head** – superior sagittal sinus, left/right transverse sinus, left/right internal cerebral vein, and left/right basal vein; **2) Neck** – left/right internal jugular vein (IJV) at three stations (Upper, Mid, Lower); and **3) Chest** – azygous vein 2 cm from junction with the superior vena cava. Measured flow parameters were total flow (mL/cycle), peak flow (mL/s), and percent retrograde flow (%). In relation to Zamboni's original criteria for detection of CCSVI using Doppler ultrasound[1], our analysis allows for assessment of directional flow in the cervical and intracranial veins (criteria 1 and 2), anomalies/stenoses of IJVs (criteria 3), and blocked outflow in cervical veins (criteria 4). *Statistics*: Group differences were assessed on a per-vessel/location basis using two-sample unpaired Student's t-tests. False discovery rate control was used to correct for multiple comparisons[5].

RESULTS: Fig. 2 displays group averages of total flow (+ standard deviation) for each measurement location. After correcting for multiple tests, no statistically significant differences between the MS and HC, MS and OND, or HC and OND were observed for any measurement location or any tested parameter. IJV flow has been shown to have high interscan variability in healthy subjects[2], potentially preventing small between-group flow alterations from being detected even with the large sample sizes shown here. However, in the intracranial veins, which are necessarily the conduit by which a venous flow disturbance would be transmitted to the brain, flow is much less variable[2] and still no differences were detected.

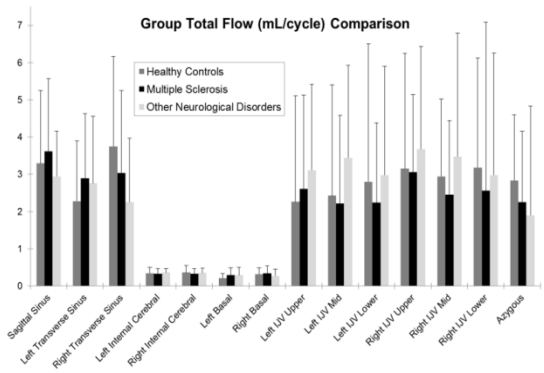

Figure 2. Groupwise comparisons of total flow (mL/cycle) for all measured locations. No statistically significant differences were found at any location

CONCLUSION: These negative results do not support a relationship between altered cerebrospinal venous drainage and MS.

Acknowledgements: We gratefully acknowledge funding from National MS Society grant #RC1003-A-1, NIH grant 2R01HL072260, and GE Healthcare for their support.

References: **1**. Zamboni et al. *Phlebology* 2010. **2.** Schrauben et al. *AJNR* 2014. **3.** Markl et al. *JMRI* 2012. **4.** Johnson et al. *JMRI* 2008 **6.** Glickman et al. *J Clin Epidemiol* 2014.

Evaluation of the renal arterial wall with High Resolution MR imaging after endovascular renal denervation.

SI-MOHAMED Salim, BROS Sébastien, SIGOVAN Monica, BOUSSEL Loic, COURAND Pierre-Yves, LANTELME Pierre, DOUEK Philippe, HARBAOUI Brahim

Purpose:

To prospectively investigate the effect of Endovascular Renal Denervation (ERD) on renal arterial wall with High Resolution MRI (HR-MRI) in patients presenting with a resistant hypertension.

Materials/Methods:

This study was approved by our hospital ethics committee and written informed consent was obtained from all subjects. 29 patients presenting with a resistant hypertension prospectively underwent a 2D ECG-triggered Black Blood T1 weighted Turbo Spin Echo (TSE) HR-MRI before and after gadolinium-based contrast injection of two main renal arteries, before (D0), 2 days (D2) and 6 months (M6) after a bilateral ERD. The following parameters were used: 6 slices perpendicular to the long axis of each renal artery, TR/TE: 1 heart beat/13ms, spatial resolution: 1.3x1.3x5mm. On a qualitative analysis, each slice was deemed as suitable or not for quantitative analysis. On each assessable slice, an internal and an external contour of the artery were manually drawn and the mean signal of the wall was recorded. The mean Signal Ratio of the Wall (mSRW), before and after contrast injection, as well as mean Wall Thickness (mWT) were calculated for each artery at time point D0, D2 and M6.
Kruskal-Wallis test with post-hoc Wilcoxon signed rank tests were used to compare mSRW and mWT at the different time points. Intraclass correlation coefficients were used to compare inter-observers variability.

Results:

Imaging protocol and follow-up were completed in 24 patients (56.5 ± 10.5 years; IQR [52–66.75] years; 16 men [66.6%] ; 8 women [33.3%]; mean 24-hour ambulatory blood pressure 157/87 ± 21/15 with 4.4 ± 1.1 antihypertensive treatments).
mSRW was significantly higher at D2 (93.34% [IQR 49.86%;137.35%]) in comparison with D0 (55.35% (IQR 16.21%;100.92%) p<0.001) and M6 (63.64% [IQR 50.86%;74.88%] p<0.001) with no difference between D0 and M6 (p=0.145) .
Similarly, mWT was significantly higher at D2 (3.13 mm [IQR 2.94; 3.32]) in comparison with D0 (2.70 [IQR 2.46; 3.01], p<0.001) and M6 (2.84 mm [IQR 2.59; 3.15],p=0.002) with no difference between D0 and M6 (p=0.10).
Intraclass correlation coefficients were 0.96 (95% CI=0.95-0.97) and 0.97 (95% CI=0.96-0.98) for inter- observers measurements, respectively for mSRW and mWT.

Conclusion:

After ERD, High Resolution MRI demonstrated a significant increase in gadolinium-based contrast agent uptake by the arterial wall of the renal arteries as well as a thickening of the wall two days after the procedure with a complete recovery at 6 month.

Flow induced artifacts in two-point Dixon fat-water separation: Incidence and potential diagnostic pitfalls.

[1] Schubert T, [1] Bannas P, [2] Sharma S, [1] Kinner S, [2] Korosec FR, [1,2] Reeder SB

Departments of [1]Radiology and [2]Medical Physics, University of Wisconsin – Madison, USA

Purpose:

Two-point "Dixon" fat-water separation methods have gained considerable interest for the use in MR angiography [1]. However, when using bipolar readout gradients, flow induced fat-water misallocation can occur [2]. The purpose of this study was to evaluate the incidence and severity of flow induced artifacts in a clinical setting.

Methods:

Fat suppressed body-MRI-scans using a two-point method (LAVA Flex, GE Healthcare, Waukesha, WI, USA) of 100 consecutive patients were retrospectively evaluated regarding flow-induced artifacts in arteries and veins. Coronal and axial images were available for all patients. Artifacts were graded on a 3-point scale (none, mild, severe).

Results:

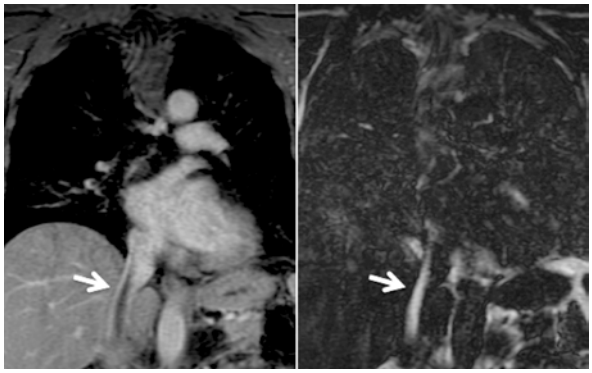

Fig. 1.: Water only (left) and fat only (right) images show flow induced signal misallocation artifact in the inferior vena cava

Figure 1 shows an example of separated water and fat images, demonstrating a typical example of a thrombus-mimicking misallocation of fat signal into the water-only image and vice versa (arrows). Figure 2 shows a similar example in the middle hepatic vein.

Flow-induced artifacts were present in 58 of 100 datasets. The artifact was graded as mild in 29 cases and severe in 29 cases. Artifacts occurred most frequently in the inferior vena cava (IVC) at the level of the diaphragm (n=44) followed by the Aorta (n=10). Misallocation of fat and water was apparent in all datasets with severe artifacts.

Artifact location and appearance are consistent with previous reports [2], however, the incidence of this type of artifact has not yet been addressed. Artifact incidence is of importance as the appearance of the artifact in water only images may be mistaken as thrombus formation, especially if fat images are not readily available.

Conclusion:

Our study shows a surprisingly high incidence of flow-induced, thrombus mimicking artifacts in two-point "Dixon" methods for fat-water separation when using bipolar readout gradients. This finding may be of importance in light of potential misinterpretation of this artifact as intravascular thrombus.

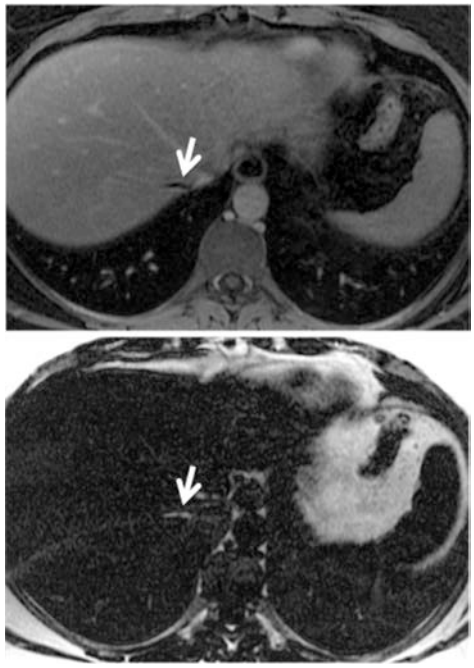

Fig. 2.: Water only (upper) and fat only (lower) image show signal misallocation artifact in the posterior liver vein.

[1] Leiner Eur Radiol. 2013,
[2] Rahimi Magn Reson Med. 2015

Compact 3T Scanner: Initial Experience with 80 mT/m, 700 T/m/s Gradients

Matt A. Bernstein[1], Shengzhen Tao[1], Joshua D. Trzasko[1], Paul T. Weavers[1], Yunhong Shu[1], Erin Gray[1], Seung-Kyun Lee[2], Jean-Baptiste Mathieu[2], Dominic Graziani[2], Christopher J. Hardy[2], John Schenck[2], Ek Tsoon Tan[2], Thomas K.F. Foo[2], and John Huston III[1]

[1]Dept. of Radiology, Mayo Clinic, Rochester, MN, United States
[2]GE Global Research, Niskayuna, NY, United States

Purpose: Under an NIH-funded Bioengineering Partnership, to develop a compact 3T scanner with high-performance gradients capable of scanning heads, extremities, and infants. Because of the smaller gradient dimension (42-cm inner diameter), peripheral nerve stimulation (PNS) is reduced compared to a conventional, whole-body system. The reduced inductance and high efficiency of the compact gradients also enables high gradient performance (slew rate and amplitude) with a standard gradient driver.

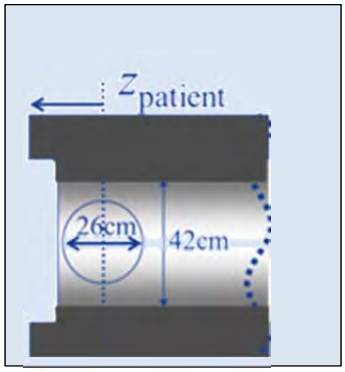

Methods: The HG2 gradient coil [1] with a 26 cm field of view (FoV) and capable of simultaneous 80 mT/m, 700 T/m/s with a conventional 1 MVA gradient driver was placed in a standard 70-cm bore 3T scanner for initial testing. The gradient coil has asymmetric design for the transverse axes, and is symmetric for the z-axis. Phantom tests included the American College of Radiology (ACR) MR battery comprising: low-contrast object detectability, spatial resolution, uniformity, slice location, slice thickness, spatial distortion, and ghosting. Testing was also performed with the ADNI phantom to measure spatial linearity [2]. The additional linear concomitant field terms present with asymmetric gradients [3] were compensated in a phantom test via an exact, closed-form solution and gradient waveform pre-emphasis [4]. Acoustic noise was measured prior to scanning 9 volunteers with a 32-channel brain coil (Nova Medical) under an IRB-approved protocol.

Results: The HG2 gradient coil passed the entire battery of ACR tests [5]. The ADNI phantom tests indicated that after high-order gradient non-linearity correction (up to 10^{th} order with both even- and odd-order terms) the RMSE < 0.4 mm, which is sufficient for serial measurement of brain volume to monitor neurodegenerative diseases. The 26 cm FoV provided whole-head coverage on all subjects, with visualization down to the C4-C5 interspace in one subject. Acoustic noise levels were measured to be under non-significant risk limits for peak unweighted (<140 dB) and A-weighted with hearing protection (<99 dBA), the latter assuming typical NRR = 29 rated earplugs. The volunteer results showed reduced EPI distortion due to shorter echo spacing, which is enabled by the increased gradient performance.

Conclusion:

Simultaneous gradient performance of 80 mT/m amplitude and 700 T/m/s slew rate was demonstrated using only a standard 1 MVA gradient driver. In vivo slew rates a factor of 3.5 higher than those of whole-body gradients produced EPI images with substantial reduction in spatial distortion and gains in SNR with high b-value diffusion. The gradient coil will be integrated with a compact 3T magnet, which is scheduled for evaluation at Mayo Clinic starting mid-2015.

References: 1. Mathieu et al, ISMRM 2015, p1019. 2) Gunter et al, Medical Physics 2009. 3) Meier et al, Magn Reson Med 2008. 4) Tao et al, ISMRM 2015, p 3376. 5) Weavers et al, accepted AAPM 2015, abstract 27111.
This work is is supported by NIH Grant BRP-R01-EB010065.

Contrast-Enhanced Perianal Fistula Imaging with Dixon-Based Fat Suppression

Eric G. Stinson, Joshua D. Trzasko, Eric A. Borisch, Phillip M. Young, Stephen J. Riederer
Mayo Clinic, Rochester, MN, USA

Purpose: A perianal fistula is an abnormal connection between the perineum and the anal canal (1). The current clinical protocol for imaging perianal fistulas at our institution consists of multi-planar T_2-weighted imaging with and without fat saturation, multi-planar T_1-weighted imaging with a gadolinium-based contrast agent with and without fat saturation, and a 3D post-contrast LAVA Flex (2-pt Dixon) sequence. While these techniques have proven satisfactory for identifying tracks not seen surgically, it is also of interest to acquire 3D images with greater spatial resolution for improved treatment of this debilitating disease. Additionally, the administration of gadolinium contrast agent (2) makes these imaging techniques similar to those used in CE-MRA. The purpose of this "works in progress" presentation is to demonstrate how MRA-like techniques can be used in perianal fistula imaging.

Methods: An interleaved multi-TE 3D spoiled gradient echo technique was developed for use in Dixon-type CE-MRA and used to image a suspected perianal fistula with appropriate modifications for pelvic imaging. Due to the nature of this research study, post-contrast imaging was performed after completion of the clinical imaging protocol – about 20 minutes after contrast administration. Imaging parameters are shown in Table 1. This initial study was performed at 1.5T, however, similar studies have been performed at 3.0T with only minor modifications to the pulse sequence and reconstruction to account for the different rate of fat dephasing. The dual-echo acquisition (with corner cutting, but no other undersampling) was Fourier transformed before Dixon-based fat/water separation with a phase constrained signal model (3) and graph-cuts optimization scheme (4).

Table 1: Imaging parameters for interleaved TE perianal fistula imaging.

$TR/TE_1/TE_2$	FA/BW	FOV	Matrix	Resolution
6.5/2.3/4.7ms	15°/±62.5kHz	28×28×15.4cm	224×224×128	1.25×1.25×1.2mm

Results: Figure 1 shows the acquired axial images and sagittal and coronal reformatted images from a perianal fistula exam. The fistula is well depicted in all images (red arrows), despite the delay between contrast injection and imaging. Good fat suppression was achieved with the phase constrained Dixon technique, and the nearly isotropic resolution allows viewing in all three planes.

Compared to our current clinical images (resolution=1.17×1.34×3.4mm), the high spatial resolution images benefit from improved depiction in reformatted planes and provide the opportunity to better model the fistulas in three dimensions. While previous work has performed high spatial resolution perianal fistula imaging with intermittent fat suppression (5) the Dixon technique provides additional SNR improvement due to the averaging effect of using two appropriately timed echoes (6). Future work will aim to further speed up imaging, particularly through the use of time-resolved techniques similar to time-resolved CE-MRA.

Conclusion: Techniques developed for Dixon-based CE-MRA have been successfully used to image perianal fistulas with high spatial resolution, high SNR, and good fat suppression.

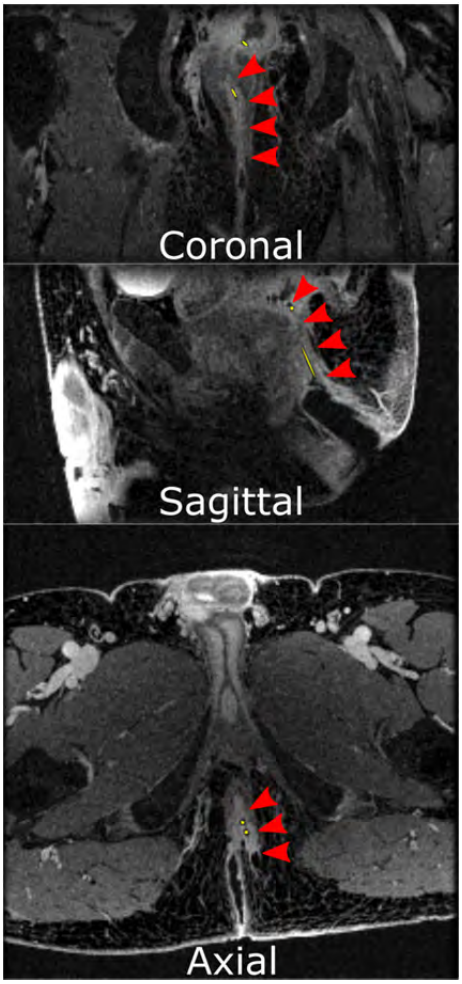

Figure 1: Coronal, sagittal, and axial plane images of a perianal fistula (red arrows) with seton (yellow markings). Water images from a Dixon-type acquisition and reconstruction depict the contrast-enhanced fistula well in all three planes (reformatted from the axial acquisition).

References:

1. De Miguel Criado J et al. RadioGraphics 2012;32:175–194.
2. Spencer JA et al. Am. J. Roentgenol. 1996;167:735–741.
3. Bydder M et al. Magn. Reson. Imaging 2011;29:216–221.
4. Hernando D et al. Magn. Reson. Med. 2010;63:79–90.
5. Loening AM et al. ISMRM. Milan, Italy; 2014. p. 2126.
6. Stinson EG et al. Magn. Reson. Med. 2015;74:81–92.

Revisit of Non-Contrast Aortic Arch FBI at 3T

Mitsue Miyazaki and Xiangzhi Zhou
Toshiba Medical Research Institute, Vernon Hills, USA

Purpose: Non-contrast aortic arch imaging at 3T using bSSFP is challenging due to strong air to tissue susceptibility causing banding artifacts. A non-contrast fresh blood imaging (FBI) technique using ECG-gated half-Fourier FSE, has been established for aortic arch imaging at 1.5T[1,2]. The aim of this study is to revisit aortic arch imaging at 3T using the FBI technique, to identify issues at 3T, and to improve the FBI image quality.

Materials and Methods: The study was approved by our institutional review board and informed consent was obtained. All volunteer studies were performed on a 3T scanner (Toshiba Medical Systems Corporation, Japan) equipped with Atlas SPEEDER spine coil and Atlas SPEEDER body coil. Followed by the localizer imaging, the aortic arch plane was carefully selected to cover the ascending and descending aorta in oblique using ECG-gated FBI with the following parameters: TR=3RR intervals, TE=60 ms with echo spacing of 5 ms, 40 slices, slice thickness=3 mm, matrix 256X256; FOV 40cmX40cm, parallel imaging factor = 2, flip angle/refocusing flip angle=90°/150°, TI=150 ms for fat suppression, in-plane resolution 1.56 mmx1.56 mm and the scan time of about 2 min. The PE direction was set to right and left and the image was acquired at diastolic phase. The FBI scan was performed with and without the partial RO flow compensation[3].

Results: FBI image acquired without partial RO flow compensation (RO=0) had flow void at the descending aorta; whereas, FBI image with RO=-10% (partial flow compensation as 100% in RO gradient to the center of echo) showed bright ascending to descending aorta without flow void artifacts in all healthy volunteers.

Discussion: Unlike bSSFP, the FBI techniqe, using a spin-echo type sequence, provides no banding artifacts. Applying a small partial RO flow compensation like RO=-10% allows less flow void at the descending aorta that is parallel to the RO direction.

Conclusion: At 3T, non-contrast FBI with partial RO flow compensation permits depicting aortic arch without flow void artifacts.

References: 1) Miyazaki M, Sugiura S, Tateish F, et al., JMRI 12:776-783, 2000. 2) Urata J, Miyazaki M, Wada, H, et al., JMRI 14:113-120, 2001. 3) Miyazaki M, Takai H, Sugiura S,et al., Radiology 227:890-896, 2003.

7-Minutes Fresh Blood Imaging using Variable TR and Variable Refocusing Flip Angle for Non-Contrast Peripheral MR Angiography at 3T

Xiangzhi Zhou[1], Mitsue Miyazaki[1]
[1]Toshiba Medical Research Institute, Vernon Hills, USA

Purpose: Fresh Blood Imaging (FBI) [1-2] scan time can be greatly reduced using variable TR technique for imaging the peripheral artery without contrast infusion [3], in which each slice encoding (SE) and the followed echo train are played in a variable TR (vTR) (TR=n*RR) pattern. In vTR FBI, the lower limit of TR depends on the length and timing of data acquisition, and it is also limited by SAR, which is mostly affected by refocusing flip angle, echo train length, and echo spacing. Often in the case of short TR FSE acquisition, SAR can be an issue for the patient with fast heart rate. To reduce the SAR so that the shortest TR can be enabled for the slice encodings at the kz edge, variable refocusing flip angle (vFA) is proposed in this work. The optimized vTR FBI sequence with vFA was applied on volunteer to achieve a 7-minutes 3 station run-off scan to cover from iliac to calf stations.

Methods: The study was approved by our institutional review board and informed consent was obtained. Four volunteers were enrolled and scanned by a Vantage Titan 3T scanner (Toshiba Medical Systems Corporation, Otawara, Japan) equipped with Atlas SPEEDER Spine coil and Atlas SPEEDER Body coil. Followed by the localizer, pelvic, thigh and calf stations were imaged using the proposed FBI sequence with ECG gating. The FBI sequence is modified to incorporate the vTR and vFA functions, i.e., the slice encoding steps at the k-space center have longer TR (increased number of RR intervals) and higher refocusing flip angle and the number of the slice encoding steps with longer TR and/or higher refocusing flip angle can be adjusted. FBI parameters: 3D coronal single shot fast spin echo (SSFSE) with half Fourier in PE direction, TR=2RR with vTR and vFA (1 extra RRs for the middle 20% SE steps), TE=60ms, 60-80 slices for each station, slice thickness=3mm, matrix 256X256; FOV 37cmX37cm, parallel imaging factor = 2, refocusing flip angle=160°/140°, the acquisition delay times (TD_{sys} and TD_{dias}) were determined by DelayTracker, which is a build-in tool with GUI to automatically calculate systolic and diastolic delay times from the heart rate; and resolution 1.4mmx1.4mm, refined in the RO, PE and SE directions.

Results: Fixed TR (TR=3RR) FBI and vTR (TR=2RR+20%3RR) FBI with vFA coronal MIP images at the 3 stations showed comparable arterial image quality across all volunteers and the scored MIP image quality has no significant difference. In terms of arterial signal intensity, the mixture feature of short and long TRs in vTR function offers a signal level between fixed long TR and short TR images, as expected. In the volunteer with narrower lumen on iliac arteries, FBI MIP images with and without vTR function can both clearly delineate the narrower lumen at different sites (Figure 1). The 3 station run-off scan for each volunteers using vTR FBI plus vFA can be performed approximately within 7 mins.

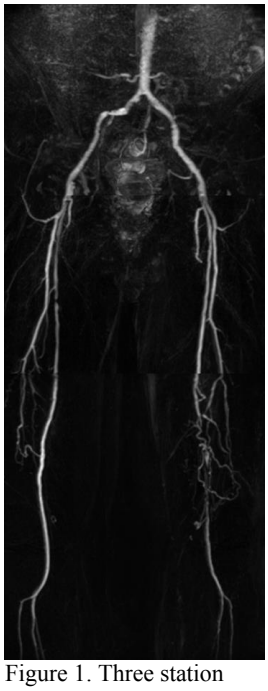

Figure 1. Three station MIP image of a volunteer using FBI with vTR and kFA functions. The total scan time is 7 mins.

Conclusion: The proposed vTR method with vFA offers significantly reduced scan time and SAR reduction for the FBI scan since the TRs for the slice encoding away from the k-space center are shortened compare to fixed long TR scan, and the refocusing flip angles for the slice encoding away from the k-space center are reduced. Compared to fixed TR FBI, the vTR FBI can shorten the total scan time by 20-40%, and vFA can reduce the SAR for the echo train inside the short TR. More advanced vTR and VFA patterns can be added to FBI with the purpose of reducing scan time and SAR while maintaining the arterial blood signal. One need to note that systolic and diastolic acquisition of FBI should have the same vTR and vFA setting to minimize the background tissue difference, which is critical to minimize background tissue signal after subtraction. Furthermore, this study demonstrated that 7-mins 3 station peripheral non-contrast MRA is feasible using the improved FBI technique. More volunteer and patient data will be collected to further evaluate the performance of vTR FBI with vFA at 3T.

References:

1. Miyazaki M. et.al, JMRI 12(5):776-783, 2000
2. Miyazaki M. et.al, Radiology 227:890-896, 2003
3. Zhou X. et.al, ISMRM #4507, 2015

Breath-hold Inner-Volume Radial Quiescent-Interval Slice-Selective (QISS) of the Heart, Aorta and Renal Arteries

Robert R. Edelman[1,2], Amit Pursnani[3], Shivraman Giri[4], Li W[1,5], O'Brien K[6], Ioannis Koktzoglou[1,5]

[1]Radiology, NorthShore University HealthSystem, Evanston, IL, [2]Radiology, Northwestern University, Chicago, IL, [3]Medicine, NorthShore University HealthSystem, Evanston, IL, [4]Siemens Healthcare, Chicago, IL, [5]Radiology, University of Chicago, Chicago, IL, [6]Siemens Healthcare, Brisbane, Australia

Introduction: Quiescent-interval slice-selective (QISS) MRA has proven to be a robust solution for the non-contrast evaluation of peripheral arterial disease and has also shown promise as an alternative to time-of-flight MRA for evaluating the extracranial carotid arteries (1,2). Current implementations of QISS MRA use a Cartesian k-space trajectory. In this pilot study, we explored the potential benefits of a non-Cartesian variant, "inner-volume QISS" which uses a highly undersampled radial k-space trajectory for breath-hold imaging. The technique was applied to imaging of the heart, aorta, and renal arteries.

Methods: Healthy subjects were scanned on a MAGNETOM Avanto 1.5 Tesla or Verio 3 Tesla MRI system (Siemens Healthcare, Erlangen, Germany) with IRB approval. The prototype inner-volume radial QISS sequence applies a slice-selective FOCI pulse followed by a user-defined quiescent interval, fat saturation, alpha/2 catalyzation, and balanced steady-state free precession (bSSFP) diastolic readout with equidistant azimuthal radial view angle increments (3). Other scan parameters include a 144 or 160 acquisition matrix, ~200-mm FOV, 48 to 96 views, 1 to 3 shots, slice thickness of ~2-mm and in-plane resolution of 0.5-mm to 0.7-mm after interpolation. For a 2-shot acquisition ~10 slices are acquired in each breath-hold (~20 sec for an RR interval of 1 sec) compared with ~20 slices using a single shot.

Results: Undersampling-related radial streak artifacts were minimal. Radial QISS images showed uniform fat and background tissue suppression at both 1.5 Tesla and 3 Tesla, without striping artifacts from off-resonance effects. Despite the use of a bSSFP readout, there was no need for a frequency scout at 3 Tesla. In the heart, radial QISS provided clear depiction of the ascending aorta and arch, proximal coronary arteries, and ventricular myocardium; in the renal vessels, radial QISS encompassed the entire length of each artery in a single breath-hold **(Figure)**. The short scan time and narrow temporal window (~100 to 150 ms, depending on the number of radial views and shots) facilitated efficient imaging without motion artifacts along both the long and short axes of each vessel.

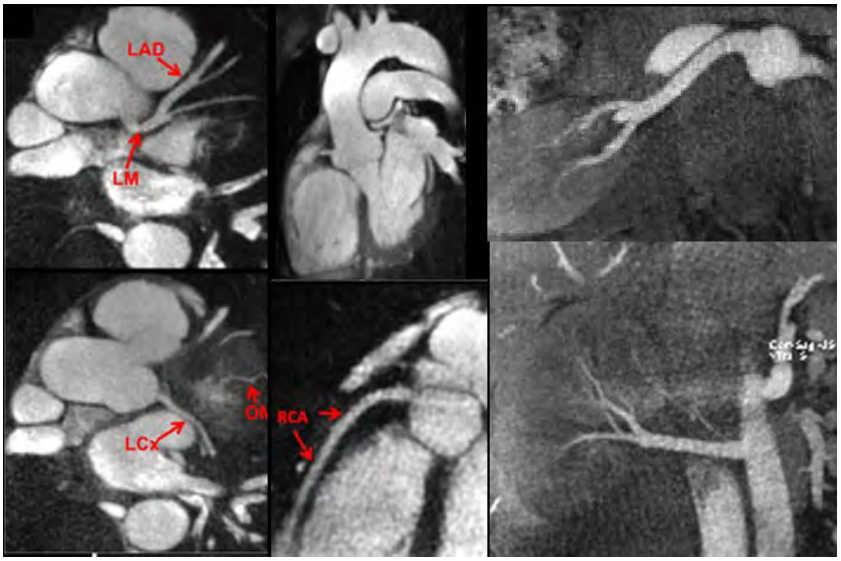

Discussion: Inner-volume radial QISS provides detailed images of the heart, aorta or renal arteries in a single breath-hold. Compared with Cartesian QISS, radial QISS facilitates more flexible selection of temporal and spatial resolution, while the smaller FOV ensures optimal shimming and avoids off-resonance artifacts even at 3 Tesla. Temporal and spatial resolutions are sufficient to depict the proximal coronary arteries and aortic root without degradation by motion artifacts. The robust multi-slice capability ensures coverage of the entire length of each renal artery in a single breath-hold. Further image quality improvements can be expected with the use of compressed sensing, while at least a two-fold improvement in multi-slice capability should be achievable using a multi-band excitation. In conclusion, inner-volume radial QISS is a promising non-contrast technique with diverse potential imaging applications, including the heart, aorta, and renal arteries.

References: 1. Edelman RR et al. MRM 2010;63:951-958. 2. Koktzoglou I et al. MRM 2015 Jun 15. doi: 10.1002/mrm.25791. [Epub ahead of print]. 3. Edelman et al. MRM. 2014;72:1522-1529.

Quiescent-Interval Slice-Selective Fast Low-Angle Shot Magnetic Resonance Angiography of the Extracranial Carotid Arteries

Ioannis Koktzoglou[1,2], Ian G. Murphy[1,3], Shivraman Giri[4], Robert R. Edelman[1,3]

[1]Radiology, NorthShore University HealthSystem, Evanston, IL, [2]Radiology, University of Chicago, Chicago, IL, [3]Radiology, Northwestern University, Chicago, IL, [4]Siemens Healthcare, Chicago, IL

Introduction: Quiescent-interval slice-selective (QISS) MRA is an accurate test for the non-contrast evaluation of peripheral arterial disease [1]. In this pilot study, we tested whether a variant of QISS using a fast low-angle shot (FLASH) readout could be used to evaluate the extracranial carotid arteries.

Methods: This study was approved by our institutional review board. Five healthy subjects and five patients with carotid atherosclerotic disease were imaged using a MAGNETOM Verio 3 Tesla MRI system (Siemens Healthcare, Erlangen, Germany). The prototype QISS sequence applied in-plane and superior-tracking frequency-offset corrected inversion (FOCI) radiofrequency pulses followed by a quiescent interval and a Cartesian FLASH readout. Other scan parameters included a TR/TE/flip of 8.9ms/5.5ms/20°, 2-shot readout, 230x460mm field-of-view, 1.15mm spatial resolution (before interpolation), 160-180 tilted 1.5mm-thick slices (tilted 45° from the axial plane) with 0.3mm overlap, 400ms inflow time from the in-plane FOCI pulse to the acquisition of central k-space, 6/8th phase partial Fourier, parallel imaging factor of 2, 500Hz/pixel receiver bandwidth, tracking venous saturation thickness/gap of 10cm/1cm. QISS imaging was performed with ECG gating, peripheral gating (scan times of 2RR/slice), and without gating (1.32s/slice). Image quality was scored by a radiologist on a segmental basis (10 segments/subject) using a 4-point scale. In patients, the severity of carotid stenosis was graded. Preliminary comparisons were made with 2D time-of-flight (TOF) MRA (all subjects) and with contrast-enhanced MRA (patients only).

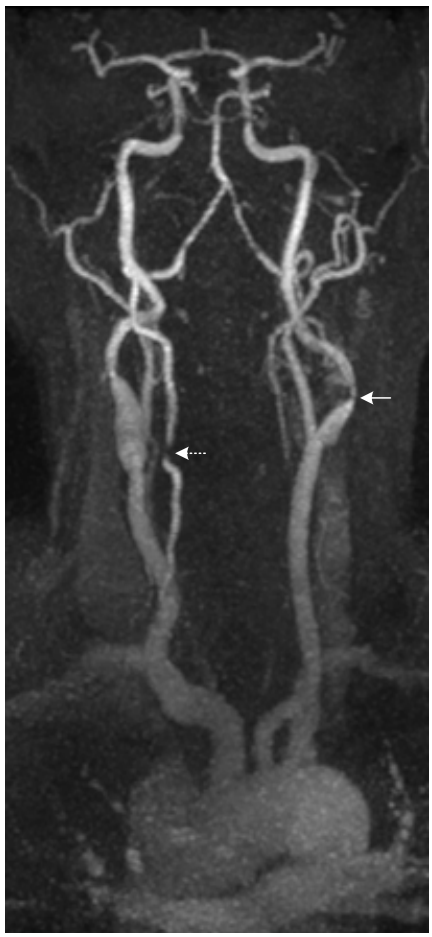

ECG-gated QISS FLASH MRA in a patient with stenoses of the left carotid (solid arrow) and right vertebral (dashed arrow) arteries, and a left vertebral artery occlusion.

Results: QISS FLASH MRA provided display of the extracranial carotid arteries from their origins through to the skull base and proximal intracranial arteries **(Figure)**. The percentage of arterial segments rated as diagnostic was 91.9% for ECG-gated QISS (mean scan time (TA) = 5.7min), 86.9% for ungated QISS (TA = 3.8min), 84.8% for pulse-gated QISS (TA = 3.8min), and 75.8% for 2D TOF (TA = 7.9min) (P = 0.015 between methods). Aggregated across the 10 arterial segments scored, the image quality of ECG-gated QISS was superior to the remaining non-contrast alternatives (P<0.05). Cohen's kappa between ECG-gated QISS and contrast-enhanced MRA for grading of disease was 0.86 (P<0.001), which indicated almost perfect agreement.

Discussion: Our study suggests that QISS MRA using a FLASH readout can display long lengths of the extracranial carotid arteries without the use of contrast material. Image quality was improved with respect to 2D TOF MRA, and there was almost perfect agreement with contrast-enhanced MRA in the grading of carotid stenoses. Further improvements in robustness and imaging speed may be anticipated with the use of non-Cartesian k-space sampling and multi-band radiofrequency excitation. In conclusion, QISS FLASH MRA is a promising non-contrast technique for the evaluation of the extracranial carotid arteries.

References: 1. Edelman RR et al. MRM 2010;63:951-958.

Non-Contrast Myocardium Perfusion: Technical Differences between 4D Time-SLIP with Tagging Aortic Root and FAIR

Mitsue Miyazaki[1], Xiangzhi Zhou[1], Tsutomu Hoshino[1], Kenichi Yokoyama[2], Rieko Ishimura[2], Toshiaki Nitatori[2]
[1]Toshiba Medical Research Institute, Vernon Hills, USA, [2]Department of Radiology, Kyorin University School of Medicine, Tokyo, Japan

Purpose: A novel non-contrast 4D Time-Spatial Labeling Inversion Pulse (Time-SLIP) technique[1, 2] (3D acquisition and time) has been developed to investigate myocardial perfusion on healthy volunteers without administration of contrast materials. We discussed the technical differences between our 4D Time-SLIP and Flow-sentitive Alternating inversion recovery (FAIR)[3, 4].

Materials and Methods: The non-contrast 4D Time-SLIP technique was applied on eight healthy volunteers to image myocardium blood flow at 1.5T. The Time-SLIP sequence has a tagging block with a non-selective inversion recovery (non-sel-IR) pulse and a spatially selective inversion recovery (sel-IR) and a control block with only the non-sel-IR pulse. Both tagging and control were followed by a 3D bSSFP readout. The tagging plane was placed at the proximal ascending aorta and imaging slab was at mid-ventricle. In the tag acquisition, the non-sel-IR pulse inverts the magnetization (-Mz), and the spatially sel-IR pulse immediately inverts back the blood magnetization at the proximal ascending aorta (+Mz). In contrast, the control acquisition applies only the non-sel-IR pulse, which inverts the longitudinal magnetization to negative magnetization (-Mz) and experiences exponential T1 relaxation. The complex subtraction between tag and control depicts only the tagged blood flowing into the myocardium and the background signal was canceled out. To reduce motion artifacts between tag and control images, each tag and control acquisition was performed alternatively within a breath hold. To achieve reasonable inversion time (TI), the readout was placed at a fixed diastolic phase in the second RR interval, this allows adjustment of TI time (100 ms to 1600 ms, depending on heart rate). As a result, each 3D tag and control acquisition can be performed within 2 RR intervals and the acquisition can be repeated with multiple TIs. To visualize the blood flow, the time resolved 3D short axis myocardial images were registered and the myocardium was segmented for the visualization of myocardial signal changes caused by the tagged blood along the TI. The non-contrast perfusion curves were also generated to identify the perfusion peaks.

Results: Our results showed that basal to apical blood flow can be observed in all volunteers using the 4D Time-SLIP technique. At the mid-ventricle, the blood flow reaches peak about 200-400 ms after tagging the aortic root blood, and then returned to baseline. This was observed across all volunteers.

Discussion: In comparison, 4D Time-SLIP is a 3D acquisition technique with time, which tags the blood at aortic root; whereas FAIR is a 2D single slice technique with the blood tagged in a global scale. Furthermore, the myocardial perfusion using FAIR was reported to have a long signla tailing effect after the peak flow[4]. Our Time-SLIP method showed no tailing signal after the peak flow, which may provide useful information for various myocardial perfusion/flow defects.

Conclusion: Our preliminary results indicate that the 4D Time-SLIP technique may permit acquiring non-contrast perfusion images with high temporal resolution, and may potentially differentiate diseased myocardium from the normal one.

References: 1) Kanazawa H and Miyazaki M, ISMRM 2002. 2) Miyazaki M, Zhou X, Hoshino T, et al., Microvasc. Res. 2015. 3) Zun Z, Wong E, Nayak, K MRM 2009. 4) Danny J. J. Wang, et al. MRM 2010.

Characteristic Streak Frequency Filtering with Modulo-Prime Spokes (MoPS) Cine-CMR

Keigo Kawaji Ph.D.[1], Hui Wang Ph.D.[2], and Amit R. Patel MD[1]

1 – Department of Medicine - Section of Cardiology, The University of Chicago. 2 - Philips Healthcare, Cleveland OH.

Introduction: Non-Cartesian sampling is used to improve the temporal resolution in cine-CMR[1-8]. Of note, a novel interleaving called Modulo-Prime Spokes (MoPS)[7] was shown to achieve true 15ms cine resolution without view sharing, a per-TR (~2 ms) sliding window from 20% undersampled radial data, and only requires a single filtering step to remove radial streaks in the temporal frequency (x-f) domain[2,3,7]. In this study, we formulate mathematical conditions that ensure such streaking to maintain specific characteristic frequencies above physiologic motion frequency range (~15Hz). We derive two major characteristic frequencies from the MoPS-undersampled streaking, and further optimize these for an effective acquisition/reconstruction. We propose a fast 6HB/slice acquisition with accelerated GPU recon for a ~80 cardiac phase recon within <10sec, or a full LV cine recon (15 x 80 = 1200 images) in less than three minutes.

Theory: MoPS interleaved cine-CMR has four parameters that dictate its interleaved acquisition. These are: 1) m (# of uniformly distributed radial spokes set to a prime ***p*** or ***p±1***), 2) nTFE (# of turbo field echoes), 3) nHB (# of heart beats per slice), and 4) nRCW (the temporal window size). For MoPS-cine, this interleaving is repeated cyclically to cover the entire cardiac cycle. Two resultant frequencies from the k-space undersampled radial streaking can be characterized as follows:

1. nTFE-periodic streaks that complete a single 360 degree rotation over nTFE consecutive sliding window frames, which contributes to a characteristic minimum frequency of f_{nTFE} = 1 /(nTFE · TR) Hz when sufficiently sampled.
2. Specific streaking artifacts remain over nRCW consecutive per-TR sliding windows. Such nRCW step size in a per-TR reconstruction therefore contributes to a characteristic frequency of f_θ = 1 / (nRCW · TR) Hz. We note here $f_\theta > f_{nTFE}$.

Considering the Nyquist criterion in the temporal frequency domain of the per-TR sliding window, we can reconstruct only one out of every R sliding windows without introducing additional aliasing in the x-f domain. Intuitively, when R is a proper divisor of nTFE, streaks remain their periodicity in the image domain. When R < nRCW, f_θ is pushed to a higher frequency.

Methods: All candidate MoPS parameters that met both prime interleaving[5] and the above characteristic frequency criterions were first derived using a numerical simulation. This exhaustive search was constrained to m ≥ 100, while achieving nTFE ≤ ~30 for f_{nTFE} ≥ ~15 Hz, ie. peak physiologic frequency captured with typical cine-CMR. We also consider TR=~2 ms, with nHB≤7 breath-hold per 2D slice. Data was collected on 4 subjects on 1.5T Philips MRI. Computation times were measured on Intel Xeon 2.4GHz Dual-CPU (12 total cores) system w. 80GB RAM and a Tesla K40 GPU (Nvidia, Santa Clara, CA). An optimized PTX-CUDA GPU implementation and standard CPU-based NUFFT were compared using MATLAB (The Mathworks, Natick MA). θ=GA/7 was also examined to analyze irrational rotation angles[6].

Results: 31 valid MoPS-parameter sets were found (m ≥ 100). Only 9 of these sets were exploitable for R-fold acceleration from additional divisibility condition: ie. R divides into nTFE (R | nTFE). Computation was performed using MoPS data sets acquired using (m, nTFE, nHB) = (180,30,6) for p=181, θ=22°, and 36 spokes/15ms window (20% density). All scans were acquired and reconstructed successfully using short-axis, 2, and 4ch views. Table 1 shows computation performance results. PTX-CUDA yielded ~0.11 sec/image at both native and interpolated resolutions on all cases, while NUFFT required 1.4 and 2.6 secs/image, respectively. MoPS-derived recon yielded additional computation benefit for dedicated NUFFT prep step by exploiting nTFE-periodicity for the look-up table generation, which must be done every time for any irrational θ. The number of such prep step equaled nTFE when R=1, or when R | nTFE. Only nTFE/R tables are required when R | nTFE, but this prep was not required for GPU recon. x-f filtering did not yield aliasing for R that satisfied both R | nTFE and R≤nRCW (Fig 1). For nTFE=30, aliasing was seen for R=4.

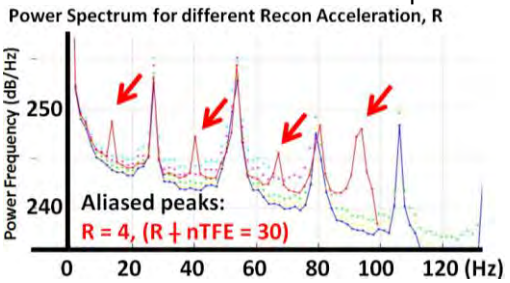

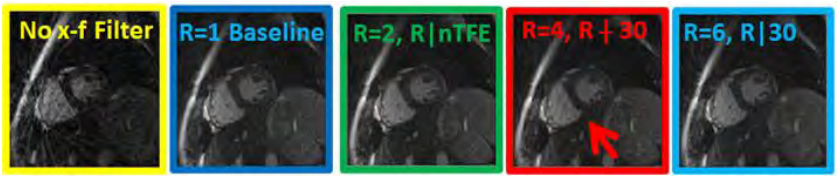

Fig 1. Power Spectrum of R-accelerated MoPS Recon. R=4 led to new alias peaks, while R | nTFE (R=2,3,5,6) preserved characteristic streak frequencies.

Discussion: An R-fold recon time reduction is feasible using a fewer number of per-TR sliding windows without introducing additional aliasing artifacts through x-f undersampling. This condition holds when R | nTFE and R ≤ nRCW, and preserves the streaking characteristic frequencies in the x-f domain as in the case of R=1. We achieved full LV volume (15 slices) MoPS-cine recon with true 15ms temporal resolution within 3 minutes without parallel imaging or iterative methods.

References: 1. Liao et al. MRM 1997. 2. Larson et al. MRM 2001. 3. Peters et al. JMRI 2004. 4. Kressler et al. MRM 2007. 5. Liu et al. MRM 2010. 6. Kawaji et al. PLoS One 2015. 7. Kawaji et al. Proc. ISMRM 2015. 8. Han et al. SCMR 2015.

Table 1: Reconstruction Computation Time Results

Acquired Data – (Recon Resolution)	Computation Times (sec)			Tot. Rec. Time (15 slices, 79 Card Phases)	
	GPU-Grid	CPU-Prep	CPU-Grid	GPU-Tot LV Vol	CPU-Tot LV Vol
MoPS – 1.5 mm (392 nFE x 36 spokes x 5 ch)	0.11 ± 0.01	4.5 (30x)	1.41 ± 0.03	~140 sec	~1600 sec
MoPS – 0.85 mm (same input; need higher res output)	0.13 ± 0.01	7.8 (30x)	2.62 ± 0.03	~150 sec	~2700 sec
GA/7 – 1.5 mm (matched input dims, 79 phases output)	0.11 ± 0.01	20.5 (79x)	1.41 ± 0.03	~140 sec	~1600 sec

Acknowlegement: This project was funded by our CTSA ITM Pilot Award - CTSA UL1 TR000430.

A qualitative assessment of first-pass perfusion bolus timings in the assessment of myocardial ischemia: A magnetic resonance study.

Matthew S[1], Weir-McCall J[1,2], Gandy SJ[3], Milne WG[3] Houston JG[1,2].

1. CVDM, Mailbox 1, University of Dundee, Ninewells Hospital, Dundee, UK, DD1 9SY.
2. Clinical Radiology, NHS Tayside, Ninewells Hospital & Medical School, Dundee, UK, DD1 9SY.
3. Medical Physics, NHS Tayside, Ninewells Hospital & Medical School, Dundee, UK, DD1 9SY.

Purpose: This study aimed to determine if a qualitative visual assessment of CMRI first pass perfusion (FPP) bolus arrival and transit times identified FPP differences between normal cardiac function and impaired function in patients with ischemic heart disease. Further, the aim was to determine if this technique is consistent with that of more time consuming ROI-based assessments.

Methods: Twenty six patient volunteers (referred for CMR FPP imaging on the basis of a suspected cardiac abnormality) were retrospectively included in this study. Approval for this study was obtained from the local ethics committee and all volunteers provided written informed consent. Each participant was assigned into one of two groups – Normal Viability Report (NVR) or Ischemic Heart Disease (IHD). In the NVR group there were 11 patients (5 male: 6 female; mean age 40 (range 17- 63) years), and in the IHD group there were 15 patients (13 male: 2 female; mean age 71 (range 56-89) years). IHD was defined as LGE in one or more of the mid-ventricular, short-axis coronary territories (American Heart Association - AHA model), consistent with ischemic aetiology. The exclusion criteria for both groups included claustrophobia and/or any other known contraindications to MRI. Volunteers were imaged on a 1.5T MRI Scanner (Aera, Siemens Medical Solutions, Erlangen, Germany). Immediately prior to imaging, an intravenous catheter was inserted into the antecubital vein of each patient and connected to a power injector (Spectris Solaris EP, MedRad Inc., Warrendale, PA). All images were acquired at end expiration breath-hold using an optimised CMR protocol and spine matrix and six-element body-array matrix radio frequency coils. Patients were injected with a standard 20ml (0.5mmol/ml) bolus of Gadoteric Acid (Guerbet, Villepinte, France). This was administered at a consistent rate of 4.0ml/s for all patients, and followed by a saline flush of 20ml. Simultaneously, single slice diastolic phase (10mm) FPP images were acquired in the short-axis, 2CH and 4CH orientations using a three-plane electrocardiographically (ECG) gated, Turbo Fast Low Angle Shot (TurboFLASH), multi-phase pulse sequence. Imaging parameters were TR = 2.3ms, TE = 1.1ms, inversion time (TI) = 100ms, FA = 12°, and an average field of view (FOV) of (360*480) mm (depending on patient size). Imaging was performed over 40 heartbeats, providing a cine series of 40 – 50 images per patient. At an average of 12.5 minutes (range 11–15 minutes) after the administration of contrast agent, multi-plane LGE images were acquired that included a short-axis stack (8mm slice thickness, 1.6mm inter-slice gap) from the base to the apex of the ventricles of each patient. A 2D phase-sensitive inversion recovery (PSIR) pulse sequence was used with the following imaging parameters; TR = 700ms, TE = 1.25ms, FA = 45° and a matrix of 192*256. The optimal myocardial null point (TI) was determined for each patient immediately prior to the acquisition of the images using a 2D cine turbo inversion recovery sequence.

Results: Bolus arrival and transit times, into and through the cardiac chambers, were visually and semi-quantitatively assessed and compared. The qualitative and semi-quantitative assessments resulted in almost identical timing values for both patient cohorts. However, the mean FPP bolus arrival time was slower for the IHD cohort relative to the NVR cohort, regardless of the analysis technique ($p<0.01$ for RA arrival, and $p<0.005$ for LV arrival). Similarly the mean FPP bolus transit time was slower for the IHD cohort relative to the NVR cohort, regardless of the analysis technique ($p<0.05$). In this study, the qualitative CMR first-pass perfusion technique was able to provide an equivalent measure of FPP bolus arrival and transit times in the cardiac chambers relative to the more time consuming semi-quantitative technique. A clear difference was also noted for mean FPP bolus arrival and transit times between the NVR and IHD cohorts. Additionally, there were marked differences in LV structure and function between the two cohorts, providing supportive evidence that qualitative delayed FPP bolus time measurements may be a useful predictor of LV dysfunction.

Conclusion: A qualitative visual assessment of bolus arrival and transit times can identify FPP differences between normal cardiac function and impaired function in patient volunteers and this technique is consistent with that of ROI-based assessments.

Title: Longitudinal assessment of renal perfusion and oxygenation in transplant donor-recipient pairs using ASL and BOLD MRI

Abstract: Arterial spin labeling (ASL) and blood oxygen level-dependent (BOLD) MRI studies were performed to measure renal perfusion (Figure 1) and R_2* in 15 renal transplant donor-recipient pairs prior to (baseline) and over 2 years following transplantation surgery. Transplant recipients were further randomized to losartan to prospectively investigate the influence of angiotensin receptor blockade on measures of kidney function. In donors, cortical perfusion in the remaining kidney decreased from 422 ± 17 ml/min/100g at baseline to 372 ± 19 ml/min/100g at 2 years ($P < 0.05$), while cortical R_2* declined modestly from 12.4 ± 0.3 s^{-1} to 11.7 ± 0.3 s^{-1} ($P < 0.05$). In transplanted kidneys, cortical perfusion decreased markedly from 412 ± 19 ml/min/100g at baseline to 271 ± 21 ml/min/100g at 2 years ($P < 0.001$), while medullary R_2* declined from 18.1 ± 0.6 s^{-1} at baseline to 16.6 ± 0.8 s^{-1} at 2 years (p = 0.06). Single-kidney eGFR increased from 43.9 ± 2.1 ml/min/1.73m^2 at baseline to 61.6 ± 2.7 ml/min/1.73m^2 ($P < 0.0001$) in donors and to 58.5 ± 4.3 ml/min/1.73m^2 ($P < 0.01$) in recipients. Cortical perfusion at 1 and 2 years in recipients receiving 25-50 mg/day losartan was 62 ± 24 ml/min/100g higher than recipients not receiving the drug ($P < 0.05$). No significant effects of losartan were observed for any other markers of renal function. These results suggest an important role for non-invasive functional monitoring with ASL and BOLD MRI in kidney transplant recipients and donors.

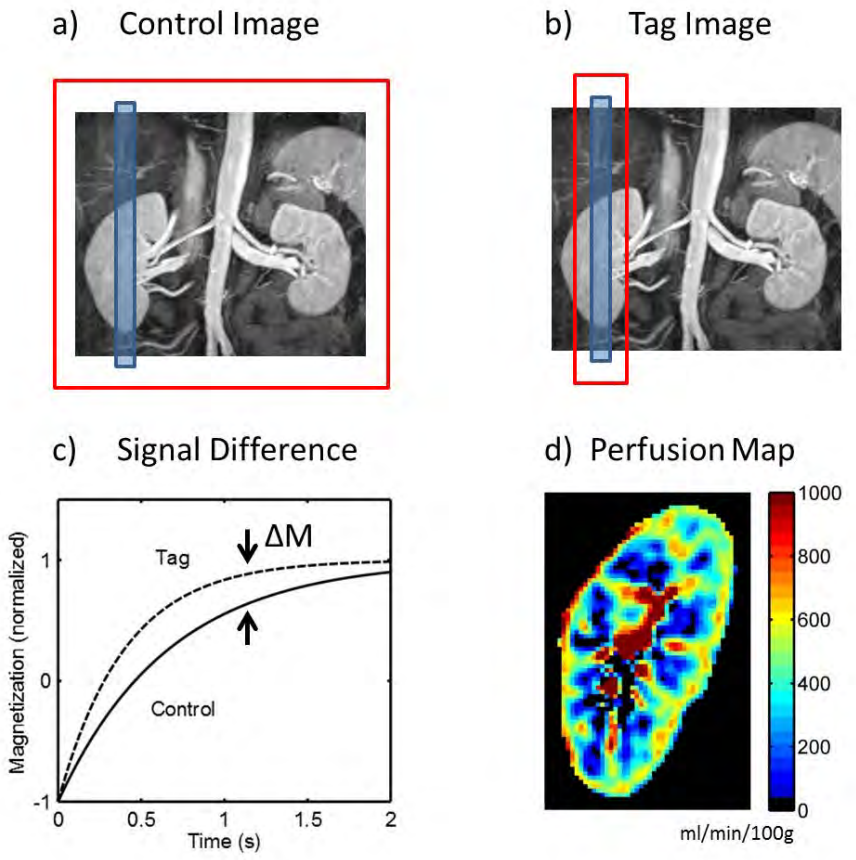

Figure 1: FAIR ASL method used to image native and transplant kidneys in the sagittal plane.

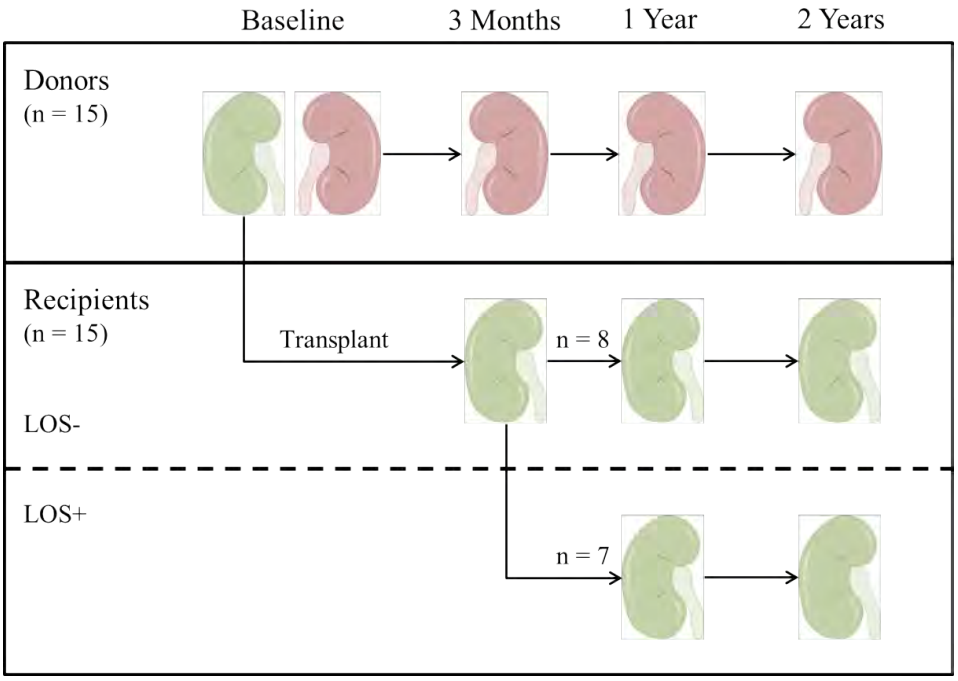

Figure 2: Imaging schedule for donors and recipients. The baseline scan was performed in donors prior to transplant surgery. For the first 3 months no recipients received losartan (LOS-), and after this time point a subset were given the drug for the remainder of the study (LOS+). The left kidney was transplanted in 14 of the 15 pairs.

Categories: Perfusion, renal, functional body MRI

High resolution MRI for characterization of inflammation within abdominal aortic aneurysm

Chengcheng Zhu, Thomas A. Hope, Henrik Haraldsson, Farshid Faraji, David Saloner, Michael D. Hope
Department of Radiology and Biomedical Imaging, University of California, San Francisco

Introduction: Abdominal aortic aneurysms (AAAs) with focal inflammation have been reported to grow 3 times faster than those without [1]. Ultrasmall superparamagnetic iron oxide (USPIO) particles can identify inflammation (macrophages) in vivo using MRI. USPIOs induce both T1 and T2* shortening. Previous studies have focused on the T2* effects, looking for signal voids or quantitative mapping with T2*-weighted images. Such techniques, however, have limited slice resolution (5mm) [1]. We aim to evaluate higher resolution techniques for USPIO imaging.

Methods: Four MRI sequences were evaluated at 3T: 1) Conventional 2D T2* mapping: 1.5x1.5x5mm resolution, scan time 3 breath-holds; 2) T1 weighted 3D blood suppressed fast-spin echo with variable flip angle train (SPACE): 1.3mm isotropic resolution, scan time of 7-8 minutes; 3) T1 weighted 3D Volume Interpolated Breath-hold Examination (VIBE): 1.3x1.3x2.6mm, scan time one breath-hold; and 4) T1 weighted Ultra short TE (UTE): 1.3mm isotropic resolution, scan time 3.5 minutes. Two phantoms with a range of USPIO concentrations were used to evaluate the relation between USPIO concentration and signal characteristics for the 4 sequences: 1) a saline phantom: 0.94mg Fe/L to 600mg Fe/L; and 2) a cell phantom: cultured macrophages were mixed with 3 concentrations of USPIO (5, 30, 100mg Fe/L). The 4 sequences were then applied to patients (n=24) with AAA disease before and 2-3 days after USPIO injection.

Results: MRI signal characteristics relative to USPIO concentration are plotted for the 4 sequences (**Figure 1**). Both SPACE and VIBE show signal increase-and-drop curves, however with different peaks (7.5 versus 60mg Fe/L). UTE signal continually rises with increasing USPIO concentrations, whereas T2* values drop. A similar trend is observed in cell phantoms: lower SPACE signal and T2* values than saline phantoms, whereas VIBE and UTE signals are comparable. In patients, signal changes with SPACE and T2* after USPIO administration were seen in 9/24 cases (**Figure 2**). Of these, 5/9 subsequently had repair for progressive AAA disease (versus 2/15 without signal change).

Discussion: Intracellular USPIO has been reported to have reduced T2* values compared to extracellular USPIO at the same concentration [2]. We observed the same finding in our saline and cell phantom studies. In addition, we found that SPACE has reduced signal with intracellular USPIO, but not VIBE or UTE. ***These findings suggest that SPACE can be used for intracellular USPIO imaging, which has been associated with fast AAA growth [1], with the advantage of higher spatial resolution than conventional T2* imaging.***

Conclusion: High-resolution MRI can be used to quantify USPIO concentration and to identity intracellular USPIO in vivo. These methods may help to risk stratify patients with AAA disease by characterizing and quantifying inflammation.

References: 1. Richards et al. Circ Cardiovasc Imaging. 2011. 2. Kuhlpeter R et al. Radiology. 2007.

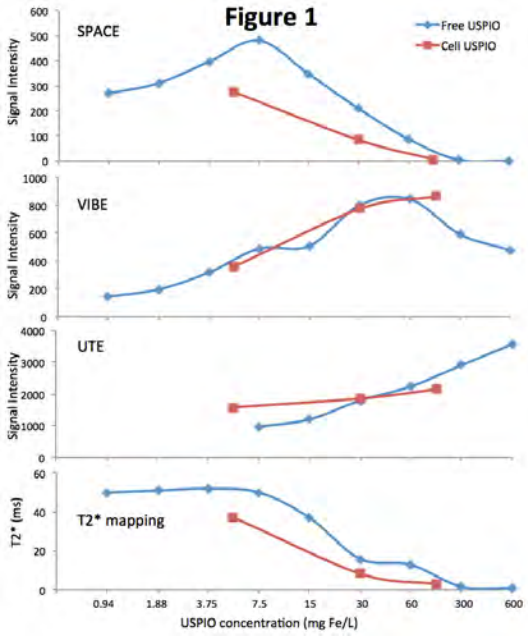

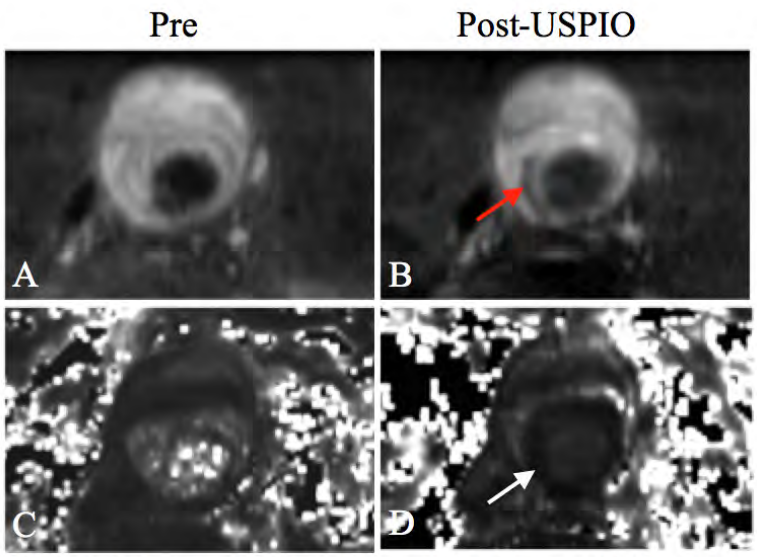

Figure 2. Red arrow shows signal drop in SPACE images. White arrows show T2* value drop.

Motion insensitive Carotid Artery Wall Imaging Using Stack of Stars technique and Inversion Recovery preparation (3D IR-Prep-SOS)

Seong-Eun Kim[1,2], Scott McNally[1,2], Gerald S Treiman[3,4], John A Roberts[1,2], Bradley D Bolster[5], Xiaoming Bi[5] and Dennis L Parker[1,2]

Utah Center for Advanced Research[1], Depart of Radiology[2], Depart of Surgery[3], University of Utah
Department of Veterans Affairs[4], VASLCHCS
Siemens Healthcare[5]

PURPOSE

Intraplaque hemorrhage (IPH) detected with carotid MRI identifies plaques at increased risk of future and recurrent stroke.[1] Carotid IPH can usually be detected very accurately with heavily T1 weighted sequences including the magnetization prepared rapid acquisition gradient echo (MPRAGE) sequence. However, our prior research has shown that hemorrhage identification with MPRAGE can be limited by motion and flow artifact at 3T.[2] The purpose of this work was to develop and evaluate a 3D carotid wall imaging technique to improve carotid IPH detection. We hypothesized that the radial stack of stars (SOS)[3] sequence with inversion recovery (IR) preparation would reduce motion artifact and provide more robust flow suppression due to its inherent oversampling of central k-space[4].

METHOD

IRB approval was obtained prior to the study. After informed consent, 27 patients with carotid disease were recruited and underwent 3T carotid MRI with a custom carotid coil. IPH was detected in 17 patients. Using a T1w 3D turbo FLASH (TFL) sequence capable of both Cartesian and SOS trajectories, IR preparation was implemented and optimized to suppress blood flow before each TFL readout train. Following the IR preparation, the same radial or k_y line for all partitions was acquired with a linear k-space ordering in the slice direction. The parameters were: coronal, FOV=160x160mm^2, isotropic voxel dimension=0.72 mm, TE/TR=2.5/8.0ms, 64 slices per slab, and TI=350ms. Scan time was 5 minutes for each trajectory with two averages. Measurement parameters were matched for both SOS and Cartesian acquisitions.

RESULTS

The 3D IR-prep-SOS sequence demonstrated excellent blood suppression and clear visualization of IPH relative to wall and lumen in study subjects. In all 27 subjects, flow artifacts were eliminated and motion artifacts decreased using the SOS acquisition. Also, IPH delineation was stronger using the SOS acquisition compared to Cartesian. SOS acquisition allows more precise and consistent depiction of carotid IPH by decreasing artifact due to motion and blood flow.

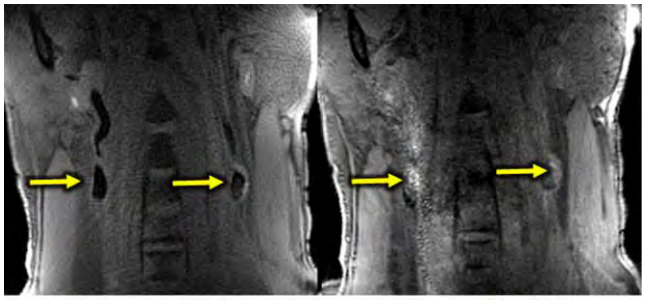

Comparison of carotid IPH sequences with SOS acquisition (left) versus Cartesian acquisition (right). Flow and motion artifact are eliminated on the SOS acquisition.

CONCLUSION

The 3D IR-prep-SOS sequence consistently improved carotid IPH images by decreasing artifact due to motion and incomplete blood flow suppression. With decreased artifact, 3D IR-prep-SOS should greatly increase the fraction of interpretable carotid MRI studies. The increased clarity will lay the foundation for studies to determine if IPH plaque volume and location can better determine stroke risk from carotid atherosclerosis. In general, it may provide a robust method to study the clinical impact of carotid atherosclerosis.

REFERENCE

1. Hosseini AA, et al Ann Neurol. 2013; 73(6):774
2. McNally JS, et al Neuroimaging 2015; 25(3):390.
3. Bi X. et al Proceeding ISRMR 2015:555
4. Song HK, et al MRM 2004;52:815.

3D Black Blood VISTA Magnetic Resonance Vessel Wall Imaging of the Thoracic Aorta in Young, Healthy Adults: Reproducibility and Implications for Efficacy Trial Sample Sizes

Anouk L.M. Eikendal, MD[1]; Björn A. Blomberg, MD[1]; Cees Haaring[1],; Tobias Saam, MD[2]; Rob J. van der Geest, PhD[3]; Michiel L. Bots, MD/PhD[4]; Hester M. den Ruijter, PhD[5]; Imo E. Hoefer, MD/PhD[5]; Tim Leiner, MD/PhD

Departments of Radiology[1], Epidemiology[4] and Experimental Cardiology[5], University Medical Center Utrecht, Utrecht, the Netherlands; Institute of Clinical Radiology[2], Ludwig-Maximilians-University Hospital, Munich, Germany; Division of Image Processing[3], Department of Radiology, Leiden University Medical Center, The Netherlands

Purpose
Pre-clinical detection of atherosclerosis enables targeted preventive strategies in asymptomatic individuals. Here, we evaluate agreement and reproducibility of an isotropic 3-dimensional, black-blood, T1-weighted, turbo-spin-echo sequence with variable flip angles (3D-T1-BB-VISTA) for quantification of aortic wall characteristics in healthy, young adults.

Methods
In 20 healthy, young adults (10 males, mean age 31.3 years) of the AMBITYON study cohort the descending thoracic aortic vessel wall was imaged with a 3.0T system using the 3D-T1-BB-VISTA sequence. The inter-scan, inter- and intra-rater agreement and reproducibility of the aortic lumen, total vessel and wall area and mean and maximum wall thickness were evaluated using Bland-Altman analyses and intra-class correlation coefficients (ICC). Based on these findings sample sizes for detecting pre-specified differences in these characteristics over time were calculated.

Results
For each aortic wall characteristic under study, the inter-scan and the non-contrast-enhanced and contrast-enhanced inter and intra-rater mean differences were small (<6%), limits of agreement were narrow and reproducibility was excellent (ICC ranging from 0.76 to 0.99). Sample sizes required to detect a 5% difference in aortic wall characteristics were 137, 86, 92, 47 and 104 for lumen area, total vessel area and vessel wall area and for mean and maximum vessel wall thickness, respectively.

Conclusions
The 3D-T1-BB-VISTA sequence provides excellent reproducibility for quantification of aortic wall characteristics and can detect small differences over time without requiring a large sample size. Hence, it may be attractive for atherosclerosis assessment from early life onwards, when vascular wall abnormalities are still subtle.

Intracranial Vessel Wall MR Registry

Qi Yang[1,2], Hongqi Zhang[2], Feng Ling[2], Yiu-Cho Chung[3], Lei Zhang[3], Zhaoyang Fan[1], and Debiao Li[1]
1.Biomedical Imaging Research Institute, Cedars Sinai Medical Center, LA, CA, United States, 2.Xuanwu Hospital, Beijing, China, 3.Shenzhen Institutes of Advanced Technology, Chinese Academic of Sciences, Guangdong, China

Introduction: Luminography-based methods may underestimate the presence of intracranial arterial pathology. Intracranial atherosclerosis, dissection, vasculitis, and aneurysm formation could yield similar appearances with either: catheter angiography; CTA; or MRA. Recently, black blood MR imaging has emerged as an effective method to evaluate intracranial vessels, specifically to detect atherosclerosis and vasculitis[1]. Vessel wall MR has a broad range of applications and is increasingly used in clinical practice[2,3]. This intracranial vessel wall MR registry sought to evaluate indications, image quality, safety and impact on patient management of clinical routine vessel wall MR in a single center.

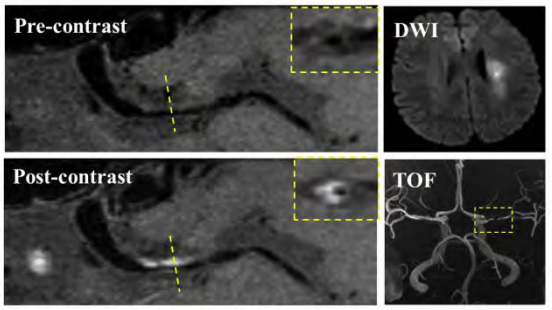

Fig. 1 Eccentric thickened wall and enhancement of a culprit plaque in a 60-year-old male. TOF MRA of the left middle cerebral artery shows moderate-severe stenosis of the M1 segment. Pre- and post-contrast 3D SPACE images show irregular wall thickening at the corresponding location (dashed lines).

Methods: This was a large single center registry with consecutive enrollment of patients. The patients were scanned with a 3.0T MR system (Magnetom Verio, Siemens, Erlangen, Germany) using a 32-channel head coil. Imaging protocol: A parameter optimized 3D high-resolution black blood MRI sequence (T1w-SPACE) was used for intracranial artery wall imaging with the following parameters: TR/TE = 938ms/24ms; iPAT = 2; spatial resolution= 0.5mm. T1w-SPACE was repeated 1~2 minutes after the contrast administration. Image analysis: Pre- and post-contrast images from T1w-SPACE were co-registered using commercial Fusion software.

Results: A total of 325 consecutive patients were enrolled. The most important indications were workup of atherosclerotic disease (32%), risk stratification in suspected dissection(25%), as well as assessment of venous sinus thrombosis (20%). Image quality was good in 92.2%, moderate in 6.2%, and inadequate in 1.6% of cases. In nearly one-thirds of patients, vessel wall MR findings impacted patient management. Importantly, in 28% of cases the final diagnosis based on vessel wall MR was different from the diagnosis before MR, leading to a complete change in management. In more than 64% of cases, MR was capable of satisfying all imaging needs so that no further imaging was required. Clinical diagnoses included atherosclerotic disease (165), cerebral venous and sinus thrombosis (42), aneurysms (41), dissections (20), moyamoya syndrome (10), CNS inflammatory disease (8), cavernous angioma (1), and no definitive clinical diagnosis (38). Ninety five of 165 with atherosclerotic disease had focal, eccentric vessel wall enhancement (Figure 1). Six of 8 with inflammatory diseases had diffuse, concentric vessel wall enhancement (Figure 2). Nineteen of 20 with dissection showed bright signal on T1, and 16 had irregular wall enhancement with a flap and dual lumen (Figure 3). Thirty five of 42 with venous thrombosis demonstrated acute and chronic stages of thrombus in sinus and/or cortical vein.

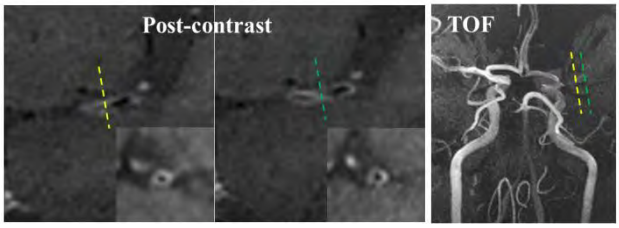

Fig. 2 33-year-old man with CNS vasculitis. T1-SPACE arterial wall coronal images of M1 with strong smooth, concentric wall enhancement and thickening. TOF-MRA shows total occlusion of the left MCA.

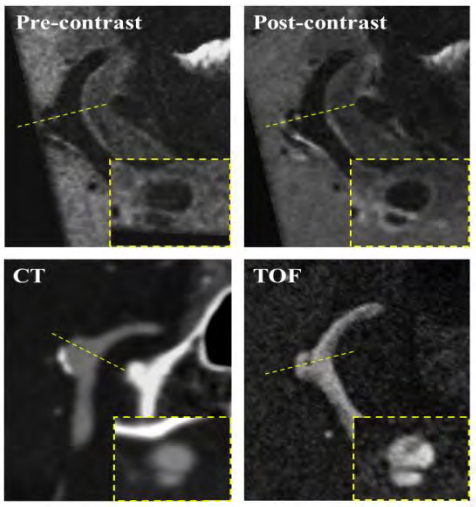

Fig.3 Widened right veterbral artery in a 56 year-old male. T1 SPACE shows additional enhancement and thickening of the wall and the intimal flip near the aneurysm. Reconstructed pre and post-contrast images ruled out fresh clot in the false lumen.

Discussion and Conclusion: High resolution intracranial vessel wall images may be reliably used in the differentiation of intracranial vasculopathy and results have strong impact on patient management.

References: [1] Dieleman et al. Circulation 2014. [2] R. H. Swartz et al. Neurology 2009. [3] Qiao Y et al. Radiology 2014.

Intracranial Vessel Wall Imaging at 3T and 7T

David Saloner[1], Chengcheng Zhu[1], Henrik Haraldsson[1], Sinyeob Ahn[2] and Gerhard Laub[2]
[1] University of California, San Francisco, United States, [2] Siemens Medical Systems

Purpose: Intracranial vessel disease is a major cause of stroke. Patients present with symptoms for which the etiology is often ambiguous. Underlying pathologies include atherosclerosis, inflammatory vasoconstriction, and dissection. The intracranial vessels are generally 2 to 3 mms in caliber and the vessel wall is sub-millimeter in thickness. Investigators are pursuing high resolution methods that might be used in evaluation of the vessel wall not only for stenotic disease but for evaluation of the wall of intracranial aneuryms. Development of these capabilities could be helpful in establishing the underlying pathophysiology, in defining the baseline anatomy and inflammatory status, and could be used to assess the response to therapeutic intervention. The aim of this study was to compare the visualization of intracranial vessel disease in symptomatic patients using high resolution imaging at 3T and 7T.

Methods: A resolution phantom was constructed with an central rod with no magnetization (representing black blood). This rod had rings of gel with known relaxation properties along its length. The rings had thicknesses of 0.5, 1.0, 1.5, and 2.0 mms. These rods were scanned with 3D SPACE sequences varying echo train lengths, and flip angle train values.

Eight patients with known intracranial vascular disease were recruited to this study using an IRB approved protocol. Patients were first scanned at 7T with the following sequences: 3D time of flight (0.4mm isotropic resolution); 3D SPACE – whole head black blood imaging, total acquisition time – 10 minutes; spatial resolution 0.5mm isotropic; echo train length of 60. 2D black blood slices were also acquired transverse to the vessel of interest. Patients were then transferred to the 3T scanner where they were imaged with a similar 3D SPACE sequence with slightly reduced resolution (0.5 x 0.5 x 0.6 mm**3) and with2D black blood imaging. A 3D CE-MRA study was then performed. Immediately following that the 3D SPACE sequence and 2D black blood sequences were repeated. Finally, the patients were returned to the 7T scanner and the 3D SPACE sequence and 2D black blood sequences were repeated.

Result: Results from the resolution phantom indicated that poor choices of parameters such as the specific k-space trajectory or flip angle train variation could result in substantially lower SNR, and edge ringing artifacts.

In vivo, excellent visualization of the vascular disease was obtained at both 3T and 7T. Enhancement of atherosclerotic lesions following Gd injection was clearly depicted (Figure 1). Although scans at both field strengths had equivalent spatial resolution, the improved SNR of 7T provided substantially improved visualization of the vessel wall. Similar results were found in the visualization of the wall of intracranial aneurysms (Figure 2.)

Conclusion: Optimized 3D black blood sequences can provide high quality imaging of the diseased wall of intracranial vessels. The thinness of these vessels and of intracranial aneurysms, requires very high spatial resolution which in turn necessitates long acquisitions. 7T imaging provides a strong improvement in image quality and in the ability to characterize intracranial vessel walls.

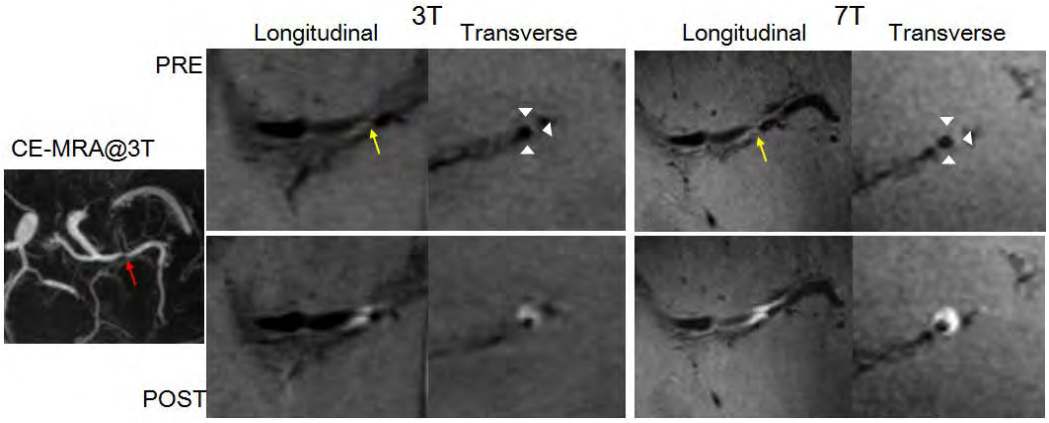

Figure 1: Patient with MCA stenosis. Pre and post Gd-injection images are shown for imaging at 3T and 7T reformatted in the plane of the vessel and transverse to the vessel. Strong enhancement of the vessel wall is noted at both 3T and 7T but significantly crisper assessment of the anatomy is depicted at 7T.

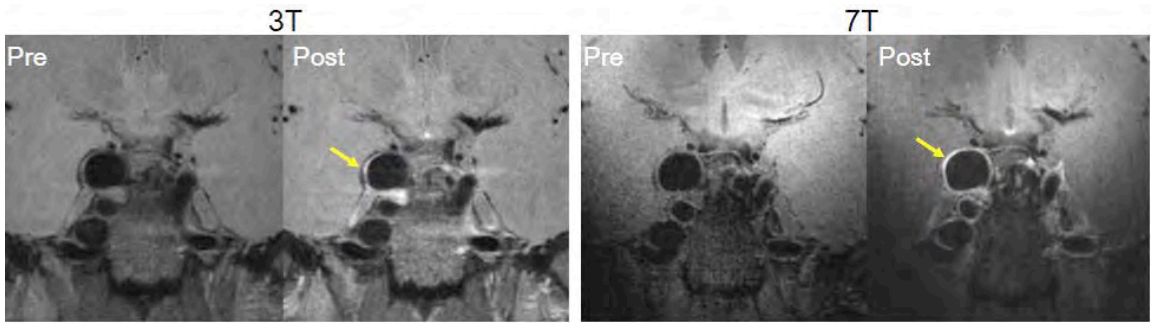

Figure 2: Patient with tri-lobed ICA aneurysm. Pre and post Gd-injection images are shown for imaging at 3T and 7T for a single plane through the 3D SPACE volume. More continuous depiction of the vessel wall with higher contrast is apparent at 7T.

Evaluation of Dissecting Aneurysm Wall of Vertebral Artery Using 3T MRI

Keiji Igase, Ichiro Matsubara, Daisuke Shoda, Kazuhiko Sadamoto
Department of Neurosurgery, Washokai Sadamoto Hospital, Matsuyama, Japan

(Introduction) It has been difficult to acquire the information as to the vessel wall of intracranial arteries because of the smallness of relevant arteries and thinness of those vessel walls. Recently 3T MRI has shown up and the new technology enabling vessel wall of intracranial arteries to be clearly delineated has also developed. Using this method we have already reported the vessel wall analysis of intracranial main arteries in the aspect of atherosclerotic changes, and this time we evaluated the interval change of the dissecting aneurysm wall of vertebral artery.

(Methods) We have collected 2 patients with a dissecting aneurysm of vertebral artery, among which one had an occlusion of unilateral vertebral artery due to the dissection, and another one had only the dissecting vessel wall. Both patients underwent 3T MRI (SIGNA HDxt: GE healthcare), with which two images of 3D-TOF and T1-CUBE, which is one of 3D-FSE sequence created by GE healthcare, were obtained. Sequentially both 2 images were also obtained at the onset, 1, 2, and 4 weeks after the onset, using those images the interval changes of the dissecting aneurysm wall were observed.

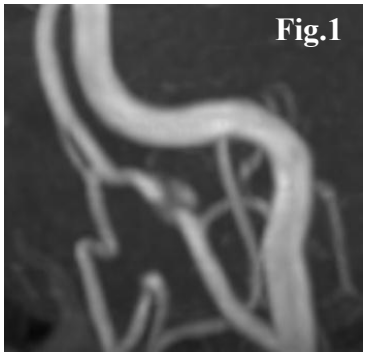
Fig.1

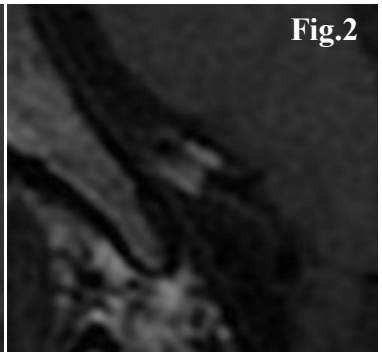
Fig.2

(Results) At the onset the occlusion case revealed obvious high intensity area on T1-CUBE image in the lesion, which was supposed to be a hematoma change, on the other hand the dissection case had irregular high intensity area surrounding the vessel (Fig.1&2), which was estimated to disclose the inflammation of the vessel wall. On T1-CUBE image obtained 4 weeks after the onset high intensity lesion of former case had been observed yet, whereas that of latter case had almost disappeared. That difference might be attributable to the difference of contents of the lesion.

(Conclusion) New sequence of T1-CUBE can delineate the destroyed vessel wall of dissecting aneurysm as the high intensity area, however the visual appearance and the interval change seem to be different depending on contents. Further investigation would be necessary to figure out that difference.

Carotid plaque permeability measured by high and low molecular weight contrast

Jason K. Mendes[1], Scott McNally[1], Seong-Eun Kim[1], Bradley D. Bolster[2], Gerald S. Treiman[1,3] and Dennis L. Parker[1]
[1]Utah Center for Advanced Imaging Research, [2]Siemens Healthcare, [3]Department of Veterans Affairs (VASLCHCS)

Purpose: Dynamic contrast enhanced (DCE) imaging is useful in evaluating the functional status of a vascular system (1). Gadofosveset is a clinically approved blood pool agent that binds to albumin resulting in a high effective molecular weight, only exiting the vessel lumen in areas of leaky neovessels and damaged endothelium (2). Studies have shown that gadofosveset is better able to discriminate atherosclerotic vessel wall in rabbits than Gd-DTPA (3) and symptomatic patients showed increased contrast agent uptake into carotid plaque as characterized by gadofosveset (4). However, changes in adventitial vasa vasorum density and permeability may not be characterized by gadofosveset if the neovessels have not yet disrupted. As a result, Gd-DTPA may be better suited to track initial disease progression and therapy outcomes (5) whereas gadofosveset may detect highly inflamed, end-stage atherosclerotic plaque. In this work we propose the use of dual contrast agent injections in conjunction with a 3D DCE radial stack of stars sequence (6).

Methods: All imaging was performed on a Siemens Trio scanner with a 3D radial stack of stars sequence. Acquisition matrix was 192x304x12, resolution 0.8mmx0.8mmx1.5mm, TE/TR=2ms/5ms, 23 total measurements over 372s (16s per measurement). Data was reconstructed using the KWIC algorithm into 16 temporal frames per measurement (1.3s effective temporal resolution) (7). Following one minute of baseline measurement, 0.3 mmol/kg of Ablavar (Gadofosveset Trisodium, Lantheus Medical Imaging) was injected at 1.2 ml/s with a 20ml saline flush. Following another three minutes of measurements 0.1 mmol/kg of MultiHance (Gadobenate Dimeglumine, Bracco Diagnostics) was injected at 2ml/s with a 20 ml saline flush. All injections were performed with dual Medrad power injectors (Radiology Solutions, Bayer). Data was analyzed with Olea Sphere post processing software (Olea Medical).

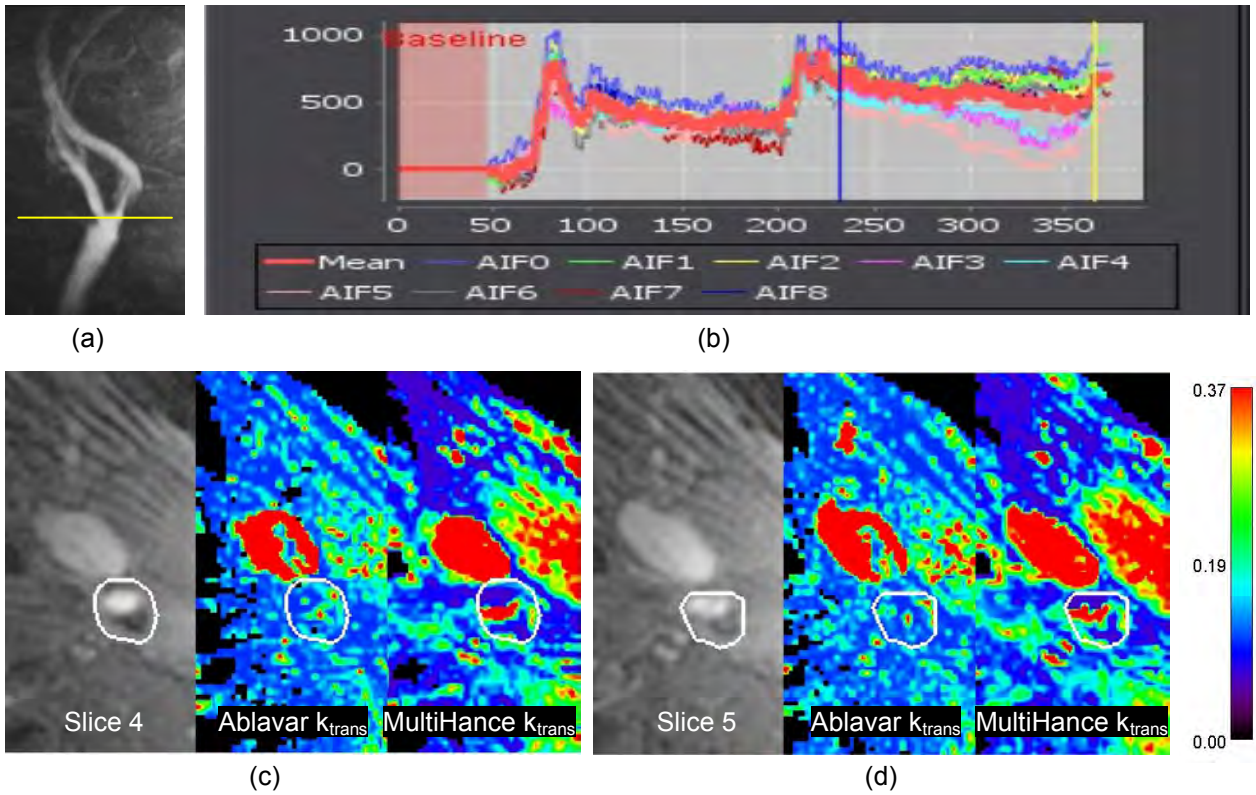

Figure1: K_{trans} calculated from dual contrast agents. A time-of-flight image is shown in (a) with the yellow line indicating the position of the two consecutive axial slices shown in (c) and (d). The arterial input function is shown in (b) with the resulting k_{trans} maps for two different slices shown in (c) and (d).

Results: The change in signal intensity can be seen in the arterial input function (b). Within this carotid plaque (c and d), there are areas of high k_{trans} as measured by low molecular weight Multihance along the juxtaluminal fibrous cap (red) and the adventitia (green). K_{trans} measurements with the high molecular weight Ablavar are decreased in comparison, reflecting differences in permeability between the two agents.

Conclusion: We have demonstrated feasibility of performing dual contrast agent injection for clinical evaluation of carotid disease. Two different molecular weight contrast agents may allow further characterization of plaque permeability in vulnerable carotid plaque.

References:(1) O'Connor et al. Br J Radiol. 2011; 84:S112-S120. (2). Caravan et al. J Am Chem Soc. 2002; 124:3152-3162. (3) Lobbes et al. Radiology. 2009;250:682-691. (4) Lobbes et al. Invest Radiol. 2010; 45:275-281. (5) Dong et al. Radiology. 2011; 260:224-231. (6) Block et al. JKSMRM. 2014; 18:87-106. (7) Song et al. Magn Reson Med. 2000; 44:825-32.

A Paradigm Shift in Cardiac MRI? Motion Reconstruction Rather Than Motion Correction

Matthias Stuber

MRI is rather signal-inefficient and as a result, scanning times are in the order of seconds or minutes, depending on the spatial resolution, signal-to-noise, volumetric coverage, and contrast requirements. However, for MRI of the beating heart, such lengthy scanning times are not acceptable since motion of the heart during signal acquisition will inevitably lead to motion artifacts and limited diagnostic quality of the images. As a result, k-space segmentation using ECG triggering is used to synchronize the MRI data collection with the heartbeat. However, in addition to the periodic contraction and relaxation of the beating heart, respiratory motion represents another major challenge, as a sustained respiration during minutes is simply not possible. As a result, navigator techniques have emerged and have been tested in multicenter settings for imaging of the coronary arteries. However, limited ease-of-use, operator dependence as well as variable and unpredictable scanning times are among the shortcomings of this technique. In response, respiratory self-navigation has been proposed in 2005. Using this technique, navigator placement is no longer needed, the only physiological determinant of scanning time is the heart rate, and ease-of-use has dramatically improved. However, motion correction over the entire range of respiratory excursions inevitably leads to motion artifacts originating from static structures such as the chest wall, while non-linear and respiratory-induced deformations of the heart cannot easily be accounted for. A number of technical developments for the improvement of self-navigation have therefore been proposed and are currently under investigation.

However, and simultaneously, *a fundamentally new concept to address the motion problem is emerging:* Non-linear reconstruction or Compressed Sensing may represent disruptive technology that obviates the need for ECG triggering or any kind of navigation for respiratory motion suppression. A signal for the synchronization to the heartbeat is directly derived from the image data and enables an entirely retrospective selection of the acquisition window width (temporal resolution) and its position in the cardiac cycle. This critically enables studies of coronary function at rest and stress as well as fetal cardiac cine imaging with high temporal and spatial resolution. Simultaneously, 3D whole-heart data acquired during free breathing can be subdivided into sub-sampled images acquired at different respiratory positions. Reconstructed using Compressed Sensing, high resolution images acquired at different respiratory positions can be extracted while respiratory motion artifacts are effectively suppressed. In combination with free-breathing, free-running whole-heart imaging, 5D data (3 spatial dimensions, one temporal dimension, and one respiratory dimension) of the heart can be reconstructed while motion artifacts are intrinsically minimized. However, and at this early stage, gold standard comparisons or studies in larger cohorts are missing and reconstruction times are on the order of hours. In summary, *non-linear reconstruction provides an extremely powerful alternative for cardiac MRI free of motion artifacts*, yet its true potential remains to be defined.

Two International, Multicenter Phase 3 Studies Evaluating both the Assessability and Quantitative Accuracy of Gadobutrol Enhanced MRACompared to Time-of-Flight (ToF) MRA in the Supra-Aortic and Renal Arteries

Jacob Agris, Radiology, Bayer HealthCare,; Sheela Agarwal, Radiology, Massachusetts General Hospital; Carl DiCasoli, Statistician, Bayer HealthCare; Dan Haverstock, Statistician, Bayer HealthCare

Purpose: MRA of the supra-aortic (including carotid and vertebral arteries) and renal arteries are routinely performed for evaluation of patients with stroke or TIAs and medically resistant hypertension, respectively. The objective was to compare the MRA with Gadobutrol, a high relaxivity and high concentration, macrocyclic MR (Magnetic Resonance) contrast agent, to 2D ToF MRA using CTA as the standard of reference.

Materials and Methods: 487 patients enrolled for evaluationof supra-aortic stenosis and 317 patients enrolled for evaluation of renal artery stenosis underwent 2D ToF followed by a Gadobutrol–enhanced MRA at a standard dose of 0.1 mmol/kg body weight administered as a bolus at 1.5cc/sec. All studies were performed at 1.5T and utilized parallel imaging (minimum 6 body or 8 head coils). The 21 supra-aortic and 6 renal artery segments were evaluated by 3 blinded readers (BR) for both MRA techniques and 3 additional blinded readers evaluated the CTA. One objective was to evaluate the superiority of Gadobutrol-enhanced MRA for assessability, i.e. defined as sufficient structural delineation to visualize the entire segment and adequate to measure its diameter. Accuracy of the vessel diameter measurements (for both the stenosis and normal diameters) was determined for any assessable segment with greater than a 10% stenosis.

Results: Gadobutrol-enhanced MRA demonstrated a statistically higher assessability rate compared to ToF MRA for both vessel territories (95.0% vs 72.7%, P<0.0001 for the supra-aortic vessels and 95.9% vs 77.6%, P<0.0001 for the renal arteries). Gadobutrol-enhanced MRA demonstrated much better visualization of the arterial segments resulting in fewer missed diagnoses in these non-visualized segments compared to ToF MRA (6% vs 41%, P<0.0001 for supra-aortic MRA and 11% vs 38%, P<0.0001 for renal artery MRA).

The quantitative measurements of the vessel diameters were more accurate with Gadobutrol-enhanced MRA compared to ToF MRA (see Figures below). In addition, more accessory renal arteries were identified with Gadobutrol-enhanced MRA compared to ToF.

Conclusions: Gadobutrol-enhanced MRA was superior to 2D ToF MRA for visualizing the both the supra-aortic and renal artery segments thereby reducing the number of non-visualized stenoses. The Gadobutrol enhanced MRA was highly accurate in the vascular diameter measurements,critical for diagnostic decisions and treatment. Gadobutrol enhanced MRA represents a safe alternative to CTA without the associated artifacts from calcified plaques nor the burden of ionizing radiation.

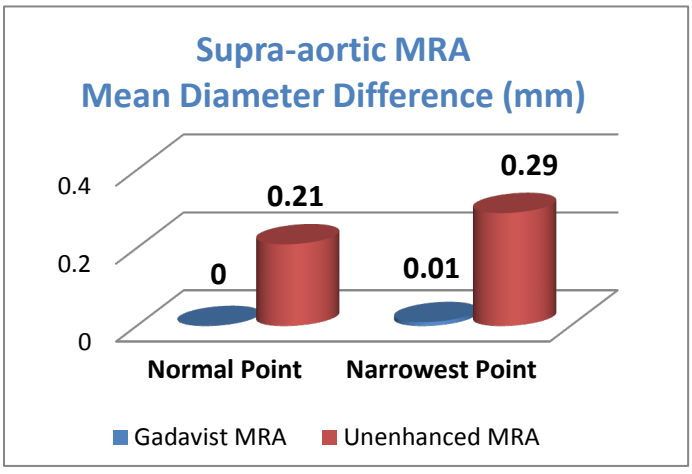

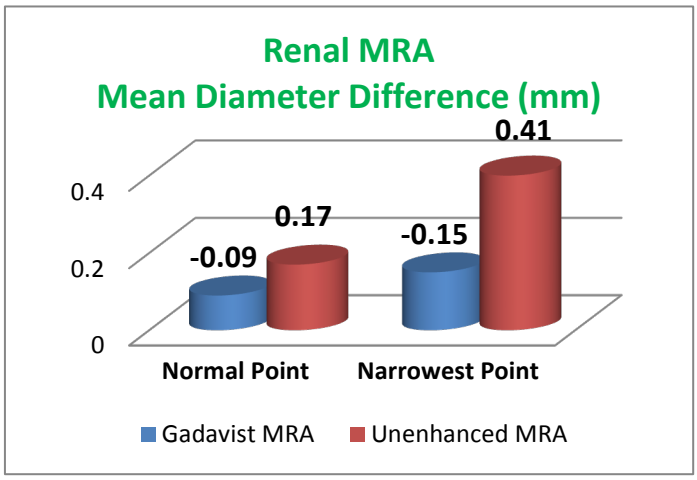

Classification of human peripheral arterial atherosclerotic plaques with T2 and Ultra-short echo time MRI

Trisha Roy[1,2], Garry Liu[1], Xiuling Qi[1], Andrew D. Dueck[1,2], Graham A. Wright[1]
[1]Sunnybrook Research Institute, [2]Division of Vascular Surgery, Department of Surgery, University of Toronto

Purpose

Many of the challenges associated with planning and performance of peripheral endovascular interventions are associated with limited visualization. X-ray fluoroscopy does not allow the visualization of the vessel wall or plaque components. This information may assist with predicting success of intervention, navigation within an occlusion, and wire and device selection.

MRI is capable of producing high quality angiograms, and in addition, we hypothesize can also characterize peripheral arterial disease (PAD) plaque morphology. Understanding PAD lesion composition may help in planning and performing peripheral endovascular interventions by identifying soft lesion components to facilitate guidewire passage. We aim to develop MRI methods for characterizing PAD lesions to ultimately use this information for preplanning endovascular interventions in patients.

Methods

MRI was performed on 15 excised human peripheral arterial diseased segments from 4 patients who underwent amputation. Each sample was imaged at 7 Tesla at high resolution (75μm^3 voxels) to produce three-dimensional T2- and T2*-weighted images. For T2-weighted imaging, a fast spin-echo sequence with an echo-train length of 8 and an effective TE of 37 ms was used. For T2*-imaging, an ultrashort echo (UTE) sequence with a 20μs echo time was used. Each sample was also imaged with microCT at high resolution (5μm^3 voxels) to identify calcium. Histology with H&E staining was used to identify thrombus. Movat's pentachrome staining was used to identify lumen, adipose tissue, soft tissue (e.g. smooth muscle) and hardened tissue (e.g. dense collagen, cholesterol clefts). 3 independent blinded image reviewers (1 cardiologist and 2 radiologists) classified 50 regions of interest on 10 axial MRI images of the peripheral arterial atherosclerotic plaques.

Results

MRI showed high sensitivity and specificity for the following peripheral plaque components: adipose (100%, 98%); soft tissue (90%, 100%); thrombus (100%, 100%); hardened tissue (92%, 99%); and calcium (67%, 97%). The limited sensitivity with calcium was only in lesions with concentric calcium rings and may reflect an unfamiliarity with histologic-level peripheral arterial lesion anatomy. There was almost perfect agreement between image reviewers ($\kappa = 0.81$, $p < 0.005$).

Conclusions

These results demonstrate the potential of high-resolution MRI to classify lesion components in human peripheral arterial atherosclerotic plaque. This study provides the foundation for future studies in predicting the lesion crossability of various PAD plaque types from MRI data sets.

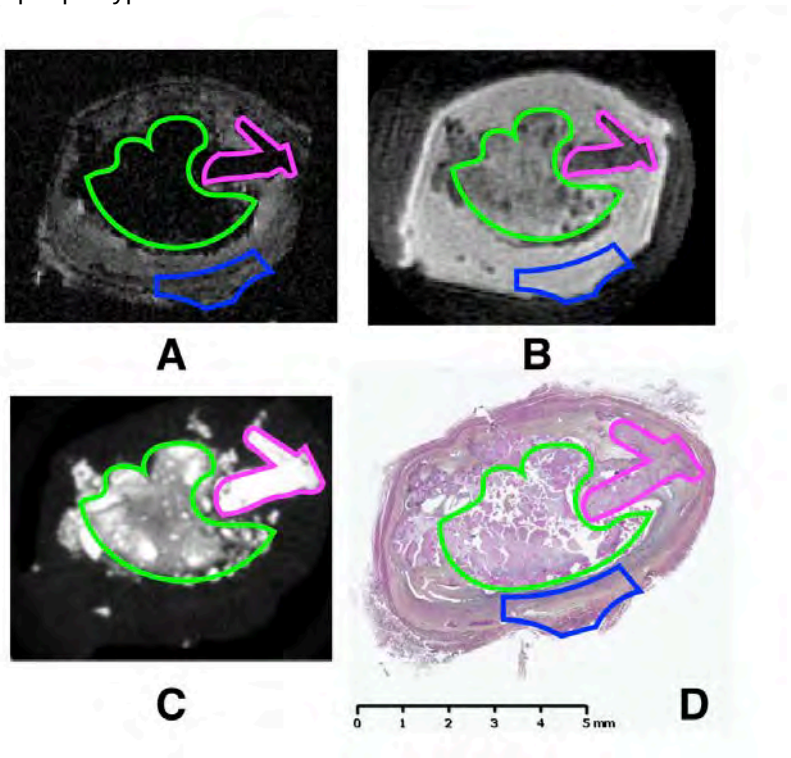

Figure 1: MRI of human popliteal artery atherosclerotic lesion with microCT and histologic validation. A) T2 sequences show the general anatomy of the lesion well. Soft tissue like smooth muscle (blue) was used as the reference intensity, Hardened tissue like dense collagen (green) and calcium (pink) does not produce signal on T2 weighted images. B) UTE sequences show calcium (pink) as strongly hypointense with respect to soft tissue, and hardened tissue is weakly hypintense (green), compared to soft tissue (blue). C) MicroCT was used to validate areas of calcium (pink). This lesion shows a unique pattern of segmented calcium with interspersed collagen (green) in the centre of the lesion. D) Movat's penatchrome was used to validate areas of soft tissue (blue) and hardened tissue (green).

Global measures of myocardial strain predict infiltrative cardiomyopathy at heart deformation analysis: A feasibility study at 1.5T

Marcos P Ferreira Botelho, MD[1]; Kevin Kalisz, MD[1]; Peter M Smith, MD[1]; Benjamin Freed, MD[2]; Daniel Lee, MD[2]; Bruce Spottiswoode, PhD[3]; Maria Carr, MD[1]; James C Carr, MD[1]; Jeremy D Collins, MD[1]

Departments of [1]Radiology and [2]Cardiology, Northwestern University, Chicago, IL; [3]Cardiovascular MR R&D, Siemens Medical Solutions, Chicago, IL

Purpose:
Cardiac MR (CMR) derived strain parameters have been studied for ischemic and some non-ischemic cardiomyopathies (NICM) (1-2). The potential utility of such techniques includes higher sensitivity to early changes in myocardial function before reduction in systolic function. We explored the use of standard balanced steady-state free precession (bSSFP) cine imaging for obtaining global LV and RV strain data in biopsy-proven NICM using deformation analysis, stratifying results by ventricular systolic function and comparing with data in healthy volunteers. We hypothesize that biventricular strain obtained from bSSFP cine data at heart deformation analysis (HDA) is more sensitive to functional changes NICM than routine measures of global systolic function.

Methods:
26 patients (21 men, avg age 64 yrs) with biopsy proven NICM (18 amyloidosis/8 fibrosis) and 20 healthy volunteers (14 men, avg age 44 yrs) underwent CMR at 1.5T with bSSFP segmented cine imaging with a temporal resolution of 25-40 msec. Images were retrospectively evaluated using prototype software employing deformation field analysis to generate Lagrangian strain values for the left (LV- radial, circumferential, longitudinal) and right ventricles (RV- longitudinal) (3,4). LV and RV ejection fraction (LVEF/RVEF) were calculated on a dedicated workstation. LVEF was defined as preserved if ≥ 55%; RVEF was defined as preserved if ≥ 45%. The student's t-test assessed differences between groups.

Results:
HDA was feasible in all subjects. Mean LVEF and RVEF for the patient cohort was 41.2% and 35.9%, respectively, whereas all volunteers demonstrated LVEF and RVEF ≥ 55% and 45%, respectively. Mean (SD) global strain values for patients and [volunteers] were: LV longitudinal -10.8 (3.9) [-15.5 (2.5)]; LV circumferential -10.9 (4.1) [-17.2 (1.9)]; LV radial 20.1 (11.4) [36.2 (8.6)]; RV longitudinal -13.4 (4.9) [-18.3 (3.5)]. All strain parameters were significantly different between patients and volunteers ($p<0.001$). In the 8 patients with preserved LVEF, mean (SD) global average LV strain parameters were also significantly different from healthy volunteers (LV longitudinal -14.1 (3.1), LV circumferential -13.3 (2.7), LV radial 26.1 (5.7); $p<0.01$). In the 13 patients with preserved RVEF, mean (SD) average global RV longitudinal strain was similar to healthy volunteers (RV longitudinal 16.3 (3.6), $p>0.05$).

Conclusions:
This study demonstrated significant differences in LV and RV myocardial strain parameters between patients with NICM and healthy volunteers using standard bSSFP cines. Significantly different global strain values were noted in NICM patients with preserved LVEF; however, RV longitudinal strain analysis was not able to distinguish a difference between NICM subjects with preserved RVEF from those in healthy volunteers. Additional studies are warranted to validate our results, assess strain changes with age and explore this technique to identify early changes preceding irreversible myocardial injury.

References: 1. Young et al. CV Res 2001. 2. Neizel et al. Circ CV Imag 2009. 3. Guetter et al. Proc. ISBI, 2011. 4. Jolly et al. Proc. ISBI, 2010.

Dynamic MR Imaging of Carotid Webs

Boesen ME[1,5,6], Singh D[3,7], Mitha A[2,3,5], Goyal M[2-7], Menon BK[2-7], Frayne R[1-3,5,6]

[1]Biomedical Engineering, [2]Radiology, [3]Clinical Neurosciences and [4]Community Health Sciences, [5]Hotchkiss Brain Institute, University of Calgary; [6]Seaman Family Centre, and [7]Calgary Stroke Program, Foothills Medical Centre, AB Health Services, Calgary

Introduction: Fibromuscular dysplasia (FMD) is a rare but likely under-diagnosed condition of the arteries in which pathological changes impact the cellular structure of the vessel wall. FMD of cervical vessels most commonly affects the extracranial internal carotid artery, giving a beaded appearance on angiography. Another variant of carotid FMD has the appearance of a web-like protrusion from the vessel wall into the lumen.[1] This so-called carotid "web" poses a serious risk of transient ischemic attack (TIA) and stroke due to thrombus development associated with blood flow disruptions caused by the web.[2] Due to the small size of carotid webs (~1 mm), current diagnosis relies on high-resolution imaging. Invasive angiogram has been the gold standard for imaging carotid webs but CTAs are increasingly being used. Both of these x-ray based techniques provide little information about the composition and dynamics of the vessel wall and web itself. Conventional and dynamic MR imaging [3] of carotid webs may provide pertinent information regarding a variety of vascular properties, including vessel morphology and blood flow, as well as wall composition and biomechanics.

Methods: A 60-minute MR imaging protocol was implemented to investigate carotid webs (Table 1) using a 3 T scanner (Discovery 750; General Electric Healthcare). Five patients presenting with stroke or TIA and diagnosed with carotid webs on CTA were evaluated using this protocol. Post-contrast time-of-flight (TOF) imaging was acquired to visualize the location/size of the carotid web (morphology). Axial pre- and post-contrast T1- and proton density-weighted fast spin echo (FSE) images were acquired at the level of the web to assess wall composition. Axial cine phase contrast (cinePC) and cineFSE images [3] were acquired to determine blood flow and wall dynamics, respectively.

Table 1: Carotid Web MR Imaging Protocol and Parameters

Sequence	Resolution (mm)	Flip Angle (°) + TR/TE (ms)	Other Parameters
3D TOF	0.59 x 0.59 x 0.8	15° + 22/2.4	Post-contrast imaging
2D T1-weighted FSE	0.59 x 0.59 x 1.0	90° + 1250/7.4	ETL = 12 , NEX = 2, DIR
2D PD-weighted FSE	0.59 x 0.59 x 1.0	90° + 2400/7.3	ETL = 12 , NEX = 2 , DIR
2D CinePC	0.59 x 0.59 x 3.0	20° + 40/7.3	VENC = 150 cm/s
2D CineFSE	0.59 x 0.59 x 1.0	90° + 2500/7.7	ETL = 12, eNEX = 4, DIR

TOF = time of flight, FSE = fast spin echo, ETL = echo train length, NEX = number of excitations, DIR = double inversion recovery, PD = proton density, PC = phase contrast, VENC = velocity encoding, eNEX = equivalent NEX

Results: The carotid webs were visualized on all MR sequences, with the exception of cinePC (due to the 3 mm thick slice). 3D TOF images acquired after contrast injection depicted the size and location of the webs at the carotid bifurcation (Figure 1a). On axial 2D images, the carotid webs appeared as a false bifurcation, inferior to the actual carotid bifurcation (Figure 1b, bottom panel). FSE images showed wall thickening and increased PD signal intensity surrounding the web, as compared to the contralateral vessel wall (Figure 1e). CineFSE qualitatively depicted greater pulsatile distension on one side of the web, compared to the rest of the vessel wall (Figure 1f). CinePC images demonstrated overall cardiac pulsatility of the carotid artery (data not shown).

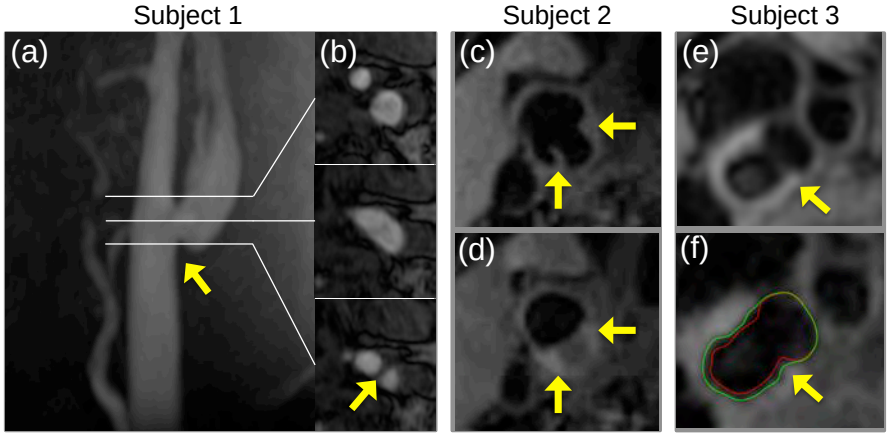

Figure 1: A selection of images from three subjects: (a) TOF maximum intensity projection of the axial source images shown in (b), (c,d) pre- and post-contrast T1-w FSE, showing enhanced signal from slow blood flow within the web, (e) PD-w FSE, and (f) systolic cineFSE image with manual lumen tracing in green and overlaid with diastolic lumen tracing in red. Carotid webs in each patient are marked (yellow arrow), as applicable.

Conclusions: This MR imaging protocol is capable of resolving carotid webs and provides an in-depth evaluation of local vessel wall properties. With refinement and after additional experience imaging patients, this MR imaging protocol may provide insight into the cause and detrimental effects of FMD on the carotid artery.

References:

[1] Morgenlander JC and Goldstein LB. *Stroke*. 1991; **22**: 94.
[2] Lenck S, *et al*. *Eur J Neurology*. 2014; **21:** 586.
[3] Boesen ME, *et al*. *Magn Reson Med*. 2014; ePub ahead of print. doi: 10.1002/mrm.25494.

In vivo Cardiac Blood Oxygen Saturation Mapping using Quantitative Susceptibility Mapping

Yan Wen, Thanh Nguyen, Pascal Spincemaille, Dong Zhou, Jonathan Weinsaft, Jiwon Kim, Yi Wang

Weill Cornell Medical College, New York, NY, USA

Introduction

The quantification of blood oxygen saturation (SO_2) within the heart chambers plays an important role in the detection and management of cardiac shunt and pulmonary disorders. The purpose of this study was to demonstrate feasibility of in vivo SO_2 mapping in the heart using Quantitative Susceptibility Mapping (QSM).

Methods

Three healthy volunteers were scanned at 1.5T using an 8-channel cardiac coil and a 2D ECG-triggered multi-echo GRE sequence (8 echoes, first TE= 3.6 ms, ΔTE = 3.2 ms, TR = 28.4 ms, voxel size ~ 1.4x1.4x4 mm^3, 8 views per heartbeat, flow compensation in the readout direction). A stack of short-axis images were acquired in consecutive breath-holds of approximately 15 sec each.

Cardiac QSM maps were obtained by performing phase unwrapping of the phase images using a region growing algorithm [1], followed by background field removal using Projection onto Dipole Field method [2] and dipole inversion using a piecewise constant model [3] consisting of three regions (left ventricle (LV), right ventricle (RV), and myocardium). The blood susceptibility difference between LV and RV was used to calculate SO_2 using the model described by Jain et al [4].

Results

The difference in blood susceptibility between RV (deoxygenated blood) and LV (almost fully oxygenated blood) measured in the three volunteers were 388, 478, and 404 ppb. Assuming 100% oxygenation of LV blood, the blood oxygen saturation in RV were 75.2%, 69.5% and 74.2% (73.0% $\pm$ 3.0%). Figure 1 shows an example of short-axis magnitude image, local field, and QSM map.

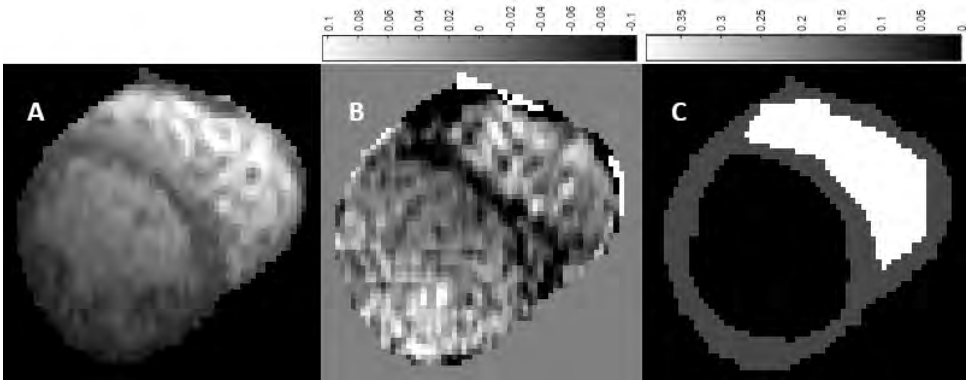

Figure 1. A) Magnitude image, B) local field map, and C) piecewise constant QSM map of the heart.

Discussion

We have demonstrated the feasibility of using the piecewise constant dipole inversion algorithm to noninvasively quantify blood oxygenation in the heart. SO2 derived from QSM in healthy volunteers was similar to values reported in the literature [5]. Future work will focus on accelerated 3D acquisition with full flow compensation and the use of more advanced dipole inversion algorithms such as MEDI [6].

Reference

1) Xu W et al. *IEEE Trans Geosci Remote Sens* 1999; 37-11. 2) Liu T et al. *NMR Biomed* 2011;24:1129-1136. 3) de Rochefort L et al. *Magn Reson Med* 2010;60:1003-9. 4) Jain V et al. *Magn Reson Med* 2012;68:863-7. 5) Margreiter, J et al. *Anesthesia & Analgesia* 2002;94;794-798. 6) Liu J et al. *Neuroimage* 2012;59;2560-2568

High Resolution Whole Heart Coronary Plaque Characterization with Integrated Anatomical Reference

Yibin Xie[1], Jianing Pang[1], Young-Jin Kim[3], Qi Yang[1], Jung-Sun Kim[3], Christopher Nguyen[1], Byoung Wook Choi[3], Zhaoyang Fan[1], Daniel Berman[1], Hyuk-Jae Chang[3], Debiao Li[1,2]

[1]Cedars-Sinai Medical Center, Los Angeles/USA; [2]University of California, Los Angeles/USA; [3]Yonsei University College of Medicine, Seoul/South Korea

Purpose: The detection of high-risk coronary atherosclerotic lesions before severe plaque complications is the "holy grail" in cardiology. Recently T1-weighted (T1w) MRI with [2] or without [3] contrast enhancement (CE) has been used for characterizing coronary plaques showing promising prognostic capability [4]. However the drawbacks of current protocols using conventional Cartesian acquisition and navigator gating hinder the clinical application of this technique: a) coverage is limited to proximal coronary segments; b) spatial resolution is low and often anisotropic; c) since the background tissue in T1w images is highly suppressed, a separate MRA acquisition is needed to provide anatomical reference. **The purpose of this work is to develop a highly efficient 3D radial acquisition technique for coronary plaque characterization with 1) whole-heart coverage, 2) isotropic high spatial resolution, and 3) simultaneously acquired bright-blood anatomical reference.**

Methods: An ECG-gated, inversion recovery (IR) prepared spoiled gradient echo with golden angle 3D radial trajectory were used to acquire dark-blood T1w images and bright-blood reference images in an interleaved fashion (**Fig.1**). Retrospective motion correction was performed to allow 100% respiratory gating efficiency. Both dark-blood and bright-blood k-space data were segmented into six respiratory bins and an image-based affine motion correction algorithm [5] was used to estimate respiratory motion using the higher SNR bright-blood data. Identical motion transformation were then used to correct motion in both dark-blood and bright-blood images. Healthy volunteers (n=12) and CAD patients with stable and unstable angina (n=26) were recruited with informed consent and scanned on a 3T scanner (Siemens Magnetom Trio) before and after contrast enhancement (Gadoterate meglumine@0.1 mmol/kg). Scan parameters: 3D slab covering the entire heart with FOV = 330^3 mm^3; spatial resolution = 1.1^3 mm^3; TR/TE = 4.6/2.3 ms; number of radial projections = 8500; scan time = ~10 minutes depending on heart rate. After completing MRI, 21 CAD patients underwent interventional X-ray angiography and intracoronary optical coherence tomography (OCT) for coronary plaque evaluation.

Results: All 38 subjects successful completed the pre-CE T1w MRI. All 12 healthy volunteers and 23 eligible patients also completed the post-CE T1w MRI. None of the healthy subjects showed coronary hyper-intensive plaques (CHIPs) in either pre-CE or post-CE T1w MRI. Three patients showed CHIPs on pre-CE T1w MRI and 4 patients showed CHIPs on post-CE T1w MRI, respectively. **Fig.2** shows a representative patient case with a CHIP on pre-CE T1w MRI. Pre-CE T1w images showed a CHIP at middle LAD as localized on the bright-blood images. X-ray angiography confirmed significant stenosis (70%) at that location. OCT image showed large signal-poor area suggestive of possible lipid core/intra-plaque hemorrhage (yellow arrows).
Fig.3 shows a representative patient case with a CHIP on post-CE T1w MRI. Pre-CE T1w images showed no HIP. Post-CE T1w showed diffused wall enhancement at proximal RCA as localized on the bright-blood images. Corresponding X-ray angiography showed only mild stenosis (30%) at proximal RCA. CTA showed marked positive modeling at the location of the stenosis. OCT image showed strong multi-focal back reflections and signal heterogeneity within the overlying tissue suggestive of high macrophage density (yellow arrows).

Conclusion: Time-efficient T1w whole heart coronary plaque characterization with isotropic high resolution and simultaneously acquired anatomical reference was feasible. The proposed method showed the potential to detect intra-plaque haemorrhage and inflammation.

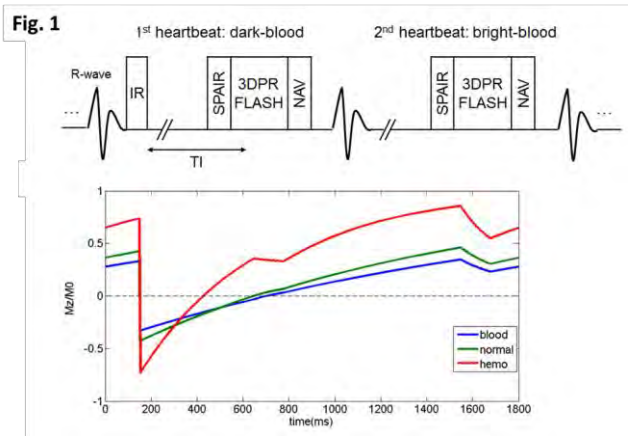

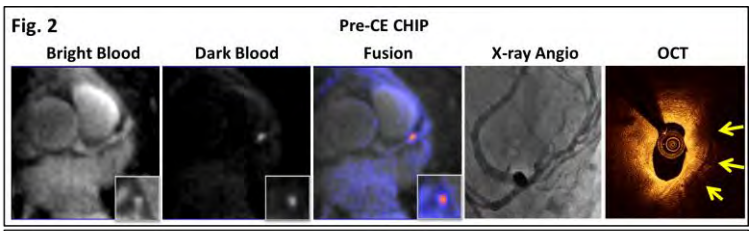

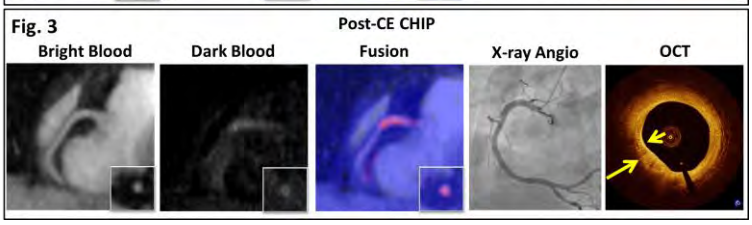

References: [1] Naghavi M. et al., Circ.; 2003:108. [2] Maintz D. et al., Eur Heart J; 2006:27. [3] Kawasaki T. et al., JACC Imaging; 2009:2. [4] Noguchi T. et al., JACC; 2014:18. [5] Pang J. et al., MRM; 2014:71.

Patient-specific 3D printed models of the aorta for pre-procedural planning in transcatheter aortic valve replacement: A proof of concept study

Beth Ripley MD, PhD[2], Tatiana Kelil MD[1], Michael K. Cheezum MD[1], Alexandra Goncalves MD, PhD[1], Frank Rybicki MD, PhD[1], Mike Steigner MD[1], Dimitrios Mitsouras PhD[1], Ron Blankstein MD[1]

[1] Department of Radiology, Brigham and Women's Hospital, Harvard Medical School, Boston, MA [2]University of Washington, Department of Radiology, Seattle, WA, USA.

Introduction: 3D printing is a promising avenue in precision medicine, with the potential to provide information on patient-specific anatomy. This may prove particularly useful in minimally invasive procedures such as transcatheter aortic valve replacement (TAVR) where the anatomy is complex and variable between patients and is only accessible via imaging studies. In this preliminary study, we asked whether 3D printed patient-specific models of the aortic valve complex could aid in understanding anatomy prior to TAVR and potentially predict paravalvular aortic regurgitation (PAR), a common complication of TAVR.

Methods: In this IRB approved, retrospective study, 9 patients who developed PAR following TAVR with a Sapien Valve (Edwards Life Sciences, Irvine, CA) were identified, along with 7 age, sex and valve size-matched controls. All patients had a pre-procedural planning CT angiogram (CTA) and a post-procedural transthoracic echo (TTE) to assess for PAR. Pre-procedure CTAs were used to create a 3D printed model of each patient's aortic root complex (Figure 1). Briefly, the blood pool of the aortic root was manually segmented using 3D visualization software (Vitrea 6.7, Vital Images) by a radiologist (B.R.) blinded to TTE findings and exported as 3D-printable (STL) files into computer aided design software (3-matic, Materialise) for further post-processing. Models were then printed on a stereolithography printer (Form 1+, Formlabs). The valve model of size corresponding to each patient's actual implanted valve (23, 26 or 29 mm) was positioned in individual aortic models at the level of the AV annulus. The presence of leak was then determined via projection of light through the left ventricular outflow tract onto a thin film, captured with a digital camera.

Figure 1. 3D printed models accurately depict aortic morphology

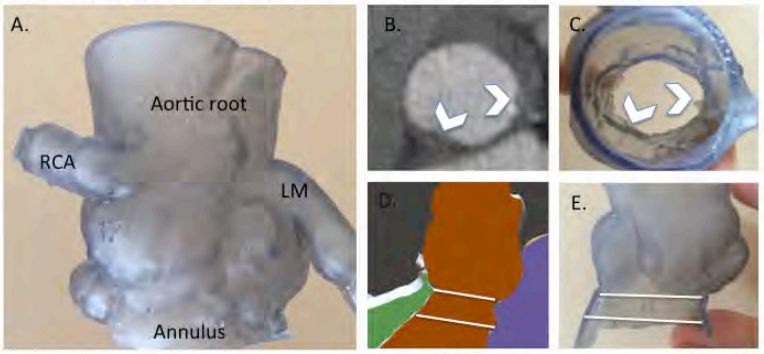

A. 3D printed aortic valve complex from patient 12. B. CTA multiplanar reformatted image at the level of the aortic annulus in patient 12. C. 3D printed aortic annular complex depicts the shape of the aortic annulus, including contour irregularities (white arrowheads). D. Volume-rendered image from the CTA of patient 12 demonstrates the patient-specific shape of the landing zone for valve deployment, which is reproduced in the 3D printed model (E).

Figure 2. A simple light transmission test designed to predict PAR

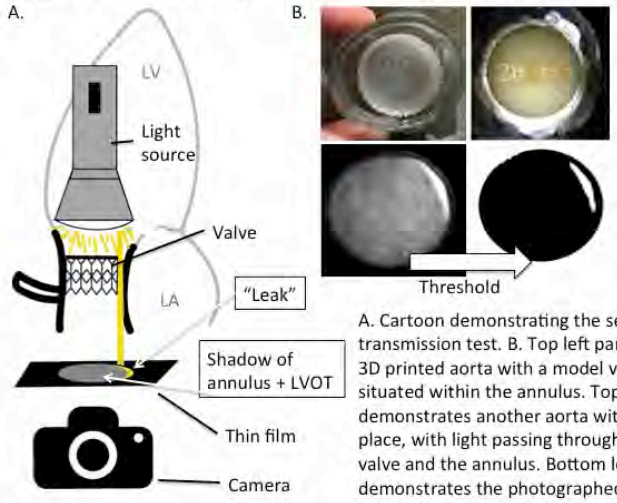

A. Cartoon demonstrating the set up for the light transmission test. B. Top left panel demonstrates a 3D printed aorta with a model valve (29 mm) situated within the annulus. Top right panel demonstrates another aorta with a 26 mm valve in place, with light passing through gaps between the valve and the annulus. Bottom left panel demonstrates the photographed projection onto thin film. Bottom right panel demonstrates the thresholded result.

Results: 3D models correctly predicted PAR in 6 of 9 patients and correctly ruled out PAR in 5 of 7 patients (Figure 3). The 3 false negative patients and 2 false positive patients did not have obvious features that differentiated them from the correctly predicted cases.

Figure 3. Predicted vs. actual leaks

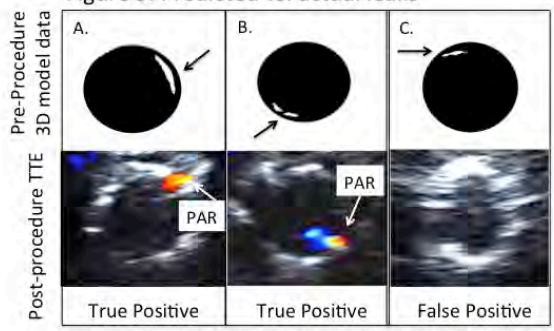

A. Upper panel demonstrates predicted PAR from the 3D model. Lower panel demonstrates the TTE data from the same patient, demonstrating actual PAR (white arrow). B. Example from another patient in which PAR was correctly predicted. C. Incorrectly predicted PAR from the 3D model (upper panel) in a patient without paravalvular regurgitation (false positive).

Conclusions: TAVR is revolutionizing the treatment of valvular disease. The technology is rapidly evolving, demanding novel approaches to optimize procedural planning while minimizing device-related complications. Patient-specific 3D printed models provide a feasible, noninvasive technique to aide visualization of patient specific variations in the AV complex, and present a novel opportunity to plan TAVR device placement *in situ*. Further work to improve predictive accuracy and determine feasibility of 3D printing from MRA data are ongoing.

MR Evaluation of the Cerebrovasculature in the Neonatal ICU

Beth M. Kline-Fath[1], Jean A. Tkach[2], Stephanie L. Merhar[3], Charles L. Dumoulin[2]

[1]Department of Radiology, Cincinnati Children's Hospital Medical Center, Cincinnati, OH, [2]Imaging Research Center, Department of Radiology, Cincinnati Children's Hospital Medical Center, Cincinnati, OH; [3]Division of Neonatology and Pulmonary Biology, Cincinnati Children's Hospital Medical Center, Cincinnati, OH;

Purpose: In order to mitigate the patient risks and logistical challenges associated with performing clinical MR exams of Neonatal Intensive Care Unit (NICU) patients, a small footprint 1.5T MR system designed specifically for the neonate, was developed and installed in the NICU at our institution. Since May 2012, the system has and continues to be used to perform clinical MR exams in the NICU patients. A number of the clinical brain exams have included time-of-flight (TOF) MR angiography sequences to evaluate the arterial and/or venous circulation in these infants. This purpose of this study was to review and document our experience with these MR flow techniques in our NICU population.

Methods: MR imaging was performed on a small footprint 1.5T MR system sized specifically for the neonate and installed in the Neonatal Intensive Care Unit (NICU) at our Institution (1, 2). The neonates were imaged free breathing and without sedation. The following time-of-flight (TOF) sequences were applied to obtain diagnostic information about the cerbrovasculature to help inform the clinical diagnosis and management of these NICU patients: 1) MR Arterial Circulation evaluation (MRA) - Axial 3D Multi Slab Flow Compensated Spoiled Gradient Echo (SPGR) TOF sequence (TR/TE/FA= 25msec/2.9-3.4msec/20°; FOV=13-16cm, matrix=224x32, Frequency direction =A/P, 75-100% Phase FOV, receiver bandwidth (RBW)= 31.25kHz, 3 slabs 22 partitions each with 6 partition overlap, acquired sequentially superior to inferior, partition thickness = 1.4mm, , 1 superior saturation pulse to suppress venous flow, 1 average; 17 exams), 2) MR evaluation of the Venous Circulation (MRV) – Coronal 2D Flow compensated 2D Spoiled Gradient Echo (SPGR) sequence (TR/TE /FA=40msec/6.9/45°; FOV=13-18cm, matrix =128x256; Frequency direction = S/I, 75-100% Phase FOV, 66 (or number varied as needed) - 1.4mm slices acquired sequentially posterior to anterior, 1 inferior saturation pulse to suppress arterial flow, 1 average; 23 exams. Maximum Intensity Projection (MIP) images along the S/I and R/L directions were generated from each 3D MRA and 2D MRV data set.

Results: A total of 294 MR brain exams were performed from May 2012 to July of 2015. In this cohort, 27 exams (9%) in 24 neonates were performed with MR flow related sequences. The flow related sequences included 17 MRA studies (Figure a) and 23 MRV (Figure b) exams. In 12 of these neonates, both MRA and MRV were performed with the most common indication being the presence of a hemorrhagic infarct. In one of these studies, transverse sinus thrombosis was identified. In four exams, the presence of large intraventricular hemorrhage and/or extraaxial hemorrhage instigated obtaining flow related sequences. In one of the four, a sagittal sinus thrombosis was defined. Three infants showed evidence for intracranial ischemia, for which MRA imaging was obtained. One demonstrated abnormal flow in the middle cerebral artery. A single infant had an arteriovenous fistula (Figure c), and three studies were performed with both MRA and MRV sequences confirming this entity. Two infants with underlying anomalies, including septo-optic dysplasia and agenesis of the corpus callosum, were found to have an arterial anomaly and venous thrombosis.

Representative MIP images generated from neonatal MRA (a) with carotid narrowing and MRV (b) showing venous thrombosis. An arteriovenous fistula was well visualized in the MRA exam performed in one of the infants (c).

Conclusions: Non-contrast 3D and 2D TOF techniques are a viable means of obtaining detailed images of the cerebrovasculature in the neonate utilizing a small foot print NICU MRI system. The most common indication for MRA and MRV is hemorrhagic infarction, though the sequence is important in infants with ischemia and vascular malformations, sometimes in association with a congenital anomaly.

References: 1. JA Tkach, et al., Pediatr Radiol 42:1347-1356 (2012)., 2. JA Tkach, et al., Amer J Roentgen 202:W95-W105 (2014).

Ferumoxytol across the Age Spectrum: a Single Center Experience of Safety

[1]Kim-Lien Nguyen, MD, [1]Takegawa Yoshida, [2]Ihab Ayad, MD, [3]Brian L. Reemtsen, MD, [4]Gary M. Satou, MD, [1]Peng Hu, PhD, [5]Isidro Salusky, [1]J. Paul Finn, MD

[1]Department of Radiological Sciences, [2]Department of Anesthesiology, [3]Department of Cardiothoracic Surgery, [4]Department of Pediatric Cardiology, [5]Division of Pediatric Nephrology, David Geffen School of Medicine at University of California, Los Angeles

Purpose: To review the frequency, type and severity of adverse reactions to ferumoxytol as an MRI contrast agent over a broad spectrum of ages and indications in a single center study.

Methods: Following informed consent and with approval from our IRB, we performed ferumoxytol enhanced MRA (FEMRA) for the assessment of pathologic arterial and /or venous anatomy in 149 patients (age 36 ± 28 years, range 3 days to 94 years, 38% female). Both bolus and slow infusions were given (total dose of 4 mg /kg, 166 injections). Sixty-two patients were examined under general anesthesia; three had pacemakers and six were pregnant. First pass and steady state FEMRA were performed in 119 patients and 30 patients had only steady state imaging. Continuous monitoring of ECG, pulse oximetry, and non-invasive blood pressure was performed in all patients and the electronic medical records were reviewed to assess for follow up events.

Results: In all cases, patients remained stable throughout the FEMRA studies and there were no serious adverse events. In two patients, systolic blood pressure (SBP) transiently decreased by 10-15 mmHg and in 22 patients SBP increased by 10-15 mmHg. In eight patients with congenital heart disease, blood oxygenation decreased by 1-5% during the MRI study. Three patients developed nausea following injection of ferumoxytol but in all cases the studies were completed successfully.

Conclusion: In our single center experience to date, there were no serious adverse events with the use of ferumoxytol for MRI, whether injected as a bolus or infused slowly. Although encouraging, many more patient studies from multiple centers will be needed to accurately establish the safety and adverse event rate with ferumoxytol as an MRI contrast agent.

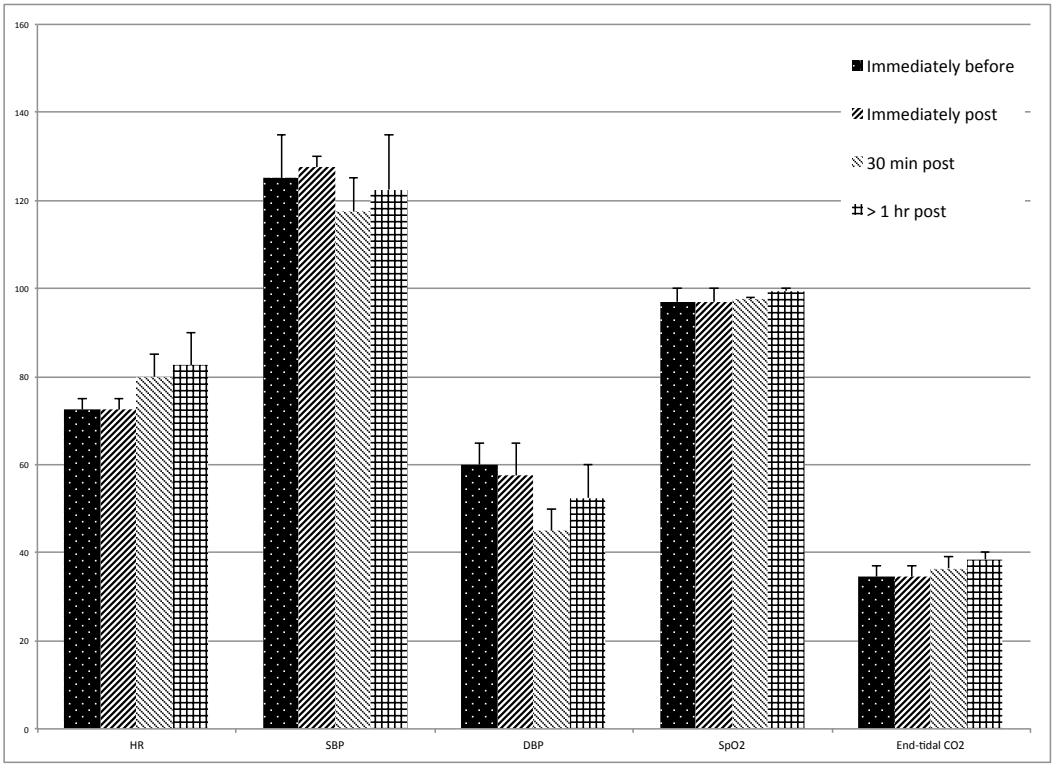

Figure 1. Patients with continuous monitoring under anesthesia. Heart rate (HR), systolic (S) and diastolic (D) blood pressure (BP), pulse oximetry, and end-tidal CO_2 immediately before ferumoxytol injection, immediately post, 30 minutes post, and >1 hour post injection. Units are: DBP=mmHg; End-tidal CO_2=mmHg, HR=beats per min, spO_2=%

Black-Blood Late Gadolinium-Enhancement MR Imaging of Myocardium

Gregory J. Wilson[1], Dongxiang Xu[1], Niranjan Balu[1], Jinnan Wang[1,2], Chun Yuan[1], Jeffrey H. Maki[1]
[1]University of Washington, Department of Radiology, Seattle, WA, USA.
[2]Bayer Healthcare, Whippany, NJ, USA.

Introduction: Cardiac late gadolinium-enhancement (LGE) MR is an important clinical tool for evaluating myocardial infarction and infiltrative cardiomyopathies. Traditionally, LGE-MR is performed 10-20 minutes after administration of gadolinium contrast using a 2D inversion recovery turbo gradient echo sequence with appropriate inversion time to null normal myocardium and highlight scar. Unfortunately, the blood pool also appears bright on LGE, particularly when using phase sensitive IR (PSIR) techniques where TR is doubled. This can decrease scar conspicuity, particularly for subendocardial lesions bordering the blood pool. Our goal was to develop a black-blood method for 3D late gadolinium-enhancement (LGE) myocardial MR imaging that preserves myocardial image quality and improves the depiction of subendocardial scar.

Methods: Second-moment motion-sensitized driven equilibrium (m2MSDE) was implemented as a black-blood prepulse (~20 ms duration) to the standard inversion-recovery 3D or 2D gradient-echo LGE imaging sequence (Fig. 1) on a Philips 3T Ingenia unit. The pre-pulse utilized a motion-sensitized gradient scheme to null the first gradient moment, thus reducing sensitivity to bulk motion and improving myocardial image quality compared to standard MSDE. While bulk motion (1st order motion) was unaffected, intraventricular blood was nulled by 2nd or higher order motion sensitization during the m2MSDE prepulse.

With IRB approval, m2MSDE LGE has thus far been applied to 2 volunteers (no Gd) and 7 patients undergoing conventional LGE in order to begin parameter optimization and evaluate efficacy. After further optimization, a 60 patient study is planned to compare 3D m2MSDE LGE with conventional 2D and 3D LGE.

Results: Using a LGE sequence without contrast agent, good blood suppression can be obtained with m2MSDE (Fig. 2). Keeping shot duration ("T1-TFE" block in Fig. 1) short and properly timing readout wrt the cardiac cycle is required to achieve good blood suppression without motion artifacts. Our data suggested that keeping total shot duration less than 50ms is necessary post-contrast, as the short $T1_{blood}$ leads to rapid recovery of the blood pool (Fig. 3). Low-high k-space acquisition is requisite.

Discussion: Other studies demonstrate MSDE can suppress enhanced flowing blood in the arteries (1), but standard MSDE is not applicable for cardiac imaging. Our early evaluation demonstrates m2MSDE can suppress gadolinium-enhanced blood in the heart with low-high k-space acquisition with minimal startup echoes and short shot durations. Further optimization through k-space acquisition strategy/duration is being evaluated for 3D m2MSDE IR-TFE, and this technique is being merged with 3D RAPID (2) for PSIR reconstruction. Optimal parameters are being investigated and will be reported along with ongoing clinical results.

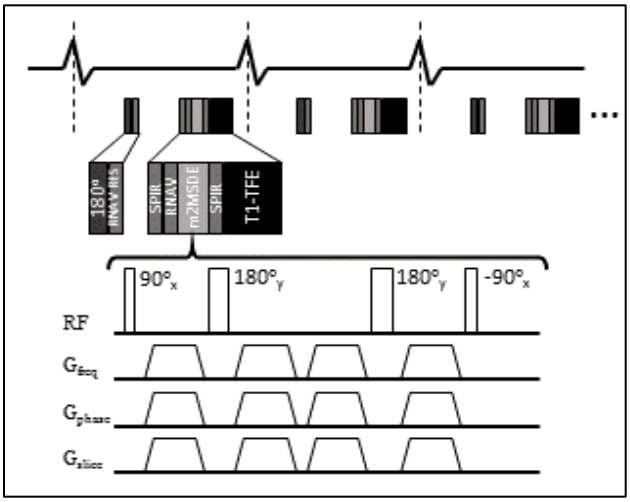

Figure 1. Schematic of segmented IR-TFE sequence with m2MSDE prepulse.

References:

1) Wang et al. *J Magn Reson Imaging* (2010) May;31(5):1256–1263.
2) Wang et al. *Magn Reson Med* (2014) Sep;72(3):806-15.

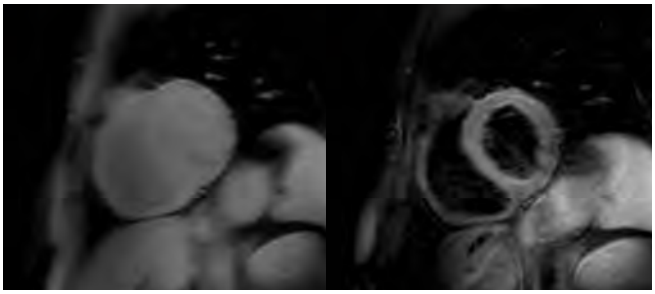

Figure 2. Non-contrast 2D IR-TFE without (l) and with (r) m2MSDE (same TI). Good blood suppression, minimal artifact.

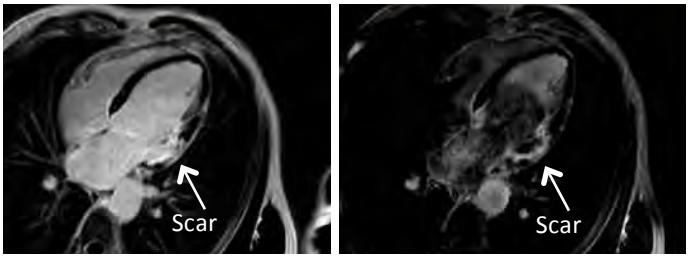

Figure 3. Focal lateral basal infarct. 20 min post Gd with standard 2D LGE (l) and m2MSDE LGE (r). Note partial blood pool suppression and improved contrast of myocardial scar.

Assessment of tortuosity & flow in abdominal aortic aneurysms with ferumoxytol-enhanced MRI

Faraji F [1,2], Seguro F [1,2,3], Haraldsson H [1,2], Saloner D [1,2], Hope MD [1,2]
[1] SF Veterans Affairs Medical Center, [2] UCSF Department of Radiology, [3] Federation Française de Cardiologie

PURPOSE Risk assessment and intervention thresholds for abdominal aortic aneurysms (AAAs) are based on maximal vessel diameter. However, research suggests that other variables including hemodynamics may better inform management decisions regarding aortic disease.[1] 4-dimensional flow fields can be measured in vivo with MRI, and may be useful for understanding the progression of AAA disease and intraluminal thrombus formation. Studies have demonstrated that the aberrant flow that may be implicated in this progression occurs in tortuous vessels.[2,3] We seek to investigate the relationship between vessel tortuosity and abnormal flow in patients with AAAs.

METHODS 13 patients with AAAs (> 3cm) were studied with the following MRI protocol: 3D ferumoxytol-enhanced MR angiography to capture the aortic geometry, and 3D-CINE phase-contrast (4D-flow) imaging to assess the velocity fields in the abdominal aorta. Data analysis was conducted using in-house developed Matlab tools. Vessel tortuosity and hemodynamic patterns were evaluated 1) qualitatively by two independent observers and 2) using the simple quantitative measures described below. Quantitative Tortuosity Index was defined as the distance along an aortic centerline from the level of the renal arteries to the aortic bifurcation, divided by the shortest distance between these two points (**Figure 1a**). Tortuosity was qualitatively scored based on the maximum angulation of the aorta between the renal arteries and iliac bifurcation (mild: 0-30°, moderate: 30-60°, severe: 60-90°). Flow visualization and analysis was performed at peak systole with EnSight, and included qualitative assessment of persistent slow flow, flow reversal, and vortical flow (**Figure 1b**). Quantitative flow measures included calculation of slow flow as the percentage of voxels within the AAA volume having a velocity magnitude lower than 5, 10, & 20% of the maximal systolic velocity, and flow reversal was defined as the percent of voxels within the aneurysm having a negative velocity.

RESULTS Average AAA diameter was 4.5cm. The inter-observer agreement for qualitative measures using Bland-Altman was good with a bias = -0.06 +/- 0.57 and the 95% limits of agreement contained 100% of the difference scores. Strong agreement between qualitative and quantitative measures of vessel tortuosity was found (r=0.82). The average quantitative Tortuosity Index was measured to be 1.12 +/- 0.07. The only flow variable to exhibit a significant correlation with vessel tortuosity was flow reversal: a positive correlation (r=0.72) between Tortuosity Index and flow reversal was demonstrated (**Figure 2**). Of the various flow measures studied, only flow reversal showed a significant relationship with vessel tortuosity.

CONCLUSION We show good agreement between our qualitative and simple quantitative measures of aortic tortuosity and systolic flow patterns. This is a simple and semi-automated metric that may prove to be helpful in characterizing aortic geometric factors beyond diameter for the risk stratification of AAA disease. This type of simple analysis may help to better understand the relationship between 3D aortic geometry and abnormal flow that may drive thrombus formation and AAA disease progression.

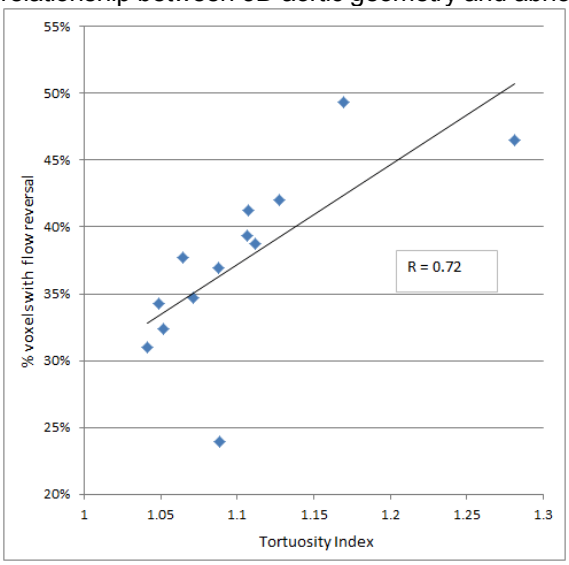

Figure 2: Correlation between flow reversal & Tortuosity Index

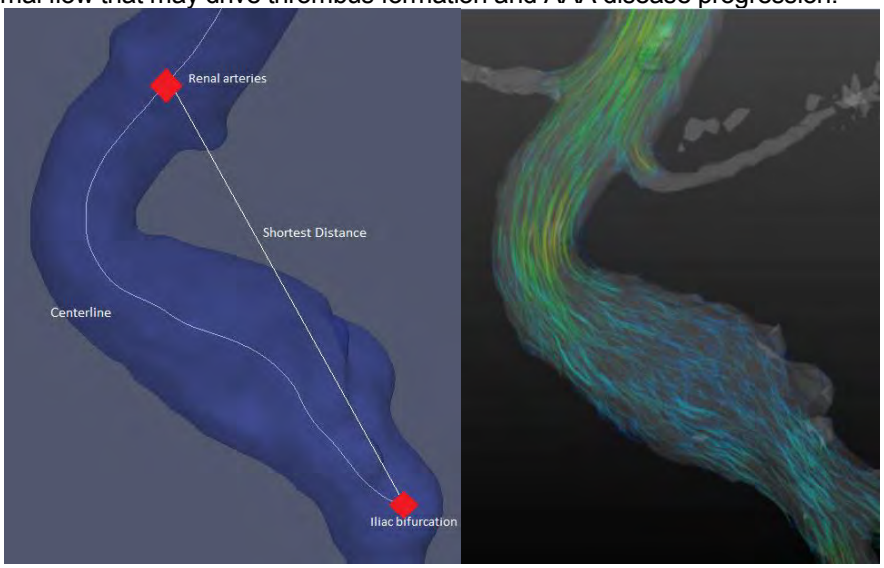

Figure 1: **A**: simple assessment of tortuosity using centerline **B**: Example of particle traces generated from AAA 4D flow data demonstrating slow flow in the belly of the aneurysm.

REFERENCES

1. Hope MD, Hope TA. Curr Opin Cardiol. 2013 Nov;28(6):609-18.
2. Xie X, Wang Y, Zhou H. J Biomech. 2013 Jul 26;46(11):1833-41.
3. Arzani A et al. Am J Physiol Heart Circ Physiol. 2014 Dec 15;307(12):H1786-95.

Signal intensity measurement of the liver vessels in patients suffering from liver lesions with Gd-Eob-DTPA and Gd-BOPTA enhanced MRA/ MRV

Background: The goal of this study was to determine as to whether Multihance® or Primovist® is superior in differentiating liver vessels from surrounding parenchyma.

Material and Methods: After determining and applying the proper selection criteria 10 patients who were injected with either Multihance® or Primovist® for evaluation of at least one liver lesion were splint into 2 groups corresponding with the contrast agent. Group 1 consisted of patients injected with Primovist®, whilst group 2 consisted of patients who received Multihance®. Signal intensity measurement was performed in proximal segments of the vessels. For the comparison of the results in both groups, the signal intensity ratio between the vessel and the surrounding parenchyma was established.

Results: Signal intensity of the vessels was higher in patients who were injected with Primovist® rather than Multihance®. Due to the high signal enhancement of the liver in group P the ratio is shifted in favour of group M.

Conclusion: Multihance® seems to be favourable for differentiating liver vessels. 3 D recon was only possible with the sequences used with Multihance® (Fig.3) and was helpful in diagnosis

Fig.1: Primovist®

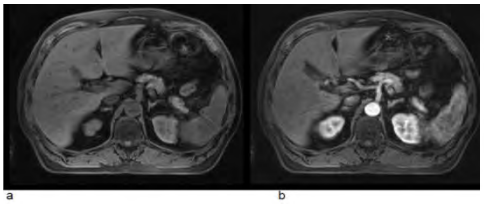

Fig.2: Multihance®

a:nativ b:arterial c:portalvenous,d:equilibrium

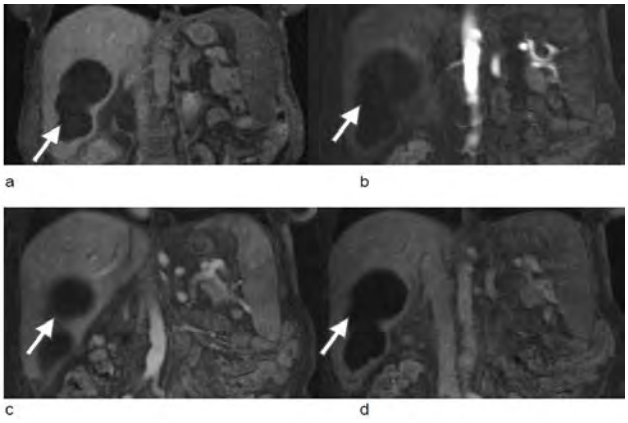

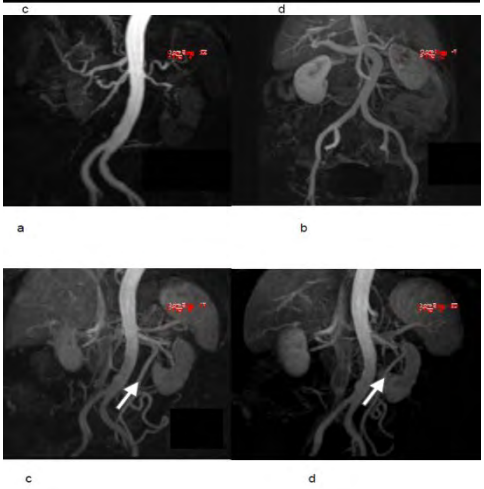

Fig.3:3D recon Multihance®: abnormalities: insufficiency of left testicular vein, right side double renal vein

Title: **Diffuse myocardial fibrosis in diabetes mellitus type-II (DM-II) assessed by Cardiac Magnetic Resonance T1 mapping technique: preliminary results.**

Authors: F. Ciolina, N. Galea, A. Fiorelli, R. Pofi, T. Feola, M. Francone, C. Catalano, **I. Carbone**.
Institution: Department of Radiological Sciences, Oncology and Pathology Sapienza University of Rome, Italy

Purpose

Diabetic cardiomyopathy (DCM) consists in progressive impairment of ventricular contraction eventually leading to heart failure, independently of ischemic heart disease or hypertension. Early stages of DCM are asymptomatic and characterized by various degree of myocardial fibrosis. Our aim was to detect myocardial fibrotic infiltration in DM-II patients by using T1-mapping technique.

Methods & Materials

Thirty-one diabetic patients (24 men;age 63yrs) with preserved ventricular function and no history of ischemic cardiopathy and 20 controls underwent to CMR. Imaging protocol included: modified Look-Locker sequence before and 20 minutes after 0.2 mmol/kg gadoterate meglumine injection; T2 mapping; ventricular function module; conventional T2-weighted and late gadolinium enhanced (LGE) imaging. Native T1 (nT1), T2 and extracellular volume fraction (ECV) values were calculated and correlated to glycated haemoglobin (HbA1c) and duration of disease. Pearson Correlation, Mann-Whitney test and unpaired T-test were used for statistical analysis.

Results

Patient group had higher nT1 and ECV values compared to controls (1035±94ms vs. 975±38ms, 28.2±3.3%vs.24.8±4.3% respectively, $p<0.05$ for both), whereas no significant differences occurred in T2 measurements (45.8±2.4ms vs. 47.0±2.8ms respectively, p: 0.23).
nT1 and ECV showed direct correlations with HbA1c (nT1:r^2=0.98, $p<.0001$; ECV:r^2=0.95, $p<.0001$) and disease duration (nT1:r^2=0,98 $p<.0001$; ECV:r^2=0.55, $p<.0001$) in diabetic patients. An inverse correlation was found between T2 and HbA1c (r=-0,46; p=0,009).
Areas of ischemic LGE were found in two patients as marker of silent infarction.

Conclusion

Diabetic patients with preserved ventricular function have increased nT1 and ECV as reflection of silent diffuse myocardial fibrosis, which degree correlates with HbA1c and disease duration.

References:

1. Giannetta E, Isidori AM, Galea N, Carbone I, Mandosi E, Vizza CD, Naro F, Morano S, Fedele F, Lenzi A: **Chronic Inhibition of cGMP phosphodiesterase 5A improves diabetic cardiomyopathy: a randomized, controlled clinical trial using magnetic resonance imaging with myocardial tagging**. *Circulation* 2012, **125**(19):2323-2333.
2. Ng AC, Auger D, Delgado V, van Elderen SG, Bertini M, Siebelink HM, van der Geest RJ, Bonetti C, van der Velde ET, de Roos A *et al*: **Association between diffuse myocardial fibrosis by cardiac magnetic resonance contrast-enhanced T(1) mapping and subclinical myocardial dysfunction in diabetic patients: a pilot study**. *Circulation Cardiovascular imaging* 2012, **5**(1):51-59.

Application of Full Turbulent Tensor in Estimation of MR-Based Relative Pressure

Sarah Kefayati[1], Henrik Haraldsson[1], Petter Dyverfeldt[2], Belén Casas Garcia[2], Jonas Lantz[2], Tino Ebbers[2], and David Saloner[1]
[1] University of California, San Francisco, United States, [2] Linköping University, Sweden

Introduction: Estimation of relative pressures has been enabled by recent advances in Magnetic Resonance (MR) velocimetry, which allow 3-component velocity-vector fields to be measured in space and time. However, in turbulent flow significant errors occur if the pressure equations are solved with the assumption of laminar flow and neglecting turbulent components, namely Reynolds normal and shear stresses. Turbulent flow can be present in the vasculature where there is abnormal lumen narrowing and results in energy dissipation and unrecoverable pressure loss. This study investigates the importance of including turbulent terms in calculating pressure in comparison with laminar flow assumption. The current technique of MR-based turbulence quantification [1] is limited to only three Reynolds normal stresses. Recently, some studies have focused on obtaining not only normal stresses but also Reynolds shear stresses [2]. This study employs one of the recently proposed MR-based methods of quantifying the full turbulence tensor – including three Reynolds shear stresses – to obtain all the six components required to solve the partial pressure equation.

Methods: For this study, pressure quantifications were performed based on three different methods: MR-simulated flow, MR-measured flow, and pressure catheter measurement. A steady inlet flow condition of ~ 4000 Reynolds number was applied in a tube with a 75% stenosis (by area). For both MR-simulated and MR-measured results, six flow-encoding directions based on the ICOSA6 encoding scheme [3] were performed. The signal drop due to turbulence in the six flow encoded directions enabled estimation of variance and covariance components of velocities (turbulence tensor).

For MR simulation, the Navier-Stokes equations were solved (ANSYS CFX 14.5) followed by resolving turbulent flow fluctuations using a Large Eddy Simulation (LES)[4] which was then used to derive phase-contract MRI (PC-MRI) simulations by re-gridding to 1.5-mm isotropic voxels. For MR measurements, PC-MRI with ICOSA6 velocity encoding was acquired with a flow rate of 50 ml/s. FOV = 384×120×40 with 1mm isotropic resolution. TR/TE = 7.1/4.3.ms. VENC = 1 m/s. Pressure was measured directly using Millar 5F pressure catheter which was inserted in the tube from the outlet towards the inlet and was displaced longitudinally to measure multiple points. Pressure gradients of Navier-Stokes equations were first derived employing only mean velocities and then by also including Reynolds stresses (blue-colored terms of equation).

Results: In the commonly used MR-based methods of pressure estimation, only the three components of velocity are applied. However, as shown in Figure 1, effect of turbulence is highly notable in six covariance components. Figure 2 shows the effect of including the Reynolds turbulent terms for MR-simulated (a) and MR-measured (b) estimation, which results in detecting the lower pressure recovery compared to the laminar case. In the MR-simulated case, the turbulent pressure recovery level is about the same as the recovery for CFD results (35%). For validation, MR-based pressure was then compared to catheter-based measurements shown in Figure 2c. Results from both methods show excellent agreement in relative pressure, which recovers to 49% after the drop.

Conclusion: Our finding shows that including the turbulent terms in the computation of the pressure gradients from Navier-Stokes equation results in notable change in pressure recovery estimations. Good agreement was found when MR-based result was compared with catheter pressure measurement, which is the common clinical method. The goal is to enable accurate relative pressure measurement that can replace the invasive catheterization.

References: [1] Dyverfeldt et al., Magn Reson Med (2006), [2] Elkins et al., Exp Fluids (2009), [3] Zwart and Pipe, Magn Reson Med (2013), [4] Ebbers and Farnebäck, Magn Reson Med (2009).

$$\frac{\partial \overline{P}}{\partial x_i} = -\rho\left(\overline{v}_1\frac{\partial \overline{v}_i}{\partial x_1} + \overline{v}_2\frac{\partial \overline{v}_i}{\partial x_2} + \overline{v}_3\frac{\partial \overline{v}_i}{\partial x_3} + \frac{\partial \overline{v'_1 v'_i}}{\partial x_1} + \frac{\partial \overline{v'_2 v'_i}}{\partial x_2} + \frac{\partial \overline{v'_3 v'_i}}{\partial x_3}\right) + \mu\left(\frac{\partial^2 \overline{v}_i}{\partial x_1^2} + \frac{\partial^2 \overline{v}_i}{\partial x_2^2} + \frac{\partial^2 \overline{v}_i}{\partial x_3^2}\right), \quad i = 1,2,3$$

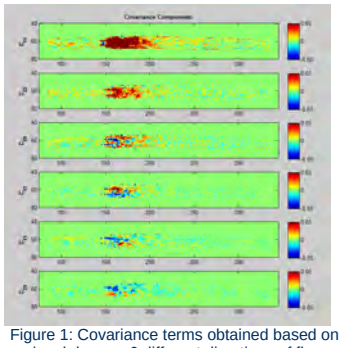

Figure 1: Covariance terms obtained based on signal drop on 6 different directions of flow encoding.

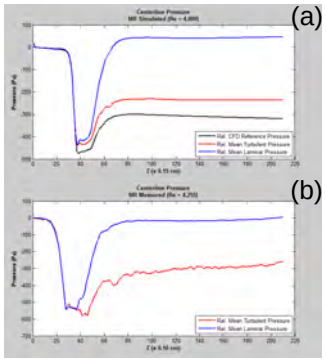

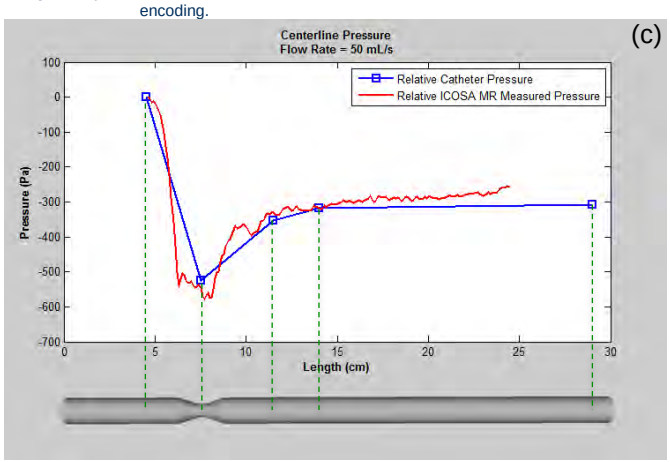

Figure 2: Relative pressure measurement using (a) MR-simulated and (b) MR measured velocities. (c) Comparison of relative pressure based on MR and catheter measurements.

Feasibility of time-of-flight MR angiography in human pregnancy for imaging the fetal and placental vasculature

Jaladhar Neelavalli[1,2], Uday Krishnamurthy[1,2], Ehsan Hamtaei[1], Pavan K. Jella[1], Brijesh K. Yadav[1,2], Swati Mody[1], Edgar Hernandez-Andrade[3,4], Lami Yeo[3,4], Maria D. Cabrera[1], Ewart M. Haacke[1,2], Sonia S. Hassan[3,4], Roberto Romero[3]
[1]Department of Radiology, [2]Department of Biomedical Engineering, [4]Department of Obstetrics and Gynecology, Wayne State University, Detroit, Michigan, USA. [3]Perinatology Research Branch, NICHD/NIH/DHHS, Bethesda, Maryland, and Detroit, Michigan, USA

Objectives: Proper development of fetal and placental vasculature is crucial for healthy fetal growth. Doppler Ultrasound (US) is the standard clinical tool used today for evaluating utero-placental and fetal vasculature and hemodynamics. On the other hand, advantages of magnetic resonance imaging (MRI) over US, which include large field of view imaging, high resolution, better soft tissue contrast and operator dependence [1,2], make it an attractive alternative. Angiographic imaging in pregnancy could help in studying normal versus abnormal development of the human fetal and placental vasculature. Furthermore, to take advantage of advanced MR imaging techniques like arterial spin labeling, phase contrast imaging and MR blood oxymetry [3] which can help quantitatively characterize fetal and placental health, it is important to localize relevant afferent and efferent vessels of the organ of interest. Thus MRA of the fetal and utero-placental circulation could play an important role in obstetrical research. Use of exogenous contrast agents is contraindicated during pregnancy. Hence we evaluated the feasibility of obtaining good quality time-of-flight based non-contrast MRA data during pregnancy that allowed for 3D visualization of the utero-placental and fetal vasculature. In addition the potential utility of 2D compressed sense (CS) sampling [4] in speeding up data acquisition was also evaluated through simulations.

Methods: MR imaging was performed on a 3.0T Siemens Verio scanner under normal breathing conditions with no maternal sedation. The standard multislice 2D time of flight MRA sequence used in adults was adapted to fetal imaging. The following aspects were considered while modifying the sequence: (a) specific absorption rate (SAR), (b) flow velocities in the vessels (c) vessel diameter and, (d) scan time. As in any fetal imaging sequence, fast data acquisition is important in avoiding fetal motion. The resultant sequence acquired a single slice of MRA data in approximately every 4 seconds with a reconstructed voxel size of 0.4-0.7 mm in-plane and 2mm through plane. Imaging parameters were: TE-4.92ms; TR – 22ms and FA - 50^0 with a parallel imaging factor of 2 along the phase encoding direction. Fetal and placental vessels were visualized by creating maximum intensity projections (MIPs) and/or 3D reconstructions. The sequence was applied in third trimester fetuses and results from 7 different subjects (gestational age range: 29 to 39 weeks) are presented. For simulating a 2D CS sampling scheme, we created a mask with only 30% of total number of phase encoding lines (128 lines), with variable density distribution in kspace [5]. This is equivalent to 3.3 times faster than full k-space acquisition or factor 1.5 when we consider parallel imaging. The mask was then applied on individual 2D kspace of the slices and input into a CS reconstruction algorithm we developed in MATLAB [5]. We then compared the CS reconstruction with the original fully sampled images by visually comparing the individual 2D slices.

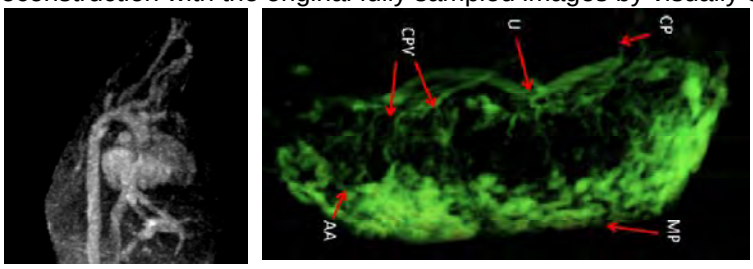

Figure 1: Maximum Intensity Projection of a fetal heart along with the great vessels; GA-37 weeks. *Figure 2*: MRA of placental vasculature - 3D rendering: Vessels on the maternal side (MP) and chorionic side of the placenta (CP) are clearly seen, while umbilical (U) cord, chorionic plate vessels (CPV) and arcuate arteries (AA) are also visible. GA-29 weeks.

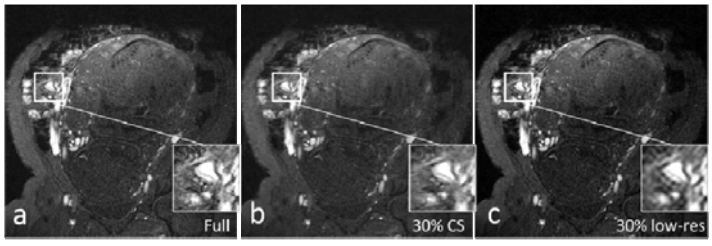

Figure 3:. Comparison of the umbilical cord cross section (a) fully sampled, (b) 30% CS and (c) 30% low-resolution reconstructions (zero filled). The 30% CS is able to resolve more details in the image compared to 30% low-resolution, although the acquisition time is the same for both.GA-37 weeks.

Results: Placental vessels on the chorionic surface merging to form the umbilical vessels were clearly visualized. Vessels on the maternal surface of the placenta were also seen. When MRA was acquired covering the entire abdomen of the mother, blood supply of the uterine tissue along with the uterine artery were visualized. In the fetus, the heart, the inferior venacava, the aortic arch, the carotid arteries and the jugular veins were also seen. SAR in all cases was <0.6 Watt/kg. Simulated CS reconstructions provided good quality images without significant artifacts even with 30% data.

Conclusion: It is possible to obtain good quality angiographic images of the fetal and placental vasculature using an optimized, off the shelf 2D time-of-flight based MRA sequence. Compressed sense sampling has a role to play in feto-placental MRA in further speeding up data acquisition without much loss in image quality.

References: [1]Levine, D. Top Magn Reson Imaging (2001) [2]Andescavage, N, et al. Sem in Perinatalogy (2015). [3]Neelavalli, J, et al. JMRI;39;4 (2014): 998-1006. [4]Lustig et.al., MRM, 2007. 58: p. 1182–1195. [4]Hamtaei et.al., CS and joint imaging in MRI. MS thesis 2013, dept. of BME, Wayne State University.

A 9 Channel Carotid Coil Designed for Integration with Clinical Head Coils

Michael Beck[1], Dennis L. Parker[1], Bradley D. Bolster[3], Seong-Eun Kim[1], Scott McNally[2], Gerald S. Treiman[1,4], and J. Rock Hadley[1]

[1]Utah Center for Advanced Imaging Research, [2]University of Utah Department of Surgery, [3]Siemens Healthcare, [4]Department of Veterans Affairs (VASLCHCS)

Purpose: High Resolution Magnetic Resonance Imaging (MRI) of the human carotid arteries is difficult to achieve due to the complex and varied geometries of the head and neck anatomy. Many coils have been designed specifically for imaging the carotid bifurcation (1-5), yet use of these coils has not found its way into mainstream clinical imaging. Coils used in standard clinical imaging are typically designed to accommodate the full range of patient sizes at the expense of Signal-to-Noise Ratio (SNR) (Fig 1). In order to achieve quality clinical carotid imaging, the coil elements should be designed to fit in close proximity to the human anatomy, be robust and consistently provide quality images. It should also accommodate imaging of the carotid bifurcation regardless of its varied position and should be integrated with a custom head array or with existing commercial head coils for extended carotid imaging. In this work we have developed a robust, high sensitivity carotid coil with the potential to be integrated with commercial head coils that could provide repeatable high quality MRA of the carotid from the aortic arch to the circle of Willis.

Methods: The carotid coil designed in this work was constructed on a slightly flexible thermoplastic former that fits close to and covers the surface of the anterior half of a human neck (Fig 1). It was designed to fit against the neck in conjunction with an existing commercial head coil (Fig 1, neck coil also shown). In order to make the coil robust, it was designed using a ladder array configuration. Copper traces (7 mm wide) were made from copper clad Kapton substrate (polyimide film – Dupont) and were soldered to fiberglass circuit boards at fixed locations in the array. The circuit boards were glued to the thermoplastic former and provided copper trace junctions and capacitor gaps in the array. Electromagnetic simulations showed that, for a 15 cm diameter neck, 9 channels provided the best signal sensitivity at the depth of the carotids. The coil elements in the array were approximately 2.5–3 cm wide and varied 12 to 6 cm in height, covering a large range of possible bifurcation locations. Each element was attached to a preamp via 60 cm RG316 cables of which approximately 20 cm was used to form a solenoid cable trap at the center of the cable. Electrically shortened bazooka baluns were also used between the solenoid trap and coil elements to further reduce unwanted common mode currents on the cables. Each channel was actively and passively decoupled (>40dB isolation) and isolation between elements of the array was achieved with capacitive decoupling in the common leg between elements. Maximum correlation between elements in a correlation plot was less than 0.4.

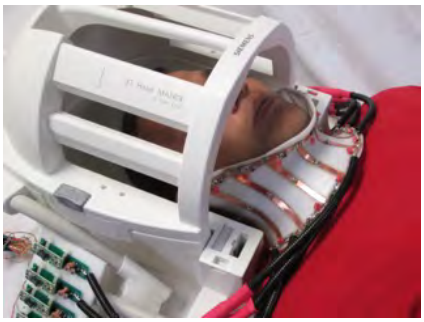

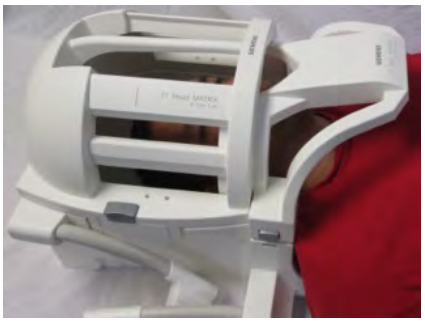

Figure 1: The 9ch carotid coil with Siemens 3T Trio commercial head array (left) and the commercial 16ch head/neck array.

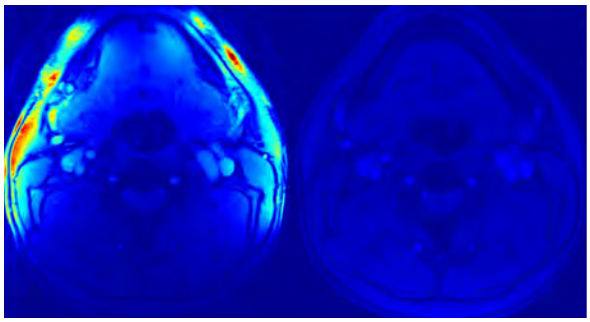

Figure 2: SNR plots for the 9ch (left) and 16ch (right) coils.

Results: Figure 2 shows SNR results using the 9 channel carotid array and the Siemens 3T Trio commercial head/neck array. The 9ch carotid array provided approximately 3 times more SNR at the bifurcation than the commercial coil for this volunteer. The 9ch coil integrates geometrically with the head/neck coils of the Siemens 3T Trio and Skyra clinical scanners, providing the future capability to scan simultaneously with these coils. Future work will include final integration and testing of the 9ch carotid array in conjunction with the Siemens commercial coils. Finally, The 9ch coil may provide additional clinical use by improving SNR in other anterior neck anatomy.

Conclusion: We have presented a 9 channel carotid coil design that provides significantly higher SNR than the standard Siemens 3T Trio commercial head/neck coils at the location of the carotid bifurcation (factor of 3). The 9ch coil is designed to integrate with commercial head coils providing greater coil sensitivity in the carotid bifurcation and extending total coverage of carotid imaging towards the aortic arch.

References: 1. Hadley et al. Relative RF coil performance in carotid imaging. Magn Reson Imaging 2005;23:629-639. 2. Hayes et al. Surface coil phased arrays for high-resolution imaging of the carotid arteries. J Magn Reson Imaigng 1996;6:109-112. 3. Liffers et al. Geometrical optimization of a phased array coil for high-resolution MR imaging of the carotid arteries. Magn Reson Med 2003;50:439-443. 4. Balu et al. Improvements in carotid plaque imaging using a new eight-element phased array coil at 3T. 2009;30:1209-1214. 5. Tate et al. Increased vessel depiction of the carotid bifurcation with a specialized 16-channel phased array coil at 3T. Magn Reson Med 2013;69:1486-1493.

Ferumoxytol MRA and Non-Contrast CT Fusion in TAVR Candidates with Renal Failure

[1]Takegawa Yoshida, [1]Fei Han, [1]Ziwu Zhou, [2]Olcay Aksoy, [2]William Suh, [1]Peng Hu, [1]Paul Finn.

UCLA [1]Radiological Sciences and [2]Division of Cardiology.

Introduction: One of the advantages of CTA over MRA for TAVR planning is the ability to define aortic valve and arterial calcification which may influence procedure planning. However, although patients who are TAVR candidates are in general at low risk for radiation exposure, frequent renal impairment greatly increases the risk from iodinated contrast media. Further, in patients with severe renal impairment, gadolinium based agents may be problematic because of the perceived risk of NSF. Non contrast CT is a simple and frequently performed test and can be easily incorporated into the diagnostic workup. We hypothesized that in patients where ferumoxytol is a suitable alternative to CTA, vascular and valvular calcification may be accurately displayed over luminal anatomy by fusing non-contrast CT and FEMRA in these patients.

Methods: Two patients who underwent ferumoxytol enhanced MRA (FEMRA) for assessment of arterial access anatomy prior to TAVR had additional non-contrast CT of the thorax and abdomen. CT and MR dicom data were processed in Mimics software V17.0 (Materialize) and the calcium from the CT was isolated and registered to the FEMRA data.

Results: In both cases, the calcification was fused successfully with the 3D FEMRA data and volume rendered images were generated showing the degree and distribution of calcification clearly (figure 1), forming the basis for more confident procedure planning.

Conclusion: By fusing non-contrast CT and FEMRA, both luminal anatomy and vascular calcification can be accurately defined, addressing one of the main limitations of MR over CT for TAVR planning.

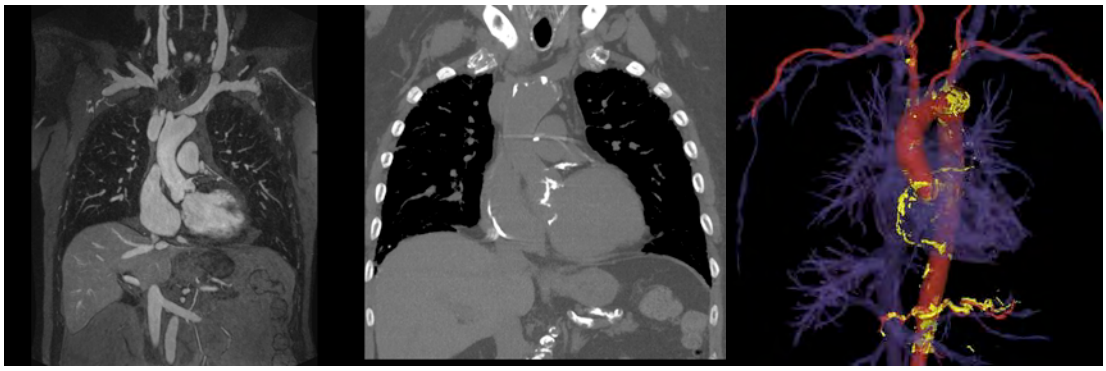

Figure 1. FEMRA (left), non-contrast CT (middle) and Volume rendered FEMRA with calcium overlay (right) in an 84 year old male patient with calcific aortic stenosis who had successful TAVR placement.

Estimating brain distensibility with quantitative magnetic resonance CSF flow measurements

Annamarie T Helpling[2], Christopher M Ireland[1,2], J. Matthew Lanier[2], Charles L Dumoulin[2]

[1]Department of Biomedical Engineering, University of Cincinnati, Cincinnati, Ohio, United States

[2]Imaging Research Center, Cincinnati Children's Hospital Medical Center, Cincinnati, Ohio, United States

PURPOSE: The brain's elasticity has rarely been measured although it contributes to the brain's mechanical response to trauma and hydrocephalus. Assuming the skull is rigid and fully encapsulates the brain, and the production of cerebrospinal fluid (CSF) is negligible over the course of a heartbeat, the volume of CSF displaced by brain expansion at systole is equivalent to the change in volume of the brain tissue from diastole to systole. We hypothesize that brain compliance can be measured using the following equation: $\Delta V/(V_0 \Delta P)$ where ΔV is the change in brain volume in response to increased blood pressure at systole, V_0 is the baseline volume of the brain at diastole, and ΔP is the change in blood pressure over the cardiac cycle.

METHODS: A flow phantom was constructed in an 1.5T Philips Ingenia™ MRI magnet to quantify fluid flow in a rigid pipe and validate using 2D Phase-Contrast Imaging in the formal experiment. Distensibility measurements were made in the brain of a healthy 59 year old male volunteer. 10 3D MRI anatomical images of the brain were acquired using a high-resolution imaging pulse sequence. Cardiac-gated 2D phase-contrast MRI velocity data of CSF through an axial slice at the mid C2 vertebra in the neck were then acquired 10 times. Systolic and diastolic blood pressure was measured 6 times in the left arm using an automated GE™ Dinamap Pro 300v2 BP Monitor.

RESULTS: For the phantom study the flow had a parabolic velocity profile across the diameter of the pipe consistent with laminar fluid.

In the formal experiment, the subject's change in blood pressure (ΔP) was 36.83±2.73 mmHg. volBrain™ segmentation software calculated a baseline brain volume (V_0) of 1263.61±3.15 ml. Post-processing software was used to find the flux of CSF around the area of the spinal cavity (Figure 1). Flux was then integrated to find the downward CSF volume at systole (ΔV) as 0.35±0.06 ml (Figure 2). The subject's brain distensibility calculated was $7.53*10^{-6} \pm 0.64*10^{-6}$ $mmHg^{-1}$.

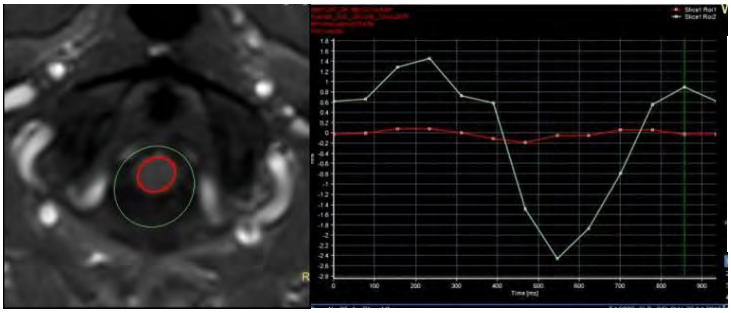

Figure 1 (Left): Spinal cord ROI (red) and CSF flow ROI (green)

Figure 2 (Right): Flux of spinal cord (red) and CSF (green)

CONCLUSION: This new approach to non-invasively quantifying brain distensibility may have significant utility for studying brain trauma, hydrocephalus, and physiologic changes in the brain associated with normal development and aging. Future studies will focus on comparing MRE and the technique proposed here to evaluate both non-invasive measurements for determining brain distensibility.

REFERENCES:
1. Dumoulin, C. L., D. J. Doorly, and C. G. Caro. "Quantitative Measurement of Velocity at Multiple Positions Using Comb Excitation and Fourier Velocity Encoding." Magn. Reson. Med. Magnetic Resonance in Medicine 29.1 (1993): 44-52. Web. 8 July 2015.
2. Elster, Allen D., MD. "Phase Contrast MRA." Questions and Answers in MRI. AD Elster, Elster LLC, 2014. Web. 16 July 2015.
3. Hill, Dr. Lisa, and Dr. Carl Gwinnut. "Cerebral Blood Flow and Intracranial Pressure." Cerebral Blood Flow and Intracranial Pressure (n.d.): n. pag. Web. 8 July 2015.
4. J. V. Manjón, P. Coupé. volBrain: An online MRI brain volumetry system, Organization for Human Brain Mapping 15, 2015.
5. Kruse, Scott A., Gregory H. Rose, Kevin J. Glaser, Armando Manduca, Joel P. Felmlee, Clifford R. Jack Jr., and Richard L. Ehman. "Magnetic Resonance Elastography of the Brain." NeuroImage 39 (2008): 231-37. National Center for Biotechnology Information, U.S. National Library of Medicine. Web. 8 July 2015.
6. Prabhakar, H., P. Bithal, A. Suri, G. Rath, and H. Dash. "Intracranial Pressure Changes During Valsalva Manoeuvre in Patients Undergoing a Neuroendoscopic Procedure." Min - Minimally Invasive Neurosurgery Minim Invasive Neurosurg 50.2 (2007): 98-101. Web. 24 July 2015.
7. Stone, Michael B., Catherine M. Tubridy, and Robert Curran. "The Effect of Rigid Cervical Collars on Internal Jugular Vein Dimensions." Academic Emergency Medicine 17.1 (2010): 100-02. Web. 22 July 2015.

Arm Position Alters the Geometry of Brachial Artery and Basilic Vein

Conor MacDonald[1], Nicolas Aristokleous[2], Shona Matthew[2], Stephen Gandy[3], Malcolm H. Dunn[1], and J. Graeme Houston[3]

[1]School of Physics and Astronomy, University of St Andrews, UK
[2]Department of Cardiovascular and Diabetes Medicine, School of Medicine, University of Dundee, Dundee, UK
[3]Medical Physics, NHS Tayside, Ninewells Hospital and Medical School, Dundee DD1 9SY, UK

Purpose

The brachial artery and basilic vein are two vessels commonly used for arterio-venous fistula creation in patients with end stage renal disease. Advantages are that it produces superficial fistula with a high flow rate and offer good long term patency [2]. Few studies have assessed the impact of vessel geometry on the internal haemodynamics of these vessels. Certain geometric parameters such as the curvature and tortuosity of the blood vessels are known to affect the blood flow profiles inside the vessel, and thus influence levels of wall shear stress (WSS) - the driving force in vascular remodeling [1]. This study aims to estimate the impact of two different arm positions (supine and 'superman') on significant geometrical features associated with haemodynamics.

Methods

The group of volunteers consisted of eight healthy men and women (Age 32.7 years, range 27 - 42 years). Magnetic Resonance (MR) images were obtained with a 3T MR unit (Siemens MAGNETOM Trio) using a surface coil (8 Channel, Siemens) wrapped around the participant's arm of interest. Images were taken using a high-resolution sequence called Multi Echo Data Image Combination (MEDIC). The pulse sequence implemented a TE of 16 ms, a TR of 29 ms and a flip angle of 8°.
The solid surface models were constructed from the MR images, using a semi-automatic segmentation technique in ITK-Snap and then post-processed in vascular modeling toolkit (VMTK). All properties were determined according to relevant published definitions. Figure 1 shows the bifurcation angle, generated from space vectors on the centerline, calculated in VMTK.

Fig.1: Angle bifurcation of the Basilic vein.

Results

Figure 2 (left) shows the changes of basilic vein bifurcation angle. The changes of the brachial artery curvature for both arm positions and for each volunteer independently represented on the right histogram. To test the reproducibility of our study between analysts, the models of a volunteer were created by two members of our team. Results showed small changes: a) in the bifurcation angle (12%) and b) on the models volume (3.7%).
A change in arm position influenced the bifurcation angle, with six out of eight volunteers showing an increased angle in the supine position. The mean change corresponded to a 15% change. The results were not statistically significant (P>0.05) likely due to the large amount of variance in the results and the small sample size.
Razavi et al. [4] investigated a range of angles for an idealised coronary bifurcation using computational flow dynamics found that WSS values increased with angle at the outer, lower and upper boundaries of the bifurcation. Using these models in similar simulations are expected to reproduce these effects. Few studies have investigated the effect of curvature on haemodynamics. It is accepted that the vessel geometry has an effect on the flow field inside the vessel. Friedman et al. [3], suggested that the geometry of the vessel may have an effect on the likelihood of developing atherosclerosis, proposed the idea of 'geometric risk factors'. We can see from these results that arm position clearly affects the curvature of the brachial artery, inferring that the haemodynamics of the vessel will change with arm position.

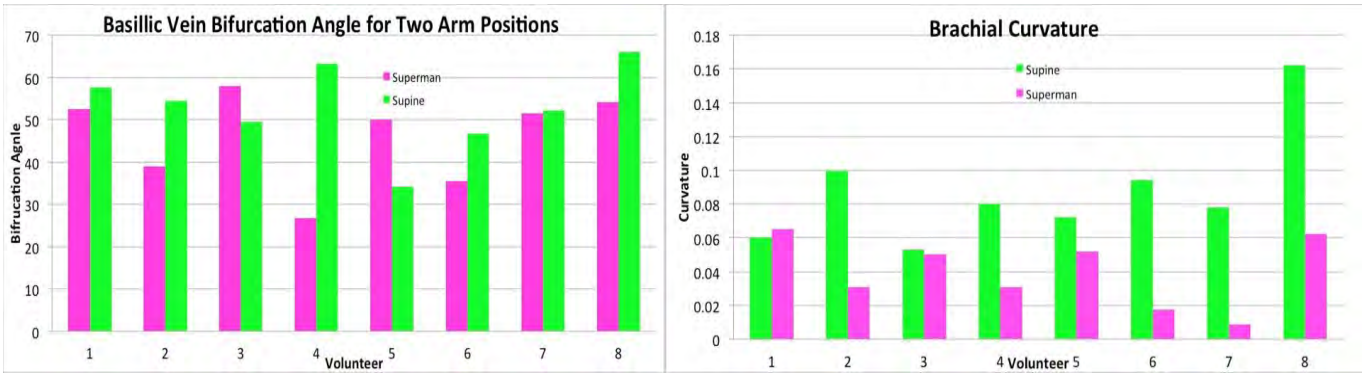

Fig. 2: Change in bifurcation angle of the basilic vein and curvature of the brachial artery for 8 volunteers.

References

[1] Achneck, H. E., and B. Sileshi. 2010. Semin. Dial 23:25–33.
[2] Dix, F., Y. Khan, and H. Al-Khaffaf. 2006. European Journal of Vascular and Endovascular Surgery 31 (1):70 – 79.
[3] Friedman, M. H., and et al. 1983. Atherosclerosis 46 (2):225–231.
[4] Razavi, S. E., A. A. Omidi, and M. S. Zanjani. 2014. Bioimpacrs 4 (4):199–204.

Acknowledgements

This work has received funding from the European Unions 7th Framework Program for research, technological development and demonstration under grant agreement no. 3244487 (ReDVA).

Free-Breathing Non-Contrast Pulmonary MRA in the Neonatal ICU

Jean Tkach[1], Laura Walkup[2], Stephanie Merhar[3], Paul Kingma[3], Robert Fleck[4], Jason Woods[2]

[1]Imaging Research Center, Department of Radiology, Cincinnati Children's Hospital Medical Center, Cincinnati, OH; [2]Center for Pulmonary Imaging Research, Division of Pulmonary Medicine and Department of Radiology, Cincinnati Children's Hospital Medical Center, Cincinnati, OH; [3]Division of Neonatology and Pulmonary Biology, Cincinnati Children's Hospital Medical Center, Cincinnati, OH; [4]Department of Radiology, Cincinnati Children's Hospital Medical Center, Cincinnati, OH

Purpose: Many neonatal abnormalities disrupt pulmonary vascular growth and result in impaired gas exchange, abnormal vasoreactivity, and/or pulmonary vascular remodeling, all of which are associated with significant morbidity and mortality (1). Idiopathic pulmonary arterial hypertension (PAH) occurs in some infants with putatively normal lung parenchyma but remodeled pulmonary vasculature. Similarly, pulmonary vascular disease (PVD) is common in neonates with bronchopulmonary dysplasia (BPD) and congenital diaphragmatic hernia (CDH), often resulting in PAH. Two recent studies reported a 2 year mortality rate in infants with BPD of 33-38% after PAH diagnosis (2). CT and dynamic contrast enhanced (DCE) MRA are the two techniques most commonly used to assess pulmonary vasculature in older children and adults. However, CT involves ionizing radiation and the concern over the use of IV contrast poses challenges for applying DCE MRA in the neonate, particularly in the NICU environment. Hence, there is a compelling need to develop an alternative approach to image the pulmonary vasculature in the neonate. The objective of this study was to develop a non-contrast, free-breathing MR imaging approach to allow for the longitudinal assessment of the pulmonary vasculature in the neonate.

Methods: MR imaging was performed on a small footprint 1.5T MR system sized specifically for the neonate and installed in the Neonatal Intensive Care Unit (NICU) at our Institution (3,4). 9 neonates with normal pulmonary function, 4 with lung disease related to prematurity (e.g. BPD) and 7 with CDH were evaluated. The neonates were imaged free breathing and without sedation. The following sequences were applied in the axial plane, with the intention of evaluating the pulmonary vasculature: 1) 2D TOF (TR/TE/FA= 6.6-10.5ms/3.5-4.6ms/45-60°; FOV=16-17cm, matrix=192x320 , 1.5 - 3mm thick slices with 30-38% overlap; acquired sequentially inferior to superior, 1-4 averages; 17 patients), 2) 2D Fat Saturation FIESTA (TR/TE/TI/FA=4.7-7.7ms/1.2-2.2ms/200ms/45-70°; FOV=20-24cm, matrix =256x256; , slice thickness=3-5mm, 1-2averages; 3 patients), 3) 3D FGRE (TR/TE/FA=6.3ms/1.8ms/4°-10°; FOV=18-20cm, matrix=256x256; 28-32 3mm partitions, 5 averages; 17 patients). Maximum Intensity Projection (MIP) images along the S/I direction were generated from each data set. The ability of each technique to visualize the pulmonary vasculature (e.g. number of branches seen) was evaluated in the base and projection images by 2 independent observers.

Results: The number and extent (number of branches) of the pulmonary vessels visualized were significantly greater for the 2D TOF sequence as compared to the other two techniques (Figure). The small fields of view and slice thickness required to image the neonate led to prolonged TR's for the 2D FIESTA, resulting in reduced transverse coherence (hence reduced blood signal), increased motion artifact and significant banding. Differentiation between the vasculature and lung parenchyma was also difficult in the presence of lung pathologies. As compared to the spin-density weighted 3D FGRE, the vessels exhibited higher signal and were better discriminated from the parenchymal abnormalities (e.g. bronchiectasis, atelectasis) in the BPD infants reflecting the enhanced inflow effects and background suppression inherent to the 2D TOF technique.

Conclusions: Free-breathing, non-contrast 2D TOF techniques are a viable means of obtaining detailed images of the pulmonary vasculature in the neonate longitudinally. This approach and the information provided holds promise to provide a method to follow these infants and advance the diagnosis and long term management of PVD and PAH in infants that cannot undergo traditional DCE MRA.

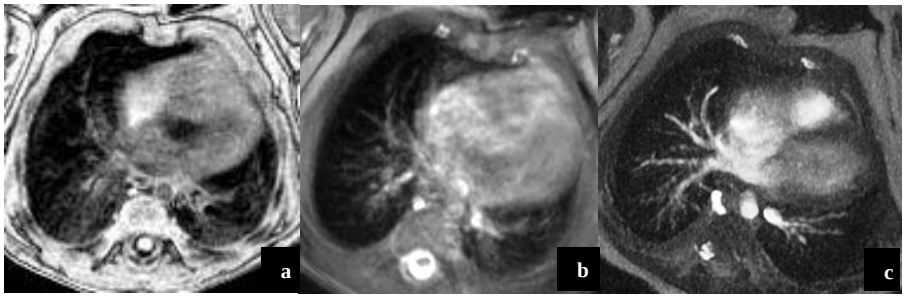

Spin density weighted 4° 3D FGRE image (a), 2D Fast Saturation FIESTA MIP (b) and 2D TOF MIP (c) images in a 3.3kg male infant with left congenital diaphragmatic hernia evaluated post repair.

References: 1. RH Steinhorn, Pediatr Crit Care Med 11(2Suppl):S79-S84, (2010), 2. CD Baker, et al., Pediatr Allergy, Immun and Pulm 27:8-16, (2014), 3. JA Tkach, et al., Pediatr Radiol 42:1347-1356 (2012), 4. JA Tkach, et al., Amer J Roentgen 202:W95-W105 (2014).

Quantification of myocardial motion patterns in patients with hypertrophic- and dilated-cardiomyopathy using heart deformation analysis

Kai Lin[1], Jeremy Collins[1], Marie-Pierre Jolly[2], Julie Blaisdell[1], Michael Markl[1], James Carr[1]

1 Department of Radiology, Northwestern University Feinberg School of Medicine, Chicago, IL 2 Siemens Corporation

Purpose To test the hypothesis that heart deformation analysis (HDA) is able to characterize left ventricle (LV) motion patterns of patients with hypertrophic (HCM) and dilated cardiomyopathy (DCM).

Methods

Following the approval of the institutional review board (IRB), standard cine images (with two-chamber, four-chamber and short-axis views) of 45 subjects, including 15 asymptomatic volunteers, 15 HCM patients and 15 DCM patients were analyzed using the HDA tool. Post processing using the HDA tool using a succinct workflow: Cine MRI images, including 2-chamber, 4-chamber and a stack of short-axis images were loaded to a dedicated image processing workstation (Dell, STUDIO, SPS 435T) and analyzed with prototype software programmed in Visual C++ (TrufiStrain, Siemens Corporation, Corporate Technology, Princeton, NJ) by an experienced analyzer (1, 2). See figure 1. The variations of global myocardial motion indices, including radial (Drr) and circumferential (Dcc) displacement, radial (Vrr) and circumferential (Vcc) velocity, radial (Err), circumferential (Ecc) and shear (Ess) strain and radial (SRr) and circumferential (SRc) strain rates, were calculated through the cardiac cycle. Peak motion indices were related to LVEF and compared between three subject groups.

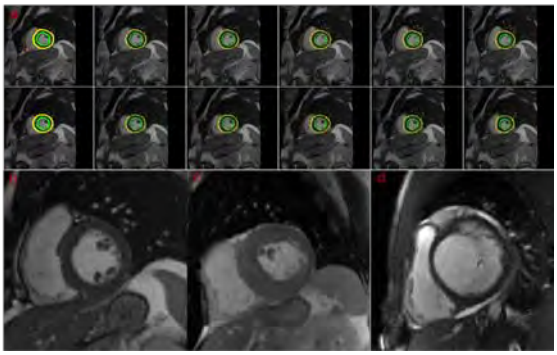

Figure 1 The "One-stop-shop" work flow of HDA for the analysis of displacement, velocity, strain and stain rate in healthy volunteers, HCM and DCM patients. a The contours of the LV were automatically drawn by the HDA tool. b A male healthy volunteer with normal LV wall. c A male HCM patient with a thickened LV wall (> 15mm). d A male DCM patient with a thin LV wall.

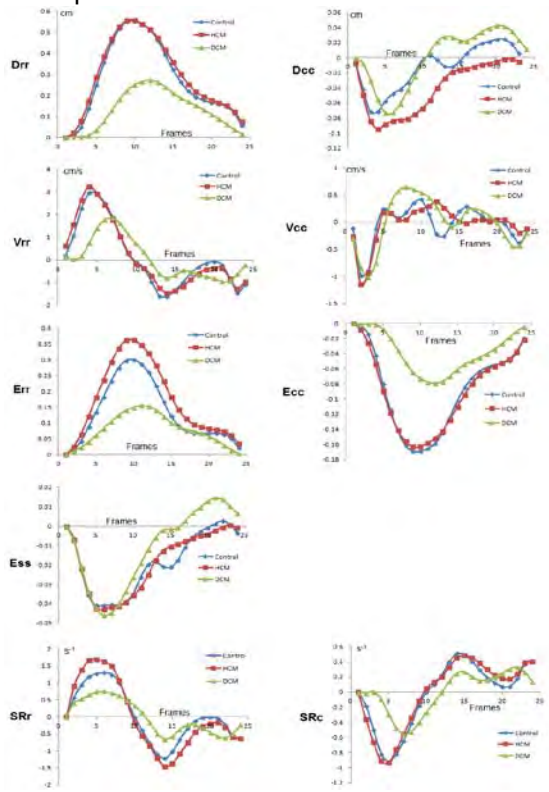

Figure 2 The variances of displacement, velocity, strain and strain rate in 3 subject groups.

Results

DCM vs. HCM patients: DCM patients have significantly lower peak Drr (0.29±0.11 vs. 0.57±0.10 cm, p < 0.001), Vrr-sys (2.14±0.72 vs. 3.41±1.07 cm/s, p = 0.001), Err (0.17±0.08 vs. 0.38±0.12, p < 0.001), Ecc (-0.08±0.03 vs. -0.17±0.03, p < 0.001), SRr-sys (0.91±0.44 vs. 1.85±0.82 s^{-1}, p = 0.001) and SRc-sys (-0.64±0.27 vs. -1.00±0.29 s^{-1}, p = 0.002) than HCM patients. HCM patients have lower peak Vcc-dia (0.78±0.30 vs. 1.07±0.38 cm/s, p = 0.028) than DCM patients. **DCM patients vs. healthy volunteers:** DCM patients have significantly lower peak Drr (0.29±0.11 vs. 0.58±0.12 cm, p < 0.001), Vrr (2.14±0.72 vs. 3.08±1.07 cm/s, p = 0.001), Err (0.17±0.08 vs. 0.31±0.08, p < 0.001) , Ecc (-0.08±0.03 vs. -0.17±0.02, p < 0.001), SRr (0.91±0.44 vs. 1.39±0.34 s^{-1}, p = 0.003) and SRc (-0.64±0.27 vs. -0.95±0.21 s^{-1}, p = 0.002) than healthy volunteers.**HCM patients vs. healthy volunteers:** There are no significant differences of peak Drr, Dcc, Vrr, Vrr, Err, Ecc, Ess, SRr and SRc in systole and diastole between HCM patients and healthy volunteers. See figure 2 and table 1. HDA-derived peak global displacement, velocity, strain and strain rate are closely related with LVEF (r = 0.449 - 0.883). See figure 3.

Peak values	Volunteers	HCM	DCM
Drr (cm)	0.57± 0.10*	0.58±0.12**	0.29± 0.11
Dcc (cm)	-0.09± 0.04	-0.13±0.09	-0.09± 0.06
Vrr-sys (cm/s)	3.08±0.46*	3.41±1.07**	2.14±0.72
Vrr-dia (cm/s)	-2.39±0.60	-2.21±0.65	-1.92±0.86
Vcc-sys (cm/s)	-1.19±0.41	-1.30±0.59	-1.38±0.57
Vcc-dia (cm/s)	0.83±0.35	0.78±0.30**	1.07±0.38
Err	0.31±0.08*	0.38±0.12**	0.17±0.08
Ecc	-0.17±0.02*	-0.17±0.03**	-0.08±0.03
Ess	0.05±0.02	0.05±0.03	0.05±0.03
SRr-sys (s-1)	1.39±0.34*	1.85±0.82**	0.91±0.44
SRr-dia (s-1)	-1.64±0.77	-1.95±0.90**	-1.22±0.82
SRc-sys (s-1)	-0.95±0.21*	-1.00±0.29**	-0.64±0.27
SRc-dia (s-1)	0.70±0.24	0.71±0.21	0.58±0.35

Table 1 Comparisons of peak motion indices among subject groups * There are significant differences (p < 0.05) between healthy volunteers and DCM patients. ** There are significant differences (p < 0.05) between HCM and DCM patients.

Conclusion

HDA is able to discriminate characteristic LV motion patterns between HCM and DCM patients. HDA has the potential to serve as an efficient tool for the evaluation of myocardial motion patterns.

References: 1. Jolly M-P et al. Statistical Atlases and Computational Models of the Heart Imaging and Modelling Challenges.2012;7085:98-108. 2. Guetter C et al. 2011 IEEE International Symposium, 2011:590-593.

Linear sign in cystic brain lesions ≥ 5mm on T2-weighted images and time-of-flight MR angiography: A suggestive feature of enlarged perivascular space on 3.0-T MR imaging

Jinkyeong Sung, MD, Jinhee Jang, MD, Song Lee, MD, Hyun Seok Choi, MD, So-Lyung Jung, MD, Kook-Jin Ahn, MD, Bum-soo Kim, MD
Department of Radiology, Seoul St.Mary's Hospital, The Catholic University of Korea, Seoul, KOREA

PURPOSE: To determine the prevalence of linear sign within enlarged perivascular space (EPVS) and chronic lacunar infarction (CLI) ≥ 5 mm on T2-weighted imaging (T2WI) and time-of-flight MR angiography (TOF-MRA), and to evaluate the diagnostic value of the linear sign on these MR images for EPVS over CLI.
MATERIALS AND METHODS: The institutional review board approved this retrospective study and waived the requirement for informed consent. This study included 101 patients (44 men, 57 women; mean age, 67.1 years) with cystic lesions ≥ 5 mm who underwent brain MR imaging that included TOF-MRA at 3.0 T. Two experienced neuroradiologists classified the cystic lesion into EPVS or CLI. Two other reviewers independently assessed linear signs on T2WI and TOF-MRA using three-point scale in the lesions that both neuroradiologists classified as EPVS or CLI. The prevalence of T2 and TOF linear signs was compared by using Chi-square test. Sensitivity and specificity were compared by using McNemar statstics.
RESULTS: Forty-six and 51 lesions were classified as EPVS and CLI, repectively. Inter-observer agreement was substatntial for the T2 linear sign (κ = 0.759) and almost perfect for the TOF linear sign (κ = 0.956). The prevalence of both T2 and TOF linear signs was significantly higher n the EPVS group than in the CLI group ($P < .001$). Definite linear sign on T2WI and TOFMRA yielded high specificity (98%-100%) and positive predictive value (96.4%-100%). The presence of linear sign yielded significantly higher specificity on TOF-MRA (100%) than T2WI (70.6% - 72.6%) for the diagnosis of EPVS ($P < .001$).
CONCLUSION: The linear signs on T2WI and TOF-MRA were more frequently observed in EPVS ≥ 5 mm than CLI at 3.0 T and provided high specificity and PPV for differentiating EPVS from CLI.

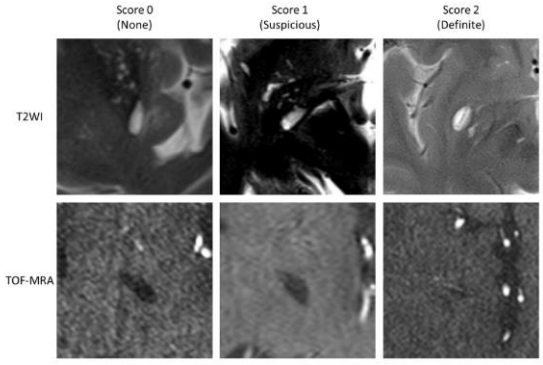

Figure 1. Classification of T2 and TOF linear signs Left to right, the first row shows representative cases of linear sign on T2WI; score 0 (none), 1 (suspicious), and 2 (definite). The second row shows representative cases of linear sign on TOF-MRA; score 0 (none), 1 (suspicious), and 2 (definite). In the middle column, suspicious cases had suspicious linear structures within the cystic lesions.

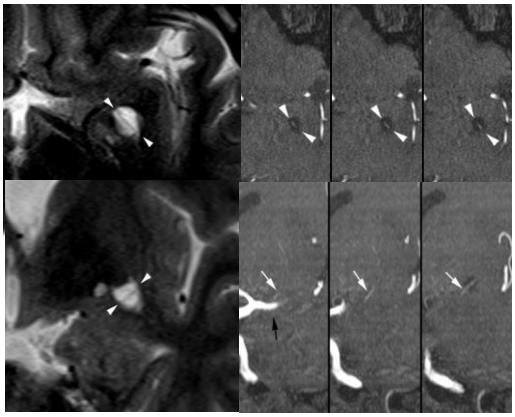

Figure 2. A 77-year-old male underwent MR imaging of the brain as a part of his evaluation for dementia. A cystic lesion of about 7 mm is seen in the inferior aspect of the left basal ganglia in axial (a) and coronal (b) T2WIs. There is a well-defined linear low signal intensity (arrowheads) at the center of the cystic lesion (T2 linear sign score 2). On serial source images of TOF-MRA (c), a fine linear vascular structure (arrowheads in c) is seen at the cystic lesion (TOF linear sign score 2), which matches well to the linear low signal on T2WI. On serial images of coronal reformatted TOF-MRA images (d), this linear flow-related signal (white arrows) arises from the M1 segment of the left middle cerebral artery (black arrow).

Single Breath-Hold Real-Time Cardiac Cine MR for Evaluation of Left Ventricular Function

Tomoyuki Kido[1], Teruhito Kido[1], Kouki Watanabe[2], Hitoshi Miki[3], Teruhito Mochizuki[1]

Department of Radiology, Ehime University Hospital[1]

Department of Cardiology, Saiseikai Matsuyama Hospital[2]

Department of Radiology, Ehime Prefectural Central Hospital[3]

Purpose

Cardiac cine Magnetic Resonance (MR) is generally accepted as the gold standard for left ventricular (LV) volume assessment. Recently, Real-Time (RT) cine with sparse sampling technique and iterative reconstruction has been applied to accelerate cine MR. The purpose of this study was to evaluate the diagnostic quality and accuracy of single-breath-hold RT cine MR for the quantification of LV function compared with multi-breath-hold standard cine MR.

Methods

Fifty participants underwent both RT and standard cine MR for the assessment of LV function on 3 tesla MRI. The cine images were obtained in 8 contiguous short axis slices spanning the entire LV. The image quality, ejection fraction (EF), end diastolic volume (EDV), end systolic volume (ESV), stroke volume (SV), and LV mass for standard cine and RT cine were compared.

Results

All RT cine showed acceptable diagnostic image quality. Standard and RT cine showed good agreement: EF (60.3±10.2% vs. 60.2±9.8%; R^2=0.89; p=0.78); EDV (132.0±36.6 ml vs. 131.1±35.9 ml; R^2=0.94; p=0.44); ESV (54.6±27.2 ml vs. 54.1±25.6 ml; R^2=0.95; p=0.53); SV (77.4±16.0 ml vs. 77.0±16.3 ml; R^2=0.84; p=0.67); LV mass (87.1±33.7 ml vs. 85.8±33.9 ml; R^2=0.97; p=0.15), respectively. The intra- and inter-observer agreement for all parameters was good.

Conclusions

The single-breath-hold sparse RT cine MR has the potential to replace the multi-breath-hold standard cine MR.

Reference

Highly accelerated real-time cardiac cine MRI using k-t SPARSE-SENSE. Feng L, et al. Magn Reson Med 2013; 70: 64-74.

Compressed sensing single-breath-hold CMR for fast quantification of LV function, volumes, and mass. Vincenti G, et al. JACC Cardiovasc Imaging 2014; 7: 882-92.

Carotidynia MRI imaging findings

George Bolotin MD, Ananth Narayan MD
Albany Medical Center

Pupose

To familiarize the reader with imaging findings of Carotidynia; an idiopathic neck pain syndrome complicated by frequently absent abnormal pathologic and imaging findings.

Methods

Imaging was reviewed from a patient who presented with unilateral neck pain and extreme tenderness to palpation in the region of the carotid bifurcation. An initial CTA ruled out thrombus, dissection and stenosis. Subsequently, an MRI of the soft tissues of the neck was obtained.

Results

CTA

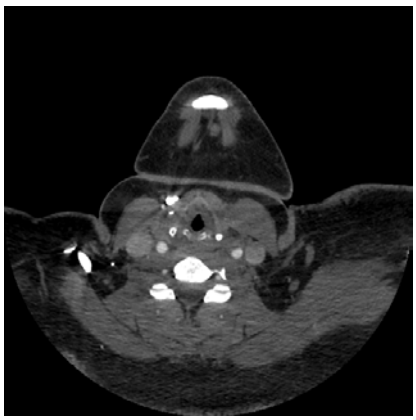

Cor STIR +C

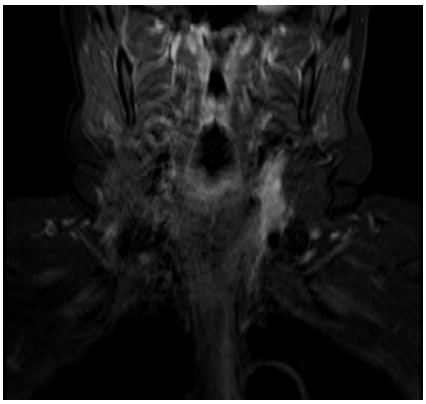

Cor STIR

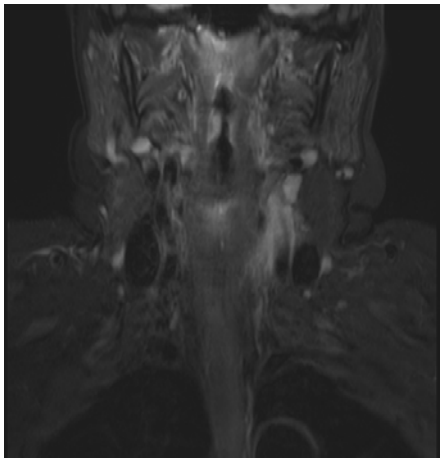

Ax STIR

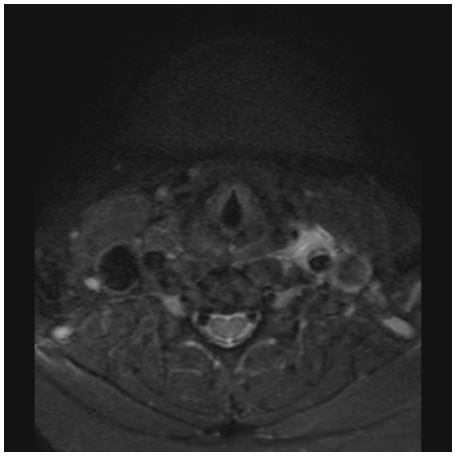

Author Index